# **Springer Theses**Recognizing Outstanding Ph.D. Research

Ivan Levkivskyi

# Mesoscopic Quantum Hall Effect



# Springer Theses

Recognizing Outstanding Ph.D. Research

For further volumes: http://www.springer.com/series/8790

### Aims and Scope

The series "Springer Theses" brings together a selection of the very best Ph.D. theses from around the world and across the physical sciences. Nominated and endorsed by two recognized specialists, each published volume has been selected for its scientific excellence and the high impact of its contents for the pertinent field of research. For greater accessibility to non-specialists, the published versions include an extended introduction, as well as a foreword by the student's supervisor explaining the special relevance of the work for the field. As a whole, the series will provide a valuable resource both for newcomers to the research fields described, and for other scientists seeking detailed background information on special questions. Finally, it provides an accredited documentation of the valuable contributions made by today's younger generation of scientists.

### Theses are accepted into the series by invited nomination only and must fulfill all of the following criteria

- They must be written in good English.
- The topic should fall within the confines of Chemistry, Physics, Earth Sciences, Engineering and related interdisciplinary fields such as Materials, Nanoscience, Chemical Engineering, Complex Systems and Biophysics.
- The work reported in the thesis must represent a significant scientific advance.
- If the thesis includes previously published material, permission to reproduce this must be gained from the respective copyright holder.
- They must have been examined and passed during the 12 months prior to nomination.
- Each thesis should include a foreword by the supervisor outlining the significance of its content.
- The theses should have a clearly defined structure including an introduction accessible to scientists not expert in that particular field.

## Ivan Levkivskyi

# Mesoscopic Quantum Hall Effect

Doctoral Thesis accepted by the University of Geneva, Switzerland



Author
Dr. Ivan Levkivskyi
University of Geneva
Geneva
Switzerland

Supervisor
Prof. Eugene Sukhorukov
University of Geneva
Geneva
Switzerland

Co-Supervisor
Prof. Jürg Fröhlich
Swiss Federal Institute of Technology
Zurich
Switzerland

ISSN 2190-5053 ISSN 2190-5061 (electronic) ISBN 978-3-642-30498-9 ISBN 978-3-642-30499-6 (eBook) DOI 10.1007/978-3-642-30499-6

Springer Heidelberg New York Dordrecht London

Library of Congress Control Number: 2012940717

#### © Springer-Verlag Berlin Heidelberg 2012

This work is subject to copyright. All rights are reserved by the Publisher, whether the whole or part of the material is concerned, specifically the rights of translation, reprinting, reuse of illustrations, recitation, broadcasting, reproduction on microfilms or in any other physical way, and transmission or information storage and retrieval, electronic adaptation, computer software, or by similar or dissimilar methodology now known or hereafter developed. Exempted from this legal reservation are brief excerpts in connection with reviews or scholarly analysis or material supplied specifically for the purpose of being entered and executed on a computer system, for exclusive use by the purchaser of the work. Duplication of this publication or parts thereof is permitted only under the provisions of the Copyright Law of the Publisher's location, in its current version, and permission for use must always be obtained from Springer. Permissions for use may be obtained through RightsLink at the Copyright Clearance Center. Violations are liable to prosecution under the respective Copyright Law.

The use of general descriptive names, registered names, trademarks, service marks, etc. in this publication does not imply, even in the absence of a specific statement, that such names are exempt from the relevant protective laws and regulations and therefore free for general use.

While the advice and information in this book are believed to be true and accurate at the date of publication, neither the authors nor the editors nor the publisher can accept any legal responsibility for any errors or omissions that may be made. The publisher makes no warranty, express or implied, with respect to the material contained herein.

Printed on acid-free paper

Springer is part of Springer Science+Business Media (www.springer.com)

### **Supervisor's Foreword**

The quantum Hall effect is one of the central subjects of the modern condensed matter physics. This effect manifests itself in the universal quantization of the Hall resistance of a two-dimensional electron gas, exposed to a perpendicular magnetic field. Being a linear function of the magnetic field in weak fields, the Hall resistance in strong fields develops a number of plateaus as a function of the filling factor  $\nu$ , which is given by the ratio of the number of electrons in a two-dimensional electron gas per magnetic flux quantum. In a two-dimensional electron gas implemented in semiconductor hetero-structures, the quantization of the Hall resistance at integer filling factors (integer quantum Hall effect) is so precise that it provides one of the most accurate values for the fine structure constant, and serves as a modern resistance standard. In the regime of the fractional quantum Hall effect, with the filling factor given by rational fractions, two-dimensional electron gas supports exotic quasi-particle excitations with fractional charge and fractional statistics and other unusual properties. Being one of the first examples of the topologically non-trivial state of matter, the quantum Hall effect has received a strong attention of experimentalists and theorists. Nevertheless, despite 30 years of intensive research and after two Nobel prizes awarded in this field, the rich and complex physics of the quantum Hall effect is not yet fully understood.

Another fascinating domain of the modern condensed matter physics, which has shown a remarkable success in the previous decades, is the mesoscopic physics. In a broad sense, it studies how the microscopic, quantum laws of nature manifest themselves at the macroscopic scale, in the classical world that we observe. Recently, a rapid progress in fabrication of small semiconductor heterostructures has made it possible to investigate electronic properties of quantum Hall systems at mesoscopic scale. Already first experiments in this direction have shown unexpected and puzzling results, such as the non-monotonous decoherence and phase rigidity in quantum Hall interferometers, missing energy paradox, non-Gaussian noise effects, etc. New exciting mesoscopic experiments are under way. The thesis of Ivan Levkivskyi theoretically investigates the physics behind these phenomena.

The mesoscopic properties of the systems exhibiting quantum Hall effect are determined by the chiral edge states, which are the quantum analogs of skipping orbits of electrons, arising at a boundary of two-dimensional electron gas in the magnetic field. Because of the reduced dimensionality of these states, the Coulomb interaction strongly alters their physical properties. It turns out, that the Fermi liquid theory, commonly used for the description of many-electron metallic systems, fails in one dimension. It becomes more appropriate to represent quantum Hall edge states in terms of weakly interacting collective boson excitations, which may be viewed as edge deformations of incompressible quantum Hall liquids. In order to describe mesoscopic properties of such states, the thesis develops several theoretical methods, including the non-equilibrium bosonization technique, the classification of the effective models of quantum Hall edge states, and the microscopic low-energy projection technique.

The non-equilibrium bosonization technique allows one to reduce the problem of finding non-equilibrium correlation functions of one-dimensional strongly interacting electrons to the evaluation of averages over the ensemble of free fermions. When applied to quantum Hall edge states at integer filling factors, this technique provides an elegant explanation to the mentioned above puzzling experimental results. However, Dr. Levkivskyi goes ahead and predicts a new phenomenon of noise induced phase transition in electronic quantum Hall interferometers. The edge states in such interferometers play the role of optical beams, and the interference effects are experimentally observed by measuring Aharonov–Bohm oscillations in the average current as a function of the magnetic flux. When edge states are exposed to a non-equilibrium noise, this leads to the suppression of the phase coherence and reduces the amplitude of Aharonov–Bohm oscillations. The phase transition manifest itself in the non-analytic dependence of the amplitude of Aharonov–Bohm oscillations on the parameters of the noise. The important role in this phenomenon is played by non-Gaussian noise effects.

The classification of edge models at fractional filling factors relies on the minimal physical requirements to the effective theory of quantum Hall edge states to be gauge invariant, to be able to describe electron and quasi-particle excitations, and on the requirement of single-valuedness of these excitations with respect to electron coordinates. For simple filling fractions  $\nu=1/m$ , where m is odd integer, such minimal and physically appealing requirements uniquely fix the model of edge states, which is not the case for more complex states, such as  $\nu=2/m$ . Dr. Levkivskyi then proposes to classify the effective models on the basis of the statistics of quasi-particle excitations. He argues, that the strong Coulomb interaction at the edge reduces further the number of possible models. He then proposes to differentiate remaining models in experiment be measuring scaling dimensions of most relevant quasi-particle excitations with the help of quantum Hall interferometers. This idea, supported by concrete theoretical predictions, yet waits for the experimental realization.

Finally, the microscopic low-energy projection technique has been developed in the thesis in order to address a conceptual problem that arises in the effective theory of open quantum Hall systems at fractional fillings, confined to a region with topologically non-trivial shape. This problem, formulated as a paradox, has attracted a strong attention of the mesoscopic physics community. To be brief, the interference of fractionally charged quasi-particles is expected to lead to Aharonov–Bohm oscillations with periods larger than the flux quantum. However, according to the Byers–Yang argument, observables of an electronic system are invariant under adiabatic insertion of a quantum of singular flux. Not only Dr. Levkivskyi resolves this seeming paradox. By doing so, he bridges the gap between two entirely different theoretical approaches to the quantum Hall physics, the microscopic and the effective theories of quantum Hall edge states.

In summary, the work of I. Levkivskyi opens a new broad domain of research at the intersection of the mesoscopic and the quantum Hall physics. The mesoscopic phenomena in quantum Hall systems are very rich and fascinating. They shed new light on the complex physics and represent one of the few cases where the sophisticated theoretical constructions, such as, e.g., the topological quantum field theory, can be used successfully in order to quantitatively describe complex experimental situations.

Geneva

Prof. Eugene Sukhorukov

### Acknowledgments

I would like to thank my supervisor Eugene Sukhorukov and my co-supervisor Jürg Fröhlich for several fruitful discussions, smart advice, and constant support while completing this work. I thank my colleagues C. W. J. Beenakker, A. Boyarsky, V. Cheianov, Iu. Chernii, P. Degiovanni, N. Magnoli, A. Koroliuk, and O. Ruchayskiy for valuable discussions. I am grateful to E. Bieri, M. Heiblum, L. Litvin, S. Oberholzer, F. Pierre, P. Roche, and C. Schönenberger for clarifying the experimental details. I would like to thank my thesis referees T. Giamarchi, B. Halperin, and L. Levitov for important comments and suggestions.

I thank our secretaries Cecile, Daniel, and Francine for help in many situations. I would like to thank my wife Ievgeniia for proofreading the thesis and support while completing this work. I thank Y. Gaponenko for the French translation of the thesis summary.

This work has been supported by the Swiss National Science Foundation.

## **Contents**

1	Intr	oductio	on	1	
	1.1	Mesos	scopic Physics	1	
		1.1.1	Two-Dimensional Electron Gas	3	
	1.2	rum Hall Effect Basics	5		
		1.2.1	Classical Hall Effect	5	
		1.2.2	Experimental Results	6	
		1.2.3	Landau Quantization	8	
	1.3	Theor	etical Approaches to Quantum Hall Effect	12	
		1.3.1	Single Particle Picture	12	
		1.3.2	Effective Theory	17	
		1.3.3	Microscopic Approach	24	
	1.4	Quant	rum Hall Effect at Mesoscopic Scales	31	
		1.4.1	Mesoscopic Systems Utilizing Edge States	31	
		1.4.2	Formulation of Problems and Outline	34	
	Refe	erences		36	
Pa	art I	Intege	r Quantum Hall Effect		
2	Equ		m and Non-Equilibrium Bosonization	41	
	2.1	Boson	nization of One-Dimensional Fermions	41	
		2.1.1	One-Dimensional Interacting Systems	41	
		2.1.2	Bosonic Fields and Hamiltonian	43	
		2.1.3	Quantization of Boson Fields and Zero Modes	46	
	2.2	Correl	lation Function at Finite Temperature	47	
	2.3	2.3 Non-Equilibrium Bosonization			
		2.3.1	Non-Equilibrium Boundary Conditions		
			and Full Counting Statistics	50	
		2.3.2	Equilibrium Boundary Conditions: A Simple Test	51	

xii Contents

2.4	Conclusions	53
Refe	erences	53
Inte		55
3.1		55
	3.1.1 Only Interfering Edge Channel is Biased	55
	3.1.2 All Edge Channels are Biased	57
3.2	Model of Mach-Zehnder Interferometer	58
	3.2.1 Fields and Hamiltonian	59
	3.2.2 Bosonization	60
		61
3 3		63
	Discussion of Experiments	66
Э.т		69
	•	71
		73
25	1	74
кете	rences	76
<b>N</b> T - *	. I. J. J. Douberton of Education	77
		77
		78
		80
		82
4.4		85
		85
		87
4.5	Conclusions	88
Refe	erences	89
Ene		91
5.1	Experimental Results	92
5.2	Theoretical Model	94
	5.2.1 Correlation Function	95
5.3	Electron Distribution Function	98
	5.3.1 Short Distances	98
		100
		102
5.4		102
		105
		103
	3.1 3.2 3.3 3.4 3.5 Refe  Nois 4.1 4.2 4.3 4.4 4.5 Refe  Ener 5.1 5.2 5.3	Interaction Induced Dephasing of Edge States. 3.1 Experimental Results 3.1.1 Only Interfering Edge Channel is Biased 3.1.2 All Edge Channels are Biased 3.2.1 Fields and Hamiltonian 3.2.2 Bosonization. 3.2.3 Strong Interaction Limit and the Universality 3.3 Visibility and Phase Shift. 3.4 Discussion of Experiments 3.4.1 Only Interfering Edge Channel is Biased 3.4.2 All Edge Channels are Biased 3.4.3 Effects of Finite Temperature  3.5 Conclusion References  Noise Induced Dephasing of Edge States 4.1 Experimental Setup and the Model 4.2 Correlation Functions 4.3 Situation with Non-Equilibrium Gaussian Noise 4.4 Noise Induced Phase Transition. 4.4.1 Non-Gaussian Noise in Markovian Limit 4.4.2 Quantum Correction at Critical Point 4.5 Conclusions References  Energy Relaxation at the Quantum Hall Edge 5.1 Experimental Results 5.2 Theoretical Model 5.2.1 Correlation Function 5.3.1 Short Distances 5.3.2 Intermediate Distances 5.3.3 Long Distances 5.4 Measured and Total Heat Fluxes 5.5 Conclusions  Proceedings of Edge States 4.4 Measured and Total Heat Fluxes 5.5 Conclusions

Contents xiii

Part II	Fractional	Quantum	Hall	Effect

6	Clas	sification of Effective Edge Models	111		
	6.1	Effective Theory of Quantum Hall Edges	112		
		6.1.1 Chern–Simons Theory and Gauge Anomaly	112		
		6.1.2 Hydrodynamics of Incompressible			
		Edge Deformations	114		
		6.1.3 Quantization of Edge Excitations	116		
		6.1.4 Gauge-Invariant Formulation	117		
	6.2	Multi-Channel Edge Models	119		
		6.2.1 Kinematics of Edge Models	119		
		6.2.2 Local Excitations	122		
		6.2.3 Scaling Dimensions of Local Excitations	123		
	6.3	Conclusions	124		
	Refe	erences	125		
7		etroscopy of Quantum Hall Edge States			
	at C	Complex Filling Factors	127		
	7.1	Minimal Models for Filling Factor $\nu = 2/m$	129		
	7.2	The Role of Coulomb Interactions	132		
	7.3	Experimental Determination of Scaling Dimensions			
		of Quasi-Particles	133		
		7.3.1 Charge Current Through Interferometer	133		
		7.3.2 Low-Temperature and High-Temperature			
		Behavior of Current	137		
	7.4	Conclusion	138		
	Refe	erences	140		
8		roscopic Theory of Fractional Quantum			
	Hall	Interferometers	143		
	8.1	Byers-Yang Paradox	145		
	8.2	Outline of Microscopic Theory	147		
	8.3	Microscopic Description of a Quantum Hall Interferometer	149		
		8.3.1 Plasma Analogy and Incompressible States	151		
		8.3.2 Low-Energy Subspace	155		
	8.4	Projection onto the Low-Energy Subspace	157		
		8.4.1 Edge Hamiltonian	158		
		8.4.2 Tunneling Hamiltonian	160		
		8.4.3 Deformations of the Ground State	163		
	8.5	Quantum Hall Interferometer Away From Equilibrium	165		
		8.5.1 Ohmic Contacts	166		
		8.5.2 Current Through the Interferometer	169		
	8.6	Conclusion	173		
	Refe	rences	174		

xiv		Contents

9	Sun	mary of Results	177
	9.1	Integer Quantum Hall Effect	177
	9.2	Fractional Quantum Hall Effect	178
Αį	pend	ices	181

# Chapter 1 Introduction

The quantum Hall effect, one of the central subjects of the modern condensed matter physics, continues to attract attention of both experimentalists and theorists after 30 years of its discovery [1]. This effect, observed in a two-dimensional electron gas in strong magnetic fields, has several exciting features such as the precise quantization of the Hall conductance in units of  $e^2/h$ , excitations with fractional charge and fractional statistics, etc. The low energy physics of the quantum Hall effect is determined by edge excitations, because there exists a gap for excitations in the bulk of the two-dimensional gas. Properties of quantum Hall edge excitations have been investigated in a number of experimental and theoretical works (for a review, see [2, 3]). However, only recently the progress in the fabrication of novel mesoscopic devices [4] has made it possible to focus closely on the electronic properties of quantum Hall edge, which were not well understood earlier.

The first experiments with these devices have shown unexpected results, such as strongly non-monotic dephasing in Mach–Zehnder electronic interferometers [5], fast equilibration along quantum Hall edge [6, 7], unusual periodicities of Aharonov–Bohm oscillations [8–12], etc. The appearance of such results indicates, that the physics of quantum Hall effect is not fully understood after 30 years of research. Namely, the mesoscopic effects in the quantum Hall regime have not been given a necessary attention and need to be studied further. Therefore, the mesoscopic physics of the quantum Hall effect has been chosen to be the subject of our theoretical investigation. In this introduction we recall basics of mesoscopic physics and quantum Hall effect, briefly describe the recent experimental findings, and present the outline of the thesis.

### 1.1 Mesoscopic Physics

We start the introduction with a brief reminder on the mesoscopic physics. This area of the condensed matter physics appeared in early 1980s as a result of the attempts to answer one simple and important question. It is well known that the conductance

1

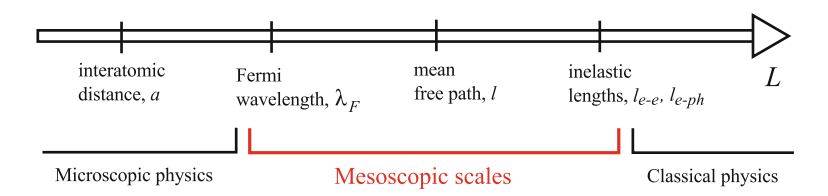


**Fig. 1.1** The main length scales that determine the physics of a condensed matter system are shown in a typical order. Mesoscopic length scales are the scales at which the system is in transition from quantum to classical behavior. Typical values of these scales are given in the Table 1.1

**Table 1.1** Typical values of lengths scales for three-dimensional metals and for two-dimensional electron gas in GaAs-AlGaAs heterostructures

	Metals	Two-dimensional electron gas
Interactomic distance	$a \sim \text{few Å}$	//
Fermi wavelength	$\lambda_F \sim { m few \ \AA}$	$\lambda_F \sim 40\mathrm{nm}$
Mean free path	$l \sim 100\mathrm{nm}$	$l\sim 1$ –100 $\mu \mathrm{m}$
Electron collision length	$l_{e-e}\sim 1$ – $10\mu\mathrm{m}$	$l_{e-e}\sim 10~\mu\mathrm{m}$
Electron-phonon scattering length	$l_{e-ph}\sim 10~\mu$ m–few mm	<i>//</i>

of a macroscopic conductor is given by the Ohm's law  $G = \sigma S/L$ , where  $\sigma$  is the conductivity of a material, S is the cross-section, and L is the length of the sample. The question is at which length scales the Ohmic behavior of the conductance breaks down. First experimental answers to this question launched a series of theoretical and experimental works which have formed an entirely new broad area of the condensed matter physics. In the mesoscopic physics, one studies the electronic transport in conductors whose characteristic length scales are in between the quantum microscopic and classical macroscopic worlds. The physical behavior of conductors at these, so called, mesoscopic scales is very reach: There are several interesting effects such as the conductance quantization [13–15], the Coulomb blockade [16, 17], and the weak localization [18] effects, etc.

Important characteristic length scales which determine behavior of a sample are the following (see Fig. 1.1 and Table 1.1). The inter-atomic distance, a, is the smallest characteristic distance of a solid [19]. The behavior at such scales is purely quantum. It determines the band structure  $\epsilon(k)$  of the material and the value of the Fermi energy,  $E_F$ . Next, the Fermi wavelength is defined as  $\lambda_F \equiv 2\pi/k_F$ , where the Fermi wavevector  $k_F$  is determined by the equation  $\epsilon(k_F) = E_F$ . Although  $\lambda_F$  may be larger than the inter-atomic distance, the physics at this scale is still quantum. Indeed, the Fermi wavelength is the shortest de-Broigle wavelength which electrons can have in the sample. Therefore, all electrons behave as waves at distances smaller than the Fermi wavelength. The mean free path, l, is the length covered by an electron before the initial momentum of the electron is relaxed by elastic scattering off impurities. The corresponding time scale  $\tau_m = l/v_F$ , where the Fermi velocity is defined as  $v_F = (1/\hbar)\partial\epsilon(k)/\partial k|_{k_F}$ , is called the momentum relaxation time. This scale takes

very different values depending on a material. The behavior at this scale might be quantum or classical depending on whether this scale is smaller or larger than another important scale, the phase relaxation length,  $l_{\phi}$ , since the static disorder itself cannot lead to dephasing. The phase relaxation length is probably the most important length scale, but it is also the most difficult to calculate and measure. At this scale the behavior of a conductor becomes classical. Ohm's law is typically established when the size of the system is larger than the Fermi wavelength, mean free path, and the phase relaxation length [4]. Processes at the inelastic lengths, such as electron–electron collision length,  $l_{e-e}$ , and electron–phonon collision length,  $l_{e-ph}$ , lead to the thermalization of electrons and of the whole sample.

Most of the pioneering works in mesoscopic physics have been done with three-dimensional metals. However, all modern experiments are made with the so called two-dimensional electron gas, since it has very high mobility. The mobility is an important characteristic of a material defined as follows. In the presence of an external electric field,  $\vec{E}$ , the steady state of electrons is reached when the rate of momentum change induced by the field is equal to the rate of its decay due to scattering off impurities:

$$\left. \frac{d\vec{p}}{dt} \right|_{\text{scattering}} = \frac{d\vec{p}}{dt} \Big|_{\text{field}}.$$
 (1.1)

The left hand side of the above equation can be rewritten as a ratio of the average momentum to the momentum relaxation time, so that we have:

$$\frac{m\vec{v}_{\rm d}}{\tau_{\rm m}} = e\vec{E},\tag{1.2}$$

where  $v_d$  is the average drift velocity, and m is the effective mass of an electron or hole. Then the mobility of a charge carrier is defined as the ratio of this drift velocity to the value of the applied electric field:

$$\mu \equiv \frac{v_{\rm d}}{E} = \frac{e\tau_{\rm m}}{m}.\tag{1.3}$$

The typical value of the mobility for three-dimensional metals is  ${\sim}10^4~\text{cm}^2/\text{V}\cdot\text{s},$  while for a two-dimensional electron gas it can be as high as  ${\sim}10^7~\text{cm}^2/\text{V}\cdot\text{s}$  [20]. In terms of length scales, it means that the mean free path for two-dimensional electrons is  ${\sim}100~\mu\text{m}$ , so that it is much easier to fabricate samples for studies of the mesoscopic effects.

### 1.1.1 Two-Dimensional Electron Gas

The two-dimensional electron gas with the best characteristics is obtained at the interface of GaAs and AlGaAs semiconductors (see Fig. 1.2). If these two materials are brought in contact, then the electrons from the wide gapped AlGaAs, which

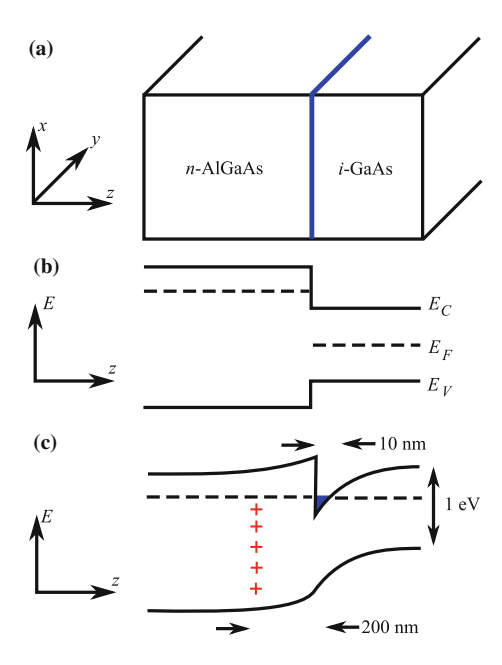


Fig. 1.2 The two-dimensional electron gas in semiconductor heterostructures. (a) The layer of two-dimensional electron states which is formed at the interface between n-doped AlGaAs and undoped GaAs is shown in *blue color*. (b) The band structure of these materials before they brought in contact.  $E_V$  is the *top* of the valence band,  $E_C$  is the *bottom* of the conductance band,  $E_F$  is the Fermi level. (c) The band structure after the equilibrium has been established. The positive charges on Si donors are shown by *red plus* symbols, two-dimensional electron states are shown in *blue color* 

has higher Fermi energy, spill over to GaAs. These electrons leave a positive charge behind themselves which creates electrostatic potential and bends the bands as shown in Fig. 1.2. In equilibrium, the Fermi level is constant in space. The electron density is sharply peaked near the interface forming a thin conducting layer which is called two-dimensional electron gas. The highest mobility (up to  $\mu = 3 \cdot 10^7 \, \text{cm}^2/\text{V} \cdot \text{s}$ ) is obtained by the so called modulation doping technique, where the concentrations of Si donors and of Al in AlGaAs are varied with the distance from the interface (see Chap. 1 of Ref. [21] for details). The typical values of main length scales in two-dimensional electron gas in comparison to metals are listed in Table 1.1.

Importantly, at the temperatures much lower than the level spacing in the effectively formed quantum well in z-direction, only the lowest quantized state  $\Psi_0(z)$  is occupied, so that the total wave function of each electron factorizes:

$$\Psi(x, y, z) = \Psi_0(z)\psi(x, y). \tag{1.4}$$

This means that from the quantum mechanical point of view, the dynamics of electrons is indeed two-dimensional. This is why the state of electrons at the surface of this semiconductor heterostructure is called two-dimensional electron gas.

The single particle spectrum of two-dimensional electron gas is quadratic,

$$E = \frac{\hbar^2}{2m} (k_x^2 + k_y^2), \tag{1.5}$$

with very small effective mass  $m=0.067 \cdot m_e$ . To calculate the density of states of two-dimensional electrons, we consider a rectangular sample with dimensions  $L_x$  and  $L_y$  and area  $S=L_xL_y$ . In such sample, assuming periodical boundary conditions, the wave vectors are quantized with  $\Delta k_i=2\pi/L_i$ , where i=x,y. This means that the total number of states with the energy less than E is equal to  $N(E)=\pi\cdot(2mE/\hbar^2)/(\Delta k_x\Delta k_y)$ . Finally, we come to the result that the density of states per unit area, per spin is *constant*:

$$\nu(E) = \frac{1}{S} \frac{dN(E)}{dE} = \frac{m}{2\pi\hbar^2} \theta(E)$$
 (1.6)

in contrast to the three-dimensional case, where it behaves as  $\sqrt{E}$ . This result simplifies some calculations in two dimensions. For example, in the degenerate limit,  $k_BT \ll E_F$ , one has the following relation for the total density of electrons:  $n_s = 2 \int dE \nu(E) f_F(E) = m E_F/\pi \hbar^2$ , where the factor 2 accounts for the two spin states. The Fermi wave vector for the two-dimensional electrons is thus given by the expression:

$$k_F = \sqrt{2\pi n_s},\tag{1.7}$$

and the Fermi wavelength  $\lambda_F = 40$  nm for the typical value of electron density is  $n_s = 10^{12}$  cm<sup>-2</sup>. It is interesting, that this length scale, which also determines the average distance between electrons, is much larger than the inter-atomic distance in the bulk of GaAs.

### 1.2 Quantum Hall Effect Basics

In this section we recall basic notions of the Hall physics and main experimental findings in the regime of the quantum Hall effect.

### 1.2.1 Classical Hall Effect

We start with the description of a simple Drude model of the classical Hall effect [19]. Our starting equation is a generalization of Eq. (1.2) in the presence of the magnetic field perpendicular to the plane of two-dimensional electron gas:

$$\frac{m\vec{v}_{\rm d}}{\tau_{\rm m}} = e \left[ \vec{E} + \vec{v}_{\rm d} \times \vec{B}/c \right]. \tag{1.8}$$

Putting all linear in drift velocity terms on the left hand side, one gets the system of two linear equations for the two components of the velocity:

$$\begin{pmatrix} m/e\tau_{\rm m} - B/c \\ B/c & m/e\tau_{\rm m} \end{pmatrix} \begin{pmatrix} v_x \\ v_y \end{pmatrix} = \begin{pmatrix} E_x \\ E_y \end{pmatrix}. \tag{1.9}$$

In the next step, we note that the current density vector is given by the product of the charge density  $en_s$  and the average drift velocity:  $\vec{j} = e\vec{v}_d n_s$ . Substituting this equation in the Eq. (1.9) and using the definition of the resistivity tensor  $\hat{\rho}$ ,

$$\vec{E} = \hat{\rho}\vec{i},\tag{1.10}$$

we find that the diagonal and off-diagonal components of the resistivity are given by:

$$\rho_{xx} = \rho_{yy} = \frac{1}{en_s \mu},\tag{1.11a}$$

$$\rho_{xy} = -\rho_{yx} = \frac{B}{en_s c}.$$
 (1.11b)

This well known result has been used for several decades for the characterization of semiconductor samples. Importantly, the Hall resistivity  $\rho_{xy}$  depends only on such characteristic of material as the density of charge carriers  $n_s$ . Therefore, one can first find this density measuring the Hall resistivity and using Eq. (1.11b), and then restore the value of the mobility from Eq. (1.11a). Here we would like to mention also the relations between resistivity  $\hat{\rho}$  and conductivity  $\hat{\sigma} \equiv \hat{\rho}^{-1}$  tensors in two dimensions for the further use:

$$\sigma_{xx} = \sigma_{yy} = \frac{\rho_{xx}}{\rho_{xx}^2 + \rho_{xy}^2},$$
 (1.12a)

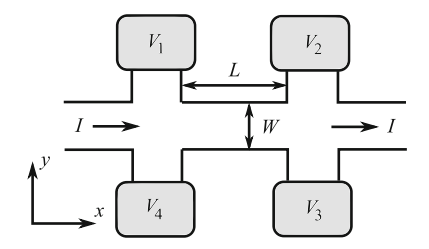
$$\sigma_{xy} = -\sigma_{yx} = \frac{\rho_{xy}}{\rho_{xx}^2 + \rho_{xy}^2}.$$
 (1.12b)

Thus, in the limit of a clean system,  $\mu \to \infty$ , one has  $\rho_{xx} = 0$  and  $\sigma_{xx} = 0$  at the same time.

### 1.2.2 Experimental Results

There are several experimental methods to determine the resistivity tensor of a material. A popular experimental setup for the determination of this tensor for a two-dimensional sample, the so called Hall bridge, is shown in Fig. 1.3. In this setup, one drives a constant current, typically of the order of a few nA, through the sample in *x* direction and measures potentials at four voltage probes.

Fig. 1.3 The setup for the measurement of longitudinal and Hall resistivity of a two-dimensional electron gas sample. A weak current is driven in *x* direction, while the potentials at four voltage probes are measured



The quantities which one is interested in are the longitudinal voltage drop  $V_x = V_1 - V_2$ , and the Hall voltage  $V_H = V_2 - V_3$ . The resistivity tensor can be then found form the relations:

$$\rho_{xx} = \frac{V_x}{I} \frac{W}{L}, \quad \rho_{xy} = \frac{V_H}{I}. \tag{1.13}$$

Following the common convention, we will refer to all off-diagonal components as to Hall components, i.e., we denote  $\sigma_{xy} \equiv \sigma_H$ ,  $R_{xy} \equiv R_H$ , etc. Importantly, the expression for the Hall resistivity is *universal*, i.e. it is independent of the sample dimensions. This means that one does not need to measure these dimensions with high accuracy to get the precise value of the Hall conductivity. Such situation is possible only in two dimensions, where the resistivity and resistance have the same dimensionality.

The first measurements of the longitudinal and Hall resistance of the high quality two-dimensional electron gas in a strong magnetic field have given exciting results. Namely, around the values of the magnetic field which correspond to the integer values of Landau levels filling factor (1.26) the longitudinal resistance becomes suppressed by a factor as high as  $10^{13}$ , while at the same time the Hall resistance becomes equal to

$$R_H = \frac{h}{ne^2},\tag{1.14}$$

where n is the integer closest to the value of the filling factor [1]. The precision of quantization of the Hall resistance at these so called Hall plateaus is extremely high, and can be as high as  $\delta R_H/R_H \simeq 10^{-10}$  in the modern samples. Such a high precision makes it possible to use the quantum Hall effect for metrology applications and for the precise determination of the fine structure constant. This is possible in particular due to a very small value of the longitudinal conductivity of a sample. Namely, if the longitudinal conductivity is zero, one can write the current trough an arbitrary cross-section a-b as

$$I_{a-b} = \int d\vec{n} \cdot \vec{j} = \sigma_H \int d\vec{l} \cdot \vec{E} = \sigma_H V_{a-b}. \tag{1.15}$$

So that the voltage drop between points a and b is independent of the geometry.

Among other interesting results, it is worth mentioning that the conductivity in the regime of integer quantum Hall effect has a very simple scaling behavior [22, 23]. Namely, around every plateau, numbered by an integer n, the conductivities satisfy the following relation

$$\left(\sigma_{xx}/\sigma_n^{(0)}\right)^2 + \left(h\sigma_H/e^2 - n - 1/2\right)^2 = 1,$$
 (1.16)

where  $\sigma_n^{(0)}$  depends only on the temperature. It is interesting, that in spite of such precise quantization and universal behavior, the distribution of currents in a sample at Hall plateaus is highly inhomogeneous and changes between the plateaus and even at the same plateau [24].

Later, it has been found that in more clean samples and at lower temperatures Hall plateaus appear near the values of magnetic field which correspond to the fractional values of Landau levels filling factor with odd denominators (see Fig. 1.4), such as  $\nu=1/3,2/3,2/5$ , etc. [25]. This effect is now called the *fractional* quantum Hall effect. One of the most exciting features of the fractional quantum Hall effect is the presence of the excitations with fractional charge. The existence of such excitations has been confirmed recently by measurements of the shot noise of backscattering currents in samples with a narrow constriction [26, 27]. The Shottky formula for the power *S* of this shot noise reads:

$$S = e^* \langle I \rangle, \tag{1.17}$$

where  $\langle I \rangle$  is the average current, and  $e^*$  is the elementary charge. The experiments show that at, e.g.,  $\nu=1/3$  the charge is  $e^*=e/3$ . Finally, there has been observed a Hall plateau at the filling factor with even denominator, namely at  $\nu=5/2$  [28]. It has been recently suggested, that some excitations at this value of the filling factor might have the so called *non-Abelian statistics* [29]. At present, there are no experiments contradicting this suggestion.

To conclude, we see that the quantum Hall effect exhibits extremely reach physics. Two Nobel prizes have been awarded for the works on quantum Hall effect. Nevertheless, even after more than thirty years of research, some experiments, in particular those discussed in this thesis, continue bringing unexpected results. Most of them utilize complex mesoscopic devices, fabrication of which has become possible recently. These experiments are described below in details. However, before we proceed with the discussion of these results, we consider some basic theoretical aspects of the quantum Hall effect.

### 1.2.3 Landau Quantization

We start by considering the quantum mechanical problem of motion of a single electron in two dimensions in a homogeneous magnetic field directed perpendicular

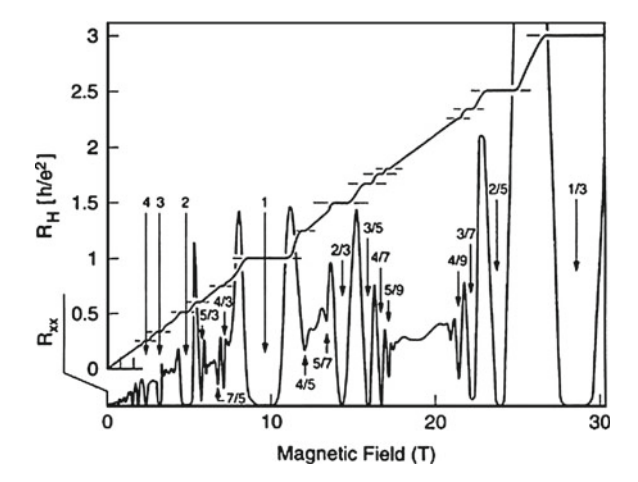


Fig. 1.4 Experimental results for the longitudinal and Hall resistance in a strong perpendicular magnetic field. The longitudinal resistance shows strong deeps at the values of magnetic field which correspond to rational values of Landau levels filling factor. The Hall resistance shows precisely quantized plateaus near these points. The effect is strongly pronounced near the integer values of the filling factor and near the simple fractions such as, e.g.,  $\nu=1/3$ . The plateaus corresponding to fractional fillings are observed only in very clean samples. Reprinted figure with permission from [28]. © American Physical Society 1987

to the plane [30]. The Hamiltonian for an electron in the electromagnetic field is given by  $H = (\vec{p} - e\vec{A}/c)^2/2m$ , so that the Schrödinger equation has the following form:

$$\frac{(\vec{p} - e\vec{A}/c)^2}{2m}\psi(x, y) = E\psi(x, y), \tag{1.18}$$

where  $\vec{A}$  is the vector potential of the magnetic field, and  $\vec{p} = -i\hbar\nabla$  is the momentum operator. It is useful to choose the so called Landau gauge for the vector potential of the homogeneous magnetic field directed along *z*-axis:

$$A_x = -By, \quad A_y = 0,$$
 (1.19)

where B is the magnitude of the field. Substituting this equation in Eq. (1.18), we find that the Schrödinger equation acquires the following form:

$$\left(\frac{(i\hbar\partial_x - eBy/c)^2}{2m} - \frac{\hbar^2\partial_y^2}{2m}\right)\psi(x, y) = E\psi(x, y). \tag{1.20}$$

The differential operator on the left hand side of Eq. (1.20) is translationary invariant in the *x*-direction, so that one can use the wave function of the following form:

$$\psi(x, y) = \exp[ikx]\chi(y). \tag{1.21}$$

Substituting this equation in Eq. (1.20), we get

$$\left(\frac{(\hbar k + eBy/c)^2}{2m} - \frac{\hbar^2 \partial_y^2}{2m}\right) \chi(y) = E\chi(y). \tag{1.22}$$

One can easily see that this is nothing but the Schrödinger equation for the harmonic oscillator whose equilibrium position  $y_0$  and the frequency  $\omega_c$  are given by

$$y_0 = \frac{\hbar ck}{eB}, \quad \omega_c = \frac{eB}{mc}.$$
 (1.23)

Thus we conclude that the energy levels for the electron in the magnetic field, the so called Landau levels, are given by the expression:

$$E(n,k) = \hbar\omega_c \left( n + \frac{1}{2} \right), \tag{1.24}$$

where n is a positive integer number. Importantly, these energies are independent of quantum number k, which implies a strong degeneracy.

To calculate the number of states in a single Landau level, we consider a rectangular sample with dimensions  $L_x$  and  $L_y$  and with periodic boundary conditions. The wave vector k is then quantized in multiples of  $\Delta k = 2\pi/L_x$ . The maximum value of the wave vector  $k_{\text{max}}$  can be found from the condition that the position of the center of oscillator  $y_0(k_{\text{max}})$  takes the value  $L_y$  and from Eq. (1.23). Thus, the total number of states is  $N = k_{\text{max}}/\Delta k = L_x L_y \cdot eB/2\pi\hbar c$ , and the density of states per unit of area is given by

$$n_{LL} = \frac{eB}{2\pi\hbar} \equiv \frac{1}{2\pi l_B^2},\tag{1.25}$$

where we have introduced the so called magnetic length:  $l_B = \sqrt{eB/\hbar c}$ . In fact, the magnetic flux through the area  $2\pi l_B^2$  is equal to the flux quantum  $\Phi_0 = hc/e$ . Next, we can define the Landau levels filling factor as the ration of electron density to the Landau level density of states:

$$\nu \equiv \frac{n_s}{n_{LL}}.\tag{1.26}$$

From a different point of view, the filling factor is the number of electrons per flux quantum. One can check, as well, that the density of states at a Landau level is equal to the density of states of two-dimensional electron gas in the absence of the magnetic field integrated over the energy interval  $\hbar\omega_c$ :

$$2n_{LL} = \frac{m}{\pi \hbar^2} \cdot \hbar \omega_c, \tag{1.27}$$

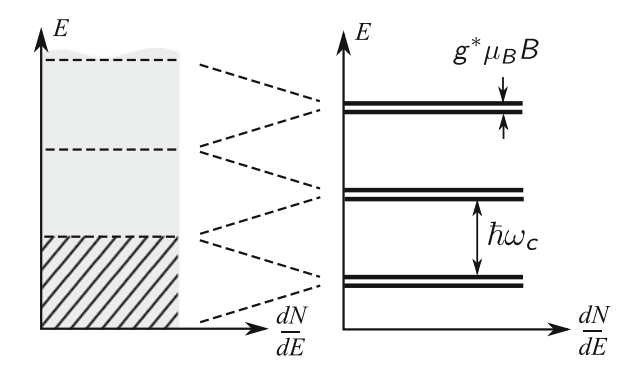


**Fig. 1.5** Density of states of the two-dimensional electron gas without (*left panel*) and with (*right panel*) magnetic field. The cyclotron gap is typically larger than Zeeman splitting. The Landau levels in a magnetic field are highly degenerate, so that the total number of states in a level is equal to the number of states of two-dimensional electron gas in corresponding (*marked*) interval of energies

where we have taken into account the fact that there is one state for each spin projection. The energy splitting between two states of an electron with different projection of spin along the magnetic field is given by the Zeeman energy. It is typically smaller than the cyclotron energy, so that the density of states of two-dimensional electron gas in magnetic field looks as shown in Fig. 1.5.

Naively, the Landau quantization may explain the appearance of at least integer quantum Hall effect. Namely, one could argue that when one increases the magnetic field, the density of states at Landau levels grows and the levels move up. When each level crosses the Fermi level, one would observe a conductivity peak, while when the Fermi level is between the Landau levels, one would see a plateau. In fact, such situation is not possible, because there are no states in between the Landau levels, and therefore the Fermi level is always stuck at the last partially filled level until it gets completely empty. Indeed, straightforward linear response calculations (see Chap. 11 of Ref. [21]) for the conductivity of non-interacting two-dimensional electrons give a simple linear dependence on the magnetic field. Moreover, one can show that the resistivity tensor should be equal to

$$\hat{\rho} = \begin{pmatrix} 0 & -B/en_s c \\ B/en_s c & 0 \end{pmatrix} \tag{1.28}$$

in arbitrary *translational invariant* system. In order to do so one just needs to note that in the reference frame moving with a velocity  $\vec{v}$  with respect to the lab frame there appears an electric field  $\vec{E} = -\vec{v} \times \vec{B}/c = -\vec{j} \times \vec{B}/en_sc$ . This is a very robust picture, valid in classical and quantum situations. Thus, for the quantum Hall effect to be observed, one needs to break the translational invariance, e.g., by adding disorder. To explain the fractional Hall effect, one needs to consider the electron–electron interactions as well.

### 1.3 Theoretical Approaches to Quantum Hall Effect

In this section we consider three most important approaches to the theoretical description of the quantum Hall effect. We start with the single particle description of the integer quantum Hall effect, then we discuss the effective theory of quantum Hall effect, and, finally, the microscopic variational function approach to the fractional quantum Hall effect.

### 1.3.1 Single Particle Picture

Let us consider the classical motion of an electron in a strong magnetic field and an external potential. If this potential is constant, then the motion of an electron is described by the equation  $\vec{r}(t) = \vec{R} + \vec{r}'(\omega_c t)$ , where  $\vec{r}'(\omega_c t)$  describes the circular motion around the center  $\vec{R}$ , with coordinates X, Y which do not depend on time. In the presence of a non-trivial external potential  $\phi$  it is instructive to consider the motion of this guiding center, defined in a general situation as:

$$\vec{R} = \vec{r} + \vec{B} \times \dot{\vec{r}} / B\omega_c. \tag{1.29}$$

The equation of motion of an electron in terms of this coordinate is  $\vec{B} \times \dot{\vec{R}} = \vec{\nabla} \varphi(\vec{r})$ . In a strong magnetic field the radius of cyclotron motion is small and one can replace  $\varphi(\vec{r})$  by  $\varphi(\vec{R})$  assuming a smooth potential. Then the guiding center drifts along the equipotential lines:

$$\vec{v}_d \equiv \dot{\vec{R}} = \frac{c}{B^2} \vec{B} \times \vec{\nabla} \varphi, \tag{1.30}$$

so that  $\varphi(X(t), Y(t)) = const.$  Typical trajectories in a disorder potential in a two-dimensional sample are shown in Fig. 1.6. Electrons drift clockwise around hills and counter-clockwise around valleys. There are also trajectories which go through the whole sample.

In the semi-classical picture, these drift trajectories correspond to wave functions localized along the equipotential lines. The energy of a state with such wave function is shifted from the Landau level energy by an amount  $\delta E$ , approximately equal to the value of the potential at the position of the corresponding equipotential line. For example, although in a homogeneous electric field  $\varphi(x, y) = Ey$  eigenfunctions (1.21) are not changed, their energies are no longer degenerate: They depend on the wave vector k, so that Eq. (1.24) takes the form

$$E(n,k) = \hbar\omega_c \left(n + \frac{1}{2}\right) + e\varphi(y_0(k)), \quad y_0 = kl_B^2.$$
 (1.31)

Importantly, the states that are far from a Landau level are all *localized*, since they drift around the hills or valleys of the potential, while the states near the Landau

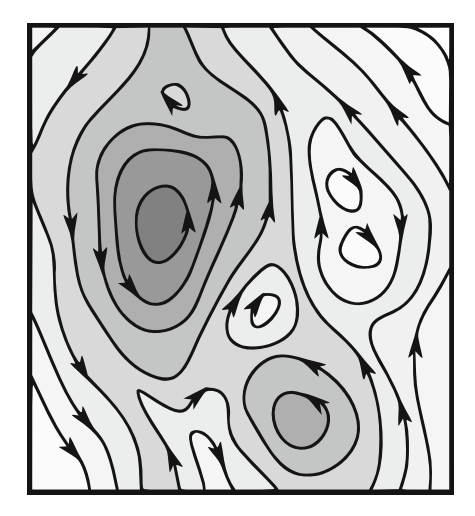


**Fig. 1.6** Schematic illustration of the semi-classical picture of the electron motion in a typical potential profile. The value of the potential is indicated by the intensity of the *gray shadow*. The electrons drift along the equipotential lines, which are shown by *thin black lines*. The direction of the drift velocity is determined by the local electric field and is indicated by the *black arrows*. Electrons encircle the hills and valleys of the potential landscape, but there are also equipotential lines which propagate through the whole sample. In the quantum case, the electron wave functions are localized along these equipotential lines

level propagate through the whole sample and may contribute to transport. The actual density of states in a disordered sample thus looks as shown in Fig. 1.7. The localized states create a "reservoir" for the Fermi level, so that the scenario described at the end of Sect. 1.2.3 becomes possible.

An important question which may arise is whether the described quasi-classical picture is applicable in the extreme quantum limit of strong fields, where  $E_F \simeq \hbar \omega_c$ . In order to clarify this point, let us consider the commutation relation for the coordinates of the guiding center. Using definition (1.29), one finds that

$$[X, Y] = il_B^2. (1.32)$$

Therefore, in strong magnetic field limit,  $l_B \to 0$ , the coordinates of the guiding center become effectively classical. Intuitively, this can be understood by considering the expression for magnetic length  $l_B^2 = \hbar c/eB$ . The Plank constant enters this equation in the form of the ratio to the magnetic field, thus the strong magnetic field suppresses quantum effects. Moreover, the disorder in real samples is typically very smooth, because the impurities are separated from the two-dimensional electron gas plane by a distance of order of  $100\,\mathrm{nm}$ , while the magnetic length is of order of  $10\,\mathrm{nm}$ . Therefore, the semi-classical approximation is applicable.

Next important effect which needs to be explained is the high precision of the conductance quantization. The key feature of the motion in a magnetic field, which

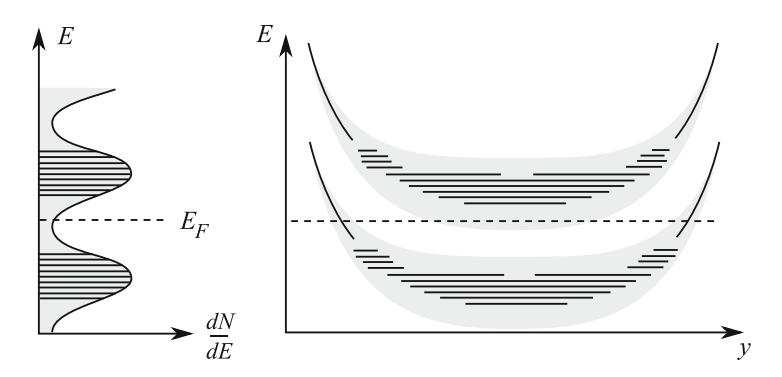


**Fig. 1.7** Electron density of states in a disordered sample. *Left panel*: The disorder leads to broadening of the Landau levels. The conducting, delocalized states are present in the *dashed regions* near the centers of Landau levels. The *gray shadow* indicates the localized states, which are more widely spread in energy. *Right panel*: The positions of the corresponding states are shown in the real space. The positions of the edge states are shown by *thick black lines*. The value of the Fermi energy in this figure corresponds to the situation at a Hall plateau

is responsible for this phenomenon, is the fact that the coordinates of electrons are proportional to their momenta (1.23). This means that the states with opposite momenta are located at the opposite sides of a macroscopic sample. This, in turn, leads to strongly suppressed backscattering, and as follows from the Landauer–Büttiker formalism, to the quantization of conductance. Namely, let us consider the situation where the Fermi level is in the mobility gap, as shown in Fig. 1.7. Only delocalized states near the Fermi level, i.e. the states near the actual edge of a sample contribute to the current. Each state gives a contribution to the current proportional to its group velocity:

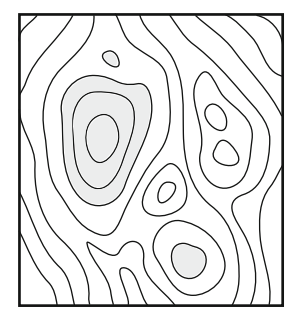
$$I = e \sum_{n} \int \frac{dk}{2\pi} v(n, k) = e \sum_{n} \int dk \frac{1}{h} \frac{\partial E(n, k)}{\partial k}.$$
 (1.33)

Performing the change of variables in the above integral, we come to the conclusion that the current is given by

$$I = -\frac{e}{h} \sum_{n=0}^{\Delta \mu} \int_{0}^{\Delta \mu} dE = n \frac{e^2}{h} V, \qquad (1.34)$$

where n is the number of filled Landau levels and V is the potential difference between the two edges.

The described above picture is, of course, an idealization. According to the experiment [24], there always exist some delocalized states in the bulk of a two-dimensional electron gas, which also carry some current density. However, it is important that scattering between the states in the bulk does not spoil the quantization of the Hall conductance. When the Fermi level is close to the Landau level, the edge states





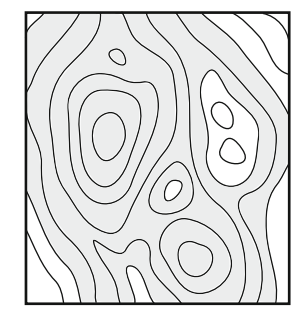


**Fig. 1.8** Schematic illustration of the percolation transition in random potential landscape. *Left panel*: Most of the states are empty, so that the electrons fill only few "lakes" of localized states. This is an insulating state. *Middle panel*: At half filling the shoreline percolates, so that the states from opposite edges approach each other. In this state the conductance is finite because of the strong backscattering. *Right panel*: Most of the states are filled, so that there are only few "dry islands". This state is also insulating. However, two opposite edge states contribute to a quantized Hall conductance

percolate through the whole sample, as show in Fig. 1.8, and may approach each other. This means that in between the Hall plateaus the backscattering is no longer suppressed, and the longitudinal conductivity  $\sigma_{xx}$  has a large peak, in agreement with the experimental results. Moreover, the quantum percolation picture predicts the scaling behavior of the length L of the "shoreline" between filled and empty states as a function of the detuning  $\delta$  from the Landau level:

$$L \sim |\delta|^{-7/3}.\tag{1.35}$$

This prediction is also in a good agreement with experiments [31].

The idea that the transitions between different Hall plateaus exhibit scaling behavior has shown to be very fruitful. Namely, the theoretical studies of renormalization group flow of the conductivity tensor demonstrate a good agreement with the experimental behavior (1.16). The renormalization group flow found in these works for a non-interacting two-dimensional system in a magnetic field and with Gaussian correlated disorder is shown in Fig. 1.9. The longitudinal conductivity  $\sigma_{xx}$  goes to zero as the size of the system grows, while there are several fixed points at  $\sigma_{xx} = 0$  and  $\sigma_H = ne^2/h$ . This result agrees with the experimental finding that the most precise quantization is obtained for the conductance of large samples.

It turns out that the fixed points of the renormalization group flow in quantum Hall effect have a topological nature. To show this, we follow the ideas proposed in works of Thouless (see Chap. 11 of Ref. [21] and references therein). Indeed, let us consider a two-dimensional electron gas sample with a geometry where the voltage source and the ammeter are replaced with two fluxes, as described in Fig. 1.10. In this geometry, the current operators are conjugated to the corresponding fluxes  $I_i = \partial H/\partial \Phi_i$ , i = x, y, where H is the Hamiltonian of the system. Taking this into account, we come to the conclusion that the Kubo formula for the Hall conductance reads:

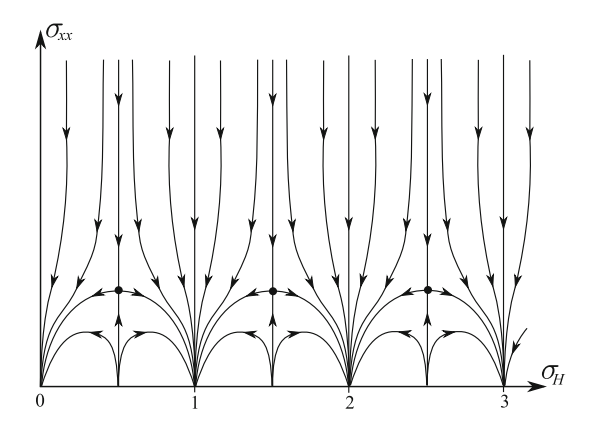


**Fig. 1.9** Two-parametric renormalization group flow of the conductivity, in units of  $e^2/h$ , of a non-interacting electron gas in random delta correlated potential, after Ref. [32]. The electron gas becomes insulating in the infrared limit. The Hall conductivity in this limit takes integer values at corresponding IR fixed points

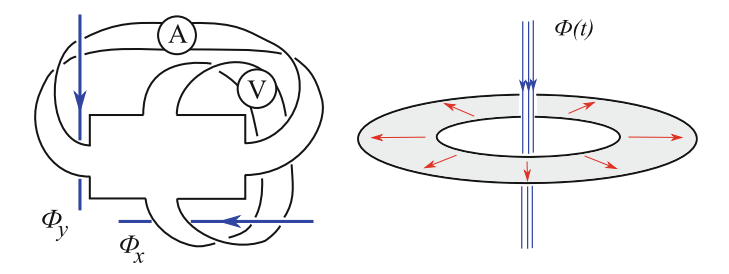


Fig. 1.10 Topological arguments for the integer quantization of the Hall conductance. *Left panel*: One can replace the voltage source (V) and the ammeter (A) in the classical Hall bar geometry with the two fluxes. Then, one can use the flux  $\Phi_x$  to generate the voltage drop, and the flux  $\Phi_y$  to monitor the current. The topology of two-dimensional electron gas in such gedanken setup is equivalent to the torus with a single hole. The edge state at the edge of this hole does not contribute to the current and can be shrank. The conductance of the two-dimensional electron gas in such setup is given by the topological invariant (1.37). *Right panel*: The Corbino disk is threaded by a singular flux tube shown in *blue color*. When the flux is adiabatically increased, the induced electric field leads to the charge current shown by *short red arrows*. The flux quantum can be gauged away, which leads to the conclusion that the corresponding transferred charge should be integer

$$G_{H} = i\hbar \langle \Psi_{0} | \frac{\partial H}{\partial \Phi_{x}} \frac{P_{0}}{(H - E_{0})^{2}} \frac{\partial H}{\partial \Phi_{y}} - \frac{\partial H}{\partial \Phi_{y}} \frac{P_{0}}{(H - E_{0})^{2}} \frac{\partial H}{\partial \Phi_{x}} | \Psi_{0} \rangle, \qquad (1.36)$$

where  $P_0$  projects off the ground state, and  $E_0$  is the ground state energy. Next, we rewrite this equation using the expression for the derivatives of the wave function,  $|\partial \Psi_0/\partial \Phi_i\rangle = P_0(H-E_0)^{-1}\partial H/\partial \Phi_i|\Psi_0\rangle$ , given by the first order perturbation theory, so that:

$$G_{H} = \frac{e^{2}}{2\pi\hbar} \int_{0}^{\Phi_{0}} d\Phi_{x} d\Phi_{y} \left( \langle \frac{\partial \Psi_{0}}{\partial \Phi_{x}} | \frac{\partial \Psi_{0}}{\partial \Phi_{y}} \rangle - \langle \frac{\partial \Psi_{0}}{\partial \Phi_{y}} | \frac{\partial \Psi_{0}}{\partial \Phi_{x}} \rangle \right). \tag{1.37}$$

Here we have formally integrated Eq. (1.36) in the range of one flux quantum and divided it by  $\Phi_0^2$ , since the conductance should not depend on the boundary conditions set by  $\Phi_i$ , if the Fermi level is inside the mobility gap. The wave function is periodic with respect to the singular fluxes, thus  $|\Psi_0\rangle(\Phi_x,\Phi_y)$  can be considered as mapping from the torus  $(\Phi_x,\Phi_y)$  to the complex projective space of wave functions. The integral in (1.37) is thus the integral of the Jacobian of this mapping. Such integral is topologically invariant and can take only integer values. Mathematically speaking, the Hall conductance is given by the first *Chern number* of this mapping.

Another simple and reliable argument has been proposed by Laughlin in [33] and developed by Halperin in [34]. Namely, they consider the Corbino disc threaded by the singular magnetic flux tube, as shown in Fig. 1.10. When one changes the flux, the induced electric field around the flux induces the Hall current and therefore the charge is transferred form one edge of the disk to another:

$$\Delta Q = \int dt I = \int dt \sigma_H \frac{\partial \Phi}{\partial t} = \sigma_H \Delta \Phi. \tag{1.38}$$

After the insertion of a flux quantum, the system should move from one eigenstate to another, since the singular flux quantum is a pure gauge. Since the charge of an arbitrary excitation is integer times the electron charge, we conclude that the Hall conductance should be integer times  $e^2/h$ .

All our considerations in this section concern the non-interacting electrons. In real samples electrons do interact, and one may wonder about the applicability of discussed results. However, the last two considerations, in fact, do not rely on the absence of interactions. Indeed, as soon as the Fermi level lies in a mobility gap, and if the ground state on a torus is non-degenerate, or only integer charged excitations are present in the system, then at least one of these two arguments holds, and the Hall conductance *must* be quantized as  $\sigma_H = n \cdot e^2/h$ , with integer n. Therefore, the discovery of fractional values of the Hall conductance in units of  $e^2/h$  came as a surprise. It implies, that both mentioned conditions might be broken simultaneously in a system with strong interaction. And indeed, the minimal charge of excitations was experimentally found to be less than electron charge in the regime of fractional quantum Hall effect. The explanation of this striking phenomenon and other features of the fractional quantum Hall effect are discussed in the next two sections.

### 1.3.2 Effective Theory

In this section we start our consideration of the fractional quantum Hall effect with the simplest, and probably the most powerful approach to the quantum Hall physics:

the effective theory. The main idea of this approach is to construct the low-energy action of the quantum Hall effect from general arguments, without recurse to any microscopic calculations, as in, e.g., the Landau–Ginzburg theory of the superconductivity. We start by considering an infinitely extended incompressible quantum Hall liquid, and address boundary effects later. Let us assume that a quantum Hall liquid carries a conserved current  $J^{\mu}$ , where the index  $\mu = 0, 1, 2$  enumerates time and spatial coordinates. The continuity equation,  $\partial_{\mu}J^{\mu} = 0$ , may be solved by introducing potentials  $B_{\mu}$ :

$$J^{\mu} = \frac{1}{2\pi} \epsilon^{\mu\nu\lambda} \partial_{\nu} B_{\lambda}. \tag{1.39}$$

From now on, we use units where  $e=\hbar=1$  and adopt the Einstein summation convention, unless specified otherwise. The current is invariant under the gauge transformations

$$B_{\mu} \to B_{\mu} + \partial_{\mu}\beta.$$
 (1.40)

This means that the action for the field  $B_{\mu}$  should be also gauge-invariant with respect to this transformation. Generally, one can therefore write

$$S[B] = \alpha_0 \int d^3r \epsilon^{\mu\nu\lambda} B_\mu \partial_\nu B_\lambda + \alpha_1 \int d^3r \partial_{[\mu} B_{\nu]} \partial^{[\mu} B^{\nu]} + \dots$$
 (1.41)

By counting dimensions, it is easy to see that the first term in the above action, the so called Chern-Simons action

$$S_0[B] = \alpha_0 \int d^3r \epsilon^{\mu\nu\lambda} B_\mu \partial_\nu B_\lambda, \qquad (1.42)$$

has zero dimension. By contrast, the second, Maxwell-like term, as well as all other possible terms not displayed in Eq. (1.41), have lower dimensions, i.e., they are irrelevant at large distance and low energy scales. Note that the action (1.42) breaks the time reversal symmetry, which is not prohibited for a system exposed to an external magnetic field. It is also important to mention, that the action (1.42) is *topological*, i.e., it does not depend on the metric of a manifold on which it is defined (see Appendix F for a more detailed discussion).

Next, the interaction of the quantum Hall current with an external electromagnetic field, described by a vector potential  $A_{\mu}$ , is given by the term:

$$S_{\rm int}[A, B] = \int d^3r A_{\mu} J^{\mu} = \frac{1}{2\pi} \int d^3r A_{\mu} \epsilon^{\mu\nu\lambda} \partial_{\nu} B_{\lambda}. \tag{1.43}$$

Integrating out the fields  $B_{\mu}$ , we arrive at an effective action for the electromagnetic field in the Chern-Simons form:

$$S_{\text{eff}}[A] = \frac{1}{(4\pi)^2 \alpha_0} \int d^3 r \epsilon^{\mu\nu\lambda} A_\mu \partial_\nu A_\lambda. \tag{1.44}$$

The average current  $\langle J^{\mu} \rangle = \delta S_{\text{eff}}[A]/\delta A_{\mu}$  is then given by the Hall's law:

$$\langle J^{\mu} \rangle = \sigma_H \epsilon^{\mu\nu\lambda} \partial_{\nu} A_{\lambda}, \tag{1.45}$$

where  $\sigma_H = 1/(8\pi^2\alpha_0)$  is the Hall conductivity. Thus, we conclude that for an infinitely extended quantum Hall liquid the action (1.42) correctly describes the quantum Hall current. Already at this point we must notice, that the ground state of topological theories is typically degenerate on compact manifolds [35], so that the assumption made in the Thouless argument may in fact be incorrect.

Having constructed the gauge invariant low-energy action for an incompressible quantum Hall liquid, we proceed with the analysis of the spectrum of local excitations. It has been demonstrated [35] that all the states in the topological field theory with the Chern–Simons action (1.42) are described by Wilson lines (see Appendix F). For instance, an operator which annihilates a local excitation at point r and creates it at point r' has the following form:

$$W_q(r,r') = \exp\left(iq \int_{r'}^r dr^{\mu} B_{\mu}\right), \tag{1.46}$$

where q is a constant. In order to demonstrate this, we note that the charge operator  $Q_{\rm em}$  is given by the integral of the charge density  $J^0=(1/2\pi)\epsilon^{\nu\lambda}\partial_\nu B_\lambda$  over a space-like region enclosed by some contour  $\gamma$ . Therefore, it may be written as the counter integral

$$Q_{\rm em} = (1/2\pi) \int_{\gamma} dr^{\mu} B_{\mu}. \tag{1.47}$$

One can show that the commutator of these two operators is given by  $[Q_{\rm em}, \mathcal{W}_q] = \pm q \mathcal{W}_q/(4\pi\alpha_0)$ , if the  $\gamma$  encloses only one of the two points r and r', and it vanishes otherwise. Therefore, the operator  $\mathcal{W}_q$  creates two local excitations with the charges  $q/(4\pi\alpha_0)$  and  $-q/(4\pi\alpha_0)$ . For the details of the derivation, see Appendix F.

Next, we note that the statistical phase  $\theta_{12}$  of two excitations (1.46) with charges  $q_1/(4\pi\alpha_0)$  and  $q_2/(4\pi\alpha_0)$ , is determined by braiding the corresponding Wilson lines, [35] and is equal to  $\theta_{12}=\pi q_1q_2/4\pi\alpha_0$  (see Appendix F for the derivation). We apply the constraint that the spectrum of excitations in the effective theory must contain electrons. This means that the excitation (1.46) with unit charge has to have the Fermi statistics. Thus we require  $\pi(4\pi\alpha_0)^2/4\pi\alpha_0=\pi m$ , where m is an odd integer. This constraint gives  $\alpha_0=m/4\pi$ , and therefore the Hall conductivity takes the value  $\sigma_H=1/8\pi^2\alpha_0=1/2\pi m$  in units  $e=\hbar=1$ , which corresponds to the so called Laughlin series of the fractional quantum Hall effect states at filling factor  $\nu=1/m$ .

Apart from an electron, which corresponds to q=m, there are also other local excitations (1.46) with other values of q. The natural condition on the physical excitations is that they must have a single valued wave-function, or in terms of

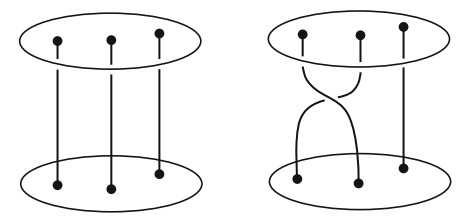


**Fig. 1.11** Schematic illustration of the statistics of excitations in two dimensions. The final quantum state of three quasi-particles on the *left panel* can be different from the state of quasi-particles on the *right panel*. This is because the trajectories on the *right* are topologically inequivalent to those on the *left*. The consecutive application of the permutations shown here to several quasi-particles naturally has a group structure and form the so-called braid group [36]

effective theory, an integer statistical phase with respect to electrons. In the considered case this leads to the condition that the number q should be integer. Interestingly, the state (1.46) with q=1 has fractional charge  $Q_{\rm em}=e/m$ . Therefore, the Laughlin argument is no longer applicable. Moreover, these excitations have the so called fractional statistics, i.e., their statistical phase is  $\theta=\pi/m$ .

Such exotic statistics are in fact allowed only in two dimensions. This statement follows from the idea that the space of quantum states is a representation of a symmetry group of a system. An arbitrary many-body system always has the particle exchange symmetry, thus such a system in three or higher dimensions is the representation of the permutation group [30]. In other words, the exchange of two particles can only lead to the additional phase multiplier  $\pm 1$  in the wave function. In two dimensions, however, this multiplier does not need to be only  $\pm 1$ , since the path of one particle going around another is not contractible (see Fig. 1.11). Therefore, the space of states should be a representation of the so called braid group, which is much more wider than the permutation group [36]. In spite of the fact that the theory predicts such kind of excitations in quantum Hall systems, there is no direct confirmation of their existence up to now.

The discussed above effective model describes quantum Hall effect at filling factors  $\nu=1/m$  only. To describe other filling factors, one needs to assume that there are several separately conserved currents distinguished by some quantum numbers, so that the total current is

$$J^{\mu} = \sum_{\alpha} J^{\mu}_{\alpha} = \frac{1}{2\pi} \sum_{\alpha} \epsilon^{\mu\nu\lambda} \partial_{\nu} B_{\alpha\lambda}. \tag{1.48}$$

In the case of the integer quantum Hall effect the physical meaning of this quantum number is obvious: it is just the Landau level number. Namely, in the low energy limit electrons from any two Landau levels are distinguishable, and the effective theory for  $\nu=n$  is described by the direct sum of n copies of action (1.42) with  $\alpha_0=1/4\pi$ . In the case of complex fractions, physics of these quantum numbers is not always clear. Nevertheless, one may consider the action of the following form:

$$S[B, A] = (1/4\pi) \sum_{\alpha\beta} K_{\alpha\beta} \int d^3r \epsilon^{\mu\nu\lambda} B_{\alpha\mu} \partial_{\nu} B_{\beta\lambda} + \int d^3r A_{\mu} J^{\mu}, \qquad (1.49)$$

where  $K_{\alpha\beta}$  is an integer valued matrix, so that  $\sum_{\alpha\beta} K_{\alpha\beta}^{-1} = 2\pi\sigma_H$ . Finally, the effective theory approach does not exclude the models with the non-Abelian Chern-Simons action [37]. The excitations in such models form a non-Abelian representation of the braid group, so that the exchange of two quasi-particles leads to multiplication of a wave function by some finite-dimensional unitary operator. This kind of excitations, if exist, are very useful for quantum computation applications, however, as it has been already mentioned, they have not yet been found experimentally.

We have described the effective theory of an infinitely extended quantum Hall state. In the situation where a quantum Hall liquid at filling factor  $\nu=1/m$  is confined to a finite region D, the total effective action in the presence of an external electromagnetic field,

$$S[A, B] = S_0[B] + S_{\text{int}}[A, B] = \frac{1}{4\pi} \int_{D} d^3r \epsilon^{\mu\nu\lambda} \Big[ 2A_{\mu} + mB_{\mu} \Big] \partial_{\nu}B_{\lambda},$$
 (1.50)

is not gauge invariant. Namely, one can easily see that under a gauge transformation

$$A_{\mu} \to A_{\mu} + \partial_{\mu}\alpha, \quad B_{\mu} \to B_{\mu} + \partial_{\mu}\beta$$
 (1.51)

the action (1.50) transforms as  $S[A, B] \rightarrow S[A, B] + \delta S[A, B]$  with

$$\delta S[A, B] = \frac{1}{4\pi} \int_{D} d^{3}r \epsilon^{\mu\nu\lambda} \Big[ 2\partial_{\mu}\alpha + m\partial_{\mu}\beta \Big] \partial_{\nu} B_{\lambda}$$

$$= \frac{1}{4\pi} \int_{\partial D} d^{2}r [2\alpha + m\beta] \epsilon^{\mu\nu} \partial_{\mu} b_{\nu}, \qquad (1.52)$$

where  $b_{\nu}$  is the restriction of the bulk field  $B_{\nu}$  to the boundary  $\partial D$ . A physical reason for the gauge anomaly is the fact that in a quantum Hall liquid confined to a finite region the bulk Hall current (1.39) is not conserved. Consequently, the electric charge may be accumulated at the edge of the system.

In order to restore the gauge invariance of the effective theory, we take into account the boundary degrees of freedom. It is easy to see that the simplest boundary action

$$S[\phi] = \frac{m}{4\pi} \int_{\partial D} d^2r \left[ D_t \phi D_x \phi - h(D_x \phi) + \epsilon^{\mu\nu} b_\mu \partial_\nu \phi \right], \tag{1.53}$$

where the coordinate x parameterizes the boundary, cancels the gauge anomaly (1.52), if one assumes that the edge field  $\phi$  transforms as

$$\phi \to \phi - (2/m)\alpha - \beta,\tag{1.54}$$

and the covariant derivative is given by the expression

$$D_{\mu}\phi = \partial_{\mu}\phi + (2/m)a_{\mu} + b_{\mu}. \tag{1.55}$$

Note that the commutation relations for the field  $\phi(x)$  are determined by the first term in the canonical action (1.53):

$$[\partial_x \phi(x), \phi(y)] = \frac{2\pi i}{m} \delta(x - y). \tag{1.56}$$

However, the precise form of the boundary Hamiltonian density  $(m/4\pi)h(D_x\phi)$  is not fixed by the effective theory. The only requirement is that the Hamiltonian density should be a positive definite function of  $D_x\phi$ . The simplest possible expression  $h = v(D_x\phi)^2$ , justified in the case of smooth confining potentials at the boundaries, gives the Hamiltonian

$$\mathcal{H} = \frac{mv}{4\pi} \int dx (D_x \phi)^2, \tag{1.57}$$

and leads to the chiral edge dynamics with a linear dispersion law, as it follows from the equation of motion. Finally, the expression for the charge density at the edge of a quantum Hall system may be found by evaluating the derivative  $\rho = -\delta S/\delta a_t$  of the total action with respect to the boundary field. The result reads:

$$\rho = \frac{1}{2\pi} D_x \phi. \tag{1.58}$$

Next, we analyze the spectrum of local excitations at the edge. It is natural to assume that such excitation may be created by the local operator (1.46) with the Wilson line starting and terminating at the boundary  $\partial D$  of the quantum Hall system. Note, however, that this operator is not gauge invariant. Similarly to the situation with the gauge anomaly in the action S[A, B], this problem can be fixed by taking into account the edge degrees of freedom. In particular, the gauge invariant operator that creates a Laughlin quasi-particle and quasi-hole at the edge of a quantum Hall system may be written as

$$W_1(\xi, \xi') \exp\left(i/m \int_{\xi'}^{\xi} dr^{\mu} A_{\mu}\right) = e^{i\phi(x)} \exp\left(i \int_{\xi'}^{\xi} dr^{\mu} \left[B_{\mu} + \frac{2}{m} A_{\mu}\right]\right) e^{-i\phi(x')},$$
(1.59)

where the one-dimensional coordinates x and x', and two-dimensional coordinates  $\xi$  and  $\xi'$  are the different parameterizations of the boundary  $\partial D$ . The gauge invariance of the operator (1.59) may be checked by directly applying the transformations (1.51) and (1.54).

We are particularly interested in the situation where the operator (1.59) describes tunneling of a Lauglin quasi-particle. In this case, the tunneling points  $\xi$  and  $\xi'$ , are very close to each other:  $\xi \to \xi'$ . Then the integrals in the operator (1.59) vanish, and denoting the resulting tunneling operator with  $\mathcal{A}_{qp}^{\dagger}(\xi)$ , we write:

$$\mathcal{A}_{\text{GD}}^{\dagger}(\xi) = e^{i\phi(x)}e^{-i\phi(x')}.\tag{1.60}$$

The operator (1.60) creates a pair of local charges at the boundary  $\partial D$  of the value 1/m and -1/m, which may be checked by evaluating the commutator of this operator with the charge density operator (1.58) with the help of Eq. (1.56). It then becomes obvious, that an electron annihilation operator at the edge can be written as

$$\psi_{\rm el}(x) = \exp[im\phi(x)]. \tag{1.61}$$

This operator has the charge 1 and the fermionic statistical phase.

Finally, it is instructive to write down the oscillator mode expansion for the edge field  $\phi$ . Considering, for a moment, a single edge, we denote its length by W, choose the gauge  $A_{\mu} = B_{\mu} = 0$ , and apply periodic boundary conditions on the field to arrive at the expression:

$$\phi(x) = -\phi_N/m + 2\pi Nx/W + \sum_{k>0} \sqrt{\frac{2\pi}{kW}} \left[ a_k e^{ikx} + a_k^{\dagger} e^{-ikx} \right], \tag{1.62}$$

where the creation and annihilation operators for plasmon modes satisfy the commutation relations  $[a_k, a_{k'}^{\dagger}] = (1/m)\delta_{kk'}$ , and zero modes satisfy  $[N, e^{i\phi_N}] = e^{i\phi_N}$ . Substituting this expansion into the edge Hamiltonian (1.57), we arrive at the expression

$$\mathcal{H} = \pi v m N^2 / W + m \sum_{k>0} v k a_k^{\dagger} a_k. \tag{1.63}$$

Thus we conclude, that the edge Hamiltonian describes chiral edge plasmon modes with the linear dispersion. The effective model of the edge states with the Hamiltonian (1.63), also referred to as the chiral conformal field theory, successfully describes several recent experiments (see, e.g., Ref.[38]). Equation (1.61) with m=1 is nothing but the main equation of the bosonoization theory, discussed in details in Chap. 2 of this thesis. This equation provides a connection between the effective theory and the single particle approach. We will also show in what follows, that the effective theory is a sort of the "meeting point" of several theoretical approaches to quantum Hall effect. Again, one may introduce several edge fields to describe complex fractions. The general classification of multi-field models is more complicated than in the bulk case. It is discussed in detail in Chap. 6.

24 1 Introduction

### 1.3.3 Microscopic Approach

The effective theory of the quantum Hall effect agrees well with the single particle description of the integer quantum Hall effect and provides a consistent picture of the fractional quantum Hall effect. However, some microscopic considerations are needed to understand the nature of the ground state degeneracy and of the fractional charge arising in the context of the effective models. Moreover, it is important to find the physics of the new gap, which leads to the fractional quantization of conductance. Some works on the renormalization group flow of conductivity (see, e.g., Ref. [39]) suggest that the interaction leads to additional fixed points. In order to understand their nature we will use the variational function method, also referred to as the microscopic approach. Within this method, it is more convenient to use the axial gauge for a homogeneous magnetic field,

$$A_x = -\frac{1}{2}By, \quad A_y = \frac{1}{2}Bx,$$
 (1.64)

and to introduce complex coordinates z = x + iy in the xy plane of the twodimensional electron gas. In this gauge and using these coordinates, the single electron Schrödinger equation may be written as

$$\frac{\hbar\omega_c}{2} \left( -4l_B^2 \partial \bar{\partial} + \frac{|z|^2}{4l_B^2} + z\partial - \bar{z}\bar{\partial} \right) \psi(z, \bar{z}) = E\psi(z, \bar{z}), \tag{1.65}$$

where  $\partial$  is a short notation for  $\partial/\partial z$ . Next, one can introduce operators  $a=\sqrt{2}(\partial+\bar{z}/4)$  and  $b=\sqrt{2}(\bar{\partial}+z/4)$ , which form two canonical pairs, so that  $[a^{\dagger},a]=[b^{\dagger},b]=1$ , while all other commutators are zero. In terms of these operators, the Hamiltonian of the electron in magnetic field is equivalent to the Hamiltonian of a degenerate oscillator:

$$H = \hbar\omega_c(a^{\dagger}a + 1/2). \tag{1.66}$$

The ground state wave function  $\psi_0(z,\bar{z})$  is fixed by the conditions  $a|\psi_0\rangle=b|\psi_0\rangle=0$ . The solution of these equations is given by  $\psi_0(z,\bar{z})=\exp[-|z|^2/4l_B^2]$ , thus one concludes that the wave functions

$$\psi_{m,n}(z,\bar{z}) = (a^{\dagger})^{m+n} (b^{\dagger})^n \exp[-|z|^2 / 4l_R^2]$$
 (1.67)

are the eigenfunctions of Eq. (1.65). Here the quantum number n is the Landau level number, and the number m is the eigenvalue of the angular momentum  $L \equiv \hbar(z\partial - \bar{z}\bar{\partial}) = \hbar(a^{\dagger}a - b^{\dagger}b)$  along the axis perpendicular to the two-dimensional electron gas plane. This operator commutes with the Hamiltonian, thus one obtains:

$$L\psi_{m,n}(z,\bar{z}) = \hbar m \psi_{m,n}(z,\bar{z}). \tag{1.68}$$

It is important to note, that the lowest Landau level states are given by  $\psi_{m,0}(z,\bar{z}) = z^m \exp[-|z|^2/4l_B^2]$ . In other words, any wave function on the lowest Landau level can be written as:

$$\psi(z,\bar{z}) = f(z) \exp[-|z|^2/4l_B^2], \tag{1.69}$$

where f(z) is a purely analytic function of the complex coordinate z.

Let us first consider a ground state of a system of *N* noninteracting electrons. In the absence of the disorder, the ground state is degenerate, since electrons can occupy states with arbitrary angular momenta. But if one assumes a very weak potential with a minimum at the origin, then the electrons will preferably occupy the states with lower angular momenta. The ground state is then given by the *Slater determinant* of corresponding states from the lowest Landau level:

$$\Psi(z_1, \dots, z_N) = \begin{vmatrix} 1 & z_1 & \dots & z_1^{N-1} \\ 1 & z_2 & \dots & z_2^{N-1} \\ \vdots & \vdots & \ddots & \vdots \\ 1 & z_N & \dots & z_N^{N-1} \end{vmatrix} \prod_{i}^{N} \exp\left[-\frac{|z_i|^2}{4l_B^2}\right].$$
 (1.70)

The determinant on the right hand side of the above equation is nothing but a Vandermonde determinant, and the wave function of N electrons can be rewritten as:

$$\Psi(z_1, \dots, z_N) = \prod_{i < j}^{N} (z_i - z_j) \exp\left[-\sum_{i=1}^{N} \frac{|z_i|^2}{4l_B^2}\right].$$
 (1.71)

Note that this wave function vanishes if an arbitrary pair of electrons has same coordinates, as it should be for fermions.

The electron density in the state described by Eq. (1.70) can be calculated as the sum of single-particle contributions:

$$\rho(z) = \sum_{m=0}^{N-1} |\psi_m(z)|^2 = \frac{1}{2\pi l_B^2} \sum_{m=0}^{N-1} \frac{|z|^{2m}}{2^m l_B^{2m}} \exp\left[-\frac{|z|^2}{2l_B^2}\right]. \tag{1.72}$$

The sum on the right hand side of the above equation is simply the first N terms of the Taylor expansion of  $\exp[-|z|^2/2l_B^2]$ . Therefore, the density is constant and equal to  $1/2\pi l_B^2$  in the bulk of the quantum Hall droplet and exponentially decays at the edge, as shown in Fig. 1.12. Note, that this state is incompressible, since it costs a cyclotron gap to add an electron in the bulk of a droplet.

Next, we proceed with the construction of a variational wave function for interacting electrons. We start with the quantum problem of motion of two interacting electrons in the magnetic field. Moreover, we would like to constrain them to the lowest Landau level. The wave functions in the case of an axially symmetric interaction potential  $V(|z_1-z_2|)$  should be an eigenfunction of the relative angular momentum. As we have seen above, at the lowest Landau level, the angular behavior determines

26 1 Introduction

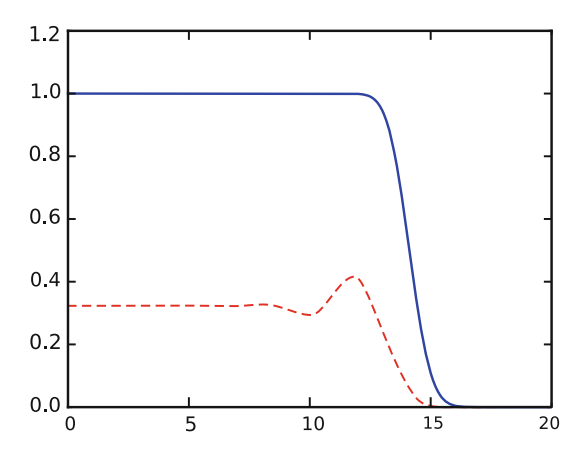


Fig. 1.12 Density of electrons in an axially symmetric quantum Hall droplet in units of the density  $1/2\pi l_B^2$  of the fully filled Landau level is plotted as a function of the distance from center in units of the magnetic length  $l_B$ . Blue, solid curve is the density profile for the state (1.70) describing the filling factor  $\nu = 1$  state. Red, dashed curve is the density profile for the state (1.75) describing the filling factor  $\nu = 1/3$  state. Note slight variations of the density and the overshoot at the edge

the radial behavior as well. Therefore, the wave functions of two electrons

$$\Psi_{mM}(z_1, z_2) = (z_1 - z_2)^m (z_1 + z_2)^M \exp\left[-\frac{|z_1|^2 + |z_2|^2}{4l_B^2}\right],$$
 (1.73)

where m is the relative angular momentum and M is the center of mass momentum, are the eigenfunctions for an *arbitrary* interaction potential, once we neglect mixing of Landau levels. Only the corresponding eigenvalues

$$v_m = \frac{\langle mM|V|mM\rangle}{\langle mM|mM\rangle},\tag{1.74}$$

referred to as Haldane pseudo-potentials [40], will be different for different interaction potentials. The discrete energy spectrum (1.74) is obtained here for the repulsive interaction due to the presence of the homogeneous magnetic field. Intuitively this can be viewed as two electrons orbiting around each other so that the repulsion force is balanced by the Lorentz force.

Now we proceed with the analysis of the variational *N*-electron wave function proposed by Laughlin [41]:

$$\Psi_L(z_1, \dots, z_N) = \prod_{i < j} (z_i - z_j)^m \exp\left[-\sum_i^N \frac{|z_i|^2}{4l_B^2}\right].$$
 (1.75)

The fermion statistics of electrons requires the number m to be odd integer. At m equal to one, this function coincides with the Slater determinant (1.70). For larger values of m, wave function (1.75) as a function of coordinates of each pair of electrons has a zero of order m, which helps to reduce the Coulomb energy. In order to understand why this wave function is a good approximation, let us write down the electron interaction potential as

$$V = \sum_{m'} \sum_{i < j} v_{m'} P_{m'}(ij), \tag{1.76}$$

where  $v_{m'}$  are the Haldane pseudo-potentials and  $P_{m'}(ij)$  is the projector on the state with relative angular momentum m' for particles with numbers i and j. If we assume that all pseudo-potentials  $v_{m'} = 0$  for  $m' \ge m$ , then the wave function (1.75) is an *exact eigenfunction* of (1.76) with zero energy. This is because the relative angular momentum of each pair of electrons in the state (1.75) is at least equal to m. Moreover, since the angular momentum takes integer values, this state has a gap. Indeed, an excitation in the state with m = 3 forces at least one pair of electrons to have the relative angular momentum 1, which costs energy of the order of  $v_1$ .

The Haldane pseudo-potentials for the long-range Coulomb potential are non zero, of course, they decay with m. Nevertheless, the numerical simulations show, that the Laughlin variational wave function (1.75) has a very large overlap with the true ground state of the system [41]. Moreover, the state (1.75) is adiabatically connected to the true ground state, i.e., when one adiabatically switches off all higher-order pseudo-potentials the gap never closes. Thus we conclude that the wave function (1.75) is indeed a good approximation. Importantly, the Laughlin wave function is m-fold degenerate on a torus [42], which confirms the effective theory result.

In the next step, we consider local excitations of the ground state (1.75). In order to create a local excitation, one can pinch the state (1.75) with a singular flux at the origin and increase the value of the flux from zero to the flux quantum. The flux quantum is a pure gauge, therefore, the system must arrive at an eigenstate. The exact behavior of the wave function is complex and is difficult to describe. However, far away from the flux, every single electron eigenstate shifts as  $\psi_{m,0}(z,\bar{z}) \to \psi_{m+1,0}(z,\bar{z})$ . Using this simple argument, Laughlin has proposed in Ref. [41] the following wave function for a quasi-particle localized at the point  $\xi$ :

$$\Psi_{qh}(z_1, ..., z_N; \xi) = \prod_{i}^{N} (\xi - z_i) \Psi_L(z_1, ..., z_N).$$
 (1.77)

For the filling factor  $\nu=1$ , i.e., for m=1, this state is nothing but the state (1.70) with an electron annihilated at the point  $\xi$ . For higher values of m, the state (1.77) might be considered as an eigenstate of the model with finite number of non-zero pseudo-potentials. Numerical calculations show that this state is also very close to a real eigenstate for a system with the Coulomb interaction [41].

In order to find the electron density in this state for the case of  $m \neq 1$ , we use the so-called classical plasma analogy [41] (for the details, see the discussion in

28 1 Introduction

Sect. 8.3.1). The main idea of this approach is to rewrite the density of electrons in the state (1.77) as the density of the classical two-dimensional Coulomb gas:

$$\rho_{\xi}(z) = \int d^2 z_1 \dots d^2 z_N \sum_i \delta^2(z - z_i) |\Psi_{qh}(z_1, ..., z_N; \xi)|^2$$

$$= \int d^2 z_1 \dots d^2 z_N \sum_i \delta^2(z - z_i) e^{-mE_{pl}}, \qquad (1.78)$$

where m plays a role of the inverse temperature, and the energy is given by the following expression

$$E_{\text{pl}} = -\sum_{i < j} \ln|z_i - z_j|^2 + \sum_i \left[ \frac{|z_i|^2}{2ml_B^2} - \frac{1}{m} \ln|z_i - \xi|^2 \right]. \tag{1.79}$$

The first term describes the Coulomb repulsion of fictitious two-dimensional particles, the second term describes a homogeneous neutralizing background, and the third term is an external charge at the point  $\xi$ . It is well known, that the two-dimensional Coulomb plasma has a uniform density in the bulk equal to the background density  $\rho = (1/4\pi) \cdot \Delta |z|^2/2ml_B^2 = (1/m) \cdot 1/2\pi l_B^2$ , so that the filling factor for the function (1.75) is, naturally,  $\nu = 1/m$ . Importantly, the two-dimensional plasma screens the charge of an additional particle at the Debye length  $l_B$ , thus there is a local deep in the density at this point with the total charge e/m. Intuitively, on the classical level this state can be understood as a vortex in the electron liquid. It is stable, because the Coulomb forces, which tend to shrink the hole, are balanced by the Lorentz force. The existence of such stable fractionally charged excitations again confirms the results of the effective theory.

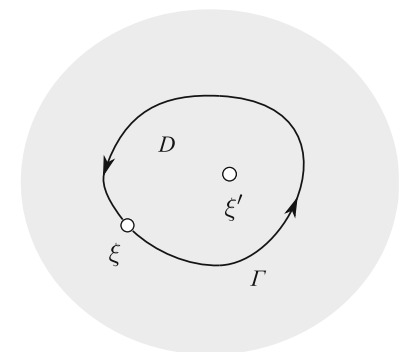
Moreover, one can show that the excitations (1.77) obey fractional statistics. In order to do so, let us calculate the Berry phase for the situation where one quasi-hole is moved around the other along a contour  $\Gamma$ , as illustrated in Fig. 1.13:

$$\gamma = \oint_{\Gamma} d\xi \langle \Psi_{qh}(\xi, \xi') | \frac{\partial}{\partial \xi} | \Psi_{qh}(\xi, \xi') \rangle 
= \oint_{\Gamma} d\xi \langle \Psi_{qh}(\xi, \xi') | \sum_{i} \frac{1}{\xi - z_{i}} | \Psi_{qh}(\xi, \xi') \rangle.$$
(1.80)

Here we calculated the derivative using Eq. (1.77). Next, rewriting the right hand side of the above equation in terms of the electron density, we get:

$$\gamma = \oint_{\Gamma} d\xi \int d^2z \frac{\rho_{\xi,\xi'}(z)}{\xi - z} = 2\pi \int_{D} d^2z \rho_{\xi'}(z), \tag{1.81}$$

**Fig. 1.13** Illustration of the calculation of the Berry phase in Eqs. (1.80) and (1.81). The quasi-hole at point  $\xi$  is adiabatically moved along the contour Γ with the help of, e.g., auxiliary "box" potential. The second quasi-hole is placed at the point  $\xi'$ . The resulting phase is proportional to the total charge in the region D enclosed by the contour Γ



where  $\rho_{\xi,\xi'}(z)$  is the electron density in the state with quasi-holes at points  $\xi$  and  $\xi'$ , and D is the region enclosed by the contour  $\Gamma$ . The integral in (1.81) has two contributions: the contribution from the homogeneous density  $2\pi B \cdot \text{area}(D)/m\Phi_0$  corresponding to the Aharonov–Bohm phase, and the contribution from the quasi-hole  $2\pi/m$  corresponding to the statistical phase, in agreement with the effective theory.

Until now, we have not discussed the conductivity of the state (1.75). It is indeed equal to  $(1/m)e^2/h$ , since the state (1.75) is translationary invariant in thermodynamic limit, and its conductivity is determined only by its density. The situation in the presence of a disorder and bounding potential is similar to the situation in the integer quantum Hall effect regime. The only difference is that now the quasi-holes are localized around the hills of the potential landscape, providing a reservoir for the Fermi level and thereby supporting the plateaus of finite width. One cannot use directly the percolation picture, as in integer quantum Hall effect, to explain the peaks in longitudinal conductance, since the wave function (1.75) is not a Slater determinant. Alternatively, one can argue that the islands occupied by localized quasi-holes and quasi-particles grow if the filling factor detunes from  $\nu = 1/m$ , and tunneling between these islands leads to non-zero longitudinal conductivity.

In particular, let us consider the transition between  $\nu=1$  and  $\nu=1/3$  plateaus. As magnetic field increases, the density of states grows, and electrons condense in the valleys of the potential landscape. At some point the Coulomb repulsion overcomes the impurity potential so that a correlated state, given by (1.75) with m=3, becomes energetically favorable, even if some quasi-particles are localized in the valleys, as illustrated in Fig. 1.14. This is possible only in quite clean samples, where the impurity potential is not too strong. The same situation arises at the values of the magnetic field corresponding to partially filled higher Landau levels, so that there also exist plateaus at  $\nu=4/3,7/3$ , etc.

The above considerations explain the appearance of a new gapped state with fractionally charged excitations only for specific fractional values of the filling factor, such as  $\nu=1/m$ , while the experiments show Hall plateaus at several other values. In order to explain these other plateaus, Bert Halperin proposed the idea that if the

30 1 Introduction

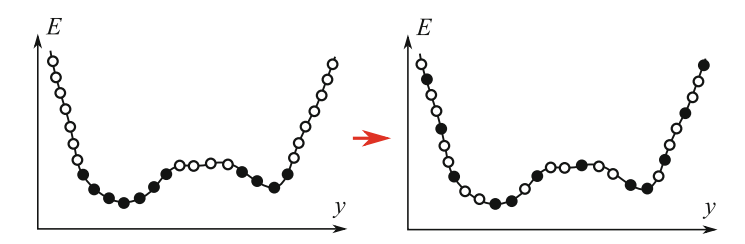


Fig. 1.14 Schematic illustration of the transition between integer quantum Hall effect at filling factor  $\nu=1$  and fractional quantum Hall effect at  $\nu=1/3$  in the presence of the disorder potential. Left panel: In strong magnetic fields electrons occupy all the states in the valleys of the potential landscape, i.e., they form lakes described by the functions similar to (1.70). Right panel: At even stronger magnetic fields, the magnetic length  $l_B \sim 1/\sqrt{B}$  becomes very small and the Coulomb energy starts to dominate. It is then energetically favorable for electrons to form the Laughlin state (1.75) with the three times smaller density. However, some quasi-particles occupy states in the valleys. Note that the state (1.75) is not a Slater determinant, and the picture in the right panel is very schematic

density of quasi-holes is large enough they also condense in a Laughlin type state (see Chap. 7 of Ref. [43]). To understand this situation it is useful to introduce the so-called quasi-particle representation of the wave function:

$$|\Psi\rangle = \int \prod_{l}^{M} d^{2}\xi_{l} \exp\left(-\frac{|\xi_{l}|}{4ml_{B}^{2}}\right) \psi^{*}(\xi_{1}, \dots, \xi_{M}) \prod_{l < k}^{M} (\xi_{l} - \xi_{k})^{\alpha} \prod_{l}^{M} \hat{\psi}(\xi_{l}) |\Psi_{L}\rangle.$$
(1.82)

Then, numerical calculations show that the Schrödinger equation for the "wave function"  $\psi(\xi_1,\ldots,\xi_M)$  of quasi-holes is very similar to the Schrödinger equation for electrons in the perpendicular magnetic field of some effective value, provided one has chosen  $\alpha=1/m$ . Thus, one can conclude that the wave function with the quasi-particle representation

$$\psi(\xi_1, \dots, \xi_M) = \prod_{k < l}^{M} (\xi_k - \xi_l)^{2n + \alpha} \exp\left(-\frac{1}{4ml_B^2} \sum_{l}^{M} |\xi_l|^2\right)$$
(1.83)

should be a good approximation for the eigenstate. Repeating this procedure several times we obtain the so called hierarchic construction. This construction explains the appearance of the Hall plateaus at complex filling fractions. Note, that one can relate several sorts of quasi-particles in this construction with several separately conserved currents in the effective models, thus clarifying the nature of these currents. Finally, we would like to note that higher levels of the hierarchy can be energetically favorable only in very clean samples, where the Hall plateaus are narrow. Thus, in the limit of a very clean sample one restores the picture with which we have started at the end of Sect. 1.2.3, namely, the linear dependence of the Hall resistance on the magnetic field.

Microscopic approach also clarifies the nature of gapless boundary degrees of freedom predicted by the effective theory. Namely, we have shown that all the quantum Hall effect states are incompressible. On the other hand, the edge deformations of an incompressible liquid of finite area should be gapless. In other words, these edge degrees of freedom are the quantum analogs of the edge magneto-plasmons in classical physics. These excitations have the same properties for integer and fractional quantum Hall states, and as we show below in Chaps. 3 and 5, they present a more natural language for the description of edge physics than the single particle edge states. In the end, we note the edge physics might be quite complicated because of the edge reconstruction phenomenon, the presence of neutral hydrodynamic modes, etc. However, these phenomena are not considered in the present thesis, since they seem to be irrelevant for understanding of the existing low-energy mesoscopic experiments. Moreover, we have not addressed several interesting topics in the quantum Hall effect theory in this introduction, because we concentrate on the basic ideas important for the problems considered in the thesis.

### 1.4 Quantum Hall Effect at Mesoscopic Scales

In the previous sections, we have described the basic physics of the quantum Hall effect in the bulk and at the edge of a sample and discussed earlier experimental observations. The recent progress in the fabrication of semiconductor heterostructures at mesoscopic scale has made it possible to realize more complex experiments, which utilize and study the quantum Hall edge states. In what follows, we describe these experiments in some detail.

# 1.4.1 Mesoscopic Systems Utilizing Edge States

The quantum Hall edge states have several exciting properties which make them interesting objects for experimental investigation. Namely, they are almost an ideal realization of one-dimensional electron wave guides. This fact has led to the emergence of a new branch in the experimental mesoscopic physics dubbed as electron optics. This name is connected to the fact that the electrons in quantum Hall edge states are similar to photons, namely, they have the following properties:

- *chirality*: electrons propagate unidirectionally, similar to photons;
- controlled backscattering: although there is no intrinsic backscattering along the
  quantum Hall edge, it may be realized by bringing two edge states of opposite
  chirality close to each other, thereby constructing a semi-transparent beam splitter.

However, there are also important differences between the quantum Hall edge states and photons:

• fermion statistics: electrons are fermions in contrast to photons which are bosons;

32 1 Introduction



Fig. 1.15 Fabry–Perot, Mach–Zehnder, and Hanburry-Brown–Twiss electronic interferometers are schematically shown. *Left panel*: The Fabry–Perot interferometer is the easiest interferometer to fabricate. It contains two counter-propagating edge states connected by quantum point contacts which serve as beam splitters, shown in *red* color. *Middle panel*: The Mach–Zehnder interferometer is the true two-path interferometer. Details of its fabrication are discussed below. *Right panel*: The Hanbury-Brown–Twiss interferometer allows to observe the two-particle coherent effects for electrons originating from two independent sources

• *non-zero charge*: electrically charged electron are strongly interacting particles, in contrast to photons which do not interact in a trivial way.

Such similarities on the one hand and differences on the other hand attract a great attention of both experimentalists and theoreticians, searching for a new physics.

Most of the modern experiments on quantum Hall edge states are focused on exploring of their mesoscopic properties. The first important process which deserves a special attention is dephasing. Namely, one may study the value of the corresponding length scale and its dependence on the temperature, applied voltage bias, etc. In addition, one may study different sources of dephasing such as interactions, external noise, etc. Another interesting process which occurs at mesoscopic scale is the equilibration of edge states. Namely, one may investigate the main mechanisms of equilibration, the characteristic length scales, etc. The processes of dephasing are studied with the help of various types of interferometers (see Fig. 1.15). The simplest interferometer to fabricate is the Fabry–Perot interferometer [44]. It has, however, some drawbacks, such as additional side effects masking interesting physics, e.g., multiple reflections effects and the Coulomb blockade effect. An ideal two-path interferometer which is free from these effects is the Mach-Zehnder interferometer [45]. In addition, one may study the many-particle interference effects in a more complex Hanburry-Brown-Twiss interferometers [46]. The idea of using this type of interferometers for the investigation of the two-particle Aharonov-Bohm effect has been proposed in [47] and realized recently in [48] with the help of quantum Hall edge states.

Let us illustrate the principles of electronic interferometry with the example of the Mach–Zehnder interferometer. The idea of the electronic Mach–Zehnder interferometer is the same in all recent experiments [5, 49–54]. The region of the sample, where the two-dimensional electron gas is present, is topologically equivalent to so called *Corbino disk* (see Fig. 1.16). There are at least two Ohmic contacts: one is grounded, and the second is biased by the potential difference  $\Delta \mu$ . The current I is detected at one of the Ohmic contacts. In fact, experiments that we discuss have

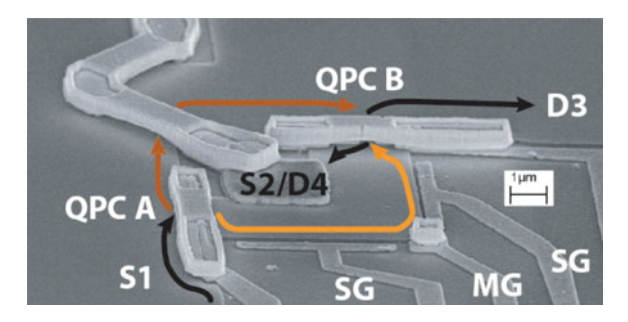


**Fig. 1.16** The electron micro-photograph of the Mach–Zehnder interferometer fabricated in the University of Basel [53, 54]. The electron gas is confined to the etched region which is topologically equivalent to the Corbino disk. The inner Omic contact *S2/D4* is connected to the measurement circuit with the help of a metallic air bridge. Two air bridges are also used to apply negative potential to the two quantum point contacts marked as *QPC A* and *QPC B*. The electron wave packets are split at the *QPC A* into coherent superposition of two packets which go either along one edge or another one, which are marked by the *yellow* and *brown lines*. These two paths enclose the magnetic flux, which can be varied by applying a negative voltage to the modulation gate marked as *MG*. After Ref. [53]

used several Ohmic contacts for the convenience of the measurement, although only two contacts are required for the realization of Mach–Zehnder interferometer. Two quantum point contacts play a role of beam splitters which mix outer edge channels (thin blue line in Fig. 1.17). The inner channels (black line in Fig. 1.17) are always reflected from quantum point contacts.

Typically, the transparencies of two quantum point contacts were varied between  $T_\ell=0$  and  $T_\ell=1$ ,  $\ell=L$ , R. However, the most interesting physics has been observed in two limits: in the regimes of weak tunneling  $T_\ell\to 0$  and of weak backscattering  $T_\ell\to 1$ . In the first regime one of the outer channels is biased (upper channel in Fig. 1.17) and almost completely reflected at the first quantum point contact. Then it runs on the same (upper) part of the Corbino disk. The channel that originates from the second (lower) Ohmic contact is grounded. In the second regime (shown in Fig. 1.17 as example) the biased channels are almost fully transmitted at the first quantum point contact to the opposite (lower) part of the Corbino disk. The physical consequences of the difference between these two regimes will be discussed later in Sect. 3.4.

Two Ohmic contacts are connected solely via scattering at two quantum point contacts. Consequently, there are two paths between Ohmic contacts, which contribute to the total current *I*. The first path is reflected at the right quantum point contact and transmitted at the left one, while it is the other way around for the second path. It is easy to see that two paths enclose a loop with the nonzero magnetic flux. The Aharonov–Bohm phase associated with it may be changed either by varying slightly the strength of the magnetic field, or by varying the length of one of the paths with the help of the modulation gate placed near the corresponding arm of the interferometer.

According to the frequently used single-particle picture [4], the electron edge states propagate as plane waves with the group velocity  $v_F$  at Fermi level. They are

34 1 Introduction

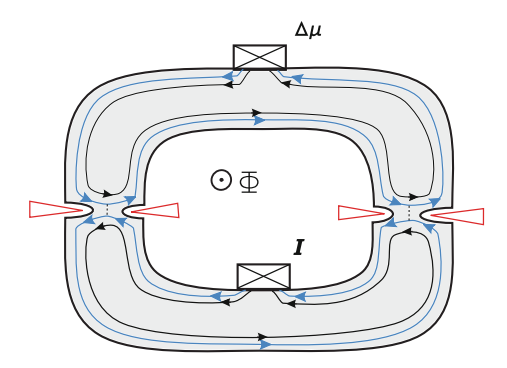


Fig. 1.17 The Mach–Zehnder interferometer is schematically shown as a Corbino disk which contains the two-dimensional electron gas. In strong magnetic field at filling factor  $\nu=2$  two chiral one-dimensional channels are formed and propagate along the edge of two-dimensional electron gas. Inner channels (*black line*) are always reflected from both quantum point contacts, while outer channels (*blue line*) are mixed by quantum point contacts. Bias  $\Delta\mu$  applied to the upper Ohmic contact causes the current I to flow to the lower Ohmic contact. This current is due to scattering at quantum point contacts and contains the interference contribution sensitive to the magnetic flux  $\Phi$  and leading to Aharonov–Bohm oscillations. After Ref. [38].  $\odot$  American Physical Society

transmitted through the Mach–Zehnder interferometer (see Fig. 1.17) at the left and right quantum point contacts with amplitudes  $t_L$  and  $t_R$ , respectively. In the case of low transmission, two amplitudes add so that the total transmission probability oscillates as a function of the Aharonov–Bohm phase  $\varphi_{AB}$  and bias  $\Delta \mu$ . The visibility of the oscillations of the differential conductance  $\mathcal{G} \equiv dI/d\Delta \mu$  is defined as

$$V_{\mathcal{G}} = \frac{\mathcal{G}_{\text{max}} - \mathcal{G}_{\text{min}}}{\mathcal{G}_{\text{max}} + \mathcal{G}_{\text{min}}}.$$
 (1.84)

Then the Landauer–Büttiker formula [55] applied to the differential conductance gives the following result for the visibility and the Aharonov–Bohm phase shift:

$$V_{\mathcal{G}} = \frac{2|t_L t_R|}{|t_L|^2 + |t_R|^2}, \quad \Delta \varphi_{AB} = \frac{\Delta L}{v_F} \Delta \mu, \tag{1.85}$$

where  $\Delta L$  is the length difference between two paths of the Mach–Zehnder interferometer. Thus we arrive at the result that in the absence of interaction the visibility is independent of bias, while phase shift grows linearly with bias.

# 1.4.2 Formulation of Problems and Outline

The first experiments with Mach–Zehnder interferometers brought completely unexpected results. The most remarkable observation made in experiments [5, 49–54] is

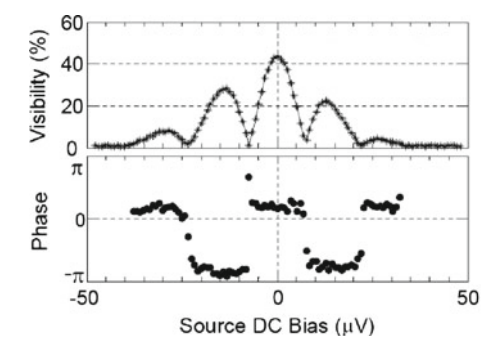


**Fig. 1.18** Experimental results for the dependence of the visibility and phase shift of the Aharonov–Bohm oscillations on the voltage bias obtained in Ref. [5] using lock-in technique at the filling factor  $\nu=2$ . Note the lobe type pattern of the visibility with respect to the bias and the phase jumps on  $\pi$  at zeros of the visibility. Reprinted figure with permission from [5]. © American Physical Society 2006

that the simple single-particle picture of edge states described in the previous section fails to correctly describe the Aharonov–Bohm effect in Mach–Zehnder interferometers. Essentially, the results can be summarized as following: The visibility of Aharonov–Bohm oscillations is not constant, but rather strongly depends on bias  $\Delta\mu$ . It oscillates, showing a new energy scale, and may vanish at specific values of bias (see Fig. 1.18). Although this behavior is observed in subsequent experiments, the details are different and very important for understanding the underlying physics. Therefore, we group these observations according to specific important features of the experimental set-up, and describe them in detail in Chap. 3. There are only few experiments on the equilibration of edge states yet, but they have already shown unexpected results. Namely, it has been found that at filling factor  $\nu=2$  the equilibration length is very short, and the measured energy flux along the edge is lower that the naive theoretical bound [6, 7].

Besides mentioned above unexpected experimental results, there are purely theoretical problems concerning the physics of edge states. One of them is that the effective theory allows several models for each complex fraction, e.g., for  $\nu=2/3,2/5,3/7$ , etc. At the same time, no experimental ways to discriminate these models have been proposed. Moreover, there are no general theoretical arguments that allow to choose a specific model. Another theoretical problem is related to the so called Byers–Yang paradox. Its formulation is very simple: The existence of fractionally charged quasi-particles naively leads to the Aharonov–Bohm oscillations with periods larger than the flux quantum. On the other hand, the microscopic Hamiltonian is invariant under the insertion of the singular flux quantum. There have been earlier attempts to resolve this paradox, but all of them rely on assumptions which require further justifications (see Chap. 8).

These unexpected and intriguing experimental results together with existing theoretical problems became a subject of further extensive investigations. A part of these investigations forms the basis of this thesis. All the material presented in the thesis

36 1 Introduction

is split in two parts. First part is devoted to the study of the mesoscopic effects in the integer quantum Hall effect. Namely, in this part we:

- *develop* a new theoretical approach to one-dimensional interacting systems: the non-equilibrium bosonization technique. We describe it in Chap. 2 and then apply this technique to several situations discussed in the following chapters;
- *explain* in Chaps. 3 and 4 all the unexpected results of experiments on dephasing in Mach–Zehnder interferometers with the help of a single model;
- *make predictions* for the temperature dependence of dephasing length in Chap. 3 and for the equilibration length scales in Chap. 5. We also investigate the dephasing of quantum Hall edge states due to coupling to external noise in Chap. 4 and predict the noise induced phase transition.

In the second part we generalize the ideas of the previous part to address the fractional quantum Hall effect and study the specific features of the fractional states. Namely, in the second part we:

- *develop*, in Chap. 6, the classification of effective edge models in terms of the plasmon modes which is based on the results of the previous part;
- *propose an experiment*, in Chap. 7, which allows to distinguish possible effective models for complex fractions using edge state interferometry;
- provide explicit derivation of the effective theory from the microscopic approach in the case of a non-trivial topology and thus resolve the Byers–Yang paradox; see Chap. 8.

Finally, the detailed summary together with a discussion of the obtained results for both parts is provided in Chap. 9.

### References

- 1. K. v. Klitzing, G. Dorda, M. Pepper, Phys. Rev. Lett. 45, 494 (1980)
- 2. A.M. Chang, Rev. Mod. Phys. 75, 1449 (2003)
- 3. X.-G. Wen, Adv. Phys. 44, 405 (1995)
- S. Datta, Electronic transport in mesoscopic systems (Cambridge University Press, Cambridge, 1999)
- 5. I. Neder, M. Heiblum, Y. Levinson, D. Mahalu, V. Umansky, Phys. Rev. Lett. 96, 016804 (2006)
- 6. H. le Sueur et al., Phys. Rev. Lett. 105, 056803 (2010)
- 7. C. Altimiras et al., Phys. Rev. Lett. **105**, 226804 (2010)
- 8. F.E. Camino, W. Zhou, V.J. Goldman, Phys. Rev. B **72**, 075342 (2005)
- 9. F.E. Camino, W. Zhou, V.J. Goldman, Phys. Rev. Lett. 98, 076805 (2007)
- 10. F.E. Camino, W. Zhou, V.J. Goldman, Phys. Rev. B 74, 115301 (2006)
- 11. R.L. Willett, L.N. Pfeiffer, K.W. West, PNAS **106**, 8853 (2009)
- R.L. Willett, L.N. Pfeiffer, K.W. West. arXiv:0911.0345
   YuV Sharvin, Sov. Phys. JETP 21, 655 (1965)
- B.J. van Wees, H. van Houten, C.W.J. Beenakker, J.G. Williamson, L.P. Kouwenhoven, D. van der Marel, C.T. Foxon, Phys. Rev. Lett. 60, 848 (1988)
- 15. B.J. van Wees, H. van Houten, C.W.J. Beenakker, J.G. Williamson, L.P. Kouwenhoven, D. van der Marel, C.T. Foxon, Phys. Rev. B 43, 12431 (1991)

References 37

- 16. C.J. Gorter, Physica 17, 777 (1951)
- 17. C.W.J. Beenakker, Phys. Rev. B 44, 1646 (1991)
- 18. L.P. Gorkov, A.I. Larkin, D.E. Khmelnitskii, JETP Lett. 30, 248 (1979)
- N.W. Ashcroft, N.D. Mermin, Solid State Physics (Holt, Rinehart, and Winston, New York, 1976)
- 20. V. Umansky, R. de-Picciotto, M. Heiblum, Appl. Phys. Lett. 71, 683 (1997)
- 21. A. Comtet, T. Jolicoeur, S. Ouvry, F. David (eds.), *Topological Aspects of Low Dimensional Systems* (Springer, Berlin and Les Editions de Physique, Les Ulis, 2000)
- 22. H.P. Wei, A.M. Chang, D.C. Tsui, M. Razeghi, Phys. Rev. B 32, 7016 (1985)
- 23. H.P. Wei, D.C. Tsui, A.M.M. Pruisken, Phys. Rev. B 33, 1488 (1986)
- 24. Ebert G., von Klitzing K., Weimann G., J. Phys., C 18, L257 (1985)
- 25. D.C. Tsui, H.L. Stormer, A.C. Gossard, Phys. Rev. Lett. 48, 1559 (1982)
- 26. L. Saminadayar, D.C. Glattli, Y. Jin, B. Etienne, Phys. Rev. Lett. **79**, 2526 (1997)
- R. de-Picciotto, M. Reznikov, M. Heiblum, V. Umansky, G. Bunin, D. Mahalu. Nature 389, 162 (1997)
- R. Willett, J.P. Eisenstein, H.L. Stormer, D.C. Tsui, A.C. Gossard, J.H. English, Phys. Rev. Lett. 59, 1776 (1987)
- 29. X.G. Wen, Phys. Rev. Lett. 66, 802 (1991)
- 30. L.D. Landau, E.M. Lifshits, *Theoretical Physics*, vol. 3 (Butterworth-Heinemann, Oxford)
- 31. H.P. Wei, D.C. Tsui, M.A. Paalanen, A.M.M. Pruisken, Phys. Rev. Lett. 61, 1294 (1988)
- 32. D.E. Khmelnitskii, JETP Lett. 38, 552 (1983)
- 33. R.B. Laughlin, Phys. Rev. B 23, 5632 (1981)
- 34. B.I. Halperin, Phys. Rev. B 25, 2185 (1982)
- M. Marino, Chern-Simons Theory, Matrix Models, and Topological Strings (Oxford University Press, Oxford, 2005)
- 36. C. Kassel, V. Turaev, Braid Groups (Springer, Heidelberg, 2008)
- 37. E. Witten, Commun. Math. Phys. 121, 351 (1989)
- 38. I.P. Levkivskyi, E.V. Sukhorukov, Phys. Rev. B 78, 045322 (2008)
- R.B. Laughlin, M.L. Cohen, J.M. Kosterlitz, H. Levine, S.B. Libby, A.M.M. Pruisken, Phys. Rev. B 32, 1311 (1985)
- 40. F.D.M. Haldane, Phys. Rev. Lett. **51**, 605 (1983)
- 41. R.B. Laughlin, Phys. Rev. Lett. **50**, 1395 (1983)
- 42. F.D.M. Haldane, E.H. Rezayi, Phys. Rev. B 31, 2529 (1985)
- 43. R.E. Prange, S.M. Girvin, *The Quantum Hall Effect* (Springer, New York, 1987)
- 44. F.E. Camino, W. Zhou, V.J. Goldman, Phys. Rev. Lett. 95, 246802 (2005)
- 45. Y. Ji et al., Nature (London) 422, 415 (2003)
- 46. H.-S. Sim, E.V. Sukhorukov, Phys. Rev. Lett. 96, 020407 (2006)
- 47. P. Samuelsson, E.V. Sukhorukov, M. Buttiker, Phys. Rev. Lett. 92, 026805 (2004)
- 48. I. Neder, N. Ofek, Y. Chung, M. Heiblum, D. Mahalu, V. Umansky, Nature 448, 333 (2007)
- P. Roulleau, F. Portier, D.C. Glattli, P. Roche, A. Cavanna, G. Faini, U. Gennser, D. Mailly, Phys. Rev. B 76, 161309 (2007)
- P. Roulleau, F. Portier, D.C. Glattli, P. Roche, A. Cavanna, G. Faini, U. Gennser, D. Mailly, Phys. Rev. Lett. 100, 126802 (2008)
- 51. L.V. Litvin, H.-P. Tranitz, W. Wegscheider, C. Strunk, Phys. Rev. B 75, 033315 (2007)
- L.V. Litvin, A. Helzel, H.-P. Tranitz, W. Wegscheider, C. Strunk, Phys. Rev. B 78, 075303 (2008)
- E. Bieri, Correlation and interference experiments with edge states. Ph.D. thesis, University of Basel (2007)
- E. Bieri, M. Weiss, O. Goktas, M. Hauser, C. Schonenberger, S. Oberholzer, Phys. Rev. B 79, 245324 (2009)
- 55. M. Büttiker, Phys. Rev. Lett. **57**, 1761 (1986)

# Part I Integer Quantum Hall Effect

# **Chapter 2 Equilibrium and Non-Equilibrium Bosonization**

In this chapter we consider one of the most important theoretical methods in one-dimensional physics—the bosonization approach. This method allows one to exactly diagonalize the Hamiltonian of interacting fermions [1, 2]. The main result of this method is that the excitation spectrum of such a system in one-dimension consist of gapless boson modes, in striking contrast with the Fermi liquid picture. This is because the restricted dimensions enhance the scattering between the electrons and completely destroy the quasi-particle picture in one dimension. We start with the basic introduction to the bosonization approach in Sect. 2.1. Then we compute the equilibrium correlation functions of interacting fermions in the framework of this approach. Finally, in Sect. 2.3 we generalize the bosonization technique to the non-equilibrium situation and introduce a new method—the non-equilibrium bosonization, which will be used in several chapters of this thesis.

### 2.1 Bosonization of One-Dimensional Fermions

## 2.1.1 One-Dimensional Interacting Systems

Let us consider a system of one-dimensional fermions. These can be electrons in quantum wires, quantum Hall edge states, etc. Here we would like to introduce a general approach, where one considers n one-dimensional channels of either same or different chiralities. In the case of integer quantum Hall effect,  $\nu$  edge states have the same chirality, while in fractional Hall states some one-dimensional channels might have opposite chiralities. Let us denote the operator of annihilation of an electron in a state with wave vector k in  $\alpha$ th channel as  $c_{k\alpha}$ . These operators obey the fermionic

Some text sections in this chapter are reproduced from Phys. Rev. B 78, 045322 (2008), Phys. Rev. Lett. 103, 036801 (2009), © American Physical Society.

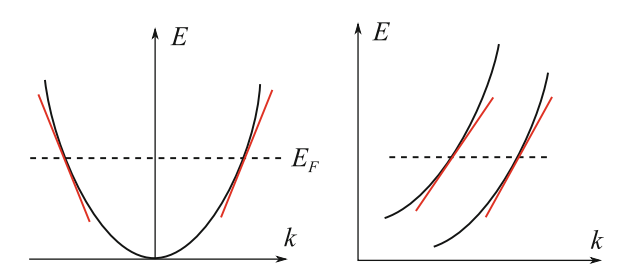


Fig. 2.1 Illustration of the linearization of spectrum of one-dimensional electrons. Left panel shows the spectrum of electrons in quantum wires. The electrons with energies near the Fermi energy  $E_F$  give a contribution to transport. Thus, one can linearize the actual spectrum (black curve) and replace it with two branches (red, straight lines) of left and right moving chiral electrons with the same Fermi velocity. Right panel shows the situation at the edge of a two-dimensional electron gas in the regime of integer quantum Hall effect. Here the Fermi surface is located near the actual edge of the sample. Different branches correspond to different Landau levels. The spectrum can be linearized in this case too, and one obtains several channels of the same chirality. Note that the Fermi velocities are generally different in the case of integer quantum Hall effect (Color figure online)

anti-commutation relations, i.e.,

$$\{c_{k\alpha}^{\dagger}, c_{k'\beta}\} = \delta_{kk'}\delta_{\alpha\beta},\tag{2.1}$$

while all other anti-commutators are zero. The free single-particle Hamiltonian can be written as:

$$\mathcal{H}_0 = \sum_{\alpha} \sum_{k=-\Lambda}^{\Lambda} \epsilon_{k\alpha} c_{k\alpha}^{\dagger} c_{k\alpha}, \qquad (2.2)$$

where  $\epsilon_{k\alpha}$  are single-particle energies (see Fig. 2.1), and we introduced an ultraviolet cut-off  $\Lambda$ . If one is interested in low energy physics, such as a transport through the system, then one may choose  $\Lambda \ll E_F$  and linearize the spectrum of fermions, so that  $\epsilon_{k\alpha} = v_{F\alpha}k$ , where the wave vector in each channel is defined with respect to the corresponding Fermi wave vector. For convenience, we also redefine the index  $\alpha$  so that it enumerates the *Fermi points*, for example, the left and right movers in a quantum wire, referred as two different channels.

Next, we would like to introduce the set of fermion field operators in each channel as follows:

$$\psi_{\alpha}(x) = \frac{1}{\sqrt{W}} \sum_{k} c_{k\alpha} e^{ikx}, \qquad (2.3)$$

where W is the length of the system. These operators obey the standard anticommutation relations  $\{\psi_{\alpha}^{\dagger}(x), \psi_{\beta}(y)\} = \delta_{\alpha\beta}\delta(x-y)$ , and the free Hamiltonian (2.2) can be written in terms of these operators as following:

$$\mathcal{H}_0 = -i \sum_{\alpha} v_{F\alpha} \int dx \psi_{\alpha}^{\dagger}(x) \partial_x \psi_{\alpha}(x). \tag{2.4}$$

A naive definition of the charge density operator at a point x in terms of the fermion field is  $\rho_{\alpha}(x) = \psi_{\alpha}^{\dagger}(x)\psi_{\alpha}(x)$ . However, such definition leads to the divergent result for the ground state density:

$$\langle \rho_{\alpha}(x) \rangle = (1/W) \sum_{k,k'} e^{ix(k'-k)} \langle c_{k\alpha}^{\dagger} c_{k'\alpha} \rangle = (1/W) \sum_{k} \langle c_{k\alpha}^{\dagger} c_{k\alpha} \rangle. \tag{2.5}$$

This result is partly an artifact of the introduced linearization, but in the case of quantum Hall effect it has a physical meaning. Namely, there is no preferred choice of minimal momentum, starting from which we attribute a state to the edge and not to the bulk. Fortunately, this divergent contribution is constant. Therefore, we define the edge density operator where this divergent constant is subtracted:

$$\rho_{\alpha}(x) = :\psi_{\alpha}^{\dagger}(x)\psi_{\alpha}(x) : \equiv \psi_{\alpha}^{\dagger}(x)\psi_{\alpha}(x) - \langle \psi_{\alpha}^{\dagger}(x)\psi_{\alpha}(x) \rangle. \tag{2.6}$$

One can check that the fermion operator annihilates a unit local charge:

$$[\psi_{\alpha}(x), \rho_{\beta}(y)] = \delta_{\alpha\beta}\psi_{\alpha}(x)\delta(x - y). \tag{2.7}$$

Finally, we would like to take into account the fact that electrons interact with each other. In general, the interaction Hamiltonian is a functional of the density  $\mathcal{H} = \mathcal{H}_0 + \mathcal{H}_{int}[\rho_{\alpha}(x)]$ . Here we will consider only the case of (screened) Coulomb interaction, so that:

$$\mathcal{H}_{\text{int}} = \iint dx dy U_{\alpha\beta}(x - y) \rho_{\alpha}(x) \rho_{\beta}(y), \qquad (2.8)$$

where  $U_{\alpha\beta}(x-y)$  is the Coulomb interaction potential.

### 2.1.2 Bosonic Fields and Hamiltonian

In this section we would like to introduce and investigate the Fourier modes of the density field which are defined as following,

$$\rho_{k\alpha} \equiv (1/W) \int dx e^{ikx} \rho_{\alpha}(x) = (1/W) \sum_{k'} c^{\dagger}_{k+k'\alpha} c_{k'\alpha}, \quad k \neq 0,$$
 (2.9)

and the zero mode operator:

$$\pi_{\alpha} = (1/W) \int \rho_{\alpha}(x) dx, \qquad (2.10)$$

representing the homogeneous part of the charge density. One can check the relation  $\rho_{-k\alpha} = \rho_{k\alpha}^{\dagger}$ , which follows from the fact that the density field is real. Importantly,

the operators (2.9) have bosonic nature, namely, one can check that the commutators of two such operators are zero:

$$[\rho_{k\alpha}, \rho_{k'\beta}] = 0, \quad k \neq -k'. \tag{2.11}$$

However, for the case k' = -k and  $\alpha = \beta$  the above commutator is ill defined if the summation in the definition (2.9) goes up to infinity. The expression for this commutator can be written in terms of the occupation number operators  $n_{k\alpha} \equiv c_{k\alpha}^{\dagger} c_{k\alpha}$ :

$$[\rho_{k\alpha}, \rho_{-k\alpha}] = (1/W^2) \Big[ \sum_{k' < -\Lambda} (n_{k'-k,\alpha} - n_{k'\alpha}) + \sum_{k' \ge -\Lambda} (n_{k'-k,\alpha} - n_{k'\alpha}) \Big]. \quad (2.12)$$

If we assume, that all the states below the cut-off are always filled, then we can shift the summation variable in the second sum and get

$$[\rho_{k\alpha}, \rho_{-k\alpha}] = \pm \frac{k}{2\pi W},\tag{2.13}$$

where we have taken into account the quantization of the wave vector  $\Delta k = 2\pi/W$ , and the sign stays for the chirality of the corresponding channel. This anomalous commutator will be important in Chap. 6 for the connection between the bulk and the edge effective theories in the classification of the edge model of fractional quantum Hall effect. Here we only note, that this commutation relation completes the canonical bosonization of the density operators.

The most important step in the bosonization procedure is to express the fermion fields in terms of the density fields [1, 3]. Namely, one can check that the expression:

$$\psi_{\alpha}(x) = \frac{1}{\sqrt{a}} \exp\left[i\varphi_{\alpha} + 2\pi i \cdot \pi_{\alpha} x + \sum_{k} \frac{2\pi i}{k} \rho_{k\alpha} e^{ikx}\right], \qquad (2.14)$$

where  $\varphi_{\alpha}$  is zero mode canonically conjugated to  $\pi_{\alpha}$  and  $a=2\pi/\Lambda$ , has all the properties of the electron operator. First of all, one can check that the commutation relation with charge density operators (2.7) holds for the operator (2.14). Second, the operator (2.14) has fermionic statistics:

$$\{\psi_{\alpha}^{\dagger}(x), \psi_{\beta}(y)\} = \delta_{\alpha\beta}\delta(x - y). \tag{2.15}$$

In fact, it is more convenient to introduce new fields  $\phi_{\alpha}(x)$ , related to the densities as

$$\rho_{\alpha}(x) = \frac{1}{2\pi} \partial_x \phi_{\alpha}(x). \tag{2.16}$$

Then, it follows from (2.16), (2.11) and (2.13) that these fields satisfy the commutation relations of the following form:

$$[\phi_{\alpha}(x), \phi_{\beta}(y)] = \pm i\pi \operatorname{sgn}(x - y)\delta_{\alpha\beta}$$
 (2.17)

where the sign stays for the chirality of the corresponding channel. In terms of the boson fields  $\phi_{\alpha}$ , Eq. (2.14) becomes much simpler:

$$\psi_{\alpha}(x) = \frac{1}{\sqrt{a}} e^{i\phi_{\alpha}(x)}.$$
 (2.18)

This expression is one of the main equations of the bosonization approach.

In the next step we represent the Hamiltonian (2.2) in terms of the boson fields as well. In order to do so, we note that the equation of motion for the density modes generated by this Hamiltonian is given by:

$$[\mathcal{H}_0, \rho_{k\alpha}] = v_{F\alpha} k \rho_{k\alpha}. \tag{2.19}$$

Taking into account the commutation relations (2.11), (2.13) for bosons, one concludes that the Hamiltonian could be expressed as follows:

$$\mathcal{H}_0 = \sum_{\alpha} \frac{v_{F\alpha}}{4\pi} \int dx (\partial_x \phi_\alpha(x))^2$$
 (2.20)

This result can be obtained alternatively substituting Eq. (2.18) into Eq. (2.4) and performing point splitting procedure [4]. Thus, we finally conclude, that in the case of interactions sensitive to the long wavelength part of the densities, the total Hamiltonian becomes *quadratic*:

$$\mathcal{H} \equiv \mathcal{H}_0 + \mathcal{H}_{int} = \sum_{\alpha\beta} \iint \frac{dx dy}{8\pi^2} V_{\alpha\beta}(x - y) \partial_x \phi_{\alpha}(x) \partial_y \phi_{\beta}(y), \tag{2.21}$$

where the interaction potential is simply shifted by the Fermi velocity,

$$V_{\alpha\beta} = U_{\alpha\beta} + 2\pi v_{F\alpha} \delta_{\alpha\beta} \delta(x - y). \tag{2.22}$$

In fact, the effective edge theory action of fractional quantum Hall edge states (1.53) in absence of external fields coincides with the result of the bosonization approach. This means that the boson language is more universal than the fermion one, since the fermion single particle description exists only for integer quantum Hall effect, while the boson action of the same structure can be used to describe both integer and fractional quantum Hall effect.

### 2.1.3 Quantization of Boson Fields and Zero Modes

In this section we consider some important details of the above discussed construction, namely, the role of zero modes. The boson fields  $\phi_{\alpha}(x)$  can be written in terms of boson creation and annihilation operators  $a_{k\alpha}^{\dagger} \equiv \sqrt{W/2\pi k}\rho_{k\alpha}$  and  $a_{k\alpha} \equiv \sqrt{W/2\pi k}\rho_{-k\alpha}$ , which commutes as  $[a_{k\alpha}^{\dagger}, a_{k'\beta}] = \delta_{\alpha\beta}\delta_{kk'}$ , and in terms of the modes  $\varphi_{\alpha}$ ,  $\pi_{\alpha}$ , as

$$\phi_{\alpha}(x) = \varphi_{\alpha} + 2\pi \cdot \pi_{\alpha} x + \sum_{k>0} \sqrt{\frac{2\pi}{Wk}} \left[ a_{k\alpha} e^{ikx} + a_{k\alpha}^{\dagger} e^{-ikx} \right]. \tag{2.23}$$

We would like to recall that zero modes satisfy the canonical commutation relation  $[\pi_{\alpha}, \varphi_{\alpha}] = i/W$ , where W is the total size of the system. In the end of calculations we take the thermodynamic limit  $W \to \infty$ , so that W drops from the final results. The Hamiltonian acquires the following form in terms of the introduced operators:

$$\mathcal{H} = (1/2\pi) \sum_{k\alpha\beta} k \, V_{\alpha\beta}(k) a_{k\alpha}^{\dagger} a_{k\beta} + (W/2) \sum_{\alpha\beta} V_{\alpha\beta}(0) \pi_{\alpha} \pi_{\beta}, \tag{2.24}$$

where  $V_{\alpha\beta}(k)$  is the Fourier transform of the potential (2.22).

The vacuum for collective excitations is defined as  $a_{k\alpha}|0\rangle=0$ . The special care has to be taken about zero modes, because as we show in Sect. 3.4, zero modes determine charging effects and phase shifts, which are not small and important for the explanation of some experimental results in Chap. 3. From the definition (2.10) it is clear that the zero mode  $\pi_{\alpha}$  has a meaning of a homogeneous density at the channel  $\alpha$ . Therefore, we define "vacuum charges"  $Q_{\alpha}$ 

$$\pi_{\alpha}|0\rangle = O_{\alpha}|0\rangle,\tag{2.25}$$

which are in fact charge densities at the one-dimensional channels accumulated in accordance with electrochemical potential in a given channel. The energy  $E_0$  of the ground state, defined as  $\mathcal{H}|0\rangle = E_0|0\rangle$ , is then given by

$$E_0 = (W/2) \sum_{\alpha\beta} V_{\alpha\beta}(0) Q_{\alpha} Q_{\beta}. \tag{2.26}$$

Since the edge excitations in integer quantum Hall effect propagate along the equipotential lines, edge channels can be considered as metallic surfaces. We therefore can apply the well known electrostatic relation [5] for the potentials  $\Delta\mu_{\alpha}$  of the edge channels:

$$\Delta\mu_{\alpha} \equiv (1/W)\delta E_0/\delta Q_{\alpha} = \sum_{\beta} V_{\alpha\beta}(0)Q_{\beta}. \tag{2.27}$$

Thus the quantity  $V_{\alpha\beta}(0)$  is the inverse capacitance matrix. Using now Eq. (2.24), (2.25), and the commutation relation for zero modes, we arrive at the following important result for the time evolution of zero modes

$$Q_{\alpha}(t) = \sum_{\beta} V_{\alpha\beta}^{-1}(0) \Delta \mu_{\beta}, \quad \varphi_{\alpha}(t) = \varphi_{\alpha} - \Delta \mu_{\alpha} t.$$
 (2.28)

Sometimes, the zero modes discussed in this section are included in the fermion field in terms of the so called Klein factors. We think, however, that the formulation proposed here is more straightforward and clear, and thus can be easily generalized to different situations.

### 2.2 Correlation Function at Finite Temperature

After we have recast the Hamiltonian in a quadratic form, one can easily diagonalize it. Namely, one only needs to find a transformation matrix for boson fields, which preserves the commutator structure (2.17) and diagonalizes the interaction matrix (2.22). For the purely chiral case of integer quantum Hall effect such transformation is just an orthogonal transformation  $q_{\alpha j}$  so that  $qq^T=1$  and

$$V_{\alpha\beta}(k) = \sum_{j} q_{\alpha j} \omega_{j}(k) q_{j\beta}. \tag{2.29}$$

Here  $\omega_j(k)$  are the dispersion relations of the boson eigenmodes, which depend on the particular form of the interaction. Relation (2.16) indicates that these boson eigenmodes are in fact plasmons, the collective charge excitations. In the case of a short range interaction the dispersion is always linear  $\omega_j(k) = v_j k$ , and the transformation matrix is independent of k. Therefore, one can introduce diagonal fields defined as  $\phi_j(x) = q_{j\alpha}\phi_\alpha(x)$ . In terms of these fields, every fermion operator has a form  $\psi_\alpha = \exp\left(i\sum_j p_j\phi_j\right)$ , where  $p_j = q_{j\alpha}$ . In fact, similar operators with different values of the coefficients  $p_j$  appear in context of the effective theory of fractional quantum Hall edge. Thus, for further convenience we will do all the calculations in terms of these coefficients.

The main quantity which determines the physics of a fermion system is the time dependent two-point correlation function. In our case it can be written in the following form:

$$i\langle\psi^{\dagger}(x,t)\psi(0,0)\rangle = e^{i\varphi_0}K(x,t), \qquad (2.30)$$

where the first factor is the zero-mode contribution and the second one is the contribution of the oscillator operators. The phase induced by zero modes is given by  $\varphi_0 = \sum_i p_j \langle \pi_j \rangle (x - v_j t)$  and in the case of integer quantum Hall effect it can be

<sup>&</sup>lt;sup>1</sup> Note that  $\Delta \mu_{\alpha j}$  is the electrochemical potential, because our definition (2.22) contains a single-particle contribution.

written in a simple physical form:

$$\varphi_0 = \Delta \mu_0 t - 2\pi Q_0 x. \tag{2.31}$$

In the next step, we calculate the contribution of fluctuations. For the equilibrium state, this contribution can be rewritten in terms of the boson fields as:

$$\ln[K(x,t)] = \sum_{ij} p_i p_j \langle [\phi_i(x,t) - \phi_i(0,0)] \phi_j(0,0) \rangle.$$
 (2.32)

Introducing the notation  $X_j \equiv x + \sigma_j v_j t$ , where  $\sigma_j$  denotes the chirality of the corresponding eigenmode, we express the fields in terms of creation and annihilation operators,

$$\phi_j(x,t) = i \sum_k \sqrt{\frac{2\pi}{Wk}} \Big[ \tilde{a}_j(k) e^{ikX_j} + \tilde{a}_j^{\dagger}(k) e^{-ikX_j} \Big].$$
 (2.33)

Substituting this expression into Eq. (2.32), we obtain the following expression for the fluctuations contribution

$$\ln K = \sum_{j} p_{j}^{2} \int_{0}^{\Lambda} \frac{dk}{k} \left\{ f_{j}(k) (e^{-ikX_{j}} - 1) + [1 + f_{j}(k)](e^{ikX_{j}} - 1) \right\}, \quad (2.34)$$

where  $f_j(k) = [\exp(\beta v_j k) - 1]^{-1}$  are the equilibrium boson occupation numbers at inverse temperature  $\beta$ , and  $\Lambda$  is the ultraviolet cutoff.

The best way to proceed is to expand the occupation numbers in Boltzmann factors,  $f_j(k) = \sum_{n=1}^{\infty} \exp(-\beta v_j n \, k)$ , and integrate each term separately. This gives us

$$\ln K = -\sum_{j} p_{j}^{2} \sum_{n=-\infty}^{\infty} \ln[\Lambda(i\beta v_{j}n - X_{j})]. \tag{2.35}$$

Combining this expression with Eq. (2.30), we finally arrive at the following result for the fermion correlation function:

$$i\langle\psi^{\dagger}(x,t)\psi(0,0)\rangle \propto e^{i\varphi_0} \prod_{i} \left[\frac{v_i}{\pi T} \sinh\left(\pi \frac{TX_i}{v_i}\right)\right]^{-\delta_i},$$
 (2.36)

where  $\delta_i = p_i^2$ . The total scaling dimension of the correlation function  $\Delta \equiv \sum_i \delta_i$ , which determines the power law behavior or the correlation function at small times may be different in different cases. For example, in the situation of quantum wires it is expressed in terms of the Luttinger parameter [3]. Below in the thesis we calculate this dimension in several particular situations. However, it is important to note that the scaling dimension can be only equal to 1 in the situation of purely *chiral* system.

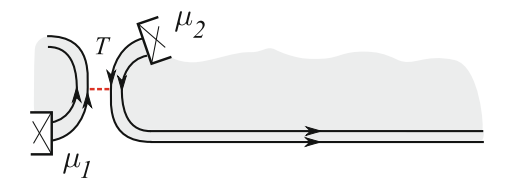


**Fig. 2.2** Example of the situation where the equilibrium bosonization cannot be used. Typically, the distribution function of one-dimensional electrons is fixed by the reservoir from which they originate. But in the situation with tunneling (shown by the *red*, *dashed line*) between two edges with different chemical potentials, the distribution function of outgoing electrons in the bosonic language is strongly non-equilibrium, if the tunneling is not weak (Color figure online)

Indeed, in this case

$$\sum_{i} \delta_{i} = \sum_{i} p_{i}^{2} = \sum_{i} q_{i\alpha} q_{\alpha i} = \delta_{\alpha \alpha} = 1, \qquad (2.37)$$

because of the orthogonality of the transformation. Therefore, the correlation function in chiral systems behaves as  $\langle \psi^{\dagger}(t)\psi(0)\rangle \sim 1/t$  even in the presence of interaction.

### 2.3 Non-Equilibrium Bosonization

In the previous section we have solved the interacting one-dimensional Hamiltonian and found the fermion correlation function. However, we did this only for an equilibrium state of electrons. In fact, the more general non-equilibrium conditions can not be included in the usual bosonization approach. For example, the problem appears in the situation where electron distribution function  $f(\epsilon)$  at the boundary is not a Fermi function  $f_F(\epsilon - \mu)$  but has a double step shape, i.e.,

$$f(\epsilon) = Rf_F(\epsilon - \mu_1) + Tf_F(\epsilon - \mu_2). \tag{2.38}$$

Of course in this situation one can bosonize the Hamiltonian and the fermion operators, but it is extremely difficult to express the distribution function (2.38) in terms of bosons. In order to treat the situations of such kind, as, e.g., illustrated in Fig. 2.2, we propose the non-equilibrium bosonization technique.

# 2.3.1 Non-Equilibrium Boundary Conditions and Full Counting Statistics

The Hamiltonian (2.21), together with the commutation relations (2.17), generates equations of motion for the fields  $\phi_{\alpha}$ . This equations have to be accompanied with boundary conditions. The key idea of the non-equilibrium bosonization approach is to describe the non-equilibrium state in terms of these boundary conditions. Namely, we write:

$$\partial_t \phi_{\alpha}(x,t) = -\frac{1}{2\pi} \sum_{\beta} \int dy V_{\alpha\beta}(x-y) \partial_y \phi_{\beta}(y,t), \qquad (2.39a)$$

$$\partial_t \phi_{\alpha}(0, t) = 2\pi j_{\alpha}(t). \tag{2.39b}$$

Here  $(1/2\pi)\partial_t\phi(x,t)$  is the expression for the edge currents in terms of the boson fields, and  $j_\alpha(t)$  are the operators of current in terms of fermion degrees of freedom at the boundary. For example, in the situation depicted in Fig. 2.2, the  $j_\alpha(t)$  are the tunneling currents.

The equations of motion (2.39a) are first order linear differential equations. Thus, these equations together with the boundary conditions (2.39b) can be easily solved with the help of the Green's functions method. The answer generally has the following form:

$$\phi_{\alpha}(x,t) = \sum_{\beta} \int dt' G_{\alpha\beta}(x,t-t') Q_{\beta}(t'), \qquad (2.40)$$

where, the Green's function  $G_{\alpha\beta}(x,t-t')$  depends on the particular form of the interaction potential  $U_{\alpha\beta}(x-y)$ , and we have introduced the charge operators defined as

$$Q_{\alpha}(t) = \int_{-\infty}^{t} dt' j_{\alpha}(t'). \tag{2.41}$$

Therefore, by solving Eq. (2.39), one may express the correlation functions of the fermion fields  $\psi_{\alpha}$  in terms of the correlation function of the charge operator:

$$\langle \psi_{\alpha}^{\dagger}(x,t)\psi_{\alpha}(y,0)\rangle = \prod_{\beta} \left\langle \exp\left[-i\int dt' G_{\alpha\beta}(x,t-t')Q_{\beta}(t')\right] \right.$$

$$\times \left. \exp\left[i\int dt' G_{\alpha\beta}(y,-t')Q_{\beta}(t')\right]\right\rangle. \tag{2.42}$$

Here, averaging on the right hand side is defined over the *free* electrons, e.g., over the distribution function (2.38). All the interaction effects are encoded in the Green's function. In general, the fields  $\phi_{\alpha}$  influence fluctuations of the currents  $j_{\alpha}$ , leading to the dynamical Coulomb blockade in the quantum low-energy regime [6], and to

cascade corrections to noise in the classical limit [7]. Importantly, simplification arises in such situations where such back-action effects are *absent*, e.g. for chiral edge states [8, 9]. As a consequence, the electron transport through the quantum point contact (see Fig. 2.2) is not affected by interactions, which has been recently confirmed in the experiment [10, 11].

In a chiral case with a short range interaction, the Green's function of Eq. (2.39a) can be found explicitly and it is given by a sum of delta functions. One can check by the direct substitution, that the solution for the boson fields is given by the following equation:

$$\phi_{\alpha}(x,t) = 2\pi \sum_{j\beta} q_{\alpha j} q_{j\beta} Q_{\beta}(t - x/v_j). \tag{2.43}$$

The above expression simplifies further in several cases considered in this thesis because of the special form of the transformation matrix q. In these cases one can express the correlation function (2.42) via the so called generator of full counting statistics of noise, defined as [12]

$$\chi_{\alpha}(\lambda, t) = \langle e^{i\lambda Q_{\alpha}(t)} e^{-i\lambda Q_{\alpha}(0)} \rangle. \tag{2.44}$$

This quantity is the quantum analog of the Fourier transform of the distribution function P(Q) of charge  $\chi(\lambda) = \langle e^{i\lambda Q} \rangle \equiv \int dQ P(Q) e^{i\lambda Q}$ . Main property of the generator (2.44) is that it gives all the irreducible moments of the current in the long-time limit:

$$\partial_{i\lambda}^{n} \log(\chi_{\alpha})/t = \langle \langle j_{\alpha}^{n} \rangle \rangle. \tag{2.45}$$

The full counting statistics generator (2.44) has been extensively studied recently [13], and it is known in several situations. In the next chapters we will study and use this generator for the statistics of electrons tunneling through a quantum point contact.

# 2.3.2 Equilibrium Boundary Conditions: A Simple Test

The simplest test of the non-equilibrium bosonization approach is to consider an infinite quantum Hall edge and formally split it in two parts at the point x=0. Then, the boundary conditions at this point describe only the thermal equilibrium fluctuations of the charge density. Thus, one can calculate the electron correlation function within our approach, and compare it to the well known result for the finite temperature correlator in a chiral one-dimensional system (2.36). The solution of the equations of motion (2.39) in the system with single channel and short range interaction is simple:

$$\phi(x,t) = Q(t - x/v), \tag{2.46}$$

where  $v = v_F + U/2\pi$ . The non-equilibrium bosonization prescription gives the expression for the correlation function  $\psi^{\dagger}(x,t)\psi(0,0) = \chi(2\pi,t-x/v)$ .

The thermal fluctuations have Gaussian statistics, therefore one can write down the generating function as follows:

$$\log[\chi(\lambda, t)] = -(\lambda^2/2)\langle Q_{\alpha}^2(t) - 2Q_{\alpha}(t)Q_{\alpha}(0) + Q_{\alpha}^2(0)\rangle. \tag{2.47}$$

Taking into account the definition of charge operator (2.41) one can rewrite this result via the power spectrum of current fluctuations:

$$\log[\chi(\lambda, t)] = -(\lambda^2/2) \int \frac{d\omega}{2\pi\omega^2} (1 - e^{i\omega t}) S(\omega), \qquad (2.48)$$

where  $S_{\alpha}(\omega) \equiv \int dt e^{i\omega t} \langle j_{\alpha}(t) j_{\alpha}(0) \rangle$ .

In the next step we use the expression for the *fermion* current to calculate the equilibrium noise power spectrum. The current of non-interacting fermions at finite time can be written as:

$$j(t) = \iint dE d\omega c_{\omega+E}^{\dagger} c_E e^{i\omega t}.$$
 (2.49)

Using this expression and the statistics of the Fermi distribution, one can find that the noise spectrum at inverse temperature  $\beta$  is given by the following equation [14]:

$$S_{\alpha}(\omega) = \frac{1}{2\pi} \frac{\omega}{1 - e^{-\beta\omega}}.$$
 (2.50)

Note, that r.h.s. of this equation is proportional to the Bose equilibrium distribution function. Substituting this expression in Eq. (2.48) one gets:

$$\log[\chi(\lambda, t)] = \lambda^2 / 4\pi^2 \int \frac{d\omega}{\omega} \frac{1 - e^{-i\omega t}}{1 - e^{-\beta\omega}}.$$
 (2.51)

This integral can be evaluated expanding in Boltzmann factors and integrating each term. Finally, we take into account that in our situation  $\lambda=2\pi$  and come to the conclusion that the correlation function equals to

$$\psi^{\dagger}(x,t)\psi(0,0) = \frac{\pi/\beta}{\sinh[\pi(t-x/\nu)/\beta]}.$$
 (2.52)

We see that the result is consistent with the predictions of the usual bosonization approach (2.36).

To summarize, here we have explicitly illustrated that the usual bosonization approach may be split in two steps. First one is the calculation of the statistics of the boundary conditions, and the second one is the solution of the equations of motion for the excitations at the edge. Below, in Chap. 4, we make another test of non-equilibrium bosonization by considering an example of a more complex system.

2.4 Conclusions 53

### 2.4 Conclusions

We have shown that the bosonization approach is very powerful tool for the theoretical description of one-dimensional systems. The main idea of the bosonization approach is to rewrite the fermion field operators in terms of new collective boson fields. This allows one to recast the Hamiltonian of the interacting one-dimensional fermions with linear spectrum in a quadratic form and thus diagonalize it and find correlation functions of electrons. This approach is suitable, however, only for finding the equilibrium correlation functions. The non-equilibrium generalization of the bosonization procedure, introduced in this section, allows one to reduce the problem of finding a non-equilibrium correlation function of an interacting system to the problem of finding some correlation functions of non-interacting electrons.

The key idea of this approach is to take advantage of the absence of back-action of the interaction effects on the statistics of processes which determine the boundary conditions. Such situation is realized in chiral systems with short range interaction and several other systems. In some of these cases, the non-equilibrium bosonization allows one to rewrite the correlation function in terms of the *full counting statistics* generator. As we will see below, this method gives a simple and efficient approach to several problems.

### References

- 1. A.O. Gogolin, A.A. Nersesyan, A.M. Tsvelik, *Bosonization and Strongly Correlated Systems* (Cambridge University Press, Cambridge, 1998)
- 2. A wide introduction to the bosonization technique can be found in S. Eggert, arXiv:0708.0003. <!- Missing/Wrong Year ->
- 3. T. Giamarchi, Quantum Physics in One Dimension (Oxford University Press, Oxford, 2003)
- 4. S.B. Treiman, R. Jackiw, D.J. Gross, *Lectures on Current Algebra and its Applications* (Princeton University Press, Princeton, 1972)
- L.D. Landau, E.M. Lifshits, *Theoretical Physics*, vol. 8 (Butterworth-Heinemann, Oxford, 2004)
- For a recent experiment, see C. Altimiras, U. Gennser, A. Cavanna, D. Mailly, F. Pierre, Phys. Rev. Lett. 99, 256805 (2007).
- 7. K.E. Nagaev, Phys. Rev. B 66, 075334 (2002)
- 8. E.V. Sukhorukov, V.V. Cheianov, Phys. Rev. Lett. 99, 156801 (2007)
- 9. I.P. Levkivskyi, E.V. Sukhorukov, Phys. Rev. B 78, 045322 (2008)
- E. Bieri, Correlation and Interference Experiments with Edge States. Ph.D. Thesis, University of Basel, 2007.
- E. Bieri, M. Weiss, O. Goktas, M. Hauser, C. Schonenberger, S. Oberholzer, Phys. Rev. B 79, 245324 (2009)
- 12. L.S. Levitov, H. Lee, G.B. Lesovik, J. Math. Phys. 37, 4845 (1996)
- 13. For a review, see Y.V. Nazarov, Quantum Noise in Mesoscopic Physics (Springer, Berlin, 2003).
- 14. Y.M. Blanter, M. Büttiker, Phys. Rep. **336**, 1 (2000)

# **Chapter 3 Interaction Induced Dephasing of Edge States**

First experiments on finite bias dephasing in electronic Mach-Zehnder interferometers utilizing quantum Hall edge states showed unexpected puzzling results. In this chapter we use the bosonization approach to show that these experiments at filling factor  $\nu=2$  can be explained using the model which takes into account *Coulomb interaction* at the edge of the sample. In addition, we make predictions for temperature dependence of dephasing of the quantum Hall edge states within the framework of this model. The main idea of the electronic Mach-Zehnder interferometer is described in Sect. 1.4.1. Here we start with the detailed description of experimental setups and results.

## 3.1 Experimental Results

All experimental setups can be roughly grouped in *two types*, depending on the biasing scheme. Here we describe the specific features of experimental setup of each type and the corresponding experimental results.

# 3.1.1 Only Interfering Edge Channel is Biased

The first experimental situation that we wish to address is reported in Ref. [1]. In this experiment the bias is applied to the outer channel only. This situation is achieved by splitting incoming inner and outer channels with the help of an additional quantum point contact, so that two channels originate in fact from different Ohmic contacts. This allows to apply different biases to the two channels at the same edge.

Some text sections in this chapter are reproduced from Phys. Rev. B 78, 045322 (2008), © American Physical Society.

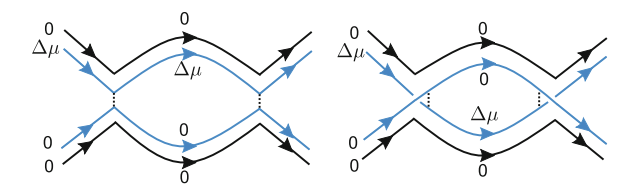


Fig. 3.1 Schematic representation of the experimental set-up in Ref. [1]. Only one edge channel of the Mach-Zehnder interferometer is biased. *Left panel* shows the *weak tunneling* regime: Outer edge channels that propagate at different arms of the Mach-Zehnder interferometer are weakly coupled to each other at two quantum point contacts. *Right panel* shows the *weak backscattering* regime: Outer edge channels almost completely propagate through quantum point contacts to opposite arms of the Mach-Zehnder interferometer and only weakly coupled via backscattering. After Ref. [2]. © American Physical Society

The Mach-Zehnder interferometer in this situation is schematically shown in Fig. 3.1 for the regimes of weak tunneling  $T_\ell \to 0$  (left panel), and of weak backscattering  $T_\ell \to 1$  (right panel). This schematics is obtained from Fig. 1.17 by splitting each Ohmic contact attached to the Corbino disk and deforming two interfering paths so that they run from left to right. After this procedure, the symmetry between two scattering regimes becomes obvious: In order to go from the set-up on the left panel of Fig. 3.1 to the one on the right panel, one simply needs to flip the interferometer vertically. This symmetry is important, and will be shown in Sect. 3.4 to result in the symmetry between weak tunneling and weak backscattering regimes.

The Ref. [1] discovered an unexpected Aharonov-Bohm effect which is inconsistent with the single-particle picture of edge channels. The following observations where reported:

- Lobe-type structure in the dependence of the visibility of Aharonov-Bohm oscillations on the DC bias with almost equal widths of lobes. The visibility vanishes at specific values of the bias. This behavior persists for various fixed values of magnetic field and for various transparencies of quantum point contacts;
- The rigidity of the Aharonov-Bohm phase shift followed by sharp  $\pi$ -valued jumps at the points where the visibility vanishes;
- The stability of both mentioned effects with respect to changes in the length of one of the interferometer paths.

The experiment [1] was theoretically analyzed in several recent works [3–6]. The Ref. [3] focuses on  $\nu=1$  case and suggests that the suppression of the visibility is due to the resonant interaction with the counter-propagating edge channel located near one of the arms of the interferometer. At present, this idea seems to be a reasonable guess, as far as the dephasing at  $\nu=1$  is concerned. However, the experiments [1]

<sup>&</sup>lt;sup>1</sup> In Fig. 1 of the Ref. [1] the counter-propagating edge state goes from the source S3 to quantum point contact QPC0 and under the air bridge comes very closely to the upper arm of the interferometer, which is the part of the channel between quantum point contact QPC1 and quantum, point contact QPC2.

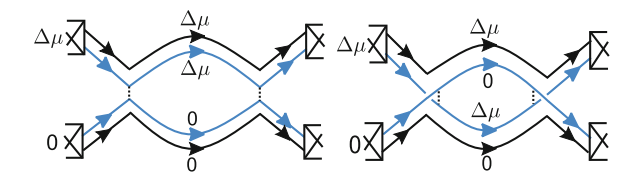


Fig. 3.2 Schematic representation of the experimental set-up in Refs. [7, 8]. Two incoming edge channels of the Mach-Zehnder interferometer are biased with the same potential difference  $\Delta\mu$ , and other channels are grounded. *Left panel* shows the *weak tunneling* regime, while the *right panel* shows the *weak backscattering* regime. After Ref. [2]. © American Physical Society

and [7, 8] concentrate on the  $\nu=2$  regime, where two edge channels coexist. These and new experiments [9–12], where the counter-propagating edge channel has been removed, prompt a new theoretical analysis. The authors of the Ref. [4] consider a long-range Coulomb interaction at the edge and make an interesting prediction about the temperature dependence of the visibility. However, they are not able to propose an explanation of the lobe-type behavior of the visibility. The Refs. [5, 6] suggest that dephasing in Mach-Zehnder interferometers is due to shot noise generated by the partition of the edge channel at the first quantum point contact. While this idea may correctly capture a part of the physics at  $\nu=1$ , the drawback of this explanation is that the shot noise vanishes in weak tunneling and weak backscattering regimes, where the experiments nevertheless demonstrate strong dephasing. Moreover, the experiment which we discuss below illuminates the special role that the second inner edge channel at  $\nu=2$  plays in dephasing.

## 3.1.2 All Edge Channels are Biased

In contrast to the work [1], the experimental set-up in Refs. [7, 8] does not contain an additional quantum point contact that would allow to split two edge channels at  $\nu=2$  and to apply potentials to each of them separately. Therefore, in Refs. [7, 8] two edge channels that originate from the same Ohmic contact are biased by the same potential difference  $\Delta\mu$ . For the convenience of the following analysis we again unfold the Mach-Zehnder interferometer on Fig. 1.17 and represent it schematically as shown in Fig. 3.2.

Now it is easy to see the asymmetry between regimes of weak tunneling and of weak backscattering. In the first regime (left panel) two channels on the upper arm of the interferometer are equally biased with the potential difference  $\Delta\mu$ . The situation is different in the second regime (right panel): The inner channel is biased on the upper arm of the interferometer, while the outer channel is biased on the lower arm. We believe that this asymmetry is responsible for entirely different behavior of the visibility of Aharonov-Bohm oscillations in the experiment [7, 8]:

- Lobe-type structure with the visibility vanishing at certain values of bias is
  observed only in the weak tunneling regime. The central lobe is approximately
  two times wider than side lobes. In the weak backscattering regime the visibility
  shows oscillations and decays as a function of the bias;
- No phase rigidity is found at all transparencies of quantum point contacts;
- The asymmetry in the visibility as a function of the transparency of the first quantum point contact is observed. In particular, the visibility always decays as a function of the bias in the regimes of weak tunneling. In contrast, in the regime of weak backscattering the visibility first grows around zero bias, and only then it decays.

It is the last observation which is very important. It indicates that charging effects induced by different biasing of edge channels may be responsible for differences in the results of experiments [1] and [7, 8]. This idea seems to agree with the conclusion of the authors (P. Roche, private communication) of the experiment [9]. In this chapter we develop this idea and propose a simple model that is capable of explaining on a single basis all the experimental observations described above. Namely, we assume a strong (Coulomb) interaction between two edge channels that belong to the same quantum Hall edge. The interaction effect is complex: First of all, it leads to charging of edge channels and induces experimentally observed phase shifts. Second, the interaction is partially screened, which leads to the emergence of the soft mode and of a new low energy scale associated with it. The width of lobes in the visibility and the temperature dependence are determined by this energy scale. Finally, the interaction is responsible for the decay of coherence at large bias.

Further details of our model are given in Sect. 3.2. In Sect. 3.3 we express the visibility of Aharonov-Bohm oscillations in terms of electronic correlation functions. In Sect. 3.4 we present a detailed comparison of our results with the experimental observations. Finally, in Sect. 3.5 we briefly summarize our results.

### 3.2 Model of Mach-Zehnder Interferometer

Before we proceed with the mathematical formulation of the model we wish to stress the following points. The experimentally found new energy scale [1, 7–12] is very small. For instance, the width of lobes in the visibility is approximately  $20\mu V$ . We show below that this energy is inverse proportional to the size of the Mach-Zehnder interferometer, few micrometers. Thus it is much smaller than any other energy scale associated, e.g., with the formation of compressible strips [13]. Therefore, we use an effective model appropriate for the description of the low energy physics of quantum Hall edge excitations. Namely, we consider the inner and outer edge channels at  $\nu=2$  as two chiral boson fields and introduce the Luttinger-type Hamiltonian [14–16] to describe the equilibrium state. Second, we introduce the density-density interaction, which is known to be irrelevant in the low-energy limit [17]. This fact has no influence

on the physics that we discuss below, because we focus on the processes at finite energy and length scale, which take place inside the Mach-Zehnder interferometer.

#### 3.2.1 Fields and Hamiltonian

We assume that at filling factor  $\nu=2$  there are two edge channels at each edge of the quantum Hall system and two chiral fermions associated with them and denoted as  $\psi_{\alpha s}(x)$ ,  $\alpha=1,2$  and s=U,D. Here the subscript 1 corresponds to the fermion on outer channel, and 2 to the fermion on inner channel (see Fig. 3.3), while the index s stands for upper and lower arms of the interferometer. The total Hamiltonian of the interferometer

$$\mathcal{H}_{\text{tot}} = \mathcal{H}_0 + \mathcal{H}_{\text{int}} + \mathcal{H}_T \tag{3.1}$$

contains single particle term  $\mathcal{H}_0$ , interaction part  $\mathcal{H}_{int}$ , and the tunneling Hamiltonian  $\mathcal{H}_T$ .

The single-particle Hamiltonian describes free chiral fermions [17]:

$$\mathcal{H}_0 = -iv_F \sum_{\alpha s} \int dx \, \psi_{\alpha s}^{\dagger} \partial_x \psi_{\alpha s}, \tag{3.2}$$

where  $v_F$  is Fermi velocity, which is assumed to be the same for each edge channel. This assumption is not critical, because, as we will see below, the Fermi velocity is strongly renormalized by the interaction.

We postpone for a while a detailed discussion of the interaction and at the moment write the interaction Hamiltonian in terms of local densities  $\rho_{\alpha s}$  in the following general form:

$$\mathcal{H}_{\text{int}} = (1/2) \sum_{\alpha\beta s} \iint dx dy \, U_{\alpha\beta}(x - y) \rho_{\alpha s}(x) \rho_{\beta s}(y). \tag{3.3}$$

Note that this effective Hamiltonian is not microscopically derived. However, the experiment indicates (P. Roche, private communication), that the interaction has a Coulomb long-range character and leads to charging effects at the edge. Below we show that once this assumption is made, it leads to a number of universalities in the Mach-Zehnder interferometer physics and correctly captures most of the experimental observations.

We have already mentioned in the introduction that the interference in Mach-Zehnder interferometers originates from scattering processes at quantum point contacts. In the case when interaction is strong, the scattering has to be assumed weak and treated *perturbatively*. Fortunately, this limitation does not detract from our theoretical approach, because neither the interference nor its suppression are necessarily weak in the case of weak scattering. Moreover, we would like to stress again that

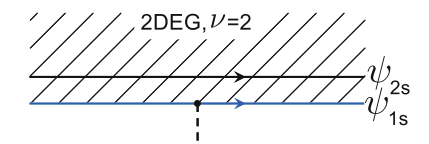


**Fig. 3.3** Structure of the quantum Hall edge at  $\nu=2$ . Two chiral electrons,  $\psi_{1s}$  and  $\psi_{2s}$ , are propagating along the edge. Tunneling is possible only from and to the outer channel ( $\psi_{1s}$ , blue line). After Ref. [2]. © American Physical Society

most interesting physics takes place in the regimes of weak tunneling and of weak backscattering.

Both regimes can be described by the tunneling Hamiltonian:

$$\mathcal{H}_T = A + A^{\dagger} \equiv \sum_{\ell} (A_{\ell} + A_{\ell}^{\dagger}), \quad \ell = L, R, \tag{3.4}$$

where the tunneling amplitude

$$A_{\ell} = t_{\ell} \psi_{1D}^{\dagger}(x_{\ell}) \psi_{1U}(x_{\ell}) \tag{3.5}$$

connects outer edge channels and transfers the electron from the lower arm to the upper arm of the Mach-Zehnder interferometer. It is worth mentioning already here that at low energies the electron tunneling is relevant and leads in fact to the Ohmic behavior of the quantum point contacts, in agreement with experiments [1, 7, 8]. The Aharonov-Bohm phase may now be included in the tunneling amplitudes via the relation  $t_R^*t_L = |t_Rt_L|e^{i\varphi_{AB}}$ .

#### 3.2.2 Bosonization

In order to account for the strong interaction at the edge, we take advantage of the commonly used bosonization technique [16], and represent fermion operators in terms of chiral boson fields  $\phi_{\alpha s}$ :

$$\psi_{\alpha s} \propto e^{i\phi_{\alpha s}},$$
(3.6)

which satisfy the commutation relations  $[\phi_{\alpha s}(x), \phi_{\alpha s}(y)] = i\pi \text{sgn}(x - y)$ . The Hamiltonian of the edge states in terms of these fields can be written as

$$\mathcal{H} \equiv \mathcal{H}_0 + \mathcal{H}_{int} = \sum_{\alpha,\beta,s} \iint \frac{dx dy}{8\pi^2} V_{\alpha\beta}(x - y) \partial_x \phi_{\alpha s}(x) \partial_y \phi_{\beta s}(y), \tag{3.7}$$

where the interaction potential is shifted by the Fermi velocity,

$$V_{\alpha\beta} = U_{\alpha\beta} + 2\pi v_F \delta_{\alpha\beta} \delta(x - y). \tag{3.8}$$

The crucial point is that now the Hamiltonian (3.7) for quantum Hall edge is quadratic in boson fields.

Next, we quantize fields by expressing them in terms of boson creation and annihilation operators,  $a_{\alpha s}^{\dagger}(k)$  and  $a_{\alpha s}(k)$ ,

$$\phi_{\alpha s}(x) = \varphi_{\alpha s} + 2\pi \pi_{\alpha s} x + \sum_{k>0} \sqrt{\frac{2\pi}{Wk}} \left[ a_{\alpha s}(k) e^{ikx} + a_{\alpha s}^{\dagger}(k) e^{-ikx} \right]. \tag{3.9}$$

The vacuum for collective excitations is defined as  $a_{\alpha s}(k)|0\rangle = 0$ . As we have discussed in Sect. 2.1.3, the special care has to be taken about zero modes, because as we show in Sect. 3.4, zero modes determine charging effects and phase shifts, which are not small. Zero mode  $\pi_{\alpha s}$  has a meaning of a homogeneous density at the edge channel  $(\alpha, s)$ . Therefore, we define "vacuum charges"  $Q_{\alpha s}$ 

$$\pi_{\alpha s}|0\rangle = Q_{\alpha s}|0\rangle,\tag{3.10}$$

which are in fact charge densities at the edge channels, generated by the bias, as discussed in Sect. 2.1.3. The time evolution of zero modes induced by the Hamiltonian is then given by

$$Q_{\alpha s}(t) = \sum_{\beta} V_{\alpha \beta}^{-1} \Delta \mu_{\beta s}, \quad \varphi_{\alpha s}(t) = \varphi_{\alpha s} - \Delta \mu_{\alpha s} t, \tag{3.11}$$

where  $\Delta\mu_{\alpha s}$  is a bias voltage applied to corresponding edge channel. These voltages are equal to either  $\Delta\mu$  or 0, depending on the biasing scheme as have been discussed in the Sect. 3.1.

## 3.2.3 Strong Interaction Limit and the Universality

It is quite natural to assume that edge channels interact via the Coulomb potential. It has a long-range character and the logarithmic dispersion  $V_{\alpha\beta}(k) \propto \log(ka)$ . Here a is the shortest important length scale, e.g. the width of compressible stripes [13], or the inter-channel distance. The dispersion is important in the case  $\nu=1$ , because it generates dephasing at the homogeneous edge [4]. However, taken alone the dispersion is *not able* to explain lobe-type behavior of the visibility. What is more important it is the fact that the logarithm may become relatively large when cutoff at relevant long distances.

We therefore further assume that the Coulomb interaction is screened at distances D, such as  $L_U, L_D \gg D \gg a$ , where  $L_U$  and  $L_D$  are the lengths of the arms of the Mach-Zehnder interferometer. In fact, some sort of screening may exist in

Mach-Zehnder interferometers. For instance, in the experiments [1, 7-12] the cutoff length D may be a distance to the back gate, or to the massive metallic air bridge. There are several consequences of screening on the intermediate distances D. First of all, it allows to neglect the interaction between two arms of the interferometer (see however the discussion in Sect. 3.4). Second, at low energies we can neglect the logarithmic dispersion and write

$$V_{\alpha\beta}(x-y) = V_{\alpha\beta}\delta(x-y), \tag{3.12}$$

so that for the Fourier transform we obtain  $V_{\alpha\beta}(k) = V_{\alpha\beta}(0) \equiv V_{\alpha\beta}$ . And finally, the mutual interaction between inner and outer edge channels, located on the distance of order  $a \ll D$  from each other, is strongly reduced.

Therefore, one can parametrize the interaction matrix as follows

$$V_{\alpha\beta} = \pi \begin{pmatrix} u + v \ u - v \\ u - v \ u + v \end{pmatrix}, \tag{3.13}$$

where

$$u/v = \log(D/a) \gg 1,\tag{3.14}$$

is a new large parameter, the most important consequence of the long-range character of Coulomb interaction.

Indeed, we now diagonalize the interaction,  $V = q^{\dagger} \Lambda q$ , with the result

$$\Lambda = 2\pi \begin{pmatrix} u & 0 \\ 0 & v \end{pmatrix}, \qquad q = \frac{1}{\sqrt{2}} \begin{pmatrix} 1 & 1 \\ 1 & -1 \end{pmatrix}. \tag{3.15}$$

Thus we find that the Coulomb interaction at the  $\nu=2$  edge leads to the separation of spectrum on the fast (charge) mode with the speed u and slow (dipole) mode with the speed v. In Sect. 3.4 we show that the lobe structure in the visibility is determined by slow mode, while the fast mode is not excited at relevant low energies. That is why at  $\nu=2$  the logarithmic dispersion of the Coulomb interaction is not important for explaining lobes.

Moreover, the Coulomb character of the interaction leads to the following *universality*. We show later that the coupling of electrons in the outer channel to the fast and slow mode is determined by the parameters  $\delta_i = |q_{1i}|^2$ , which satisfy the sum rule

$$\sum_{i} \delta_{i} = \sum_{i} |q_{1i}|^{2} = 1, \tag{3.16}$$

that follows from the unitarity of the matrix q. For the special choice (3.13) of the interaction matrix coupling constants are equal,

$$\delta_1 = \delta_2 = 1/2,$$
 (3.17)

which has an important consequence, as we show in Sect. 3.3. Note that in the limit of strong long-range interaction,  $u \gg v_F$ , the result (3.17) is stable against variations of the bare Fermi velocity  $v_F$  and is not sensitive to the physics of edge channels at distances of order a, leading to the universality of dephasing in Mach-Zehnder interferometers.

Finally, we partially diagonalize the Hamiltonian by introducing new boson operators via  $a_{\alpha s}(k) = \sum_i q_{\alpha i} \tilde{a}_{is}(k)$ . Using Eqs. (2.24), (3.13), and (3.15), we obtain new Hamiltonian for the quantum Hall edge

$$\mathcal{H} = \sum_{s,k} \left[ uk \, \tilde{a}_{1s}^{\dagger}(k) \tilde{a}_{1s}(k) + vk \, \tilde{a}_{2s}^{\dagger}(k) \tilde{a}_{2s}(k) \right] + (W/2) \sum_{\alpha,\beta,s} V_{\alpha\beta} \pi_{\alpha s} \pi_{\beta s}, \quad (3.18)$$

which completes our discussion of the model.

## 3.3 Visibility and Phase Shift

In this section we consider the transport through the Mach-Zehnder interferometers shown in Figs. 3.1 and 3.2 and evaluate the visibility of Aharonov-Bohm oscillations. Both regimes, of weak tunneling and of weak backscattering, can be considered on the same basis, by applying the tunneling Hamiltonian approach [18]. In the derivation presented below we follow the Ref. [3]. We introduce the tunneling current operator  $\hat{I} = \dot{N}_D = i [\mathcal{H}_T, N_D]$ , which differs for two regimes only by the sign. Here  $N_D = \int dx \psi_{1D}^{\dagger} \psi_{1D}$  is the number of electrons on the outer edge channel of the lower arm of the interferometer. Then we use Eqs. (3.4) and (3.5) to write

$$\hat{I} = i(A^{\dagger} - A). \tag{3.19}$$

We evaluate the average current to lowest order in tunneling and obtain

$$I = \int_{-\infty}^{\infty} dt \langle [A^{\dagger}(t), A(0)] \rangle, \qquad (3.20)$$

where the average is taken with respect to ground state in quantum Hall edges. Finite temperature effects will be considered separately in Sect. 3.4.3.

It is easy to see that the average current can be written as a sum of four terms:

$$I = \sum_{\ell \ell'} I_{\ell \ell'}, \quad I_{\ell \ell'} \equiv \int dt \langle [A_{\ell}^{\dagger}(t), A_{\ell'}(0)] \rangle, \tag{3.21}$$

where  $I_{LL}$  and  $I_{RR}$  are the direct currents at the left and right quantum point contact, respectively, and  $I_{LR} + I_{RL}$  is the interference contribution. In our model there is no interaction between upper and lower arms of a Mach-Zehnder interferometer,

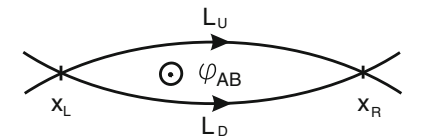


Fig. 3.4 Schematics of Mach-Zehnder interferometer introducing notations:  $L_U$  and  $L_D$  are the lengths of the upper and lower paths of the interferometer, respectively. The coordinates of the left and right quantum point contact are denoted by  $x_L$  and  $x_R$ , respectively. The magnetic flux threading the interferometer results in the Aharonov-Bohm phase  $\varphi_{AB}$ . After Ref. [2]. © American Physical Society

therefore the correlation function in (3.21) splits into the product of two single-particle correlators:

$$I_{\ell\ell'} = t_{\ell}^* t_{\ell'} \int dt \left[ \langle \psi_{1U}^{\dagger}(x_{\ell}, t) \psi_{1U}(x_{\ell'}, 0) \rangle \langle \psi_{1D}(x_{\ell}, t) \psi_{1D}^{\dagger}(x_{\ell'}, 0) \rangle \right.$$
$$\left. - \langle \psi_{1U}(x_{\ell'}, 0) \psi_{1U}^{\dagger}(x_{\ell}, t) \rangle \langle \psi_{1D}^{\dagger}(x_{\ell'}, 0) \psi_{1D}(x_{\ell}, t) \rangle \right]. \quad (3.22)$$

We note that the operator  $\psi_{1s}^{\dagger}$  applied to the ground state creates a quasi-particle above the Fermi level (with the positive energy), while the operator  $\psi_{1s}$  creates a hole below Fermi level (with the negative energy). This implies that in the first term in (3.22) all the singularities are shifted to the upper half plane of the complex variable t, and in the second term singularities are shifted to the lower half plane. This means that only one term contributes, depending on the sign of bias  $\Delta \mu$  which determines the direction of current. Apart from this, there is no difference between two terms. Therefore, we choose, e.g., the first term, shift the counter of integration C to the low half plane, and rewrite Eq. (3.22) as follows:

$$I_{\ell\ell'} = t_{\ell}^* t_{\ell'} \int dt \, \langle \psi_{1U}^{\dagger}(x_{\ell}, t) \psi_{1U}(x_{\ell'}, 0) \rangle \times \langle \psi_{1D}^{\dagger}(x_{\ell}, t) \psi_{1D}(x_{\ell'}, 0) \rangle^*, \quad (3.23)$$

where the correlators are defined in such a way that they have singularities on the real axis of t.

The correlators are evaluated in Sect. 2.2 using the bosonization technique with the result

$$i \langle \psi_{1s}^{\dagger}(x_{\ell}, t) \psi_{1s}(x_{\ell'}, 0) \rangle = \frac{\exp[i \Delta \mu_{1s} t - 2\pi i Q_{1s}(x_{\ell} - x_{\ell'})]}{(x_{\ell} - x_{\ell'} - ut)^{\delta_1} (x_{\ell} - x_{\ell'} - vt)^{\delta_2}}.$$
 (3.24)

One remarkable fact we prove below is that for  $x_\ell = x_{\ell'}$  the only role of the interaction is to renormalize the density of states at Fermi level,  $n_F = 1/(u^{\delta_1}v^{\delta_2})$ . This immediately follows from the sum rule (3.16). Therefore, for the direct currents we readily obtain

$$I_{\ell\ell} = 2\pi n_F^2 |t_\ell|^2 \Delta \mu,\tag{3.25}$$

i.e. the quantum point contacts are in the Ohmic regime, in agreement with experimental observations.

In order to present the visibility in a compact form, we introduce the electron correlation functions of an isolated edge, normalized to the density of states (see Fig. 3.4 for notations):

$$K_s(t) = \frac{\exp[2\pi i \, Q_{1s} \, L_s]}{(t - L_s/u)^{\delta_1} (t - L_s/v)^{\delta_2}}, \quad s = U, D.$$
 (3.26)

This functions contain all the important information about charging effects (phase shift generated by zero modes), and dephasing determined by the singularities. Next, adding all the terms  $I = \sum I_{\ell\ell'}$  we find the differential conductance  $\mathcal{G} = dI/d\Delta\mu$ :

$$\mathcal{G} = 2\pi n_F^2 (|t_L|^2 + |t_R|^2) + 2n_F^2 |t_L t_R| \operatorname{Im} \Big\{ e^{i\varphi_{AB}} \int_C dt e^{i\Delta\mu t} (t - \Delta t) K_U^*(t) K_D(t) \Big\},$$
(3.27)

where the time shift  $\Delta t$  is the charging effect,

$$\Delta t = 2\pi \partial_{\Delta u} (Q_{1U} L_U - Q_{1D} L_D), \tag{3.28}$$

which depends on the bias scheme, and will be calculated in Sect. 3.4 for a particular experimental situations. It is important to note that in the weak backscattering regime (see Figs. 3.1 and 3.2) tunneling occurs from the lower arm of the interferometer, therefore one should exchange indexes U and D.

The first term in Eq. (3.27) is the contribution of direct incoherent currents through quantum point contacts, while the second term is the interference contribution, which oscillates with magnetic field. Therefore, the visibility of Aharonov-Bohm oscillations (1.84) in the differential conductance  $\mathcal{G}$  and the Aharonov-Bohm phase shift take the following form

$$V_{\mathcal{G}}(\Delta \mu) = V_{\mathcal{G}}(0)|\mathcal{I}_{AB}|, \quad \Delta \varphi_{AB} = \arg(\mathcal{I}_{AB}),$$
 (3.29)

where the visibility at zero bias  $V_{\mathcal{G}}(0)$  is given by Eq. (1.85) for a non-interacting system, while all the interaction effects enter via the dimensionless Fourier integral

$$\mathcal{I}_{AB}(\Delta\mu) = \int_{C} \frac{dt}{2\pi i} \exp(i\,\Delta\mu t)(t - \Delta t) K_{U}^{*}(t) K_{D}(t), \qquad (3.30)$$

with the counter C shifted to the lower half plane of the variable t. This formula, together with Eqs. (3.26) and (3.28) is one of the central results and will serve as a starting point for the analysis of experiments. However, before we proceed

with detailed explanations of experiments, we would like to consider two examples quickly.

The first example, a non-interacting system, serves merely as a test for our theory. In this case using relevant parameters, the vacuum charges  $Q_{1U}=\Delta\mu/v_F, Q_{1D}=0$ , the group velocities  $u=v=v_F$ , coupling constants  $\delta_1=1,\,\delta_2=0$ , we obtain the correlators  $K_U(t)=(t-L_U/v_F)^{-1}\exp(i\,\Delta\mu L_U/v_F)$  and  $K_D(t)=(t-L_D/v_F)^{-1}$ . The time shift  $\Delta t=L_U/v_F$  follows from Eq. (3.28). We substitute all these results to Eq. (3.30) and finally obtain:

$$\mathcal{I}_{AB} = \int_{C} \frac{dt}{2\pi i} \frac{e^{i\Delta\mu(t - L_U/v_F)}}{t - L_D/v_F} = e^{i\Delta\mu\Delta L/v_F},$$
(3.31)

so that the visibility  $|\mathcal{I}_{AB}|=1$ , and the phase shift is  $\Delta\varphi_{AB}=\Delta\mu\Delta L/v_F$ , in agreement with Eq. (1.85).

Next, we consider a more interesting situation when the interferometer is in weak tunneling regime, and one of its arms, e.g. the upper arm of the interferometer, is much shorter than the other,  $L_U \ll L_D$ . Then the properties of the function  $\mathcal{I}_{AB}$  are determined by excitations at the lower arm of a Mach-Zehnder interferometer at energies of order  $v/L_D$ . At this energies the electronic correlator in the upper arm behaves as a correlator of free fermions:  $K_U(t) = 1/t$ . Therefore, for the visibility we obtain

$$\mathcal{I}_{AB} = \int_{C} \frac{dt}{2\pi i} e^{i\Delta\mu t} K_D(t), \qquad (3.32)$$

i.e. it is simply given by the Fourier transform of the electron correlation function at the edge. This leads to an interesting idea to use a strongly asymmetric Mach-Zehnder interferometer for the *spectroscopy of excitations* at the edge of quantum Hall system.

We now use the opportunity to analize the role of the coupling coefficients  $\delta_i$  in this simple situation. The absolute value of the Fourier transform of the function  $K_D$  is shown in Fig. (3.5). We see that  $\delta_1 = \delta_2 = 1/2$  is the special point. In this case, and taking the limit  $u \to \infty$ , the Fourier transform gives  $|\mathcal{I}_{AB}| = |J_0(\Delta \mu L_D/2v)|$ , where  $J_0$  is the zero-order Bessel function. Thus the lobes in the visibility of Aharonov-Bohm oscillations are well resolved only in the limit of strong long-range interaction. Therefore, an asymmetric Mach-Zehnder interferometer can be used to test the character of the interaction. From now on we assume that  $\delta_1 = \delta_2 = 1/2$ .

# 3.4 Discussion of Experiments

In this section we present a detailed analysis of experiments described in the introduction. It is convenient to rewrite Eq. (3.30) in slightly different form by using Eq. (3.26) with  $\delta_1 = \delta_2 = 1/2$  and shifting the time integral:

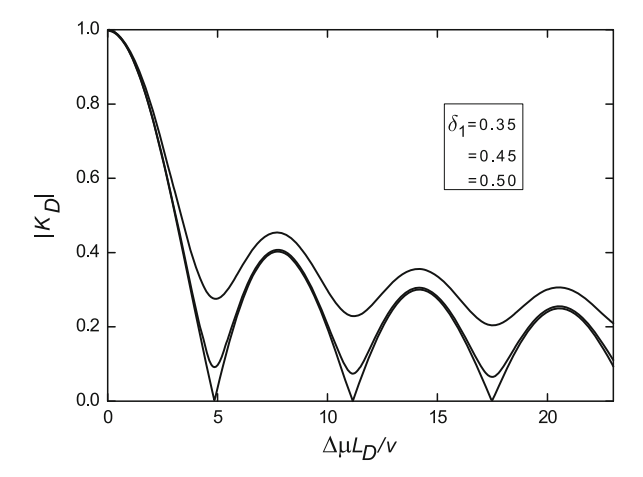


Fig. 3.5 The absolute value of the Fourier transform of the electronic correlation function  $K_D(t)$  plotted as a function of the dimensionless bias  $\Delta \mu L_D/v$  for different values of the coupling coefficient  $\delta_1$ . After Ref. [2]. © American Physical Society

$$\mathcal{I}_{AB}(\Delta \mu) = \oint_{C} \frac{dt}{2\pi i} \frac{t \exp(i\Delta \mu t)}{\prod_{s,\alpha} \sqrt{(t + \Delta t - L_{s}/v_{\alpha})}},$$
(3.33)

where  $v_1 = u$  and  $v_2 = v$ , and the contour of integration C goes around the branch cuts (see, e.g., Fig. 3.6). These branch cuts, which replace single-particle poles of correlation functions for free electrons, originate from the interaction. On a mathematical level, they are the main source of the suppression of the coherence, because at large argument  $\Delta \mu$  the Fourier transform (3.30) of relatively smooth function quickly decays. We will use this fact for the analysis of dephasing. Physically, when electron tunnels, it excites two collective modes associated with two edge channels, and they carry away a part of the phase information.

On the other hand, charging effects reflected in the parameter  $\Delta t$  lead to the bias dependent shift of the Aharonov-Bohm phase,  $\Delta\phi_{AB}$ . As it follows from Eq. (3.29), the phase slips by  $\pi$  at points where the visibility vanishes. Away from these points, in particular at zero bias, the phase shift is a smooth function of the bias. Therefore, it is interesting to consider the value  $\partial_{\Delta\mu}\Delta\phi_{AB}$  at  $\Delta\mu=0$  where  $|\mathcal{I}_{AB}|=1$ , which can be found from the expansion  $\mathcal{I}_{AB}=|\mathcal{I}_{AB}|e^{i\Delta\phi_{AB}}=1+i(\partial_{\Delta\mu}\Delta\phi_{AB})\Delta\mu$  in the right hand side of Eq. (3.33). We find it exactly:

$$\frac{\partial \Delta \phi_{AB}}{\partial \Delta \mu} = t_0 - 2\Delta t, \qquad t_0 = \frac{u + v}{2uv} (L_U + L_D), \tag{3.34}$$

where the first term  $t_0$  is the contribution of the quantum mechanical phase accumulated due to the propagation of an electron along the Mach-Zehnder interferometer. The second term, found from Eq. (3.28), is the contribution of the charge accumulated at the arms of Mach-Zehnder interferometer due to the Coulomb interaction

between edge channels. Partial cancellation of two effects leads to the phase rigidity found in Ref. [1]. This effect is discussed below.

Finally, all the experiments found that the visibility  $V_{\mathcal{G}}$  oscillates as a function of the bias  $\Delta \mu$ . Our model reproduces such oscillations and helps to understand their origin. Indeed, two well defined collective modes with speeds u and v lead to the formation of four branch points in the integral (3.33), which give relatively slowly decaying contributions. These contributions come with different bias dependent phase factors, so that the function  $\mathcal{I}_{AB}(\Delta \mu)$  oscillates. The period of oscillations is determined by the smallest energy scale  $\epsilon$ , which is given by the total size of the branch cut and can be estimated as

$$\epsilon = \frac{2uv}{(u - v)(L_U + L_D)}. (3.35)$$

In the case  $u \gg v$ , the parameter u cancels, so that the period of oscillations is determined by the slowest mode, and by the size of the interferometer.

We would like to emphasize that oscillations in the visibility appear only when at least two modes are relatively well resolved. Our model predicts a power-law decay of the visibility. In experiments [1, 7, 8] the visibility seems to decay faster. There might be several reasons for this, e.g. low frequency fluctuations in the electrical circuit [19, 20], or the electromagnetic radiation [21, 22]. Intrinsic reasons for dephasing deserve a separate consideration. We have already mentioned that the dispersion of the Coulomb interaction, neglected here, may lead to strong dephasing [4]. However, it affects only the fast mode, while the slow mode contribution to the integral (3.33) maintains the phase coherence. Therefore taken alone the dispersion of Coulomb interaction is not able to explain strong dephasing at  $\nu=2$ . The experiments seem to indicate that the slow mode is also dispersive, which may be a result of strong disorder at the edge or, more interestingly, of the intrinsic structure of each edge channel [23].

Having stressed this point, we now wish to focus solely on the phase shift and oscillations in the visibility. We use the fact that  $u \gg v$  and simplify the integral (3.33) by neglecting terms containing 1/u:

$$\mathcal{I}_{AB} = \oint_C \frac{dt}{2\pi i} \frac{t \exp(i\Delta\mu t)}{(t+\Delta t) \prod_s \sqrt{(t+\Delta t - L_s/v)}}.$$
 (3.36)

This expression contains one pole and one branch cut (see Fig. 3.6). Therefore, it can be expressed in terms of the zero order Bessel function  $J_0$ . After elementary steps we find:

$$\mathcal{I}_{AB} = e^{-i\Delta\mu\Delta t} \Big[ F(\Delta\mu) - i\Delta t \int_{-\infty}^{\Delta\mu} d\Delta\mu' F(\Delta\mu') \Big]$$

$$F \equiv e^{i\Delta\mu t_0} J_0(\Delta\mu\Delta L/2v), \tag{3.37}$$



Fig. 3.6 Analytic structure of the Fourier integral (3.33) in case of single biased channel [1]. Left panel: Two branch cuts (shown apart for convenience) of the integrand come from the product of two single-particle correlation functions. Right panel: In the limit  $u \gg v$  two branch points corresponding to the fast mode shrink to a single pole at  $t = -L_U/2v$ , while the slow mode produces the branch cut going from  $t = L_U/2v$  to  $t = L_D/v - L_U/2v$ . The blue line shows the contour of integration C. After Ref. [2]. © American Physical Society

where  $t_0 = (L_U + L_D)/2v$ , and  $\Delta L = L_D - L_U$ . We now proceed with the analysis of experiments discussed in the introduction.

## 3.4.1 Only Interfering Edge Channel is Biased

We start with the experiment [1]. Using Eqs. (3.11) and (3.13) we find

$$\begin{pmatrix} Q_{1s} \\ Q_{2s} \end{pmatrix} = \frac{1}{4\pi u v} \begin{pmatrix} v + u \ u - v \\ u - v \ v + u \end{pmatrix} \begin{pmatrix} \Delta \mu_{1s} \\ \Delta \mu_{2s} \end{pmatrix}. \tag{3.38}$$

In the weak tunneling regime, shown on the left panel of Fig. 3.1, only outer channel in the upper arm of the interferometer is biased,  $\Delta\mu_{1U}=\Delta\mu$  and  $\Delta\mu_{2U}=\Delta\mu_{\alpha D}=0$ . Therefore we obtain

$$Q_{1U} = \frac{u+v}{4\pi u v} \Delta \mu, \quad Q_{1D} = 0. \tag{3.39}$$

Then Eq. (3.28) gives  $\Delta t = L_U(u+v)/2uv$ . Substituting  $\Delta t$  into Eq. (3.34), we find that at zero bias

$$\frac{\partial \Delta \phi_{AB}}{\partial \Delta \mu} = \frac{u+v}{2uv} \Delta L. \tag{3.40}$$

Therefore, for the symmetric interferometer,  $\Delta L=0$ , the phase shift is independent of the bias, away from phase slip points where the visibility vanishes. This may explain the phenomenon of phase rigidity observed in Ref. [1], if we assume that the interferometer is almost symmetric in this experiment. Indeed, the period of oscillations of the visibility is given by the energy scale (3.35). Therefore, the overall phase shift between zeros of the visibility can be estimated as  $\Delta L/(L_U+L_D)\ll 1$ .

The integral (3.36), evaluated numerically, is plotted in Fig. 3.7 for two values of the asymmetry,  $L_D/L_U=1.15$  and 1.35. Our main focus is first few oscillations of the visibility (upper panel), which reveal charging effects. We would like to emphasize several points. First, the width of the central lobe is equal to the width of side lobes. This is because in the case of the symmetric

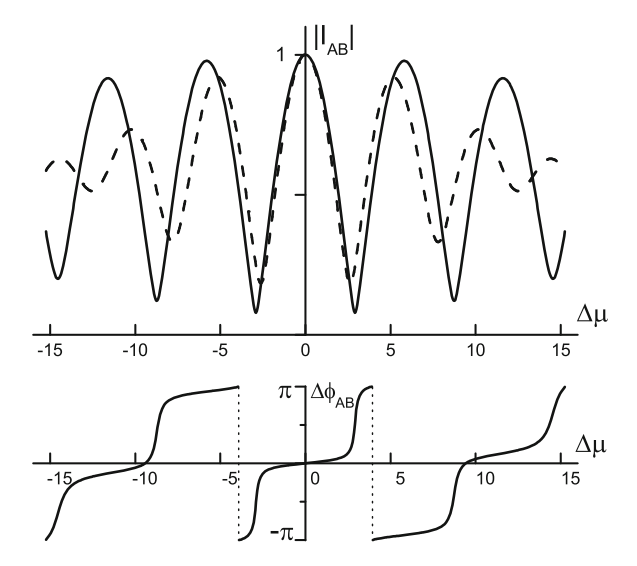


Fig. 3.7 The intrinsic visibility of Aharonov-Bohm oscillations  $|\mathcal{I}_{AB}|$  and the Aharonov-Bohm phase shift  $\arg(\mathcal{I}_{AB})$  in the case of a single biased channel [1]. Upper panel: The visibility is plotted as a function of the bias in units  $v/L_U$  for  $L_D=1.15L_U$  (solid line) and for  $L_D=1.35L_U$  (dashed line). Lower panel: The phase shift is plotted for  $L_D=1.15L_U$ . After Ref. [2]. © American Physical Society

interferometer,  $L_U = L_D = L$ , the branch cut shrinks to the pole (see Fig. 3.6), so that two poles are at  $t = \pm L/2v$ . Then Eq. (3.36) gives  $|\mathcal{I}_{AB}| = |\cos(\Delta \mu L/2v)|$ . Second, the small variation of the length  $L_D$  of the lower arm has only minor effect on the position of lobes, while the amplitude of oscillations is considerably suppressed. Finally, the lower panel of Fig. 3.7 illustrates the phenomenon of phase rigidity for almost symmetric interferometer,  $L_D = 1.15L_U$ . The Aharonov-Bohm phase shift changes slowly inside the lobes and slips by  $\pi$  at zeros of the visibility. All these observation are in agreement with the experiment [1].

To conclude this section we would like to remark that the visibility in the regime of weak backscattering (see the right panel in Fig. 3.1) can be obtained by simply replacing  $L_U$  and  $L_D$ . This is because in our model the charging effects are important only in the part of the Mach-Zehnder interferometer between two quantum point contacts, where they induce phase shifts. For the same reason, the transparency of the second quantum point contact does not affect the visibility [7, 8]. In the next section we show that the symmetry between weak tunneling and weak backscattering is broken if the bias is applied to two edge channels.

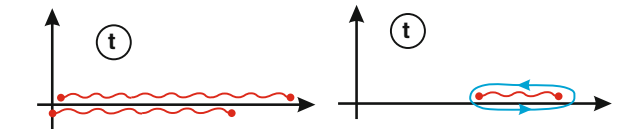


Fig. 3.8 Analytic structure of the Fourier integral (3.33) in case when two edge channels are biased [1], and in the weak tunneling regime (see Fig. 3.2). *Left panel* shows branch cuts of two single-particle correlation functions, while in the *right panel* the limit  $u \gg v$  is taken. The branch cut extends from  $t = L_U/v$  to  $t = L_D/v$ . After Ref. [2]. © American Physical Society

# 3.4.2 All Edge Channels are Biased

Next we analyze the experiment [7, 8]. The details of this experiment are discussed in the introduction. In the weak tunneling regime (see the left panel of Fig. 3.2) two edge channels are biased and almost completely reflected at the first quantum point contact. Therefore, Eq. (3.38) gives

$$Q_{1U} = \frac{\Delta\mu}{2\pi u}, \quad Q_{1D} = 0,$$
 (3.41)

and from Eq. (3.28) we find  $\Delta t = L_U/u$ .

Taking now the strong interaction limit,  $u \gg v$ , we find that  $\Delta t \to 0$ . Therefore, in the integral (3.36) the pole corresponding to the fast mode cancels (analytical structure of the integral is shown in Fig. 3.8), so that the visibility can be found exactly:

$$\mathcal{I}_{AB} = \exp[i\Delta\mu(L_D + L_U)/2v]J_0(\Delta\mu\Delta L/2v), \qquad (3.42)$$

where  $\Delta L = L_D - L_U$ . The visibility of Aharonov-Bohm oscillations, given by the absolute value of the integral (3.42), is shown in Fig. 3.10. One can see that in contrast to the case when only one channel is biased [1], the central lobe is approximately two times wider than side lobes, in agreement with the experimental observation [7, 8]. Moreover, the width of lobes is determined by the new energy scale,  $\epsilon' = v/\Delta L$ . Finally, inside the lobes the phase shift  $\Delta\phi_{\rm AB} = \Delta\mu(L_D + L_U)/2v$  always grows linearly with bias, so no phase rigidity should be observed.

We now switch to the regime of weak backscattering (see the right panel of Fig. 3.2). In the upper arm only inner channel is biased, while only outer channel is biased in the lower arm of the interferometer. Using again Eq. (3.38), we obtain

$$Q_{1U} = -\frac{u - v}{4\pi u v} \Delta \mu, \quad Q_{1D} = \frac{u + v}{4\pi u v} \Delta \mu.$$
 (3.43)

Then from Eq. (3.28) we find that  $\Delta t = (L_D + L_U)/2v + (L_U - L_D)/2u$ .

The analytical structure of the integral (3.36) is shown in Fig. 3.9. It looks somewhat similar to the structure shown in Fig. 3.6 for the case of single biased channel. However, the principal difference between these two cases is that the singularities

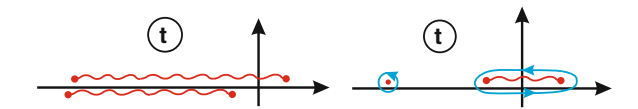


**Fig. 3.9** Analytic structure of the integral (3.33), same as in Fig. 3.8, but in the weak backscattering regime. The *right panel* shows the pole at  $t = -(L_U + L_D)/2v$  and the branch cut, which extends from  $t = -(L_D - L_U)/2v$  to  $t = (L_D - L_U)/2v$ . After Ref. [2]. © American Physical Society

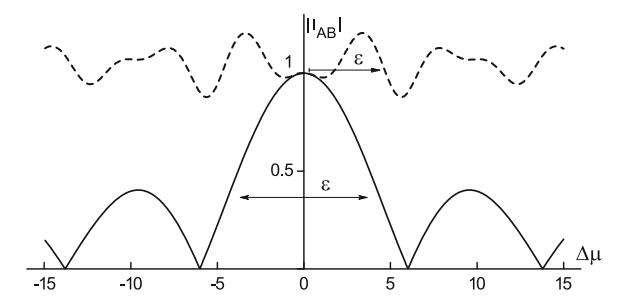


Fig. 3.10 The intrinsic visibility of Aharonov-Bohm oscillations  $|\mathcal{I}_{AB}|$  in the case when two edge channels are biased [7, 8] and for strongly asymmetric interferometer,  $L_D=1.8L_U$ . It is plotted as a function of bias  $\Delta\mu$  in units of  $v/L_U$  for the regime of weak tunneling (*solid line*) and for the regime of weak backscattering (*dashed line*). After Ref. [2]. © American Physical Society

in Fig. 3.9 are strongly asymmetric with respect to  $t \to -t$ . In order to see a consequence of this fact we take the limit  $u \gg v$  and write  $\Delta t = (L_U + L_D)/2v$ . For the phase shift (3.34) at small bias we obtain  $\partial \Delta \phi_{\rm AB}/\partial \Delta \mu = -(L_U + L_D)/2v$ . Therefore, in the weak backscattering regime and when two channels are biased no phase rigidity can be observed.

The most remarkable new feature of the visibility (see Fig. 3.10) is that, in contrast to the cases considered above, it grows as a function of bias around  $\Delta\mu=0$ , in full agreement with the experiment [7, 8]. It may even exceed the value 1 if two quantum point contacts have approximately same transparencies, so that  $V_{\mathcal{G}}(0)$  is close to 1. This behavior may look surprising, because it is expected that dephasing should suppress the visibility of Aharonov-Bohm oscillations below its maximum value (1.85) for a non-interacting coherent system. However, one should keep in mind that according to our model oscillations of the visibility as a function of bias originate from charging effects which are caused by the Coulomb interaction between edge channels. Therefore, simple arguments which rely on the Landauer formula for the conductance do not apply.

Thus in the experimental set-up where two edge channels are biased [7, 8] there is a strong asymmetry between weak tunneling and weak backscattering regimes, which is easily seen in Fig. 3.10. In order to clarify the physical origin of this effect, we evaluate the integral (3.36) in the limit of strong interaction  $u \gg v$  and for a symmetric Mach-Zehnder interferometer,  $L_U = L_D = L$ . Then the branch cut shrinks to the pole, and we obtain the following simple result:

$$\mathcal{I}_{AB} = \Delta t/t_0 + (1 - \Delta t/t_0)e^{i\Delta\mu t_0}, \qquad (3.44)$$

where  $t_0 = L/v$  is the time of the propagation of the slow mode between two quantum point contacts. We find that quite similar to the result for the phase shift (3.34), here we also have a competition of two terms,  $\Delta t$  given by Eq. (3.28), and of the flight time  $t_0$ . Whether the visibility grows or decays depends on the sign of the second term in Eq. (3.44).

In the experiment [1]  $\Delta t = L/2v = t_0/2$ , so that the visibility always decays. On the other hand, the experiment [7, 8] represent an intermediate case. In the regime of weak tunneling we have  $\Delta t = 0$ , while in the regime of weak backscattering  $\Delta t = t_0$ , so that in both regimes the visibility is constant for the symmetric Mach-Zehnder interferometer. Therefore, in Fig. 3.10 we had to consider a strongly asymmetric interferometer with  $L_D = 1.8L_U$ . Note however, that once  $\Delta t$  exceeds slightly  $t_0$ , the visibility easily becomes growing function at small bias. This is exactly what happens if we relax our assumption of good screening of the interaction and allow opposite arms of the interferometer to interact. Indeed, in order to be electro-neutral the system compensates such interaction by decreasing further the charge  $Q_{1U}$  below the value given by Eq. (3.43), so that now  $\Delta t > t_0$ . We have checked numerically that this assumption alone gives rise to a good agreement with the experiment [7, 8] even in the case of symmetric interferometer.

## 3.4.3 Effects of Finite Temperature

The temperature dependence of the visibility of Aharonov-Bohm oscillations in Mach-Zehnder interferometers has been recently measured in Ref. [10]. The most interesting fact is that the visibility scales exponentially with the total size of the interferometer  $V_{\mathcal{G}} \propto e^{-L/l_{\varphi}}$ . This is in obvious contradiction with the prediction  $V_{\mathcal{G}} \propto e^{-\Delta L/l_{\varphi}}$  for free electrons, [24] where dephasing is due to energy averaging. Moreover, the coherence length scales with temperature as  $l_{\varphi} \propto 1/T$ , which does not agree with the prediction based on Luttinger liquid model for  $\nu=1$  [4]. Here we show that the experimentally observed temperature dependence of the visibility can be explained within our model.

Indeed, according to results of Sect. 3.3, at high temperatures, neglecting charging effects which merely influence the prefactor, the visibility can be estimated as  $V_{\mathcal{G}} \propto \int dt K_D^*(t) K_U(t)$ . Here the correlators are given by the hight-temperature asymptotic form (7.26), where  $X_{\alpha}$  has to be replaced with  $L_s - v_{\alpha}t$ . Then in the non-interacting case (i.e. for  $\delta_1 = 1$ ,  $\delta_2 = 0$ , and  $v_1 = v_F$ ) we obtain the result

$$V_{\mathcal{G}} \propto \int dt e^{-\pi T \sum_{s} |t - L_{s}/v_{F}|} \propto e^{-\pi T \Delta L/v_{F}},$$
 (3.45)

which agrees with the prediction in Ref. [24]. On the other hand, in our model  $\delta_1 = \delta_2 = 1/2$ , so we obtain

$$V_{\mathcal{G}} \propto \int dt e^{-\pi T \sum_{\alpha,s} |t - L_s/v_{\alpha}|} \propto e^{-(L_U + L_D)/2l_{\varphi}},$$
 (3.46)

where the dephasing length

$$l_{\varphi} = \frac{uv}{\pi T(u - v)}. (3.47)$$

Thus we find that the visibility scales exponentially with the total size of the interferometer, and the dephasing length scales as  $l_{\varphi} \propto 1/T$ , in full agreement with the experiment [10].

Two remarks are in order. According to Eqs. (3.46), (3.47), and to the results of Sect. 3.3, the temperature dependence and the period of oscillations of the visibility are determined by the same energy scale  $\epsilon$ , given by Eq. (3.35). On the other hand, the decay of the visibility as a function of the bias  $\Delta\mu$  at zero temperature is determined by a larger energy scale  $\epsilon'$ . It is equal to  $\epsilon' = v/\Delta L$ , or, in case of the symmetric interferometer, depends on the dispersion of the slow mode.

Second, we note that v and u are the group velocities of the collective dipole and charge excitations, respectively. Very roughly, they are determined by the spatial separation between edge modes a, and by the distance to the back gate D. On the  $\nu=2$  Hall plateau, the separation a grows with the magnetic field, because the inner edge channel moves away from the edge of the two-dimensional electron gas until it disappears in the end of the plateau. Therefore, in contrast to the bare Fermi velocity, the velocity of the slow mode increases with the magnetic field. This may explain the non-monotonic behavior of  $l_{\varphi}$  observed in Ref. [10]. Indeed, according to Eq. (3.47) the decoherence length first increases with the magnetic field starting from the value  $l_{\varphi}=v/\pi T$ . Then it reaches the maximum value at  $v\approx u$  and goes down to the value  $l_{\varphi}\approx u/\pi T$  on the plateau  $\nu=1$ .

#### 3.5 Conclusion

Earlier theoretical works [20–22, 24] on dephasing in Mach-Zehnder interferometers predicted a *smooth* decay of the visibility of Aharonov-Bohm oscillations as a function of temperature and voltage bias. Therefore, when the Ref. [1] reported unusual oscillations and lobes in the visibility of Aharonov-Bohm oscillations as a function of bias, this was a great puzzle, attracted considerable theoretical attention. Reference [3] suggested the first explanation that is based on the long-range Coulomb interaction between counter-propagating edge states leading to resonant scattering of plasmons. Although this phenomenon may be encountered in a number of experimental situations, new experiments [7–12] unambiguously pointed to physics related to the intrinsic structure of the quantum Hall edge.

In the present chapter we focus on the intrinsic properties of the edge and propose a simple model which is able to explain almost every detail of existing experiments. The key ingredient of our theory is the assumption that two chiral channels at the 3.5 Conclusion 75

edge of  $\nu=2$  electron system interact via the long-range Coulomb potential. This leads to number of *universalities*, in particular, to the separation of the spectrum of edge excitations on slow and fast mode (plasmons), and to equal coupling of electrons to both modes. When electrons scatter off the quantum point contacts, which play a role of beam splitters in the electronic, they excite plasmons, depending on the energy provided by the voltage bias. The plasmons carry away the electron phase information, which leads the the decay of the visibility of Aharonov-Bohm oscillations as a function of bias.

The remarkable property of our model is that at zero temperature the phase information emitted at the first quantum point contact can be partially recollected at the second quantum point contact. This leads to oscillations and lobes in the visibility which can be interpreted as a size effect. The new energy scale in these oscillations, associated with the total size of the Mach-Zehnder interferometer and with the *slow mode*, determines also the temperature dependence of the visibility.

Physically, the lobes of visibility in our model are quite similar to the *neutrino* oscillations effect in the high-energy physics. Namely, the main reason for appearance of lobes is the existence of two distinct bases: basis of states created by the tunneling Hamiltonian, analogous to the "flavour eigenstates", and the edge Hamiltonian eigenstates, analogous to the "mass eigenstates". Each electron which tunnels to the edge thus splits in two plasmon modes—charged and dipole, which propagate with different velocities:

$$|\text{electron}\rangle = e^{i\Delta\mu L/v}|\text{charged}\rangle + e^{i\Delta\mu L/v}|\text{dipole}\rangle.$$
 (3.48)

At the distances where the phase difference between these two states is, e.g.,  $\pi$ , their sum is *orthogonal* to the initial state and the visibility is zero. In other words, the electron evolves to a different "flavor". While at distances where the phase difference is, e.g.,  $2\pi$ , the initial electron state is restored.

Importantly, within the framework of the same simple model we are able to explain a variety of ways the interaction effects manifest themselves in different experiments [1, 7–12]. This includes the lobe-type structure observed in Refs. [1, 7, 8], the phase rigidity that was found only in Ref. [1], the growing visibility and the asymmetry of the Aharonov-Bohm effect discovered in Ref. [7, 8]. All these phenomena can be interpreted as charging effects. Indeed, edge channels in quantum Hall systems move along the equipotential lines and can be regarded as one-dimensional metals. Therefore, they accumulate ground state charges, which lead to electronic phase shifts, depending on the bias scheme (see Figs. 3.1 and 3.2). These bias dependent phases determine the overall Aharonov-Bohm phase shift and the specific behavior of the visibility as a function of the voltage bias.

Finally, experimentally observed decay of the visibility as a function of bias seems to be stronger than what our model predicts. We think that this effect cannot be explained by the long-range Coulomb interaction alone, and may originate from the dispersion of the slow mode due to disorder, because of the intrinsic structure of each edge channel [23], or from the external noise, as discussed in the next chapter. This point deserves a careful experimental and theoretical investigation. Moreover, it

is interesting to find out how charging and size effects discussed here may influence the interferometry at other filling factors, where quite similar processes can take place [25]. Although the first theoretical steps have already been taken [26–30] the experiment, as usual, may bring new surprises.

#### References

- 1. I. Neder, M. Heiblum, Y. Levinson, D. Mahalu, V. Umansky, Phys. Rev. Lett. 96, 016804 (2006)
- 2. I.P. Levkivskyi, E.V. Sukhorukov, Phys. Rev. B 78, 045322 (2008)
- 3. E.V. Sukhorukov, V.V. Cheianov, Phys. Rev. Lett. 99, 156801 (2007)
- 4. J.T. Chalker, Y. Gefen, M.Y. Veillette, Phys. Rev. B 76, 085320 (2007)
- 5. I. Neder, E. Ginossar, Phys. Rev. Lett. 100, 196806 (2008)
- 6. S.-C. Youn, H.-W. Lee, H.-S. Sim, Phys. Rev. Lett. 100, 196807 (2008)
- E. Bieri, Correlation and Interference Experiments with Edge States, PhD thesis, University of Basel (2007).
- 8. E. Bieri, M. Weiss, O. Goktas, M. Hauser, C. Schonenberger, S. Oberholzer, Phys. Rev. B 79, 245324 (2009)
- P. Roulleau, F. Portier, D.C. Glattli, P. Roche, A. Cavanna, G. Faini, U. Gennser, D. Mailly, Phys. Rev. B 76, 161309 (2007)
- P. Roulleau, F. Portier, D.C. Glattli, P. Roche, A. Cavanna, G. Faini, U. Gennser, D. Mailly, Phys. Rev. Lett. 100, 126802 (2008)
- 11. L.V. Litvin, H.-P. Tranitz, W. Wegscheider, C. Strunk, Phys. Rev. B 75, 033315 (2007)
- L.V. Litvin, A. Helzel, H.-P. Tranitz, W. Wegscheider, C. Strunk, Phys. Rev. B 78, 075303 (2008)
- 13. D.B. Chklovskii, B.I. Shklovskii, L.I. Glazman, Phys. Rev. B 46, 4026 (1992)
- 14. For a review, see A.M. Chang, Rev. Mod. Phys. 75, 1449 (2003).
- 15. X.-G. Wen, Adv. Phys. 44, 405 (1995)
- 16. T. Giamarchi, Quantum Physics in One Dimension (Oxford University Press, Oxford, 2003)
- X.-G. Wen, Quantum Field Theory of Many-body Systems (Oxford University Press, New York, 2007)
- 18. G.D. Mahan, Many Particle Physics, 2nd edn. (Plenum, New York, 1993)
- 19. G. Seelig, M. Büttiker, Phys. Rev. B **64**, 245313 (2001)
- 20. G. Seelig et al., Phys. Rev. B 68, 161310 (2003)
- 21. F. Marquardt, C. Bruder, Phys. Rev. Lett. **92**, 056805 (2004)
- 22. F. Marquardt, C. Bruder, Phys. Rev. B 70, 125305 (2004)
- 23. J. Fröhlich, B. Pedrini, C. Schweigert, J. Walcher, J. Stat. Phys. 103, 527 (2001)
- 24. V.S.-W. Chung, P. Samuelsson, M. Büttiker, Phys. Rev. B 72, 125320 (2005)
- 25. C.L. Kane, M.P. Fisher, J. Polchinski, Phys. Rev. Lett. **72**, 4129 (1994)
- 26. K.T. Law, D.E. Feldman, Y. Gefen, Phys. Rev. B 74, 045319 (2006)
- 27. V.V. Ponomarenko, D.V. Averin, Phys. Rev. Lett. 99, 066803 (2007)
- E. Ardonne, E.-A. Kim, J. Stat. Mech. L04001, (2008). doi:10.1088/1742-5468/2008/04/ L04001
- 29. B.J. Overbosch, X.-G. Wen, arXiv:0706.4339.
- 30. W. Bishara, C. Nayak, Phys. Rev. B 77, 165302 (2008)

# **Chapter 4 Noise Induced Dephasing of Edge States**

Single particle theory of quantum Hall edge states suggests that at integer filling factors the low-energy edge excitations are free chiral electrons. If this were the case, it would imply that edge excitations remain coherent at long distances, and would call for various quantum information applications. Results of tunneling spectroscopy experiments [1] reasonably agree with the free-electron description of edge states. In contrast, the first experiment on Aharonov-Bohm oscillations of a charge current in the electronic Mach-Zehnder interferometer [2] has shown that the phase coherence is strongly suppressed at energies, which are inverse proportional to the interferometer's size. Moreover, subsequent experiments [3–10] have found that the visibility of Aharonov-Bohm oscillations as a function of voltage bias applied to the interferometer shows unusual lobe-type behavior, suggesting that a strong Coulomb interaction might be responsible for dephasing of edge electrons.

Early attempts to explain the unusual Aharonov-Bohm effect in Mach-Zehnder interferometers focused on the filling factor  $\nu=1$  state, and suggested different mechanisms of dephasing, including the resonant interaction with a counter-propagating edge state [11], the dispersion of the Coulomb interaction potential [12], and non-Gaussian noise effects [13, 14]. To date, however, all the experiments, reporting multiple side lobes in the visibility function of voltage bias, have been done at filling factor  $\nu=2$ . In the previous chapter, we have shown that in this case the long-range Coulomb interaction splits the spectrum of collective charge excitations at the quantum Hall edge (plasmons) in two modes: a fast charge mode and a slow dipole mode. At low energies, only slow mode is excited at the first quantum point contact. It carries away the electron phase information, but may be absorbed at the second quantum point contact. This process partially restores the phase coherence at specific values of voltage bias, and generates multiple lobes in the visibility. At the same time, thanks to the chirality of edge states, the electron transport through a single quantum point contact is not affected by interaction.

Some text sections in this chapter are reproduced from Phys. Rev. Lett. 103, 036801 (2009), © American Physical Society.

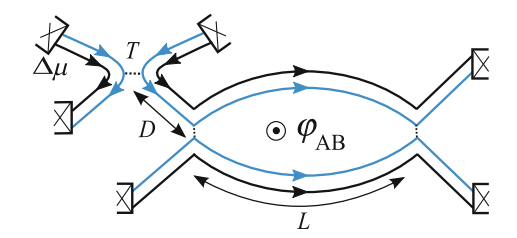


**Fig. 4.1** Schematic of the electronic Mach-Zehnder interferometer. Two chiral channels are formed at the edge of a quantum Hall liquid at filling factor  $\nu = 2$ . Outer channels (shown by *blue lines*) are mixed at two quantum point contacts and form an Aharonov-Bohm loop. Electrons are injected into the interferometer through an additional voltage biased quantum point contact, which is placed at the distance D from the interferometer and has transparency T. After Ref. [15]. © American Physical Society (Color figure online)

We argue that there are two sources of dephasing in the Mach-Zehnder interferometers: interaction and coupling to non-equilibrium noise generated by quantum point contacts. In this chapter, we apply the non-equilibrium bosonization approach to the model proposed in the previous chapter in order to investigate the second source of dephasing. Importantly, the experiments [3–10] can be roughly grouped in two categories according to the biasing scheme. In the experiments of the first group [3, 4, 6, 7], the bias is applied only to the interfering channel with the help of additional quantum point contact. In this chapter, we focus on this group of experiments, where electrons are injected into a Mach-Zehnder interferometer via an additional quantum point contact, as shown in Fig. 4.1 and study how the *partitioning noise* created by this quantum point contact affects the interference.

# 4.1 Experimental Setup and the Model

The model of a Mach-Zehnder interferometer, introduced in Chap. 3, is discussed here only briefly. We note, that experimentally relevant energy scales are very small [3–10]. Therefore, it is appropriate to use an effective theory describing edge states at filling factor  $\nu=2$  as collective fluctuations of the charge density  $\rho_{\alpha s}(x)=\partial_x\phi_{\alpha s}(x)/2\pi$ , where  $\alpha=1,2$  enumerates channels at the quantum Hall edge, and s=U,D enumerate arms of the interferometer. The total Hamiltonian of a Mach-Zehnder interferometer,  $\mathcal{H}=\mathcal{H}_0+\sum_\ell(A_\ell+A_\ell^\dagger)$ , contains a term describing edge states

$$\mathcal{H}_0 = \frac{1}{8\pi^2} \sum_{\alpha\beta s} \int dx dy V_{\alpha\beta}(x - y) \partial_x \phi_{\alpha s}(x) \partial_y \phi_{\beta s}(y), \tag{4.1}$$

where the kernel,  $V_{\alpha\beta}(x-y) = 2\pi v_F \delta_{\alpha\beta}\delta(x-y) + U_{\alpha\beta}(x-y)$ , includes a free fermion contribution with the Fermi velocity  $v_F$ , and the Coulomb interaction

potential  $U_{\alpha\beta}$ . Vertex operators

$$A_{\ell} = t_{\ell} \exp[i\phi_{1D}(x_{\ell}) - i\phi_{1U}(x_{\ell})], \tag{4.2}$$

where  $\ell=L$ , R, describing electron tunneling between outer edge channels of the interferometer at the left and right quantum point contact, are treated perturbatively. The Aharonov-Bohm phase  $\varphi_{AB}$  is taken into account via the relation for tunneling amplitudes,  $t_R^*t_L = |t_Rt_L|e^{i\varphi_{AB}}$ .

The electron current is defined as a rate of change of the electron number in the lower arm,  $I = i[\mathcal{H}, N_D]$ . To leading order in tunneling amplitudes, its average value is given by the linear response formula

$$\langle I \rangle = \int_{-\infty}^{\infty} dt \sum_{\ell \ell'} \langle \left[ A_{\ell}^{\dagger}(t), A_{\ell'}(0) \right] \rangle. \tag{4.3}$$

Here the average is evaluated with respect to the non-equilibrium state created by partitioning of the outer channel at the quantum point contact. The Aharonov-Bohm oscillations in the differential conductance  $G \equiv d\langle I \rangle/d\Delta\mu$  are characterized by the visibility

$$V_{AB}(\Delta\mu) = \frac{G_{\text{max}} - G_{\text{min}}}{G_{\text{max}} + G_{\text{min}}}.$$
(4.4)

Using the linear response formula for current, one easily finds that both the visibility and the phase shift of Aharonov-Bohm oscillations are expressed in terms of the same complex function (see Sect. 3.3), namely

$$V_{AB} = V_0 |\mathcal{I}(\Delta \mu)|, \quad \Delta \varphi_{AB} = \arg \mathcal{I}(\Delta \mu),$$
 (4.5a)

$$\mathcal{I}(\Delta\mu) = \partial_{\Delta\mu} \int_{-\infty}^{\infty} \frac{dt}{2\pi} K_U(L, t) K_D^*(L, t), \tag{4.5b}$$

where  $V_0 \propto 2|t_L t_R|/(|t_L|^2 + |t_R|^2)$ , and

$$K_s(x,t) \propto \langle \exp[-i\phi_{1s}(x,t)] \exp[i\phi_{1s}(0,0)] \rangle$$
 (4.6)

are the electron correlation functions [16] at the outer channels of the interferometer. Thus the visibility of Aharonov-Bohm oscillations probes a non-equilibrium state of a quantum Hall system via the correlators  $K_s(x,t)$ .

#### 4.2 Correlation Functions

According to the non-equilibrium bosonization technique, the equations of motion generated by the Hamiltonian (4.1) have to be accompanied with a boundary condition:

$$\partial_t \phi_{\alpha s}(x,t) = -\frac{1}{2\pi} \sum_{\beta} \int dy V_{\alpha \beta}(x-y) \partial_y \phi_{\beta s}(y,t), \qquad (4.7a)$$

$$\partial_t \phi_{\alpha s}(-D, t) = 2\pi j_{\alpha s}(t).$$
 (4.7b)

We place the boundary at the point x=-D, where the upper outer channel is interrupted by a quantum point contact. By solving equations (4.7a) one may express the fields  $\phi_{\alpha s}$  in terms of currents  $j_{\alpha s}$ . In general, the fields  $\phi_{\alpha s}$  influence fluctuations of the currents  $j_{\alpha s}$  at a quantum point contact, but such back-action effects are absent for chiral edge states, as we have shown in Chap. 2. As a consequence, in the case of  $\nu=2$  the electron transport through a single quantum point contact is *not affected* by interactions, which has been recently confirmed in the experiment [8, 9].

Following the argumentation in Chap. 3, we assume that the Coulomb potential is *screened* at distances d, with  $L \gg d \gg a$ , where a is the distance between edge channels. The screening may occur due to the presence of either a back gate, or a massive air bridge (see discussion in Sect. 3.2.3). Therefore, at low energies one can neglect the logarithmic dispersion of the Coulomb potential and write

$$U_{\alpha\beta}(x-y) = U_{\alpha\beta}\delta(x-y). \tag{4.8}$$

Nevertheless, the *long-range* character of the interaction, i.e., the fact that  $d \gg a$ , allows one to approximate  $U_{\alpha\beta} = \pi u$ , where  $u/v_F \sim \log(d/a) \gg 1$ . As a result, the spectrum of collective charge excitations splits in two modes: a fast charged mode with the speed u, and a slow dipole mode with the speed  $v \simeq v_F$ .

It is important to stress that the condition  $d \gg a$  results in a sort of universality: the solution of equations of motion (4.7a) in terms of the charged and dipole mode,

$$\phi_{1s}(x,t) = \frac{1}{\sqrt{2}} \left[ \tilde{\phi}_{1s}(x - vt) + \tilde{\phi}_{2s}(x - ut) \right]$$
 (4.9a)

$$\phi_{2s}(x,t) = \frac{1}{\sqrt{2}} \left[ \tilde{\phi}_{1s}(x - vt) - \tilde{\phi}_{2s}(x - ut) \right]$$
 (4.9b)

is only weakly sensitive to perturbations of our model, in particular to those that account for different bare Fermi velocities of edge channels and slightly different interactions strengths.

Applying now boundary conditions (4.7b) to the result (4.9) we finally solve equations of motion in terms of the boundary currents:

4.2 Correlation Functions 81

$$\phi_{1s}(x,t) = \pi \int_{-\infty}^{t_u} dt' [j_{1s}(t') + j_{2s}(t')] + \pi \int_{-\infty}^{t_v} dt' [j_{1s}(t') - j_{2s}(t')], \qquad (4.10a)$$

$$\phi_{2s}(x,t) = \pi \int_{-\infty}^{t_u} dt' [j_{1s}(t') + j_{2s}(t')] - \pi \int_{-\infty}^{t_v} dt' [j_{1s}(t') - j_{2s}(t')], \qquad (4.10b)$$

$$\phi_{2s}(x,t) = \pi \int_{-\infty}^{t_u} dt' [j_{1s}(t') + j_{2s}(t')] - \pi \int_{-\infty}^{t_v} dt' [j_{1s}(t') - j_{2s}(t')], \qquad (4.10b)$$

where we have introduced notations  $t_u \equiv t - (x + D)/u$ , and  $t_v \equiv t - (x + D)/v$ .

At relevant energies, v/L, the charged mode is not excited, which leads to a universality in the electron transport predicted in the previous chapter and observed in experiments [3–10]. Here, taking the limit  $u \to \infty$  simplifies the solution (4.10), and we obtain the result

$$\phi_{1s}(x,t) = -\pi [Q_{1s}(t) + Q_{2s}(t) + Q_{1s}(t_v) - Q_{2s}(t_v)], \tag{4.11}$$

where the charge operators are defined as  $Q_{\alpha s}(t) = \int_{-\infty}^{t} dt' j_{\alpha s}(t')$ .

Finally, we further assume that the noise source is located far away from the interferometer,  $D \gg L$ , which reasonably agrees with the experimental situation [3–10]. This assumption does not spoil the physics that we address, and may be relaxed later. It implies that all four charges in the solution for the field  $\phi_{s1}(x,t)$  are uncorrelated and contribute independently to the correlation function (4.6). Therefore, the correlator  $K_s(x, t)$  splits in the product of four terms

$$K_s(L,t) \propto \chi_{1s}(\pi,t)\chi_{1s}(\pi,t-L/v)\chi_{2s}(\pi,t)\chi_{2s}(-\pi,t-L/v),$$
 (4.12)

where the generator of full counting statistics is defined as following [17]:

$$\chi_{\alpha s}(\lambda, t) = \langle e^{i\lambda Q_{\alpha s}(t)} e^{-i\lambda Q_{\alpha s}(0)} \rangle. \tag{4.13}$$

Averaging on the right hand side is defined over free electrons.

Equation (4.12) can be illustrated by the following physical picture. Each electron splits in two plasmon modes by the interaction after tunneling at the quantum point contact, as shown in Fig. 4.2. These modes propagate with different speeds and become uncorrelated at distances  $x \gg \Delta \mu/v$ . Thus, there are four *independent* contributions to the correlation function in the outer edge channel, since tunneling to each of the edge channels leads to the emission of two plasmons. Each of these plasmons carries a  $\pm e/2$  charge in the outer channel, and therefore they are counted with  $\lambda = \mp \pi$  at the next quantum point contacts.

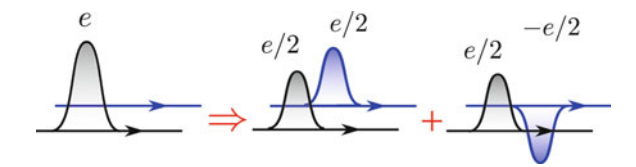


Fig. 4.2 Schematic illustration of the Coulomb interaction effect at the HQ edge at filling factor  $\nu=2$ . The electron wave-packet of the charge e created in the outer edge channel (black, lower line) decays into two eigenmodes of the Hamiltonian (4.1), the charged and dipole mode, which propagate with different speeds and carry the charge e/2 in the outer channel. As a result, the wave packets do not overlap at distances larger than their width, and contribute independently to the electron correlation function with the coupling constant  $\lambda=-\pi$ . Similar situation arises when an electron is injected in the inner channel (blue line), however in this case the charged and dipole states carry opposite charges at the outer channel. Thus, there are four independent contributions to the correlation function in the outer edge channel. After Ref. [18]. © American Physical Society (Color figure online)

# 4.3 Situation with Non-Equilibrium Gaussian Noise

In the context of the noise detection physics [17] the dimensionless counting variable  $\lambda$  in the expression (4.13) for the full counting statistics generator plays the role of a coupling constant. Typically, it is small,  $\lambda \ll 1$ , so that the contributions of high-order cumulants of current noise to the detector signal are negligible [19]. In contrast, in the physical situation that we consider in the present paper  $\lambda = \pm \pi$ , implying that the shape of the distribution function may be strongly affected by high-order current cumulants. Nevertheless, it is instructive to first consider Gaussian fluctuations, simply truncating the cumulant expansion at second order in  $\lambda$ . In this case the correlation function (4.12) may be evaluated exactly. The are many reasons for starting the analysis from considering an example of a Gaussian noise: First of all, in equilibrium the current fluctuations in a chiral one-dimensional system are always Gaussian. Second, as we show in the Appendix C, the dispersion of the charged and dipole modes leads to a suppression of higher order cumulants at large distances. Finally, on the Gaussian level it is easier to investigate and compare contributions of zero-point fluctuations and of non-equilibrium noise to the electron correlation function.

Expanding the right hand side of Eq. (4.13) up to second order in charge operators and taking into account Eq. (2.41), we obtain:

$$\log[\chi_{\alpha s}(\lambda, t)] = i\lambda \langle j_{\alpha s} \rangle t - \lambda^2 J_{\alpha s}(t). \tag{4.14}$$

The Gaussian noise contribution to the above expression is given by the following integral:

$$J_{\alpha s}(t) = \frac{1}{2\pi} \int \frac{d\omega S_{\alpha s}(\omega)}{\omega^2 + \eta^2} (1 - e^{-i\omega t}), \quad \eta \to 0, \tag{4.15}$$

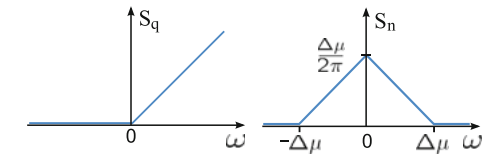


Fig. 4.3 Spectrum of noise power. Left panel shows quantum contribution  $S_{\rm q}(\omega)$  generated by the incoming Fermi sea. This contribution vanishes at low frequencies  $S_{\rm q}(0)=0$  and dominates at small times. Right panel shows non-equilibrium contribution  $S_{\rm n}(\omega)$ . This contribution determines the behavior of the second cumulant (4.15) at large times  $J_{\alpha s}(t) \propto S_{\rm n}(0)|t|$ . After Refs. [15, 18]. © American Physical Society

where the non-symmetrized noise power spectrum is defined as

$$S_{\alpha s}(\omega) = \int dt e^{i\omega t} \langle \delta j_{\alpha s}(t) \delta j_{\alpha s}(0) \rangle \tag{4.16}$$

and  $\delta j_{\alpha s}(t) \equiv j_{\alpha s}(t) - \langle j_{\alpha s} \rangle$ .

For a quantum point contact far away from equilibrium,  $\beta\Delta\mu\gg 1$ , one may simply set the temperature to zero. Straightforward calculations based on the scattering theory [20] give the following result for the spectral density of noise (4.16) of a quantum point contact:

$$S_{\alpha s}(\omega) = S_{q}(\omega) + R_{\alpha s} T_{\alpha s} S_{n}(\omega), \tag{4.17}$$

where  $S_q(\omega) = (1/2\pi)\omega\theta(\omega)$  is the quantum, ground-state spectral function, and  $S_n(\omega) = \sum_{\pm} S_q(\omega \pm \Delta\mu) - 2S_q(\omega)$ , is the non-equilibrium contribution (see Fig. 4.3). Note, that the noise power spectrum (4.17) is different from the power spectrum in a non-chiral case [19].

Evaluating the integral (4.15) we come to the following expression

$$J_{\alpha s}(t) = (1/4\pi^2)[\log t + 2R_{\alpha s}T_{\alpha s}f(\Delta \mu t)], \tag{4.18}$$

where the logarithm comes from the quantum contribution, and the dimensionless function  $f(\Delta \mu t)$ , which describes the non-equilibrium part of noise, is given by

$$f(\Delta \mu t) = \int_{0}^{1} d\tau \frac{1-\tau}{\tau^2} (1-\cos \Delta \mu t \tau). \tag{4.19}$$

This function has a *quadratic* behavior  $f(\Delta \mu t) \simeq \Delta \mu^2 t^2/4$  at small times  $t \to 0$ , while in the long-time (classical) limit, a dominant contribution to this function is *linear* in time:

$$f(\Delta \mu t) = (\pi/2)|\Delta \mu t|. \tag{4.20}$$

Finally, taking into account that  $\langle j_{\alpha s} \rangle = \Delta \mu T_{\alpha s}/2\pi$ , we find that the cumulant generating function is given by:

$$\log[\chi_{\alpha s}(\lambda, t)] = i(\lambda/2\pi)\Delta\mu T_{\alpha s}t - (\lambda/2\pi)^{2}[\log t - \pi R_{\alpha s}T_{\alpha s}|\Delta\mu t|].$$
 (4.21)

We now focus on the specific situation shown in Fig. 4.1, namely, we set  $T_{1D} = T_{2D} = T_{2U} = 1$  and  $T_{1U} = T = 1 - R$ . We evaluate the electron correlation function (4.12) in the upper arm of the Mach-Zehnder interferometer, using Eq. (4.21), and arrive at the result

$$K_U(L,t) \propto \frac{\exp[i\Delta\mu T(t-L/2v)]}{\sqrt{t(t-L/v)}} \exp[-\pi RT(|\Delta\mu t| + |\Delta\mu t - \Delta\mu L/v|)/4]. \tag{4.22}$$

On the right hand side of Eq. (4.22), the numerator in the first term originates from the average current  $T\Delta\mu/2\pi$  in (4.14), the denominator is the contribution of the quantum noise  $S_q(\omega)$ , and the last term comes from the non-equilibrium noise  $S_n(\omega)$  and describes dephasing. The correlation function in the lower arm of the interferometer can be obtained from Eq. (4.22) by setting  $\Delta\mu=R=0$  with the result

$$K_D(L,t) \propto 1/\sqrt{t(t-L/v)}$$
. (4.23)

This correlation function coincides with the result (2.36) found in Sect. 2.2 in the framework of the usual bosonization approach. Moreover, for a ballistic channel, and for L=0 the electron correlation function coincides with the one for free electrons. This explains the fact that in the  $\nu=2$  case, the Coulomb interaction does not affect an electron transport through a single quantum point contact [8, 9], and justifies our approach.

Next, we use the results for correlation functions  $K_s$  to evaluate the integral (4.5b). For a large voltage bias  $L\Delta\mu/v\gg 1$ , we obtain the following result for a Gaussian noise

$$\mathcal{I}(\Delta\mu) \propto E_{\mathrm{lb}} \partial_{\Delta\mu} \sin\left(\frac{\pi\Delta\mu}{E_{\mathrm{lb}}}\right) e^{-\Delta\mu/E_{\mathrm{df}}},$$
 (4.24a)

$$E_{\rm lb} = \frac{2\pi v}{TL}, \quad E_{\rm df} = \frac{4v}{\pi RTL}.$$
 (4.24b)

Thus the visibility  $V_{AB}$ , given by Eq. (4.5a), shows a *lobe-type behavior*: It oscillates as a function of voltage bias  $\Delta\mu$ , vanishes at certain values of bias, and decays. Since the function  $\mathcal{I}(\Delta\mu)$  is real, the Aharonov-Bohm phase shift  $\Delta\varphi_{AB}$  jumps by  $\pi$  at zeros of the visibility and remains constant between zeros, thus showing the *phase rigidity* [3]. The distance between zeros of the visibility,  $E_{lb}$ , is determined by the average current of transmitted electrons, and can be viewed as a "mean-field" contribution to the correlator (4.22). The dephasing rate, i.e., the scale of *exponential* decay of (4.24a),  $E_{df}$ , is determined by the current noise power. The ratio  $2E_{lb}/(\pi E_{df}) = R$  is given, in general, by the Fano factor of Gaussian noise.

#### 4.4 Noise Induced Phase Transition

In fact, the actual noise of the quantum point contact is non-Gaussian. Thus, in this section, we consider non-equilibrium partitioning noise and show, that in this situation the asymptotic behavior of the visibility undergoes a noise induced phase transition.

#### 4.4.1 Non-Gaussian Noise in Markovian Limit

In what follows, we consider non-Gaussian noise, and show that the contribution of high-order cumulants of current is indeed not small. Note, that the ground state contribution of the current noise,  $S_q$ , that dominates at short times, is pure Gaussian. Therefore, the denominator in the expression (4.22) remains unchanged. In the long time limit, the dominant contribution to the full counting statistics generator comes from the non-equilibrium part of noise,  $S_n$ . For a quantum point contact, it is given by the well known expression [17] for a *Binomial process*.

Let us briefly recall the derivation of these important expression. In the long-time limit, the charges Q(t) and Q(0) commute and can be treated as classical quantities. Thus, the full counting statistics generator is given by:

$$\chi(\lambda, t) = \langle e^{i\lambda[Q(t) - Q(0)]} \rangle, \tag{4.25}$$

where we have omitted the channel indexes for brevity. This classical quantity can be found directly, if one takes into account that the probability of transmission of Q particles for N attempts is given by the distribution  $P_N(Q) = C_N^Q T^Q R^{N-Q}$ :

$$\langle e^{i\lambda Q}\rangle = \sum_{Q} P_N(Q)e^{i\lambda Q} = \sum_{Q} C_N^Q (Te^{i\lambda})^Q R^{N-Q}, \tag{4.26}$$

where T is the transmission probability in a single event and R = 1 - T. Using the Newton binomial formula for the last sum in Eq. (4.26), we get the following expression for the full counting statistics generator:

$$\chi_{1U}(\lambda, t) = (R + Te^{i\lambda})^N, \tag{4.27}$$

where  $N = \Delta \mu t/2\pi$  is the number of electrons that contribute to noise. Applying the analytical continuation  $\lambda \to \pi$ , we obtain

$$\log[\chi_{1U}(-\pi, t)] = \frac{\Delta \mu t}{2\pi} \left[ \log|T - R| + i\pi\theta(T - R) \right], \tag{4.28}$$

where the imaginary part contributes to the effective *voltage bias* in the first term of the correlator (4.22), while the real part is responsible for *dephasing*.

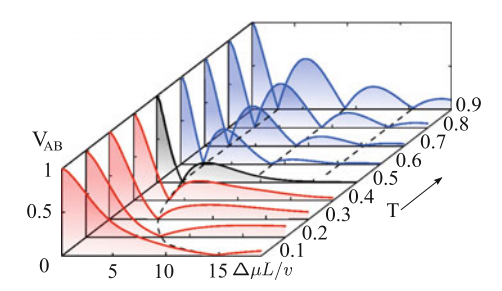


Fig. 4.4 The visibility of Aharonov-Bohm oscillations is shown as a function of the normalized voltage bias for different transparencies of the quantum point contact that injects electrons. It is evaluated numerically using the Gaussian approximation at low bias, and Markovian full counting statistics at large bias. The visibility shows several lobes for T > 1/2 (blue curves), while it has only one side lobe (red curves) for T < 1/2. The black curve shows the visibility at critical point of the phase transition. Dashed lines indicate the position of zeros. After Ref. [15]. © American Physical Society

A remarkable property of Eq. (4.28) is that high-order cumulants of current add up to cancel the dilution effect of a quantum point contact. Therefore, the continuous variation of the mean-field contribution in the correlator (4.22) is replaced with the jump in the voltage bias across a Mach-Zehnder interferometer at the point T=1/2. We evaluate the integral (4.5b) in the limit  $L\Delta\mu/v\gg 1$  and arrive at the result (4.24a), as in the Gaussian case, but with new energy scales:

$$E_{\rm lb} = \frac{2\pi v}{L}, \quad E_{\rm df} = \frac{2\pi v}{L|\log(T-R)|}, \quad T > 1/2.$$
 (4.29)

The rigidity of zeros of the visibility for T>1/2 is clearly seen in Fig.4.4. For T<1/2, the visibility may be found by taking the limit  $E_{\rm lb}\to\infty$  in Eq. (4.24a) with the result

$$\mathcal{I}(\Delta\mu) \propto (1 - \Delta\mu/E_{\rm df})e^{-\Delta\mu/E_{\rm df}}$$
. (4.30)

Thus, the only zero of the visibility scales as  $\Delta \mu = E_{\rm df}$ , given by the expression in (4.29).

The behavior of the visibility of Aharonov-Bohm oscillations, shown in Fig. 4.4, may be considered a phase transition, because strictly speaking, it arises in the classical regime, where the number of electrons that contribute to this effect is large,  $N\gg 1$ . The transition occurs at the critical point,  $\lambda=\pi$ , T=1/2, where the moment generator  $\chi_{1U}(\lambda,t)$  of a Binomial process vanishes, and can be viewed as a result of entanglement between electrons of the noise source and those that contribute to Aharonov-Bohm oscillations. However, quantum fluctuations of N at critical point smear out the sharp transition.

## 4.4.2 Quantum Correction at Critical Point

Finding quantum corrections to the full counting statistics of non-interacting electrons requires the evaluation of Fredholm determinants, which is best formulated in the wave-packet basis [17]. In the present situation a simplification arises from the fact, that in the long-time limit the dominant contribution to the generator (4.13) comes from non-equilibrium electrons in the energy interval  $\Delta\mu$ . We can thus write the full counting statistics generator (4.13) as following:

$$\chi_{1U}(\lambda, t) = \langle \Psi | U^{\dagger}(t) e^{i\lambda Q} U(t) | \Psi \rangle, \tag{4.31}$$

where the *N*-electron wave function  $\langle x_1, \ldots, x_N | \Psi \rangle = \det_{mn} W_n(x_m)$  describes the "train" of incoming wave-packets, Q is the charge counting operator, which counts the transmitted states, and U(t) is the evolutionary operator. The exponent of the counting operator can be written as  $e^{i\lambda Q} = 1 - P + e^{i\lambda}P$ , where P is the projector on the subspace of transmitted states.

The states of electrons in the "train" can be well approximated by the functions

$$W_n(x) = \sqrt{\frac{\Delta\mu}{2\pi v_F}} \frac{\sin[(\Delta\mu/2)(x/v_F - t) + \pi n]}{(\Delta\mu/2)(x/v_F - t) + \pi n}.$$
 (4.32)

Such wave packets are normalized as  $\int dx |W_n(x)|^2 = 1$ . If electrons under the action of U(t) were transmitted through the quantum point contact (which is placed at x=0 for the convenience) with the probability T and reflected with the probability T=1-T, this would lead to a Binomial process. However, the fact that wave packets have a finite width leads to the small probability  $P_n=\int_{-\infty}^0 dx W_n^2(x)$  for electrons not to reach the quantum point contact, which can be well approximated with

$$P_n = [\pi(\Delta \mu t - 2\pi n)]^{-1}. (4.33)$$

This fact is schematically illustrated in Fig. 4.5.

Thus, taking into account all three possibilities, the moment generating function can be written as

$$\chi_{U1}(\lambda, t) = \prod_{n} [(1 - P_n)(R + Te^{i\lambda}) + P_n]. \tag{4.34}$$

Far from the critical point this expression gives the Eq. (4.27) plus small corrections of order of log N. While at the critical point,  $\lambda = \pi$ , T = 1/2, Eq. (4.34) gives the following result

$$\log[\chi_{1U}] = \sum_{n} \log(P_n) = -\frac{\Delta \mu t}{2\pi} [\log(\pi \Delta \mu t) - 1]. \tag{4.35}$$

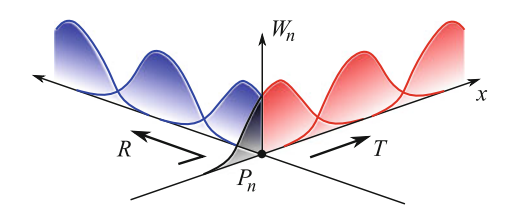


**Fig. 4.5** Illustration of quantum corrections due to the finite width of wave packets. At point x = 0, electron wave packets are transmitted with probability T or backscattered with probability T. Transmitted packets are shown in *red color*, backscattered ones are shown in *blue color*. Each wave packet has a *power-law tail* of wave function in the region before quantum point contact. Thus the probability T0 not to reach the quantum point contact is equal to the area of the *gray shadow*. It is given approximately by Eq. (4.33) (Color figure online)

Therefore, the asymptotics of the cumulant generator is *not linear* in time.

One can notice that the imaginary part of  $log[\chi_{1U}]$  comes from a branch cut of the logarithm of Eq. (4.34) and grows gradually in the interval

$$T - R \approx 1/(2\pi^2 N). \tag{4.36}$$

Therefore, the quantum corrections smear out the discontinuity in (4.28). Using Eq. (4.35) we find that exactly at the critical point the visibility scales at large biases as follows:

$$V_{\rm AB} \propto \partial_{\varepsilon} \exp\{-\varepsilon[\log(\pi^2 \varepsilon) - 1]\}/\sqrt{\varepsilon}, \quad \varepsilon = \Delta \mu L/2\pi v \gg 1.$$
 (4.37)

The result of a numerical evaluation of the visibility integral for this situation is shown by black line in Fig. 4.4.

#### 4.5 Conclusions

First experiments on electronic Mach-Zehnder interferometers brought interesting results and attracted significant attention of theoreticians. The effects found in these experiments at relatively *low bias*, such as, e.g., lobe type structure of the visibility and the phase rigidity with respect to bias can be explained by the presence of the strong Coulomb interaction at the edge. It has been found in the experiments, that the visibility decays rapidly at relatively *large bias*. We argue, that this effect is explained by coupling of electrons to the non-equilibrium noise generated at quantum point contacts. Therefore, we use the non-equilibrium bosonization technique to describe the effects of the quantum point contact, which dilutes the impinging edge channel.

Apart from diluting the incoming electron channel, this additional quantum point contact generates a partition noise. The Mach-Zehnder interferometer turns out to be *strongly coupled* to this noise, so that non-Gaussian effects, characterized by

4.5 Conclusions 89

irreducible moments (cumulants) of the current noise, become important. We express the visibility of Aharonov-Bohm oscillations in the differential conductance in terms of the cumulant generating function, and find that in the limit of large voltage bias, all the current cumulants add up to cancel the dilution effect of an additional quantum point contact. We predict, that this leads to a *phase transition* at the quantum point contact's transparency T=1/2, where the visibility function of voltage bias abruptly changes its behavior. Quantum fluctuations smear out the sharp transition in the vicinity of the critical point. Far from the critical point, the noise contributes only to the exponential envelope of the visibility.

We think that a similar behavior of the visibility, i.e., the exponential decay at large bias, will be caused as well by the noise emitted by the first quantum point contact of the interferometer. This statement, however, deserves further quantitative justification. The present theory takes into account interaction effects, discussed in the previous chapter, and the external non-equilibrium noise. Already at this point, one gets almost perfect fit to experimental data of several experiments, with few fitting parameters. Moreover, the proposed model leads to strong *qualitative* predictions, such as the existence of the noise induced phase transition, which can serve as an additional justification of the theory.

#### References

- 1. For a review, see A.M. Chang, Rev. Mod. Phys. 75, 1449 (2003).
- 2. Y. Ji et al., Nature (London) 422, 415 (2003)
- 3. I. Neder, M. Heiblum, Y. Levinson, D. Mahalu, V. Umansky, Phys. Rev. Lett. 96, 016804 (2006)
- P. Roulleau, F. Portier, D.C. Glattli, P. Roche, A. Cavanna, G. Faini, U. Gennser, D. Mailly, Phys. Rev. B 76, 161309 (2007)
- P. Roulleau, F. Portier, D.C. Glattli, P. Roche, A. Cavanna, G. Faini, U. Gennser, D. Mailly, Phys. Rev. Lett. 100, 126802 (2008)
- 6. L.V. Litvin, H.-P. Tranitz, W. Wegscheider, C. Strunk, Phys. Rev. B 75, 033315 (2007)
- L.V. Litvin, A. Helzel, H.-P. Tranitz, W. Wegscheider, C. Strunk, Phys. Rev. B 78, 075303 (2008)
- 8. E. Bieri, Correlation and Interference Experiments with Edge States. Ph.D. Thesis, University of Basel, 2007.
- 9. E. Bieri, M. Weiss, O. Goktas, M. Hauser, C. Schonenberger, S. Oberholzer, Phys. Rev. B 79, 245324 (2009)
- 10. I. Neder, F. Marquardt, M. Heiblum, D. Mahalu, V. Umansky, Nat. Phys. 3, 534 (2007)
- 11. E.V. Sukhorukov, V.V. Cheianov, Phys. Rev. Lett. 99, 156801 (2007)
- 12. J.T. Chalker, Y. Gefen, M.Y. Veillette, Phys. Rev. B 76, 085320 (2007)
- 13. I. Neder, E. Ginossar, Phys. Rev. Lett. **100**, 196806 (2008)
- 14. S.-C. Youn, H.-W. Lee, H.-S. Sim, Phys. Rev. Lett. 100, 196807 (2008)
- 15. I.P. Levkivskyi, E.V. Sukhorukov, Phys. Rev. Lett. 103, 036801 (2009)
- 16. T. Giamarchi, Quantum Physics in One Dimension (Oxford University Press, Oxford, 2003)
- 17. L.S. Levitov, H. Lee, G.B. Lesovik, J. Math. Phys. 37, 4845 (1996)
- 18. I.P. Levkivskyi, E.V. Sukhorukov, Phys. Rev. B **85**, 075309 (2012)
- 19. E.V. Sukhorukov, J. Edwards, Phys. Rev. B 78, 035332 (2008)
- 20. Y.M. Blanter, M. Büttiker, Phys. Rep. 336, 1 (2000)

# **Chapter 5 Energy Relaxation at the Quantum Hall Edge**

On the theoretical side, there are two main points of view on the physics of quantum Hall edge states. One group of theories [1, 2] suggests that at integer values of the Landau levels filling factor the edge excitations are free chiral *fermions*. The second group of theories is based on the concept of the edge magneto-plasmon picture [3–6]. The fundamental edge excitations in these theories are the charged and neutral collective *boson* modes.

The domain where these two approaches meet each other is the *low-energy* effective theory [7–9]. In the framework of this theory, both fermion and boson excitations are two forms of the same entity. Namely, they can be equivalently rewritten in terms of each other:

$$\psi(x,t) \sim \exp[i\phi(x,t)]$$

where  $\psi(x,t)$  is the fermion field, and  $\phi(x,t)$  is the boson field. However, this transformation is highly nonlinear, and in the presence of strong Coulomb interaction fermions are not stable and decay into the boson modes which are the eigenstates of the edge Hamiltonian.

Results of tunneling spectroscopy experiments [10] reasonably agree with the free-electron description of edge states. However, the first experiment on Aharonov-Bohm oscillations of a current through the electronic Mach-Zehnder interferometer [11] has shown that the phase coherence of edge states is strongly suppressed at energies, which are inversely proportional to the interferometer's size. Moreover, several subsequent experiments on Mach-Zehnder interferometers at filling factor  $\nu=2$  have shown puzzling results on finite bias dephasing [12–19] theoretically studied in [20–24]. Namely, the visibility of Aharonov-Bohm oscillations in these experiments is found to have a lobe-type pattern as a function of the applied voltage bias. Such results are difficult to explain in terms of the fermion picture, while they all follow *naturally* from the plasmon physics (see Chap. 3) where the Coulomb

Some text sections in this chapter are reproduced from Phys. Rev. B 85, 075309 (2012), © American Physical Society.

interaction plays a crucial role. Thus the boson picture of edge excitations might be more appropriate.

In contrast to the mentioned above non-local experiments, some local measurements do not seem to be able to differentiate between two physical pictures of edge states. For example, both theories predict Ohmic behavior of the tunneling current, unless it is renormalized by a non-linear dispersion of plasmons (see Appendix A). Moreover, the equilibrium distribution of the bosons is equivalent to the one of fermions (see the demonstration of this fact in Sect. 5.3.3). Therefore, it might be interesting to investigate non-equilibrium local properties of edge states.

## **5.1 Experimental Results**

Non-equilibrium behavior of one-dimensional systems has been a subject of intensive theoretical [25–28] and experimental [29–33] studies for a long time. However, only recently it has become possible to measure an electron distribution  $f(\epsilon)$  as a function of energy  $\epsilon$  with high precision [34]. The main idea of the experimental technique is to restore the function  $f(\epsilon)$  by measuring the differential conductance  $\mathcal G$  of tunneling between two edges through a single level in a quantum dot:

$$\mathcal{G}(\epsilon) \propto \partial f(\epsilon) / \partial \epsilon,$$
 (5.1)

where  $\epsilon$  is the energy of the quantum dot level, controlled by the gate voltage  $V_g$ . This technique has been used in Refs. [34–36] in order to investigate the energy relaxation at quantum Hall edge states at filling factor  $\nu=2$ . The schematics of these experiments is shown in Fig. 5.1. The main result of Refs. [34–36] is that the electron distribution relaxes toward local equilibrium Fermi distribution, and the energy splits equally between the two edge channels.

The first theoretical models based on the fermion picture [37] and on the plasmon approach [38] have come basically to *identical* conclusions. Namely, both works predict equal distribution of the energy between the edge channels, in agreement with the experimental findings. In other words, based on the results of Refs. [37, 38] the experimentalists are not able to discriminate between two alternative descriptions of the physics of quantum Hall edge. Thus, it seems to be important and timely to reanalyze the problem of the energy relaxation at the quantum Hall edge in order to make new, model specific and distinct predictions that can be verified experimentally. This is exactly the purpose of this chapter.

Here we show that the Coulomb interaction strongly affects the spectrum of collective edge excitations and leads to the formation of charged and dipole plasmons modes, which propagate with different velocities. They carry away the energy of electrons injected through the quantum point contact and equally distribute it between edge channels at distances  $L_{\rm ex}$  from the quantum point contact. In addition to this observation, which agrees with findings of previous works [37, 38], we stress that the same process splits the wave packets of injected electrons, and leads to strong

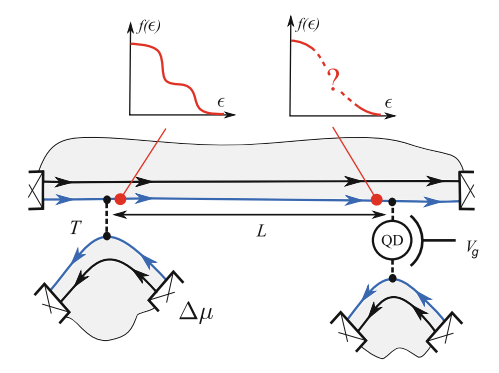


Fig. 5.1 Schematics of the experiments [34–36]. The *shaded region* is filled by the two-dimensional electron gas in the regime of the quantum Hall effect. At filling factor  $\nu=2$  there are two chiral edge states shown by the *blue* (the outer channel) and the *black* (the inner channel) *lines*. The quantum point contact of the transparency T and biased with the voltage difference  $\Delta\mu$ , injects electrons into the outer channel, and thus creates a non-equilibrium electron distribution. After the propagation along the quantum Hall edge, the distribution is detected at distances L from the source with the help of a quantum dot with a single level controlled by the gate voltage  $V_g$ . After Ref. [39].  $\mathbb O$  American Physical Society (Color figure online)

coupling of electrons to the noise of the quantum point contact current. The regime of weak injection, i.e., when the transparency of the quantum point contact is small,  $T\ll 1$ , deserves a special consideration. In this regime the current noise at relevant time scales becomes Markovian, and as a result, the function  $-\partial f(\epsilon)/\partial \epsilon$  acquires a Lorentzian shape (this effect resembles a well known phenomenon of the homogeneous level broadening). Interestingly, the width of the Lorentzian scales as  $T\Delta\mu$  at small T, where  $\Delta\mu$  is the voltage bias applied to a quantum point contact. In contrast, the width of the eventual equilibrium Fermi distribution of thermalized electrons scales as  $\sqrt{T}\Delta\mu$ . If thermalization takes place at longer distances,  $L_{\rm eq}\gg L_{\rm ex}$ , then the intermediate regime described here may be observed in experiment with a weak injection. This would indicate that interactions strongly affects the physics at the edge and that the fermion picture becomes inappropriate.

In order to theoretically describe the experiment [35, 36] and to quantitatively elaborate the physical picture, we use the *non-equilibrium* bosonization technique, which has been introduced in Chap. 2. The main idea of this approach is based on the fact that in a one-dimensional chiral system one can find a non-equilibrium density matrix by solving equations of motion for plasmons with non-trivial boundary conditions. Then, one can rewrite an average over the non-equilibrium state of an interacting system in terms of the full counting statistics [40] generators of the current at the boundary. In the situation considered in this chapter, because of chirality of quantum Hall edge states, interactions do not affect the transport through the quantum point contact alone. This leads to a great simplification, because in the Markovian limit the full counting statistics generator for free electrons is known [40].

The structure of the chapter is following: In Sect. 5.2 we briefly recall the non-equilibrium bosonization technique. Next, we use this technique in Sect. 5.2.1 in order to find the electron correlation function for different distances from the quantum point contact. Finally, we use these results to find the electron distribution function in Sect. 5.3, and present our conclusions in Sect. 5.5. Several important technical steps and the phenomena resulting from the non-linearity of the spectrum of plasmons are described in Appendices A and C.

#### 5.2 Theoretical Model

The relevant energy scales in recent mesoscopic experiments with the quantum Hall edge states [12–19, 34] are very small. Therefore, it is appropriate to use the low-energy effective theory of the quantum Hall edge. One of the advantages of this theory is that it allows to take into account strong Coulomb interactions in a straightforward way [21]. However, an additional complication arises from the fact that in the experiment [34] the injection into one of the two edge channels creates a strongly non-equilibrium state. We, therefore, use the method of non-equilibrium bosonization, proposed in Chap. 2, which is suitable for solving the type of a problem that we face.

According to the low-energy theory of quantum Hall edge, considered in previous chapters, the collective fluctuations of the charge densities  $\rho_{\alpha}(x)$  of the two edge channels,  $\alpha=1,2$ , at filling factor  $\nu=2$  are the only relevant degrees of freedom at low energies. These charge densities may be expressed in terms of the *chiral* boson fields,  $\phi_{\alpha}(x)$ , as  $\rho_{\alpha}(x)=(1/2\pi)\partial_{x}\phi_{\alpha}(x)$ . This fields satisfy the commutation relations  $[\phi_{\alpha}(x),\phi_{\beta}(y)]=i\pi\delta_{\alpha\beta}\mathrm{sgn}(x-y)$ . The vertex operator

$$\psi_{\alpha}(x) = \frac{1}{\sqrt{a}} e^{i\phi_{\alpha}(x)} \tag{5.2}$$

annihilates an electron at point x in the edge channel  $\alpha$ . The constant a in the prefactor is the ultraviolet cutoff, which is not universal and will be omitted and replaced by other normalizations. One can easily check, with the help of the commutation relations, that the operators (5.2) indeed create a local charge of the value 1 at point x, and satisfy fermionic commutation relations.

The edge Hamiltonian has the quadratic form in terms of the boson fields:

$$\mathcal{H} = \frac{1}{8\pi^2} \sum_{\alpha,\beta} V_{\alpha\beta} \int dx \partial_x \phi_{\alpha}(x) \partial_x \phi_{\beta}(x), \tag{5.3}$$

where the kernel contains free fermion contribution as well as the Coulomb interaction potential:

$$V_{\alpha\beta} = 2\pi v_F \delta_{\alpha\beta} + U_{\alpha\beta},\tag{5.4}$$

5.2 Theoretical Model 95

which is assumed to be screened at distances d smaller than the characteristic length scale L in experiments [12–19, 34], i.e.,  $L\gg d$ . Screening may occur due to the presence of either a back gate, or several top gates. Nevertheless, it is very natural to assume that the screening length d is much larger than the distance a between edge channels,  $d\gg a$ , which does not exceed few hundreds nanometers. Therefore, one can write

$$U_{\alpha\beta} = \pi u, \quad u/v_F \sim \log(d/a) \gg 1,$$
 (5.5)

i.e., the in-channel interaction strength is approximately equal to the intra-channel. As a result, the spectrum of collective charge excitations splits into two modes: a fast charged mode with the speed u, and a slow dipole mode with the speed  $v \simeq v_F$  (see the detailed discussion in Sect. 3.2.3).

In the non-equilibrium bosonization prescription, the equations of motion for the fields  $\phi_{\alpha}$ , have to be complemented with boundary conditions  $\partial_t \phi_{\alpha}(0, t) = 2\pi j_{\alpha}(t)$ . The solution for the equations of motion for the boson field has been found in Sect. 4.2 and it is given in our situation by the following expression:

$$\phi_1(x,t) = \pi [Q_1(t_u) + Q_2(t_u) + Q_1(t_v) - Q_2(t_v)], \tag{5.6}$$

where  $Q_{\alpha}(t)=\int_{-\infty}^{t}dt'j_{\alpha}(t')$ ,  $t_{u}=t-x/u$ , and  $t_{v}=t-x/v$ . The physical meaning of this result is rather simple: when charges are injected into the channel  $\alpha=1$  and 2, they excite charged and dipole mode (note the minus sign in the fourth term on the right hand side) which have different propagation speeds u and v. As a result, these charges arrive at the observation point x with different time delays x/u and x/v, and make a contribution to the field  $\phi_1$  at different times.

#### 5.2.1 Correlation Function

The experimentally found [34–36] electron distribution function at the outmost quantum Hall edge channel is given by the expression:

$$f(\epsilon) = \int dt e^{i\epsilon t} \langle \psi_1^{\dagger}(L, t)\psi_1(L, 0) \rangle. \tag{5.7}$$

Rewriting this expression via the boson fields we finally obtain

$$f(\epsilon) \propto \int dt e^{i\epsilon t} K(t), \qquad K(t) \equiv \langle e^{-i\phi_1(L,t)} e^{\phi_1(L,0)} \rangle.$$
 (5.8)

where we have introduced the electron correlation function K, evaluated at coincident points at distance L from the quantum point contact. The proportionality coefficient in (5.8) may be found from the condition that  $f(\epsilon)$  takes a value 1 for energies well below the Fermi level.

When substituting this result into the correlation function in Eq. (5.8) one may use the statistical independence of the current fluctuations at different channels and split the exponential functions accordingly:

$$K(t) = \left\langle e^{-i\pi[Q_1(t_u) + Q_1(t_v)]} e^{i\pi[Q_1(t_u - t) + Q_1(t_v - t)]} \right\rangle \times \left\langle e^{-i\pi[Q_2(t_u) - Q_2(t_v)]} e^{i\pi[Q_2(t_u - t) - Q_2(t_v - t)]} \right\rangle.$$
(5.9)

In the rest of the chapter we will be interested in the correlation function at relatively long distances  $L\gg v\tau_c$ , where  $\tau_c\simeq 1/\Delta\mu$  is the correlation time of fluctuations of the current through a quantum point contact. (We show below that at this length scale the energy exchange between two channels takes place.) In this case, the partitioned charges  $Q_\alpha$ , taken at different times  $t_u$  and  $t_v$ , are approximately not correlated, as illustrated in Fig. 4.2. This assumption is quite intuitive and may be easily checked using Gaussian approximation. We, finally, arrive at the following important result<sup>1</sup>:

$$K(t) = \chi_1^2(-\pi, t)\chi_2(\pi, t)\chi_2(-\pi, t), \tag{5.10}$$

i.e., the electronic correlation function (5.9) may be expressed in terms of the full counting statistics generator:

$$\chi_{\alpha}(\lambda, t) = \langle e^{i\lambda Q_{\alpha}(t)} e^{-i\lambda Q_{\alpha}(0)} \rangle. \tag{5.11}$$

Expression (5.10) presents formally a full solution of the problem of evaluation of an electron correlation function. Generators of the full counting statistics for free electrons in this expression, defined as (5.11), may be represented as a determinant of a single particle operator [40], and eventually, evaluated, e.g., numerically. However, a further analytical progress is possible in a number of situations, which are important for understanding physics of the energy relaxation processes. For example, the electron correlation function may be found analytically away from equilibrium for the case of a Gaussian noise. Interestingly, in the short-time limit,  $t \ll 1/\Delta\mu$ , the main contribution to the correlation function comes from zero-point fluctuations of boundary currents, and it behaves as a free-fermion correlator, i.e., it scales as 1/t. In the long-time limit,  $t \gg 1/\Delta\mu$ , the non-equilibrium zero-frequency noise dominates, and the electron correlation function decays exponentially with time. This is exactly the limit where a non-Gaussian Markovian noise should also be taken into account.

The physical situation that we consider in this chapter corresponds to the strong coupling  $\lambda=\pm\pi$ , implying that the shape of the distribution function may be strongly affected by high-order current cumulants. Nevertheless, it is instructive to first consider Gaussian fluctuations, simply truncating the cumulant expansion at second order in  $\lambda$ . Indeed, on the Gaussian level it is easier to investigate and compare contributions of zero-point fluctuations and of non-equilibrium noise to the electron

<sup>&</sup>lt;sup>1</sup> Note that for  $\nu=1$  the solution of equations of motion for boson field is  $\phi(x,t)=2\pi Q(t-x/u)$  and the correlation function (5.9) is given simply by  $\chi(2\pi,t)$ . The interaction only re-normalize the velocity in this situation, so that the electrons are effectively free and counted with  $\lambda=2\pi$ .

5.2 Theoretical Model 97

correlation function. In this case the correlation function (5.9) may be evaluated exactly. Moreover, we show in the Appendix C, the dispersion of the charged and dipole modes leads to a suppression of higher order cumulants at large distances L, and the noise becomes effectively Gaussian.

For the purpose of further analysis we need the electron correlation function in the long-time limit. The cumulant generating function in this situation has been found in Sect. 4.3:

$$\log[\chi_{\alpha}(\lambda, t)] = \frac{i\lambda}{2\pi} \Delta \mu T_{\alpha} t - \left(\frac{\lambda}{2\pi}\right)^{2} (\log t - \pi R_{\alpha} T_{\alpha} |\Delta \mu t|), \quad \Delta \mu t \gg 1. \quad (5.12)$$

Finally, substituting this result into Eq. (5.10), and setting  $T_1 = T$  and  $T_2 = 1$  according to the situation shown in Fig. 5.1, we obtain the electron correlation function in the long-time limit:

$$K(t) \propto (1/t)e^{-i\Delta\mu Tt - \pi RT\Delta\mu |t|/2}, \quad \Delta\mu t \gg 1.$$
 (5.13)

Note, that the right hand side of Eq. (5.13) contains the quantum contribution in the form of a single pole, as for free fermions, as well as the non-equilibrium contribution in the form of an exponential envelop, those width is determined by the noise power at zero frequency,  $S_1(0) = RT \Delta \mu/2\pi$  (see Fig. 4.3). The phase shift of the correlator is determined by the "average" voltage bias  $\langle \Delta \mu \rangle = \Delta \mu T$  of the incoming stream of electrons, diluted by the quantum point contact. However, we show below that this mean-field like effect of the dilution is strongly modified by a non-Gaussian component of noise.

Next, we consider the situation of non-Gaussian noise. Note, that the quantum ground state part of the current noise,  $S_q$ , that dominates at short times, is pure Gaussian. Therefore, the denominator in Eq. (5.13) remains unchanged. In the long time, Markovian limit, the dominant contribution to the full counting statistics generator comes from the non-equilibrium part of noise, which, e.g., is described by  $S_n$  in Gaussian case. For a quantum point contact, the Markovian full counting statistics generator is given by the well known expression [40] for a Binomial process:

$$\log[\chi_1(\pi, t)] = \frac{\Delta \mu t}{2\pi} \left[ \log|T - R| - i\pi\theta(T - R) \right]. \tag{5.14}$$

Substituting this expression to the correlation function (5.10), we arrive at the result

$$K(t) \propto (1/t)e^{-i\theta(T-R)\Delta\mu t + \log|T-R|\Delta\mu|t|/\pi}$$
(5.15)

where the imaginary part of the exponent determines the effective voltage bias, while the real part is responsible for dephasing.

Interestingly, at the point T=1/2 the dephasing rate is divergent, and the effective voltage bias drops to zero abruptly for T<1/2. It has been predicted in Chap. 4 that this behavior may lead to a phase transition in the visibility of Aharonov-Bohm

oscillations in electronic Mach-Zehnder interferometers. We will argue below that no sharp transition arises in the electron distribution function. However, it leads to its strong asymmetry with respect to the average voltage bias  $\langle \Delta \mu \rangle = T \Delta \mu$  of the outer channel.

#### **5.3 Electron Distribution Function**

In this section we use the results (2.52), (5.13) and (5.15) for correlation function of electrons to evaluate and analyze the electronic distribution function. We start by noting that the experiments [34–36] are done in a particular regime of strong partitioning  $T \approx 0.5$  at the quantum point contact injecting current to the channel  $\alpha = 1$ . This detail, which seem to be irrelevant from the first glance, is in fact of crucial importance. Indeed, as it follows from the expressions (5.13) and (5.15), the main contribution to the integral in Eq. (5.8) for the correlation function comes from times t of the order of the correlation time  $\tau_c \simeq 1/\Delta\mu$ , where our results based on the Markovian noise approximation are not valid. However, the numerical calculations show that the non-equilibrium distribution in this regime is very close to the equilibrium one. Therefore, the equilibration of electrons, which is reported in the experiment [34] to occur at distances  $v/\Delta\mu$ , may in fact take place at even longer distances  $L_{\rm eq} \gg v/\Delta\mu$  due to an unknown mechanism not considered here.

Indeed, if the chiral Luttinger liquid model of quantum Hall edge states is valid, then neither the strong interaction between electrons of two edges taken alone, nor the weak dispersion of plasmons resulting from a long-range character of Coulomb interaction may lead to the equilibration, because the systems remain integrable. Thus it seems to be reasonable to assume that the equilibration length  $L_{eq}$  may indeed be quite long. Therefore, in order to explore the physics of collective charge excitations at intermediate distances we propose to consider a regime of weak injection at the quantum point contact:  $T \ll 1$ . Firstly, we note that in this case our results (5.13) and (5.15) may indeed be used to evaluate the electron distribution function, because the main contribution to the integral in Eq. (5.8) arises from Markovian time scales. Secondly, and more importantly, in this regime the electron distribution function acquires a strongly non-equilibrium form and the width of the order of  $T \Delta \mu$ , which plays a role of the new energy scale. Moreover, the advantage of the weak injection regime is that it allows to investigate a non-trivial evolution of the distribution function, which arises due to bosonic, collective character of excitations and goes via several well distinguishable steps.

#### 5.3.1 Short Distances

At distances of the order of the energy exchange length scale

$$L_{\rm ex} \equiv v/\Delta\mu \tag{5.16}$$

the initial double step distribution function is strongly perturbed by the interaction between channels. As we argued in Sect. 4.2, at distances  $L \gg L_{\rm ex}$  the charged and dipole modes split and make independent contributions to the electron correlation function. Therefore, we may rely on the result (5.15). Applying the limit  $T \ll 1$  to this expression and evaluating the Fourier transform, we find:

$$-\frac{\partial f(\epsilon)}{\partial \epsilon} = \frac{\Gamma_{\rm ng}/\pi}{\epsilon^2 + \Gamma_{\rm ng}^2}, \quad \Gamma_{\rm ng} = 2T \Delta \mu/\pi. \tag{5.17}$$

Here, the missing prefactor in the correlation function has been fixed by the requirement that  $f(\epsilon)=1$  at  $\epsilon\to-\infty$ . Thus, we conclude that energy derivative of the distribution function acquires a narrow Lorentzian peak, which is shifted with respect to the average bias  $\langle \Delta \mu \rangle = T \Delta \mu$  and centered at  $\epsilon=0$ . The last effect is a unique signature of the non-Gaussian character of noise. Because of the electron-hole symmetry of the Binomial process, in the limit  $R\ll 1$  the Lorentzian peak obviously has a width  $\Gamma_{\rm ng}=2R\Delta\mu/\pi$  and centered at  $\epsilon=\Delta\mu$ .

We stress again, that the result (5.17) holds only for small enough energies close to the Fermi level, namely, for  $|\epsilon| \lesssim \Delta \mu$ , where the main contribution arises from the noise in Markovian limit. In fact, the result (5.17) fails at large energies in somewhat non-trivial way. Namely, it is easy to see that any electron distribution function has to satisfy the sum rule

$$\langle \Delta \mu \rangle \equiv \epsilon_0 + \int_{\epsilon_0}^{\infty} d\epsilon \, f(\epsilon) = -\int_{-\infty}^{\infty} d\epsilon \, \epsilon \, \partial f(\epsilon) / \partial \epsilon, \tag{5.18}$$

where  $\epsilon_0$  is the cutoff well below the Fermi level, and the "average" bias  $\langle \Delta \mu \rangle = T \, \Delta \mu$  in the case of linear dispersion of plasmons. This sum rule simply expresses the requirement of the conservation of the charge current and implies certain amount of asymmetry in the distribution function. In the present case, such an asymmetry arises in the power-law tails of the function  $-\partial f(\epsilon)/\partial \epsilon$  and originates from quantum non-equilibrium noise. It can be seen in Fig. 5.2, where the results of numerical calculations are shown.

Moreover, at energies of the order of  $\Delta\mu$  the power-law behavior of the function (5.17) has to have a cut-off, because the quantum point contact does not provide energy much larger than the voltage bias. Quantitatively, this follows from the conservation of the energy. We demonstrate below that for the system with linear dispersion of plasmons, the heat flux in the outer channel can be written entirely in terms of the single-electron distribution function (in unites  $e=\hbar=1$ ),

$$I_{\rm m} = (1/2\pi) \int d\epsilon \, \epsilon \, [f(\epsilon) - \theta(\langle \Delta \mu \rangle - \epsilon)], \tag{5.19}$$

as in the case of free electrons. We use the subscript m in order to emphasize the fact that it is this quantity that has been measured in the experiment [35, 36]. In Sect. 5.4 we show that at distances  $L \gg L_{\rm ex}$  the total heat flux injected at a quantum point contact splits equally between two edge channels, therefore integrating Eq. (5.19) by parts and substituting the heat flux for a double-step distribution, we obtain

$$I_{\rm m} = -\frac{(T\Delta\mu)^2}{4\pi} - \frac{1}{4\pi} \int d\epsilon \, \epsilon^2 \frac{\partial f(\epsilon)}{\partial \epsilon} = \frac{TR(\Delta\mu)^2}{8\pi}$$
 (5.20)

for  $L\gg L_{\rm ex}$ . One can see from Eq. (5.17) that indeed the power-law behavior has to have a cut-off at  $|\epsilon|\sim\Delta\mu$ . We stress, however, that this summation rule is less universal than the one given by Eq. (5.18), because it accounts only a single-particle energy of electrons and fails in the case of a non-linear spectrum of plasmons, considered in Sect. 5.4 in detail.

#### 5.3.2 Intermediate Distances

So far we have considered the case of a linear spectrum of plasmons. This is a reasonable assumption, taking into account the fact that non-linear corrections in the spectrum of plasmons lead to a nonlinear corrections in the Ohmic conductance of a quantum point contact. However, the experiments [34–36] seem to be done in the Ohmic regime. Nevertheless, even in the case of a weak dispersion in the spectrum of the both modes of the sort<sup>2</sup>

$$k_i(\omega) = \omega/v_i + \gamma_i \omega^2 \operatorname{sign}(\omega), \quad j = 1, 2,$$
 (5.21)

barely seen in the conductance of a quantum point contact, an intermediate length scale  $L_{\rm g}$  may arise at which high-order cumulants of current are suppressed, and the noise becomes effectively Gaussian. This situation occurs when the wave packets of the original width  $v/(T\Delta\mu)$  overlap. A simple estimate using the nonlinear correction (5.21) gives the length scale

$$L_{\rm g} = 1/\gamma (T\Delta\mu)^2, \quad \gamma \equiv \min(\gamma_i).$$
 (5.22)

We support this conclusion by rigorous calculations in Appendix C.

The dispersion is weak, if  $\gamma v T \Delta \mu \ll 1$ . This implies that  $L_{\rm g} \gg L_{\rm ex}$ , and leads to the possibility to observe non-Gaussian effects at distances  $L_{\rm ex} \ll L \ll L_{\rm g}$ , discussed in the previous section. Obviously, the same requirement also guarantees

<sup>&</sup>lt;sup>2</sup> Note that it is *not* possible to observe the non-Gaussian regime for  $\nu=1$ . This is because the Markovian contribution is zero in this case, i.e.  $\log(R+Te^{i\lambda})=0$  for the value  $\lambda=2\pi$  which is realized in this case (see footnote 1). This means that the double step function will propagate until the distances (5.22) at which the higher order cumulants starts to get suppressed.

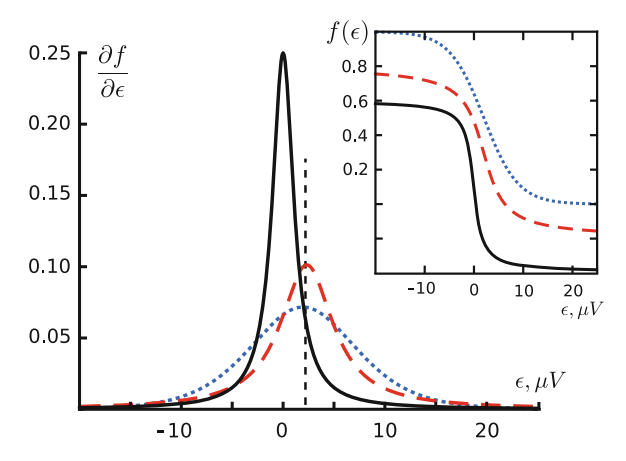


Fig. 5.2 Energy derivative of the electron distribution function,  $-\partial f/\partial \epsilon$ , is shown for different distances L from the quantum point contact injecting current. The transparency of the quantum point contact is set to T=0.05 and voltage bias is  $\Delta\mu=40\,\mu V$ . Black, solid line is  $-\partial f(\epsilon)/\partial \epsilon$  for short distances  $L_{\rm ex}\ll L\ll L_{\rm g}$ , so that the noise is non-Gaussian (5.17). Red, dashed line is  $-\partial f(\epsilon)/\partial \epsilon$  for intermediate distances  $L_{\rm g}\ll L\ll L_{\rm eq}$ , where the noise is Gaussian (5.23). Blue, dotted line is the derivative of the Fermi distribution function at the temperature given by Eq. (5.26). The vertical dashed line is a guide for eyes at the energy equal to the effective voltage bias  $\langle \Delta \mu \rangle = T\Delta \mu = 2\,\mu V$ . Inset shows the same distribution functions in the integrated form. They are shifted vertically by 0.2 intervals for clarity. After Ref. [39]. © American Physical Society (Color figure online)

that dispersion corrections to the Ohmic conductance of a quantum point contact are small. This allows us to neglect corrections to the quantum part of the electron correlation function and to use the result (5.13) for a Gaussian noise. Substituting this result to the equation (5.8), we obtain

$$-\frac{\partial f(\epsilon)}{\partial \epsilon} = \frac{\Gamma_{\rm ng}/\pi}{(\epsilon - \langle \Delta \mu \rangle)^2 + \Gamma_{\rm g}^2}, \quad \Gamma_{\rm g} = \pi T \Delta \mu/2. \tag{5.23}$$

in the case  $L_{\rm g} \ll L \ll L_{\rm eq}$ . One can see, that the width of the function (5.23) is almost twice as large compared to the one the function (5.17). Moreover, the function (5.23) satisfies the sum rule (5.18). Therefore, we do not expect any asymmetry in the high-energy tails of this function, in contrast to the situation with the non-Gaussian noise. The comparison of distribution functions in these two regimes is shown in Fig. 5.2.

So far we have considered a situation where both charged and dipole mode are dispersive. If for some reason the dispersion of one of the modes is negligible, then higher order cumulants are suppressed only by a factor of two. The derivative of the electron distribution function in this situation is given by the Lorentzian

$$\frac{\partial f(\epsilon)}{\partial \epsilon} = \frac{(\Gamma_{\text{ng}} + \Gamma_{\text{g}})/2\pi}{(\epsilon - \langle \Delta \mu \rangle/2)^2 + (\Gamma_{\text{ng}} + \Gamma_{\text{g}})^2/4}$$
 (5.24)

centered at  $\langle \Delta \mu \rangle/2 = \Delta \mu T/2$  with the width  $(\Gamma_{ng} + \Gamma_g)/2 = (1/\pi + \pi/4)\Delta \mu T$ . This is because one mode brings only Gaussian component of the Markovian noise, while the other one brings full non-Gaussian noise.

# 5.3.3 Long Distances

Next, we consider the distribution function at long distances,  $L \gg L_{\rm eq}$ , after the equilibration takes place. The temperature of the eventual equilibrium distribution may be found from the conservation of energy. In the next section we show that the heat flux produced at the quantum point contact splits equally between two edge states. In the situation of linear dispersion the distribution function acquires the form

$$f(\epsilon) = \frac{1}{1 + e^{(\epsilon - \langle \Delta \mu \rangle)/\Gamma_{\text{eq}}}}.$$
 (5.25)

The possibility of such equilibration process is suggested by the fact that the equilibrium distribution of bosons implies the equilibrium distribution for electrons, as has been shown in Sect. 2.3.2. Obviously, the distribution (5.25) satisfies the sum rule (5.18), while the energy conservation condition (5.20) may now be used in order to find the effective temperature:

$$\Gamma_{\rm eq} = \sqrt{3T/2\pi^2} \Delta \mu,\tag{5.26}$$

where we have used  $T \ll 1$ .

We conclude that the width of the equilibrium distribution scales as  $\sqrt{T}$ , in contrast to the case of a non-equilibrium distribution at shorter distances from the current source, where it scales linearly in T. Therefore, if T is small, an equilibrium and non-equilibrium distributions may easily be distinguished, as illustrated in Fig. 5.2. In the situation where the dispersion can not be neglected, the equilibrium distribution of fermions is not given by the Fermi function (5.25), see Appendix A. This situation deserves a separate consideration, which is provided in the next section.

#### 5.4 Measured and Total Heat Fluxes

We have seen that in the case of weakly dispersive plasmons,  $\gamma v T \Delta \mu \ll 1$ , the nonlinearity in the spectrum leads to the suppression of high-order cumulants of current noise at relatively long distances, which strongly affects the distribution function. On the other hand, the direct contribution of the non-linear correction in the spectrum

to local physical quantities, such as the quantum point contact conductance and the heat flux, is small and has been so far neglected. Nevertheless, it may manifest itself experimentally in a quite remarkable way. In this section we show that the weak dispersion in the plasmon spectrum contributes differently to the measured heat flux (5.19) and to the actual heat flux expected from the simple evaluation of the Joule heat. As we demonstrate below this may, under certain circumstances, explain the missing energy paradox in the experiment [35, 36].

We start by noting that the measured flux (5.19) at the distance L form the quantum point contact may be expressed entirely in terms of the excess noise spectrum  $\mathbb{S}_{\alpha}(\omega) \equiv S_{\alpha}(\omega) - (1/2\pi)\omega\theta(\omega)$  of edge channels right after the quantum point contact, where  $S_{\alpha}(\omega)$  is defined in (4.16). Namely, in Appendix B we derive the following result:

$$I_{\rm m}(L) = \frac{1}{4} \int_{-\infty}^{\infty} d\omega \{ \mathbb{S}_1(\omega)[1 + \cos(\Delta k L)] + \mathbb{S}_2(\omega)[1 - \cos(\Delta k L)] \}, \qquad (5.27)$$

where  $\Delta k \equiv k_1(\omega) - k_2(\omega)$ , and  $k_j(-\omega) = -k_j(\omega)$ . Importantly, this result holds for an arbitrary non-linear spectrum  $k_j(\omega)$  of the charged and dipole modes, and for a non-Gaussian noise in general, i.e., high-order cumulants simply do not contribute.

One can easily find two important limits of Eq. (5.27): for L=0 we immediately obtain an expected result

$$I_{\rm m}(0) = \frac{1}{2} \int_{-\infty}^{\infty} d\omega \, \mathbb{S}_1(\omega), \tag{5.28}$$

while at  $L \to \infty$  the cosine in (5.27) acquires fast oscillations, and we get

$$I_{\rm m}(\infty) = \frac{1}{4} \int_{-\infty}^{\infty} d\omega [\mathbb{S}_1(\omega) + \mathbb{S}_2(\omega)]. \tag{5.29}$$

To be more precise, this happens at  $L \gg L_{\rm ex} = v/\Delta\mu$ . At zero temperature  $\mathbb{S}_2$  vanishes, and the single-electron heat flux  $I_{\rm m}$ , created at the quantum point contact, splits equally between edge channels:  $I_{\rm m}(\infty) = I_{\rm m}(0)/2$ . Note also, that in the case of linear dispersion  $\mathbb{S}_{\alpha} = T_{\alpha}R_{\alpha}S_{\rm n}$ , where  $S_{\rm n}$  is shown in Fig. 4.3.

In the next step, we rewrite the same measured flux in terms of the plasmon distributions  $n_j(k) = \langle \tilde{a}_j^{\dagger}(k)\tilde{a}_j(k)\rangle$ , see Appendix B:

$$I_{\rm m}(\infty) = \frac{1}{4\pi} \sum_{j} \int \frac{dk}{k} \,\omega_j^2(k) n_j(k) + I_{\rm q},$$
 (5.30)

$$I_{q} = \frac{1}{8\pi} \sum_{i} \int \frac{dk}{k} [\omega_{j}^{2}(k) - (v_{j}k)^{2}], \qquad (5.31)$$

where  $v_j = \partial \omega_j / \partial k$  are the plasmon speeds at k=0. The term  $I_q$  is the contribution to the measured flux from quantum smearing of the zero-temperature electron distribution function  $f_0(\epsilon)$  close to the Fermi level, which originates from a non-linear dispersion of plasmons.

Here an important remark is in order. The integral (5.31) may diverge at large k and has to be cut off at the upper limit. This is because there is no guarantee of the free-fermionic behavior of the correlator K(t) at short times and of the zero-temperature electron distribution function  $f_0(\epsilon)$  at large energies. Thus, the integral (5.19) has to be also cut off, which is what in fact is done in experiment. In contrast, the spectrum of plasmons is linear at small k, and thus the distribution function  $f_0(\epsilon)$  has a free-fermionic behavior close to the Fermi level. Our definition of  $I_q$  corresponds to the normalization of  $f_0(\epsilon)$  to have a discontinuity of the value -1 at  $\epsilon = \langle \Delta \mu \rangle$ . The experimentally measured  $I_q$  may differ from the one defined in (5.31) by a constant, which is, on the other hand, independent on the voltage bias  $\Delta \mu$ .

Next, we note that the actual total heat flux in the case of a non-linear dispersion of plasmons acquires the completely different form<sup>3</sup>

$$I_{\rm h} = \frac{1}{2\pi} \sum_{i} \int dk \frac{\partial \omega_{j}}{\partial k} \omega_{j}(k) \, n_{j}(k), \tag{5.32}$$

and thus in general  $I_{\rm m} \neq I_{\rm h}/2$ , contrary to what has been assumed in the experiment [35, 36]. This may explain the missing energy paradox. Indeed, assuming the low  $\omega$  spectrum of the general form

$$k_j = \omega/v_j + \gamma_j \omega^{\ell_j}, \quad j = 1, 2, \tag{5.33}$$

where  $\gamma_j$  are small, and equilibration of plasmons at  $L \to \infty$ , i.e.,  $n_j(k) = n_B(\epsilon/\Gamma_{\rm eq}) = 1/[\exp(\epsilon/\Gamma_{\rm eq}) - 1]$ , we obtain the missing heat flux as

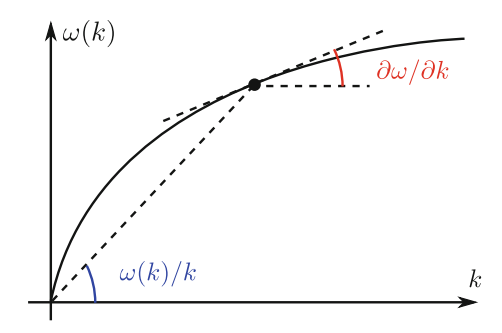
$$I_{\rm m} - I_{\rm q} - I_{\rm h}/2 = \sum_{j=1,2} c_j \gamma_j v_j \Gamma_{\rm eq}^{\ell_j + 1},$$
 (5.34)

where the constants  $c_j = (1/4\pi) \int dz z^{\ell_j+1} n_B(z)$  are of the order of 1. This result implies that experimentally, the missing heat flux may be found investigating its bias dependence and the spectrum of plasmons.

Let us consider an example where the dispersion of charged plasmon at small k arises from the screened Coulomb interaction [3]:

<sup>&</sup>lt;sup>3</sup> We note, that in general the heat flux cannot be associated with the conserved Noether current, because the Hamiltonian (3.2.1) is not local. Nevertheless, the continuity equation for the heat flux  $I_h$ , given by (5.32), may be derived in the semi-classical limit  $kv < \Delta \mu$ , which is of interest here. Moreover, one can show that for any interaction matrix (5.4) the energy flux of zero modes of plasmons does not contribute to the total heat flux, if it is defined as the Joule heat created at the quantum point contact.

Fig. 5.3 Typical spectrum of charged plasmon in the case of the Coulomb interaction screened at distances  $d \ll 1/k$ . This spectrum is concave, therefore  $\partial \omega/\partial k < \omega(k)/k$ . After Ref. [39]. © American Physical Society



$$\omega/k = 2[\mathcal{K}_0(ka) - \mathcal{K}_0(kd)] = 2\ln(d/a) - (1/2)(kd)^2\ln(2/kd), \tag{5.35}$$

where a is the high-energy cutoff, d is the distance to the gate, such as  $ka \ll kd \ll 1$ , and  $\mathcal{K}_0$  is the MacDonald function. The low-k asymptotics of this spectrum is illustrated in Fig. 5.3. One can see that the spectrum is concave, so that in this case the measured heat flux (5.30) is larger than the half of the actual heat flux (5.32). In addition, the effect is weak, because  $kd \sim 0.1$  in the experiment [35, 36]. Thus, the dispersion of the Coulomb interaction potential alone is not able to explain the missing flux paradox. Various mechanisms of convex dispersion are still possible and will be investigated elsewhere.

#### 5.5 Conclusions

Earlier theoretical works on quantum Hall edge states may be divided into two groups: fermion based theories and the boson based theories. Recent interference experiments suggest that the boson approach might be more appropriate for the description of the edge physics. However, both groups of theories give the same predictions for the local physical quantities at equilibrium. Moreover, the first theoretical works based on fermion [37] and boson [38] approaches and addressing the non-equilibrium local measurements, have not been able to make qualitatively distinct predictions. In this chapter we show that it is nevertheless *possible* to test and differentiate between two approaches with the local non-equilibrium measurements.

We address recent experiments [35, 36] with quantum Hall edge states at filling factor 2, where an energy relaxation process has been investigated by creating a non-equilibrium state at the edge with the help of a quantum point contact and reading out the electron distribution downstream using a quantum dot. We use the non-equilibrium bosonization approach [41] in order to describe the gradual relaxation of initially non-equilibrium, double-step electron distribution to its equilibrium form. In the framework of this approach the non-equilibrium initial state is encoded in the boundary conditions for the equations of motions that depend on interactions. We show that the electrons split in two plasmons: fast charged and slow dipole mode. Thus

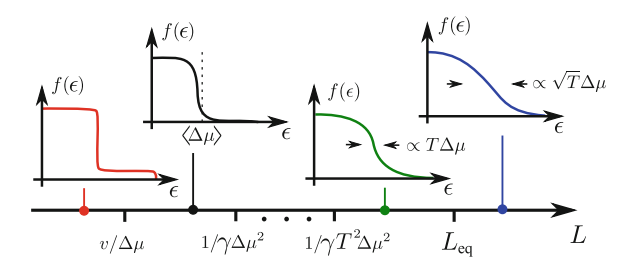


Fig. 5.4 Different length scales for energy relaxation processes and corresponding distribution functions in each regime are schematically shown. *Red*, *first curve*: The initial double-step distribution function. *Black*, *second curve*: At distances  $L \gg \Delta \mu/v$  the distribution function is strongly asymmetric with respect to the "average" bias  $\langle \Delta \mu \rangle = T \Delta \mu$ . *Green*, *third curve*: At distances  $L \gg 1/\gamma T^2 \Delta \mu^2$  the distribution function is a Lorentzian with the width that scales as  $T \Delta \mu$ . *Blue*, *fourth curve*: The final equilibrium Fermi function at large distances. For small transparencies its width scales as  $\sqrt{T} \Delta \mu$ . After Ref. [39]. © American Physical Society (Color figure online)

the electron correlation function (5.10) is expressed in terms of the four contributions, each having form of the generator of full counting statistics of free electrons with the coupling constant  $\lambda = \pi$ . Evaluating the Fourier transform of this function, we find the energy distribution function.

Before reaching eventual equilibrium form, the distribution function evolves via several steps, and its energy derivative acquires a Lorentzian shape:

$$\frac{\partial f(\epsilon)}{\partial \epsilon} = \frac{\Gamma/\pi}{(\epsilon - \epsilon_0)^2 + \Gamma^2}, \quad |\epsilon| \lesssim \Delta \mu, \tag{5.36}$$

where values of the width  $\Gamma$  and centering  $\epsilon_0$  are different in corresponding regimes. Each of the regimes, summarized below and illustrated in Fig. 5.4, has its own dominant processes:

- (i) First, after tunneling through the quantum point contact, electrons excite plasmons, which then split in two eigenmodes: one is charged fast mode with the speed u, and the other is slow dipole mode with the speed v. This process takes place at distances  $L_{\rm ex} = v/\Delta\mu$ , where  $\Delta\mu$  is the voltage bias across the quantum point contact. In this regime Eq. (5.10) applies, which eventually leads to the distribution (5.36) with the width  $\Gamma = \Gamma_{\rm ng} = 2\Delta\mu T/\pi$  centered at  $\epsilon_0 = 0$ .
- (ii) Next, a weak dispersion of plasmons, e.g., of the form  $k=\omega/v+\gamma\omega^2\mathrm{sign}(\omega)$ , leads to broadening of wave-packets of the energy width  $\epsilon$  and to their overlap. This process takes place at distances  $L\gg 1/\gamma\epsilon^2$ . As a result, high-order cumulants of the current injected at the quantum point contact are suppressed at distances  $L\gg L_{\rm g}=1/\gamma(T\Delta\mu)^2$ , the noise becomes Gaussian, and the derivative of the electron distribution function acquires the shape (5.36) with the width  $\Gamma=\Gamma_{\rm g}=\pi\Delta\mu T/2$ , centered at  $\epsilon_0=\Delta\mu T$ .
- (iii) A situation is possible, where the dispersion of one mode, most likely of the charged mode, is much stronger than the dispersion of the second mode, i.e.,  $\gamma_u \gg \gamma_v$ .

5.5 Conclusions 107

In this case, the previously described regime splits in two separate regimes. First, at distances  $L=1/\gamma_u(T\Delta\mu)^2$  the contribution of the charged mode to high-order cumulants of noise become suppressed, which leads to the distribution (5.36) with the parameters  $\Gamma=(\Gamma_{\rm ng}+\Gamma_{\rm g})/2$  and  $\epsilon_0=\Delta\mu T/2$ . Then, at longer distances  $L=1/\gamma_v(T\Delta\mu)^2$  the noise becomes fully Gaussian.

(iv) The interaction may lead to broadening of the wave-packets, but they do not decay, which implies that the interaction alone does not lead to the equilibration. This means that a different, weaker process may lead to the equilibration at distances  $L_{\rm eq}$  much longer than the discussed above length scales. In the tunneling regime,  $T\ll 1$  the width of the eventual equilibrium distribution scales as  $\sqrt{T}$ , in contrast to the above regimes, where it scales as T. Thus, to observe the described variety of regimes, we propose to perform measurements at large voltage biases and low transparencies of the quantum point contact utilized to inject electrons.

Finally, we suggest a possible explanation of the paradox of missing heat flux in the experiment [35, 36]. So far we have discussed the effects of weak dispersion. We have found that in the case of a strong dispersion of plasmons, the measured heat flux in the outmost edge channel, experimentally determined with the procedure described by Eq. (5.19), is different from the actual heat flux per channel, defined by Eq. (5.32). The screened Coulomb interaction leads to a rather weak dispersion of the charged plasmon, and the effect is of the opposite sign, because the spectrum in this case is concave. Nevertheless, other mechanisms of the convex dispersion are possible. They will be considered elsewhere.

### References

- 1. B.I. Halperin, Phys. Rev. B 25, 2185 (1982)
- 2. See M. Büttiker, Phys. Rev. B 38, 9375 (1988) and references therein
- 3. V.A. Volkov, S.A. Mikhailov. Sov. Phys. JETP 67, 1639 (1988)
- 4. D.B. Chklovskii, B.I. Shklovskii, L.I. Glaz-man, Phys. Rev. B 46, 4026 (1992)
- 5. I.L. Aleiner, L.I. Glazman, Phys. Rev. Lett. 72, 2935 (1994)
- 6. See C.d.C. Chamon, X.G. Wen, Phys. Rev. B 49, 8227 (1994) and references therein
- 7. X.-G. Wen, Phys. Rev. B 41, 12838 (1990)
- 8. J. Fröhlich, A. Zee, Nucl. Phys. B 364, 517 (1991)
- 9. J. Fröhlich, T. Kerler, Nucl. Phys. B 354, 369 (1991)
- 10. For a review, see A.M. Chang, Rev. Mod. Phys. 75, 1449 (2003)
- 11. Y. Ji et al., Nature (London) **422**, 415 (2003)
- 12. I. Neder, M. Heiblum, Y. Levinson, D. Mahalu, V. Umansky, Phys. Rev. Lett. 96, 016804 (2006)
- P. Roulleau, F. Portier, D.C. Glattli, P. Roche, A. Cavanna, G. Faini, U. Gennser, D. Mailly, Phys. Rev. B 76, 161309 (2007)
- P. Roulleau, F. Portier, D.C. Glattli, P. Roche, A. Cavanna, G. Faini, U. Gennser, D. Mailly, Phys. Rev. Lett. 100, 126802 (2008)
- 15. L.V. Litvin, H.-P. Tranitz, W. Wegscheider, C. Strunk, Phys. Rev. B 75, 033315 (2007)
- L.V. Litvin, A. Helzel, H.-P. Tranitz, W. Wegscheider, C. Strunk, Phys. Rev. B 78, 075303 (2008)
- E. Bieri, Correlation and Interference Experiments with Edge States. Ph.D. Thesis, University of Basel, 2007

- E. Bieri, M. Weiss, O. Goktas, M. Hauser, C. Schonenberger, S. Oberholzer, Phys. Rev. B 79, 245324 (2009)
- 19. I. Neder, F. Marquardt, M. Heiblum, D. Mahalu, V. Umansky, Nat. Phys. 3, 534 (2007)
- 20. E.V. Sukhorukov, V.V. Cheianov, Phys. Rev. Lett. 99, 156801 (2007)
- 21. I.P. Levkivskyi, E.V. Sukhorukov, Phys. Rev. B 78, 045322 (2008)
- 22. I. Neder, E. Ginossar, Phys. Rev. Lett. 100, 196806 (2008)
- 23. S.-C. Youn, H.-W. Lee, H.-S. Sim, Phys. Rev. Lett. 100, 196807 (2008)
- 24. J.T. Chalker, Y. Gefen, M.Y. Veillette, Phys. Rev. B 76, 085320 (2007)
- 25. C.L. Kane, M.P.A. Fisher, Phys. Rev. B 52, 17393 (1995)
- 26. V.V. Ponomarenko, D.V. Averin, Phys. Rev. B 67, 035314 (2003)
- 27. D.B. Gutman, Y. Gefen, A.D. Mirlin, Eur. Phys. Lett. 90, 37003 (2010)
- 28. D.L. Kovrizhin, J.T. Chalker, Phys. Rev. B 84, 085105 (2011)
- 29. M. Heiblum, M.I. Nathan, D.C. Thomas, C.M. Knoedler, Phys. Rev. Lett. 55, 2200 (1985)
- L.P. Kouwenhoven, B.J. van Wees, N.C. der Vaart, C.J.P.M. Harmans, C.E. Timmering, C.T. Foxon, Phys. Rev. Lett. 64, 685 (1990)
- 31. G. Granger, J.P. Eisenstein, J.L. Reno, Phys. Rev. Lett. **102**, 086803 (2009)
- 32. H. Pothier, S. Guéron, N.O. Birge, D. Esteve, M.H. Devoret, Phys. Rev. Lett. 79, 3490 (1997)
- 33. A. Anthore, F. Pierre, H. Pothier, D. Esteve, Phys. Rev. Lett. 90, 076806 (2003)
- 34. C. Altimiras, Nat. Phys. 6, 34 (2010)
- 35. H. le Sueur et al., Phys. Rev. Lett. 105, 056803 (2010)
- 36. C. Altimiras et al., Phys. Rev. Lett. **105**, 226804 (2010)
- 37. A.M. Lunde, S.E. Nigg, M. Buttiker, Phys. Rev. B 81, 041311 (2010)
- 38. P. Degiovanni et al., Phys. Rev. B 81, 121302 (2010)
- 39. I.P. Levkivskyi, E.V. Sukhorukov, Phys. Rev. B 85, 075309 (2012)
- 40. L.S. Levitov, H. Lee, G.B. Lesovik, J. Math. Phys. 37, 4845 (1996)
- 41. I.P. Levkivskyi, E.V. Sukhorukov, Phys. Rev. Lett. 103, 036801 (2009)

# Part II Fractional Quantum Hall Effect

# **Chapter 6 Classification of Effective Edge Models**

In previous chapters, we have shown that the *bosonic* description of the integer quantum Hall effect is the most natural one. Moreover, we have seen that the presence of plasmon edge modes with different velocities,  $v_i$ , is crucial for the explanation of some experiments. Namely, the separation of spectrum on fast and slow mode, and the specific values of the mixing matrix between eigenmodes and electron modes lead to a number of universalities at the mesoscopic scale. Therefore, we think that the presence of edge modes with different velocities may be also important in the case of fractional filling factors. In order to investigate this question, we use the effective theory approach introduced in Sect. 1.3.2.

We note that in contrast to prime filling factors, minimal physical requirements that an effective model of a quantum Hall edge has to satisfy do not fix a model uniquely in the case of complex filling fractions. There were some attempts to classify allowed effective models of a quantum Hall edge [1, 2]. These works, in our opinion, do not devote necessary attention to the case of edge modes with different velocities. In this chapter, we propose a classification of edge models, based on the idea that all eigenmodes of the edge Hamiltonian are chiral collective bosonic charge excitations. The spectrum of local quasi-particles in such models is described with the help of the mixing matrix between the bosons and local quasi-particles.

We start our construction with the formulation of main physical requirements to a quantum Hall edge model. Next, we consider a simple hydrodynamic model which satisfies all these conditions. In Sect. 6.2 we generalize our analysis to multichannel models. Finally, in Sects. 6.2.2 and 6.2.3 we investigate the properties of local excitations in different edge models.

Some text sections in this chapter are reproduced from Phys. Rev. B 80, 045319 (2009), © American Physical Society.

# 6.1 Effective Theory of Quantum Hall Edges

The effective theory presented in this section provides a description of the low-energy physics of a quantum Hall edge. While the correct model of edge states may depend on microscopic details of a two-dimensional electron gas, there are general physical requirements that greatly reduce the number of relevant models [3–5]. These requirements are as follow:

- Cancellation of anomaly. It is well known that the Chern–Simons theory of an incompressible quantum Hall state is anomalous, i.e., in the presence of a boundary, its gauge variation is given by a non-vanishing boundary term. The effective model of edge states has to be chosen in such a way as to cancel the anomaly of the bulk action in order for the complete theory to be gauge invariant.
- Existence of an electron operator. A two-dimensional electron gas consists of electrons. Thus, on a microscopic level, the quantum Hall state is described by an electron wave function. This implies that, in the effective edge theory, there should exist at least one local operator describing the creation or annihilation of an electron or hole, i.e., with a charge *e* and Fermi statistics.
- Single-valuedness in the electron positions. Similarly, because the quantum Hall state describes electrons, its wave function must be single-valued in the electron positions, irrespective of whether quasi-particles are present. As a consequence, in the effective theory the mutual statistical phase of a quasi-particle and an electron must be an integer multiple of  $\pi$ . <sup>1</sup>

Below we use these requirements to construct the most simple effective models of quantum Hall edge states and to classify various multi-field models in Sect. 6.2.

# 6.1.1 Chern-Simons Theory and Gauge Anomaly

First of all, in an incompressible quantum Hall fluid the electric current density, **j**, in the bulk of the system [8] is related to the electromagnetic potential **A** by Hall's law

$$j^{\mu} = \sigma_H \epsilon^{\mu\nu\lambda} \partial_{\nu} A_{\lambda}, \tag{6.1}$$

where the constant  $\sigma_H = \nu/2\pi$  is the Hall conductivity and the rational number  $\nu$  is the filling factor; (here and below, we use units where  $e=\hbar=1$ , and the Einstein summation convention is followed, unless specified otherwise). The effective action that leads to Hall's law (6.1) via  $j^\mu = \delta S_{\rm cs}/\delta A_\mu$  is the three-dimensional Chern–Simons action

<sup>&</sup>lt;sup>1</sup> We define the statistical phase  $\theta_{12}$  of two operators  $\psi_1$  and  $\psi_2$  via the relation  $\psi_1(x)\psi_2(x') = e^{i\theta_{12}}\psi_2(x')\psi_1(x)$ . The microscopic construction [6] shows that so defined statistical phase indeed takes integer values for single valued excitations of the Laughlin state [7].

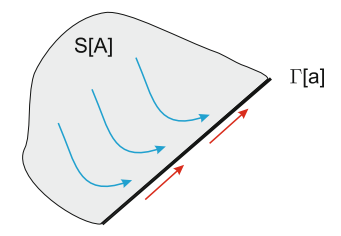


**Fig. 6.1** The Hall current in the bulk (*blue*, *curved arrows*) has an anomaly at the edge (i.e., it is not conserved). This anomaly must be canceled by the anomaly (Examples of the anomaly inflow at the edge in some other physical systems are provided by [9, 10]) of the edge current (*red*, *straight arrows*). Therefore, there is an anomalous boundary action  $\Gamma[\mathbf{a}]$  that is constrained by the requirement of anomaly cancellation in the bulk effective action  $S[\mathbf{A}]$ . After Ref. [11]. © American Physical Society

$$S_{\rm cs} = \frac{\sigma_H}{2} \int_D d^3 r \, \epsilon^{\mu\nu\lambda} A_\mu \partial_\nu A_\lambda, \tag{6.2}$$

where D is the product of the time axis and some spatial domain.

Action (6.2) is *anomalous*, i.e., it has a nonvanishing gauge variation in the presence of a boundary. Indeed, gauge transforming the potential  $A_{\lambda} \to A_{\lambda} + \partial_{\lambda} f$  in Eq. (6.2) by an arbitrary gauge function f(r) and integrating by parts, we obtain the variation of the action:

$$\delta S_{\rm cs} = \frac{\sigma_H}{2} \int_{\partial D} d^2 r \, \epsilon^{\nu\lambda} \partial_{\nu} A_{\lambda} f. \tag{6.3}$$

This anomaly originates from the fact that the current (6.1) is not conserved at the boundary:  $\partial_{\mu} j^{\mu} \neq 0$ , for  $r \in \partial D$ . Indeed, taking the derivative of Eq. (6.1), we find that

$$\partial_{\mu}j^{\mu} = \sigma_{H}\epsilon^{\mu\nu\lambda}\partial_{\nu}A_{\lambda}\partial_{\mu}\theta_{D}, \tag{6.4}$$

where the function  $\theta_D$  takes values  $\theta_D = 1$  and  $\theta_D = 0$  inside and outside the domain D, respectively.

The anomaly must be compensated by boundary degrees of freedom (see Fig. 6.1) coupled to the electromagnetic field. Namely, the total effective action, after the boundary fields are integrated out, is given by a sum of two terms,

$$S_{\text{tot}}[\mathbf{A}] = S_{\text{cs}}[\mathbf{A}] + \Gamma[\mathbf{a}], \tag{6.5}$$

where **a** is the electromagnetic field at the boundary,  $\mathbf{a} = \mathbf{A}|_{\partial D}$ , and  $\Gamma[\mathbf{a}]$  is an anomalous action at the edge [12]. The anomaly in  $\Gamma$  must be such that, under a gauge transformation  $a_{\lambda} \to a_{\lambda} + \partial_{\lambda} f$ , this action acquires a variation that cancels exactly the one of the bulk action, see (6.3):  $\delta\Gamma = -\delta S_{\rm cs}$ . Under this condition,  $S_{\rm tot}[\mathbf{A}]$  is gauge-invariant. Consequently, the edge current  $\mathbf{J}$ , defined as  $J^{\mu} = \delta(S_{\rm cs} + \Gamma)/\delta a_{\mu}$ ,

is anomalous, with divergence given by

$$\partial_{\mu}J^{\mu} = \sigma_{H}\epsilon^{\mu\nu}\partial_{\mu}a_{\nu} \tag{6.6}$$

This divergence cancels the divergence (6.4) of the bulk current. Below we discuss various models that incorporate these general ideas, starting from a simple hydrodynamical model.

# 6.1.2 Hydrodynamics of Incompressible Edge Deformations

Next, we recall some arguments in Ref. [13], with some modifications taking into account the physics related to long-range Coulomb interactions. Edge excitations can be viewed as deformations of the boundary of an incompressible quantum Hall liquid caused by the bulk current flowing towards the edge (see Fig. 6.2). We parametrize these deformations by a function y = h(x, t) and consider a low-energy limit, so that  $h \ll \ell_h$ , where  $\ell_h$  is the characteristic wave length of the deformations. Introducing an auxiliary boundary at a distance  $y_0$  from the edge, with  $\ell_h \gg y_0 \gg h$ , we represent the edge current  $J \equiv J_x$  as the integral  $J = \int_{-y_0}^h dy j_x$ , and, for the accumulated charge density at the edge,  $\rho \equiv J_t$ , we write  $\rho = n_0 h$ , where  $n_0 = \nu B/2\pi c$  is the density of the quantum Hall liquid and B is the magnetic field value.

An unpleasant aspect of this approach is that the edge current explicitly depends on the auxiliary cutoff at  $y=-y_0$ . However, we show that the resulting equation of motion for the edge deformations, h(x,t), does not contain this cutoff, and hence the edge current can be redefined to depend on h only. Indeed, charge conservation implies that  $\partial_t \rho + \partial_x J = j_y$ , where the bulk current density  $j_y$  is taken at the boundary  $y=-y_0$ . Using Eq. (6.1) and fixing the gauge  $a_x=0$ , we write  $J=\sigma_H[\varphi(x,h)-\varphi(x,-y_0)]$ , where  $\varphi(x,y)$  is the total electrostatic potential in the plane of the quantum Hall fluid. Substituting this expression for the current in the continuity equation, we observe that the terms containing  $y_0$  cancel, and the equation of motion takes the form  $\partial_t \rho + \sigma_H \partial_x \varphi = 0$ . Finally, we split the potential  $\varphi$  into two parts and write  $\partial_x \varphi = \partial_x \varphi_h - \tilde{E}_x$ , where  $\varphi_h$  is the potential at the edge caused by its deformation, and  $\tilde{E}_x$  is the external electric field evaluated at y=h. While  $\tilde{E}_x$  depends on h in general, in the low-energy limit it can be taken at y=0, to leading order in h. The equation of motion then reads,

$$\partial_t \rho + \sigma_H \partial_x \varphi_h = \sigma_H \tilde{E}_x. \tag{6.7}$$

After a redefinition of the edge current,  $J = \sigma_H \varphi_h$ , the cutoff parameter  $y_0$  is gone. In order to close the equation of motion, we need a relation between the deformation h and the potential  $\varphi_h$ . In the long wave-length limit, we can simply write  $\varphi_h = -\partial_\rho H = -(1/n_0)\partial_h H$ , where H is the density of electrostatic energy at the edge. This leads to an equation that is, in general, non-linear in the field  $\rho$ . Passing

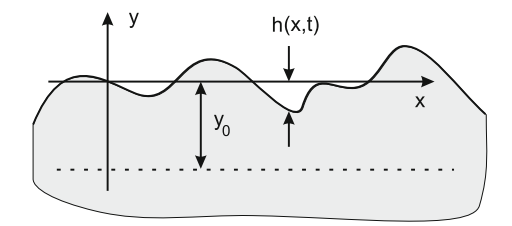


**Fig. 6.2** Deformations of the boundary (*thick line*) of an incompressible quantum Hall fluid (shown in *gray*) are parameterized by the function y = h(x, t). The auxiliary boundary, where bulk and edge currents match, is indicated by the *dashed line*  $y = -y_0$ . After Ref. [11]. © American Physical Society

to a low-energy limit, this equation can be linearized, and we arrive at the result:

$$\partial_t \rho - v \partial_x \rho = \sigma_H \tilde{E}_x, \tag{6.8}$$

where  $v = (\sigma_H/n_0^2)\partial_{hH}^2(0)$  is the group velocity of the edge excitations. For a stable quantum Hall liquid,  $\partial_h^2 H(0)$  is positive, and this equation describes the propagation of chiral excitations.

There are two contributions to the electrostatic energy: one is due to the confining potential at the edge and the second one is due to Coulomb interactions. Consequently, the group velocity of edge excitations can be written as a sum of two terms,

$$v = cE/B + \sigma_{HV},\tag{6.9}$$

where the first term is the velocity of drift in the electric field E at the edge of the quantum Hall liquid, and the second term is proportional to the integral  $V = \int dx' U_C(x-x')$  of the Coulomb interaction potential  $U_C$  at the edge. This integral is logarithmically divergent and has to be cut off at the distance, d, to the metallic gate and at the microscopic width of the edge a, so that  $V \sim \ln(d/a)$ .

Here an important remark is in order. The first term in Eq. (6.9) may be interpreted as a bare velocity,  $v_0$ , of excitations. Restoring physical units, it can be estimated as  $v_0 \sim (eE/\hbar)l_B^2$ , where  $l_B$  is the magnetic length. The ratio  $\alpha := \sigma_H/v_0 \sim e^2/\hbar v_0$  plays the role of a dimensionless interaction constant. Depending on the confinement at the edge, it is always larger than 1, and, in a typical experiment [14–22],  $\alpha \ge 10$ , which may justify the hydrodynamical model considered here. Moreover, the long-range character of the Coulomb interaction and the fact that  $d \gg a$  leads to a large parameter V. As a result, the hydrodynamical charged mode is always present in the spectrum and determines the scaling dimension in non-chiral models, as we demonstrate in Sect. 7.2.

# 6.1.3 Quantization of Edge Excitations

In order to quantize edge excitations, we consider the total electrostatic energy density  $H(\rho) = (v/2\sigma_H)\rho^2$  as a Hamiltonian that generates the homogeneous version of the equation of motion (6.8), see Ref. [13]. This equation is diagonal in Fourier space,  $\partial_t \rho_k - ivk\rho_k = 0$ . We therefore write the Hamiltonian as

$$H_k = \frac{v}{\sigma_H} \rho_k \rho_{-k},\tag{6.10}$$

where k > 0. We identify the "momentum" with  $P_k = \rho_k$  and the "coordinate" with  $X_k = i \rho_{-k}/\sigma_H k$ , so that the equations of motion take the form  $\partial_t X_k = \partial H_k/\partial P_k$  and  $\partial_t P_k = -\partial H_k/\partial X_k$ . Then the canonical commutator  $[X_k, P_{k'}] = i \delta_{kk'}$  leads to the commutator  $[\rho(x), \rho(x')] = i \sigma_H \partial_x \delta(x - x')$  in real space.

Next, we construct an electron operator. For this purpose it is convenient to represent the charge density in terms of a field  $\phi(x)$ ,

$$\rho(x) = \frac{\sqrt{\nu}}{2\pi} \,\partial_x \phi(x),\tag{6.11}$$

with commutation relations

$$[\phi(x'), \phi(x)] = i\pi \text{sgn}(x - x').$$
 (6.12)

Here, and in the following, we use the term "filling fraction",  $\nu$ , and "Hall conductivity",  $\sigma_H$ , synonymously; but we always mean the latter. Then the electron operator takes the form

$$\psi = e^{iq\phi} \tag{6.13}$$

of a local vertex operator; see, e.g., Ref. [23]. For this operator to describe the creation and annihilation of an electron or hole, we require that

$$[Q_{\rm em}, e^{iq\phi}] = e^{iq\phi}, \tag{6.14}$$

where  $Q_{\rm em} = \int dx \rho = (\sqrt{\nu}/2\pi) \int dx \partial_x \phi$  is the total electric charge at the edge. This requirement implies that the charge of an electron is equal to -1. Using the commutation relations (6.12) we find that

$$q = 1/\sqrt{\nu}.\tag{6.15}$$

In addition, an electron operator (6.13) must obey fermionic commutation relations. Applying the Baker–Campbell–Hausdorff formula, we find that  $e^{iq\phi(x)}e^{iq\phi(x')}=e^{i\pi q^2}e^{iq\phi(x')}e^{iq\phi(x')}$ . Using Eq. (6.15) and imposing Fermi statistics, we conclude that

$$e^{i\pi/\nu} = -1. {(6.16)}$$

This implies that the filling factor is given by  $\nu = 1/m$ , where m is an odd integer number. In Sect. 6.2, we show that this limitation can be overcome by constructing a multi-channel edge model.

According to the third principle formulated at the beginning of this section, the theory may describe quasi-particles with the vertex operators  $e^{ip\phi}$  that must be local relative to the electron operator  $e^{iq\phi}$ . Thus the statistical phase,  $\theta$ , of such quasi-particles with respect to an electron has to be an integer multiple of  $\pi$ . Using again the commutation relation (6.12), we arrive at the result that

$$\theta = \pi p \cdot q = \pi n$$

and the quasi-particle operator takes the form:

$$\psi_n = e^{in\sqrt{\nu}\phi(x)},\tag{6.17}$$

where n is an integer. Such operators describe Laughlin quasi-particles [7]. The correlation functions of quasi-particle operators may be calculated easily, with the result

$$\langle 0|\psi_n^{\dagger}(x,t)\psi_n(0,0)|0\rangle = (x+vt)^{-\nu n^2},$$
 (6.18)

where  $|0\rangle$  denotes the ground state of a quantum Hall fluid with filling fraction  $\nu$ . Taking into account that  $\nu=1/m$ , the properties of the operators (6.17) are as follows: they carry a charge q(n)=n/m and have the scaling dimensions  $\Delta(n)=n^2/m$ . Thus, for an elementary quasi-particle with charge 1/m, we have that  $\Delta_{\min}=1/m$ , and, for an electron,  $\Delta_{\rm el}=m$ .

# 6.1.4 Gauge-Invariant Formulation

We recall that the above derivations have been carried out in a fixed gauge  $a_x = 0$ . In this section we reformulate the theory of edge excitations presented above in a gauge-invariant form suitable for a generalization to multi-channel fluids considered in Sect. 6.2. We first rewrite the action  $S = \int dt \sum_{k>0} [P_k \partial_t X_k - H_k]$  in the linear approximation as

$$S[\phi] = \frac{1}{4\pi} \int dt dx [\partial_t \phi \partial_x \phi - v(\partial_x \phi)^2 + 2\sqrt{\nu} \phi \tilde{E}_x], \tag{6.19}$$

where we have included a term describing the coupling to an electric field  $\tilde{E}_x$ . This action can easily be generalized to nonlinear edge modes by replacing the term  $(v/4\pi)(\partial_x\phi)^2$  with the full Hamiltonian  $H(\rho)$ . However, the dynamics in general is not integrable.

Next, we replace derivatives  $\partial_{\mu}\phi$  in action (6.19) with their gauge-invariant form

$$D_{\mu}\phi \equiv \partial_{\mu}\phi + \sqrt{\nu}a_{\mu},\tag{6.20}$$

and integrate the last term by parts using the relation  $\tilde{E}_x = \epsilon^{\mu\lambda} \partial_\mu a_\lambda$ . We then arrive at the following action

$$S[\phi] = \frac{1}{4\pi} \int dt dx [D_t \phi D_x \phi - v(D_x \phi)^2] + \frac{\sqrt{\nu}}{4\pi} \int dt dx \epsilon^{\mu\lambda} a_\mu \partial_\lambda \phi.$$
 (6.21)

It is easy to check that by fixing the gauge  $a_x = 0$ , one returns to action (6.19).

The first term in action (6.21) is invariant under the gauge transformation  $a_{\mu} \rightarrow a_{\mu} + \partial_{\mu} f$ ,  $\phi \rightarrow \phi - \sqrt{\nu} f$ . The second term yields the gauge variation

$$\delta S[\phi] = -(\nu/4\pi) \int dt dx \epsilon^{\mu\lambda} \partial_{\mu} a_{\lambda} f, \qquad (6.22)$$

i.e., the edge action has the desired anomaly: It exactly cancels the anomaly (6.3) of the bulk action. Thus, the effective theory described by the total action  $S_{\text{tot}} = S_{\text{cs}}[\mathbf{A}] + S[\phi]$  is gauge-invariant. The boundary effective action  $\Gamma[\mathbf{a}]$  in Eq. (6.5) is obtained by integrating out the field  $\phi$ .

One may then check that the gauge-invariant edge current has the correct anomalous divergence (6.6). To see this, we take a variational derivative of the total action with respect to the boundary potential **a**. This yields the following expression for the edge current:

$$J_t = \frac{\sqrt{\nu}}{2\pi} D_x \phi, \quad J_x = -\frac{\sqrt{\nu}}{2\pi} v D_x \phi. \tag{6.23}$$

In a gauge where  $a_x=0$ , this expression reproduces definition (6.11) of the charge density as well as the definition of electron operator (6.13). Indeed, Eq. (6.23) for the edge current follows from point-splitting of the operator  $\psi^{\dagger}\psi$  in the presence of an electromagnetic field. Note that the current satisfies the relation  $J_x=-vJ_t$ , which exhibits its chiral nature. Finally, by varying action (6.21) with respect to  $\phi$ , we obtain the equation of motion for  $\phi$ , which is used to evaluate the divergence of the current (6.23). We then arrive at Eq. (6.6), i.e., the edge current has the desired anomalous divergence.

We conclude that the hydrodynamical model, when applied to quantum Hall states with  $\nu=1/m$  where m is an odd integer, satisfies all the requirements formulated at the beginning of this section. In Sect. 6.2, we show that by considering more than one bosonic mode at the edge of a quantum Hall liquid, one can construct effective edge models for general filling factors.

# **6.2 Multi-Channel Edge Models**

As shown in Sect. 6.1.3, a single-channel hydrodynamical model of the quantum Hall edge cannot describe all observed filling fractions. We therefore consider more general multi-channel edge models. A natural generalization of single-field action (6.21) to many fields is given by

$$S[\phi_i] = \frac{1}{4\pi} \sum_i \int dt dx [\sigma_i D_t \phi_i D_x \phi_i - v_i (D_x \phi_i)^2]$$

$$+ \frac{1}{4\pi} \sum_i \int dt dx [Q_i \epsilon^{\mu\lambda} a_\mu \partial_\lambda \phi_i],$$
(6.24)

where  $\sigma_i = \pm 1$  encodes the chirality of the ith channel,  $v_i$  is the propagation speed, and  $Q_i$  is the constant of electromagnetic coupling of the field  $\phi_i$ . The covariant derivatives are defined by  $D_\mu \phi_i = \partial_\mu \phi_i + \sigma_i \, Q_i a_\mu$ . We emphasize that any quadratic gauge-invariant action for chiral bosons can be brought to the unique form (6.24) by redefining the fields. Here we consider the general case with different propagation speeds,  $v_i$ , for different edge modes, because recent experiments [14, 16–22] show that this can occur.

The requirement of anomaly cancellation for edge action (6.24) implies that

$$\sum_{i} \sigma_i Q_i^2 = \nu. \tag{6.25}$$

One can see that, in contrast to a single-channel edge where the last term in action (6.21) is uniquely fixed by the Hall conductivity, in the multi-channel situation only the "length" of the vector  $Q_i$  is fixed to be  $\sqrt{\nu}$ , while, at this point, its direction is still arbitrary.

# 6.2.1 Kinematics of Edge Models

In order to check the second physical requirement, the existence of excitations with the quantum numbers of electron, we consider a general vertex operator

$$\psi = \exp\left(i\sum_{j}q_{j}\phi_{j}\right),\tag{6.26}$$

where  $q_i$  are some constants. Taking into account commutation relations

$$[\partial_x \phi_i(x,t), \phi_i(x',t)] = -2\pi i \sigma_i \delta_{ij} \delta(x-x'), \tag{6.27}$$

which follow from Eq. (6.24), we find that the statistical phase of operator (6.26) is given by:

$$\theta = \pi \sum_{i} \sigma_i q_i q_i. \tag{6.28}$$

The electric charge operator is given by  $Q_{\rm em} = (1/2\pi) \sum_i Q_i \int dx \partial_x \phi_i$ , in accordance with Eq. (6.24). Therefore, one finds with the help of Eq. (6.27) that the charge of field operator (6.26) is given by

$$Q_{\rm em} = \sum_{i} \sigma_i \, Q_i \, q_i. \tag{6.29}$$

Here, as in the integer quantum Hall effect, it is possible to have several electron operators differing from each other by some quantum numbers. These quantum numbers can originate, e.g., from several condensates in hierarchic construction (see Sect. 1.3.3). We label different electron operators by an additional index  $\alpha$ ,

$$\psi_{\alpha} = \exp\left(i\sum_{j} q_{\alpha j}\phi_{j}\right),\tag{6.30}$$

and assume that the number of electrons coincides with the number of channels.<sup>2</sup> All electron fields must have a unit charge, which implies that

$$\sum_{i} \sigma_i Q_i q_{\alpha i} = 1, \tag{6.31}$$

and appropriate relative statistical phases,  $\pi K_{\alpha\beta}$ , compatible with relative locality and Fermi statistics. This implies that the numbers

$$K_{\alpha\beta} = \sum_{i} \sigma_{i} q_{\alpha i} q_{\beta i} \tag{6.32}$$

must be integers and that, for  $\alpha = \beta$ , these numbers must be odd integers.

In Fig. 6.3 we schematically illustrate conditions (6.31) and (6.32) for the simple example of two channels with the same chiralities. One sees that in contrast to the single-channel case, in multi-channel models there is a freedom in choosing electron operators, even if the coupling constants  $Q_i$  are fixed. This freedom implies that different microscopic quantum Hall wave-functions may lead to the same action in the low-energy limit. In this case the low-energy projections of electronic operators may in principle be different. In fact, multi-channel models are fully determined by the numbers  $q_{\alpha i}$ , while the values of coupling constants  $Q_i$  can be obtained by solving Eq. (6.31):

 $<sup>^2</sup>$  In fact, the introduced matrix  $q_{\alpha i}$  is an analogue of the well known Cabibbo–Kobayashi–Maskawa matrix in particle physics.

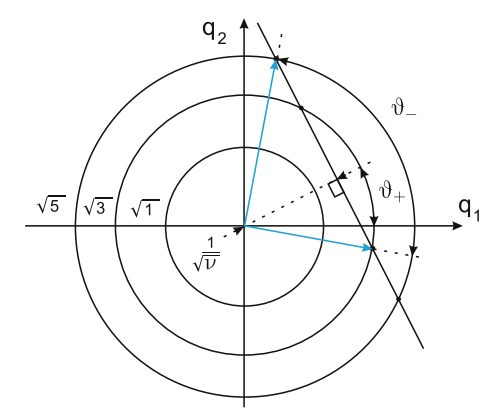


Fig. 6.3 Schematic illustration of the conditions for electron operators in a chiral two-field model. The requirement for the statistical phase of an electron operator to be fermionic is  $q_{\alpha 1}^2 + q_{\alpha 2}^2 = 2k+1$ . This means that the end points of vectors  $\mathbf{q}_{\alpha} \equiv \{q_{\alpha i}\}$  (drawn in *blue*) lie on the circle of radius  $\sqrt{2k+1}$ . The condition of unit charge,  $Q_1q_{\alpha 1}+Q_2q_{\alpha 2}=1$ , implies that the end points of vectors  $\mathbf{q}_{\alpha}$  lie on the line perpendicular to the vector  $\mathbf{Q} \equiv \{Q_i\}$ . The length of this vector is fixed by the anomaly cancellation condition (6.25), namely  $|\mathbf{Q}| = \sqrt{\nu}$ . Therefore the distance from the line through the end points of the vectors  $\mathbf{q}_{\alpha}$  to the origin is fixed to be  $1/\sqrt{\nu}$ . We denote the angle between  $\mathbf{Q}$  and the  $q_1$  axis by  $\vartheta_+$ , and the angle between the electron vectors by  $\vartheta_-$ . After Ref. [11]. © American Physical Society

$$Q_i = \sigma_i \sum_{\alpha} q_{i\alpha}^{-1}.$$
 (6.33)

The physical requirements for the effective theory can therefore be formulated as constraints on the q-matrix. Namely, the requirement that elements of the matrix K given by Eq. (6.32) are integer numbers has to be accompanied by the condition that

$$\sum_{\alpha,\beta} K_{\alpha\beta}^{-1} = \nu,\tag{6.34}$$

which follows from the requirement of anomaly cancellation (6.25) and from Eq. (6.33).

Note that we have reformulated the constraints on the matrix q as constraints on the matrix K. In Sect. 6.2.2 we show that the *kinematic* information about an effective model is encoded in the matrix K. More precisely, the spectra of statistical phases and charges of quasi-particles are entirely determined by K. For every filling factor this matrix takes values from a discrete set. For instance, in two-channel models this corresponds to the discrete set of choices of lengths of electronic vectors  $\mathbf{q}_{\alpha}$  and their relative angle  $\vartheta_{-}$  (see Fig. 6.3). From the relation (6.32) it follows that the remaining freedom in the matrix q for a given matrix K is the angle  $\vartheta_{+}$  of the simultaneous rotation of two vectors  $\mathbf{q}_{\alpha}$ . In Sect. 6.2.2 we show that the *dynamical* properties of the

model, such as the correlation functions, are not determined by the matrix K only, but depend on the whole matrix q, e.g., on the angle  $\vartheta_+$  in the case of two fields.

#### 6.2.2 Local Excitations

Next, we determine all quasi-particle operators in accordance with the requirement that they have integer statistical phases relative to all electron fields (6.30). Quasi-particle operators are vertex operators of the form

$$\psi = \exp\left(i\sum_{j} p_{j}\phi_{j}\right). \tag{6.35}$$

Their statistical phases relative to electronic fields are given by

$$\theta_{pq_{\alpha}} = \pi \sum_{i} \sigma_{i} p_{i} q_{\alpha i} = \pi n_{\alpha}. \tag{6.36}$$

The numbers  $n_{\alpha}$  must be integers. The solution of Eq. (6.36),

$$p_i = \sigma_i \sum_{\beta} q_{i\beta}^{-1} n_{\beta}, \tag{6.37}$$

is a linear combination with integer coefficients. Therefore, the whole set of allowed quasi-particle operators forms a lattice, which is dual to the lattice spanned by electronic vectors  $q_{\alpha i}$  (see Appendix E and Ref. [8] for a detailed discussion of this point).

It is interesting to note that the statistical phase and the charge of a quasi-particle operator labeled by the numbers  $n_{\alpha}$  can be expressed solely in terms of the matrix K. For the statistical phase we have that

$$\frac{\theta}{\pi} = \sum_{i} \sigma_{i} p_{i} p_{i} = \sum_{\alpha,\beta} n_{\alpha} K_{\alpha\beta}^{-1} n_{\beta}. \tag{6.38}$$

It also follows from Eqs. (6.33) and (6.37) that the charge of the operator in (6.35) is given by

$$Q_{\rm em} = \sum_{i} \sigma_i Q_i p_i = \sum_{\alpha\beta} K_{\alpha\beta}^{-1} n_{\beta}. \tag{6.39}$$

Note that the summation over the index  $\alpha$  in this equation may be viewed as the multiplication by the vector (1, 1, ..., 1).

It may happen that different matrices K generate the same set of quasi-particles. This is the case when corresponding electronic vectors  $q_{\alpha i}$  form different bases of the same lattice (see the discussion in Appendix E). An example of such an equivalence is depicted in Fig. 7.1. In the language of matrices q, an equivalence is the consequence of the fact that an integral transformation  $q'_{\alpha i} = \sum_{\beta} T_{\alpha\beta}q_{\beta i}$  (i.e., one with the elements  $T_{\alpha\beta}$  and  $T_{\alpha\beta}^{-1}$  being integer numbers) is nothing but an automorphism of the integral lattice generated by a change of basis. Using definition (6.32), this equivalence may also be written as

$$K \leftrightarrow K' = TKT^T, \tag{6.40}$$

Since the matrix T transforms an electronic basis, it preserves the charge of an electron. Taking into account Eq. (6.39), this important condition implies that the matrix T should preserve the vector  $(1, 1, \ldots, 1)$ .

# 6.2.3 Scaling Dimensions of Local Excitations

We conclude this section by presenting the correlation functions of the quasi-particle operators (6.35). A detailed calculation of this function is contained in Sect. 2.2 and yields

$$\langle 0|\psi^{\dagger}(x,t)\psi(0,0)|0\rangle \propto e^{i\varphi_0(\mathbf{n})} \prod_i (x+\sigma_i v_i t)^{-\delta_i(\mathbf{n})},$$
 (6.41)

where the exponents are given by

$$\delta_i(\mathbf{n}) = p_i^2 = \left[\sum_{\alpha} q_{\alpha i}^{-1} n_{\alpha}\right]^2. \tag{6.42}$$

Here  $\mathbf{n} \equiv \{n_{\alpha}\}$ , and  $\varphi_0$  is a phase, the exact value of which is discussed in Sect. 7.3. The scaling dimension of the correlation function, defined via its long-time behavior, is given by

$$\Delta(\mathbf{n}) = \sum_{i} \delta_{i}(\mathbf{n}). \tag{6.43}$$

Expressed in terms of the q-matrix, it reads

$$\Delta(\mathbf{n}) = \sum_{i} p_i^2 = \sum_{\alpha,\beta} n_{\alpha} (qq^T)_{\alpha\beta}^{-1} n_{\beta}. \tag{6.44}$$

An explicit calculation of  $\Delta$  in the non-chiral case with two fields is given in Appendix D. The scaling dimensions  $\Delta$  are not fully determined by the matrix K, while according to Eq. (6.38), the statistical phases

$$\frac{\theta}{\pi} = \sum_{i} \delta_i \sigma_i \tag{6.45}$$

are given by the matrix K. Comparing Eqs. (6.43) and (6.45) we conclude that  $\Delta \ge \theta/\pi$ , where equality holds in a purely chiral case.

#### 6.3 Conclusions

In this chapter, we have reviewed the construction of a low-energy theory [3–5, 8, 24] of fractional quantum Hall edge states based on the requirement of the anomaly cancellation. We have shown that for  $\nu=1/m$ , where m is an odd integer, a minimal model can be derived from an elementary hydrodynamics, while other filling factors require the introduction of several edge channels (6.24). The classification of such models, based on the physical requirements formulated at the beginning of Sect. 6.1, amounts to the classification of matrices (6.32) for statistical phases of electrons. Quasi-particle operators in each model are found to be indexed by vectors in the dual of an odd integral lattice [8]. Their charges and statistical phases are given by Eqs. (6.38) and (6.39).

We have proposed the following strategy to find inequivalent models for a given filling factor. First of all, one must find all solutions, K, of Eq. (6.34) for a given filling factor  $\nu$ , up to equivalence defined by proper integral transformations (6.40). This procedure fixes the *kinematic* content of the theory. Second, one must choose those parameters that are not constrained by the general conditions formulated at the beginning of Sect. 6.1. These parameters are the propagation speeds,  $v_i$ , of chiral edge modes, and the explicit basis,  $\mathbf{q}_{\alpha}$ , of vectors labeling electron field operators which consistent with the chosen matrix K. This last step is equivalent to choosing an element of the pseudo-orthogonal group  $SO(N_+, N_-)$ , where  $N_{\pm}$  are the numbers of modes with corresponding chirality.

Importantly, we have found that the scaling dimensions of quasi-particles depend on the last ingredient of the model in a non-chiral case. This result is consistent with a situation in the quantum wires, where the scaling dimensions depend on the Luttinger parameter [25]. In the next chapter, we will focus on the case of two channels, and show that the strong Coulomb interaction at the edge, which plays an important role in the integer case, allows to fix this degree of freedom.

Finally, we have considered only simplest *Abelian* models of the edge states. Although these models seem to be most relevant, it is also interesting to investigate the non-Abelian models too. Some first attempts in this direction have been already made [24]. However, the other physical ingredients of the classification, such as different propagation velocities of eigenmodes, might significantly change the results.

References 125

#### References

- 1. For a review, see A.M. Chang, Rev. Mod. Phys. 74, 1449 (2003)
- 2. For a review, see X.-G. Wen, Adv. Phys. 44, 405 (1995)
- 3. X.-G. Wen, Phys. Rev. B 41, 12838 (1990)
- 4. J. Fröhlich, A. Zee, Nucl. Phys. B **364**, 517 (1991)
- 5. J. Fröhlich, T. Kerler, Nucl. Phys. B **354**, 369 (1991)
- 6. A. Boyarsky, V.V. Cheianov, O. Ruchayskiy, Phys. Rev. B 70, 235309 (2004)
- 7. R.B. Laughlin, Phys. Rev. Lett. **50**, 1395 (1983)
- 8. J. Fröhlich, U.M. Studer, E. Thiran, J. Stat. Phys. 86, 821 (1997)
- 9. J.A. Harvey, O. Ruchayskiy, J. High Energy Phys. **06**, 044 (2001)
- 10. A. Boyarsky, O. Ruchayskiy, M. Shaposhnikov, Phys. Rev. D 72, 085011 (2005)
- 11. I.P. Levkivskyi, A. Boyarsky, J. Fröhlich, E.V. Sukhorukov, Phys. Rev. B 80, 045319 (2009)
- 12. S.B. Treiman, R. Jackiw, D.J. Gross, *Lectures on Current Algebra and Its Applications* (Princeton University Press, Princeton, 1972)
- X.-G. Wen, Quantum Field Theory of Many-body Systems (Oxford University Press, New York, 2007)
- 14. I. Neder, M. Heiblum, Y. Levinson, D. Mahalu, V. Umansky, Phys. Rev. Lett. 96, 016804 (2006)
- 15. Y. Ji et al., Nature (London) **422**, 415 (2003)
- P. Roulleau, F. Portier, D.C. Glattli, P. Roche, A. Cavanna, G. Faini, U. Gennser, D. Mailly, Phys. Rev. B 76, 161309 (2007)
- P. Roulleau, F. Portier, D.C. Glattli, P. Roche, A. Cavanna, G. Faini, U. Gennser, D. Mailly, Phys. Rev. Lett. 100, 126802 (2008)
- 18. L.V. Litvin, H.-P. Tranitz, W. Wegscheider, C. Strunk, Phys. Rev. B 75, 033315 (2007)
- L.V. Litvin, A. Helzel, H.-P. Tranitz, W. Wegscheider, C. Strunk, Phys. Rev. B 78, 075303 (2008)
- E. Bieri, Correlation and interference experiments with edge states, Ph.D. Thesis, University of Basel, 2007
- E. Bieri, M. Weiss, O. Goktas, M. Hauser, C. Schonenberger, S. Oberholzer, Phys. Rev. B 79, 245324 (2009)
- 22. I. Neder, F. Marquardt, M. Heiblum, D. Mahalu, V. Umansky, Nat. Phys. 3, 534 (2007)
- 23. A.O. Gogolin, A.A. Nersesyan, A.M. Tsvelik, *Bosonization and Strongly Correlated Systems* (Cambridge University Press, Cambridge, 1998)
- 24. J. Fröhlich, B. Pedrini, C. Schweigert, J. Walcher, J. Stat. Phys. 103, 527 (2001)
- 25. Th Giamarchi, Quantum Physics in One Dimension (Oxford University Press, Oxford, 2003)

# **Chapter 7 Spectroscopy of Quantum Hall Edge States at Complex Filling Factors**

The quantum Hall effect is a fascinating example of macroscopic quantum phenomena. Its large-scale physics is governed by the requirement of anomaly cancellation at the boundary of the system. It provides an example of the so called "holographic principle" (another well known examples of the holographic principle are described in the papers [1–4]), which means that the physics of the system confined to some region is encoded in the physics of the degrees of freedom at the boundary of this region (see Fig. 6.1). Understanding the physics of the quantum Hall edge states is therefore important for an understanding of the quantum Hall effect in general.

In the theoretical description of incompressible quantum Hall fluids, the "holographic principle" manifests itself in the presence of *chiral* edge channels in the lowenergy effective theory [5]. These boundary channels are thought to be described by chiral conformal field theory [6–8]. As we have shown in the previous chapter, the possible structure of this description is highly constrained by the requirements of locality, the gauge invariance (charge conservation), and the presence of excitations describing electrons (i.e., with quantum numbers of an electron or hole) in the spectrum. These requirements allow one to classify possible effective low-energy models for all observed filling factors [9, 10]. However, without taking into account microscopic properties of a particular incompressible quantum Hall state, the requirements mentioned above usually do not determine the low-energy effective theory uniquely. Already in examples of incompressible Hall fluids corresponding to simple fractions, such as  $\nu = 2/3, 2/5$ , etc., there are several physically inequivalent models satisfying all the requirements even if one limits one's attention to models with the smallest possible number of edge channels. This situation calls for experimental tests of the theory.

There are several proposals to test the quantum Hall edge physics. Concrete attempts for such tests have been made in three directions: measurement of the

Some text sections in this chapter are reproduced from Phys. Rev. B 80, 045319 (2009), © American Physical Society.

electric charge, of the statistical phase, and of the *scaling dimension* of excitations (quasi-particles and electrons). The scaling dimension of the electron field operator may be tested via the I-V curve at a tunnel junction [11]. This idea has been experimentally implemented in Refs. [12, 13]. The results of these experiments caused an extensive discussion of the well known "2.7 problem" [14]. The interpretation of the experiments described in Refs. [12, 13] is not straightforward, and one may need to take into account the existence of compressible strips [15] at the edge, of disorder

[16, 17], and of electron-phonon interactions [18]. The charge of quasi-particles may be probed by measuring the Fano factor of the tunneling current [19]. Currently, fractional charges have been observed in several experiments [20–22] at different filling factors. Several proposals have been made to use the Fabry-Perot [23] and the Mach-Zehnder [24] electronic interferometers, which utilize quantum Hall edge channels, in place of optical beams, for measurements of fractional charge and of anyon statistics of quasi-particles [25, 26].

In this chapter we propose an experiment that would allow one to find out which effective model describes a particular filling factor. The idea is to use quantum Hall interferometers in order to measure simultaneously the charge and the scaling dimension for each species of quasi-particles that may tunnel through a quantum point contact. Aharonov-Bohm oscillations in a Mach-Zehnder interferometer have recently been investigated experimentally in Refs. [27–30] and showed surprising behavior. This has been addressed in several theoretical works [31–36]. The main result of this chapter, Eqs. (7.25) and (7.31) describing the Aharonov-Bohm-oscillating contribution to the current through a Fabry-Perot interferometer at low and high temperatures, shows that the Fourier spectrum of the current as a function of the flux can be used to extract the scaling dimensions and charges of quasi-particles. As an example, we consider the well observed filling factor  $\nu = 2/3$  in some detail. We present possible effective models for this filling factor and discuss how they can be distinguished from each other with the help of their spectra of scaling dimensions.

An important property of the  $\nu=2/3$  state is that all minimal models of its edge degrees of freedom contain two edge channels. A similar situation is encountered at  $\nu=2$ , where it has been shown that the *long-range* Coulomb interaction between the channels leads to some universalities [32]. In this chapter we show that Coulomb interactions fix a freedom in the choice of the edge Hamiltonian, so that scaling dimensions are fully determined by the matrix (6.32) of statistical phases of electrons (see Sect. 7.2). We start this chapter with the explicit determination of the spectrum of scaling dimensions for the most plausible (minimal) models corresponding to  $\nu=2/3$ . Section 7.2 is devoted to an analysis of the role of Coulomb interactions. Finally, in Sect. 7.3, we investigate transport trough an electronic interferometer and show how scaling dimensions of excitations can be extracted from Aharonov-Bohm oscillations of the current through the interferometer.

# 7.1 Minimal Models for Filling Factor v = 2/m

In this section we apply the ideas discussed in the previous chapter to the particular case of filling factors v = 2/m. In Ref. [16, 17] it has been shown that models with a large number of edge channels may be unstable under the influence of disorder. To avoid such complications, we limit our analysis to models with the smallest possible number of fields. Moreover, we consider models with minimal statistical phases of electron field operators, because they are most relevant physically.<sup>1</sup>

A direct solution of Eq. (6.34) is complicated. Fortunately, in Ref. [10], some general results have been proven for the case where the statistical phases of electron operators are smaller than  $7\pi$ : all two-field models for  $\nu = 2/m$  are described by matrices K of the following form:

$$K_a = \begin{pmatrix} a & b \\ b & a \end{pmatrix}. \tag{7.1}$$

Equation (6.34) then imposes the following constraint on matrix (7.1):

$$v = \frac{2a - 2b}{a^2 - b^2} = \frac{2}{a + b}. (7.2)$$

Thus, for v = 2/m, the parameters a and b are related by a + b = m, where the odd integer a enumerates the models.

For a purely chiral model, the scaling dimensions of correlation functions (6.44) are given by the statistical phases. Therefore, for a K-matrix of the form (7.1), they are given by the expression

$$\Delta(\mathbf{n}) = \frac{1}{a^2 - b^2} [a(n_1^2 + n_2^2) - 2bn_1n_2],\tag{7.3}$$

and the charge of excitations can be evaluated as

$$Q_{\rm em} = \frac{n_1 + n_2}{m}. (7.4)$$

For non-chiral models, the expression for the charges of quasi-particles remains the same, while the scaling dimensions (6.44) depend on an additional parameter,  $\vartheta_+$ , (see Appendix D). In Sect. 7.2, we show that, in the limit of strong Coulomb interactions, this parameter takes the universal value  $\vartheta_+ = 0$ . The scaling dimensions are then given by

$$\Delta(\mathbf{n}) = \frac{1}{b^2 - a^2} [b(n_1^2 + n_2^2) - 2an_1n_2]. \tag{7.5}$$

<sup>&</sup>lt;sup>1</sup> Numerical simulations [37] show that for larger values of statistical phases the quantum Hall state is not stable, and electrons form a Wigner crystal [5].

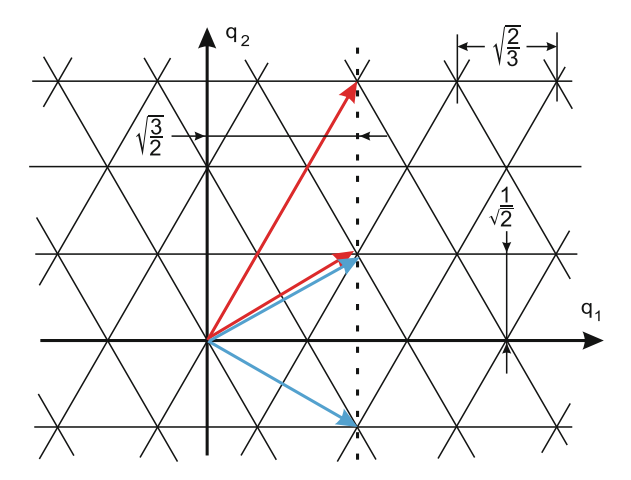


Fig. 7.1 Illustration of equivalence of two quantum Hall lattices. For two channels of different chiralities, the statistical phase satisfies  $\theta/\pi=q_1^2-q_2^2$ . Using this fact, one can easily see that the *red*, *upper pair* of vectors correspond to *K*-matrix (7.6) and the *blue*, *lower pair* of vectors correspond to the *K*-matrix (7.7), two vectors in the middle are slightly shifted for clarity. Note that these pairs of vectors are just different bases of the same lattice (which is dual to the one shown in the figure). Therefore the spectra of statistical phases in models (7.6) and (7.7) are identical. Finally, the *dashed line* constrains the charge of the electrons to be 1. The fact that all electron vectors lie on the same line implies that the constants  $Q_i$  are the same for both models. This means that the charges  $Q_{\rm em} = \sum q_i \, Q_i$  of excitations in one model coincide with those in the second model. Here we choose the angle  $\vartheta_+ = 0$ , in accordance with the conclusion of Sect. 7.2. After Ref. [38]. © American Physical Society

We have already mentioned that any two-field solution of Eq. (6.34) corresponds to one of the matrices (7.1), up to equivalence described by the transformations (6.40). An important example is the K-matrix proposed, e.g., in Ref. [39–41]:

$$K = \begin{pmatrix} 1 & 0 \\ 0 & -3 \end{pmatrix}. \tag{7.6}$$

This matrix describes a non-chiral model of the  $\nu=2/3$  state obtained by particle-hole conjugation of the  $\nu=1/3$  state. In this state, the density at the edge first increases to  $\nu=1$  and then drops to zero, which implies the presence of two edge channels with opposite chiralities. Another K-matrix for  $\nu=2/3$  state appears in the context of the composite fermion approach [42]:

$$K = \begin{pmatrix} 1 & 2 \\ 2 & 1 \end{pmatrix}. \tag{7.7}$$

It turns out that model (7.6) is equivalent to (7.7), in the sense of (6.40). Indeed, one can apply an integral change of variables transforming one K-matrix into the other one:

		,
$K_a$	$\Delta(\mathbf{n})$	$\Delta_0, \Delta_{\frac{1}{3}}, \Delta_{\frac{2}{3}}, \Delta_1, \Delta_{el}$
K <sub>5</sub>	$\frac{1}{21}(5(n_1^2 + n_2^2) + 4n_1n_2)$	$\frac{6}{21}$ , $\frac{5}{21}$ , $\frac{2}{3}$ , $\frac{11}{7}$ , 5
$K_3$	$\frac{1}{3}(n_1^2+n_2^2)$	$\frac{2}{3}$ , $\frac{1}{3}$ , $\frac{2}{3}$ , $\frac{5}{3}$ , $\frac{5}{3}$
$K_1$	$\frac{\frac{2}{3}(n_1^2 + n_2^2 - n_1 n_2)}{\frac{2}{15}(2(n_1^2 + n_2^2) + n_1 n_2)}$	$2, \frac{2}{3}, \frac{2}{3}, 2, 2$
$K_{-1}$	$\frac{2}{15}(2(n_1^2 + n_2^2) + n_1 n_2)$	$\frac{6}{15}$ , $\frac{4}{15}$ , $\frac{2}{3}$ , $\frac{8}{5}$ , 4

**Table 7.1** Scaling dimensions of excitations in different models of the v = 2/3 state

For each model described by a matrix  $K_a$ , we provide the general expression for the scaling dimensions  $\Delta(\mathbf{n})$  of quasi-particle operators labeled by pairs of integer numbers  $(n_1, n_2)$ . The minimal values  $\Delta_q$  for excitations of charge q, as well as the scaling dimensions of electron operators are listed in the right column. After Ref. [38]. © American Physical Society

$$\begin{pmatrix} 1 & 0 \\ 2 & -1 \end{pmatrix} \begin{pmatrix} 1 & 0 \\ 0 & -3 \end{pmatrix} \begin{pmatrix} 1 & 2 \\ 0 & -1 \end{pmatrix} = \begin{pmatrix} 1 & 2 \\ 2 & 1 \end{pmatrix}.$$

This transformation is of the type of (6.40), because it has the property that

$$\begin{pmatrix} 1 & 0 \\ 2 & -1 \end{pmatrix}^{-1} = \begin{pmatrix} 1 & 0 \\ 2 & -1 \end{pmatrix},$$

and it leaves the vector (1, 1) invariant. The equivalence of these two models is illustrated in Fig. 7.1.

For  $\nu = 2/3$ , the matrices (7.1) with the smallest diagonal elements (i.e., with smallest statistical phases of electron operators) are the following ones:

$$K_3 = \begin{pmatrix} 3 & 0 \\ 0 & 3 \end{pmatrix}, \quad K_5 = \begin{pmatrix} 5 & -2 \\ -2 & 5 \end{pmatrix} \tag{7.8}$$

and

$$K_1 = \begin{pmatrix} 1 & 2 \\ 2 & 1 \end{pmatrix}, \quad K_{-1} = \begin{pmatrix} -1 & 4 \\ 4 & -1 \end{pmatrix}.$$
 (7.9)

Note that the matrices (7.9) have negative determinants, and hence, in contrast to the matrices (7.8), they describe non-chiral states. We summarize the values of scaling dimensions of excitations in models (7.8) and (7.9) in Table 7.1.

It is important to note that, for every model, the minimal scaling dimension is  $\Delta_{\min} = \Delta_{1/3}$ , i.e., the operator of the Laughlin quasi-particle is the most relevant one. We note that between four models, the model  $K_1$  is presumably most stable with respect to disorder, because it has the largest scaling dimension  $\Delta_0$ . Moreover, the electron operator in this model is the most relevant operator among operators with unit charge. In addition, numerical simulations [43] and some microscopic considerations [39–41] confirm that the model with matrix  $K_1$  is most likely to describe the  $\nu = 2/3$  state. However, some signs of a phase transition in the  $\nu = 2/3$  state have been observed [44–46]. This indicates that other models may also be realized under certain conditions; see Ref. [10].

# 7.2 The Role of Coulomb Interactions

We have shown in Sect. 6.2.3 (see also Appendix D) that, in the non-chiral case, the scaling dimensions of excitations depend not only on the "kinematic" structure of the theory encoded in the K-matrix, but also on the angle  $\vartheta_+$ . This angle parametrizes the relation between the propagating modes and the electron operators. There is, however, an important class of systems in which this parameter appears to be uniquely and universally fixed. This is, for instance, the case in a system with two edge modes and strong Coulomb interactions. This fact has been discussed in Ref. [32]. The results of the analysis in Ref. [32] are essentially in perfect agreement with the experimental data of Refs. [27–30, 47–50]. Although in Ref. [32] only the case  $\nu=2$  is considered, we will show below that the conclusion of this analysis applies without significant changes to fractional fluids, too.

Let us assume that effects of disorder are negligible. This may be a reasonable assumption for an electronic interferometer, the size of which is typically only a few microns. In this case, the generic form of the Hamiltonian is given by a sum of the free Hamiltonian, the Coulomb interaction term, and a term describing the interaction with an external electromagnetic field  $a_{\mu}$ :

$$\mathcal{H} = \mathcal{H}_0 + \mathcal{H}_C + \mathcal{H}_{int}[\mathbf{a}]. \tag{7.10}$$

We show below that the actual form of the free Hamiltonian  $\mathcal{H}_0$  is not important.

Assuming the distance, a, between the edge channels to be of the order of their thickness, l, or smaller (see Fig. 7.2 for notations), the Coulomb interaction term can be written as:

$$\mathcal{H}_{C} = (1/2) \int dx dx' \rho_{em}(x) U_{C}(x - x') \rho_{em}(x'),$$
 (7.11)

where  $\rho_{\rm em}(x)$  is the total one-dimensional charge density at the point x, and  $U_C(x-x')$  is the Coulomb potential. We further assume that the interaction is screened at distances d, with  $L\gg d\gg a$ , where L is the size of the interferometer. This screening can occur due to the presence of the back gate, or the massive air bridge (see Ref. [32] for a more detailed discussion). As a consequence, we can neglect the dispersion of the Coulomb interaction and write  $U_C(x-y)=V\delta(x-y)$ , where the interaction constant,  $V\sim \ln(d/a)$ , is large. Finally, the interaction with an external electromagnetic field is described by

$$\mathcal{H}_{\text{int}}[\mathbf{a}] = -\int dx \rho_{\text{em}}(x) a_l(x), \qquad (7.12)$$

in the gauge  $a_x = 0$ .

In the limit when  $\ln(d/a) \gg 1$ , the Coulomb interaction exceeds the correlation energy. One of the most important consequences of this fact is that, independently of the form of free Hamiltonian, the full Hamiltonian is diagonal in the basis where

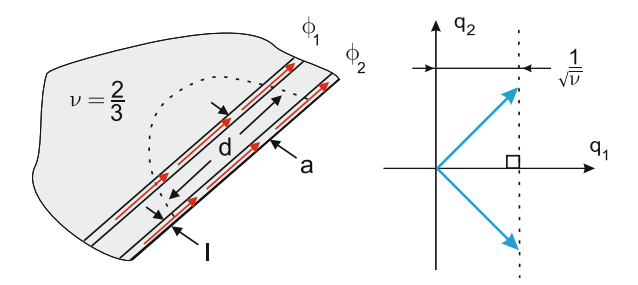


Fig. 7.2 Illustration of the effects of the strong long-range Coulomb interaction. *Left panel* shows important spatial scales at the quantum Hall edge: the width of the channels l, the distance between two channels a, and the screening length of the Coulomb interaction d. The universal limit is achieved when  $d \gg a$ , l. *Right panel* shows possible configuration of electronic excitations (*blue vectors*) in the universal strong interaction limit. Exactly this situation arises at v = 2, as shown in Ref. [32]. After Ref. [38]. © American Physical Society

one mode,  $\phi_1$ , is charged, with  $Q_1/2\pi \partial_x \phi_1 = \rho_{\rm em}$ , and the other one,  $\phi_2$ , is a dipole mode of total charge zero. Thus we can write

$$\mathcal{H} = \frac{1}{4\pi} \sum_{i} \int v_i (\partial_x \phi_i)^2 - \frac{1}{2\pi} Q_1 \int a_t \partial_x \phi_1, \tag{7.13}$$

where the speed of the charged mode,  $v_1 = \sigma_H V$ , is much larger than the speed  $v_2$  of the dipole mode determined by the free Hamiltonian (see the discussion at the end of Sect. 6.1.2). Comparing Eq. (7.13) with (6.24), we conclude that  $Q_2 = 0$ , which means that the dipole mode does not couple to the external electromagnetic field. The condition of the anomaly cancellation (6.25) therefore implies that  $Q_1 = \sqrt{\nu}$ . Thus, the angle between the vector Q and the  $q_1$ -axis is fixed to the universal value  $\vartheta_+ = 0$ . This is illustrated graphically in Fig. 7.2.

# 7.3 Experimental Determination of Scaling Dimensions of Quasi-Particles

# 7.3.1 Charge Current Through Interferometer

We have shown in Sect. 7.1 that there are several possible models for the filling factor  $\nu=2/3$  satisfying all the physical requirements formulated in Sect. 6.1. It is worth noticing that all these models have the same minimal fractional charge, 1/3, but different spectra of scaling dimensions. The experiment proposed in this section may allow one to determine scaling dimensions and, as a result, to identify the physically relevant model of the quantum Hall edge. This experiment is based on the idea to make use of an electronic Fabry-Perot interferometer.

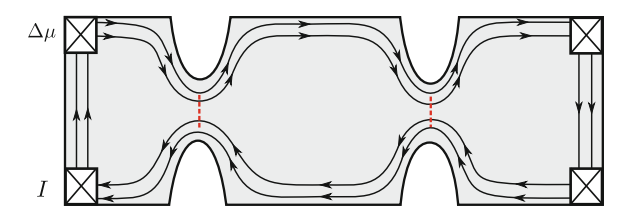


Fig. 7.3 A Fabry-Perot interferometer is schematically shown as a Hall bar, containing a two-dimensional electron gas, shown in *gray shadow*. In a strong magnetic field, at a filling factor v=2/3, two one-dimensional chiral channels are formed at the edges and propagate along the boundaries of the two-dimensional electron gas (shown by *thin black lines*). Both channels are partially transmitted at the left and right quantum point contacts. A bias voltage  $\Delta \mu$ , applied at the upper Ohmic contact, causes a current I to flow to the lower Ohmic contact. This current is caused by scattering of quasi-particles at the quantum point contacts (shown by *red*, *dashed lines*) and involves an interference contri bution sensitive to the magnetic flux  $\Phi$  that can be changed by a slight modulation of the length of one of the arms

Electronic Fabry-Perot interferometers have been realized and investigated experimentally in Refs. [51–57]. The experimental sample consists of a two-dimensional electron gas confined to a Hall bar (see Fig. 7.3). In the quantum Hall effect regime, several effectively one-dimensional conducting channels are formed at the edge. The modes in these edge channels are used as beams in the interferometer, while two quantum point contacts serve as beam splitters. Two Ohmic contacts connected to the Hall bar emit and absorb electrons. One contact is biased with a voltage  $\Delta\mu>0$ , and the other one is grounded and serves as a sink for a current I.

There are two paths for quasi-particles to travel from the upper Ohmic contact to the lower one. The first possibilities are to pass the left quantum point contact and to be reflected off the right one. The second possibility is to bounce off the left quantum point contact. It is easy to see that a nonzero magnetic flux is enclosed by these two paths. Consequently, the current *I* oscillates as a function of the magnetic flux through the interferometer. The Aharonov-Bohm flux may be varied with the help of a modulation gate near one of the arms of the interferometer that can slightly change the length of this arm.

We assume that there are several types of excitations, labeled by integers  $n_{\alpha}$ , which can tunnel between the arms at the quantum point contacts. They are created by operators

$$\psi_{\mathbf{n}} = \exp\left(i\sum_{j} p_{j}(\mathbf{n})\phi_{j}\right), \quad p_{j}(\mathbf{n}) = \sigma_{j}\sum_{\alpha} q_{\alpha j}^{-1} n_{\alpha}.$$
 (7.14)

Thus, the tunneling Hamiltonian is given by

$$\mathcal{H}_T = \sum_{\ell,\mathbf{n}} t_{\ell,\mathbf{n}} \psi_{U,\mathbf{n}}^{\dagger}(x_{\ell}) \psi_{D,\mathbf{n}}(x_{\ell}) + \text{h.c.} \equiv \sum_{\ell,\mathbf{n}} \left( A_{\ell,\mathbf{n}} + A_{\ell,\mathbf{n}}^{\dagger} \right), \tag{7.15}$$

where the subscripts U, D indicate that the quasi-particles are created and annihilated at the upper arm and at the lower arm of the interferometer (see Fig. 7.4). Moreover,  $t_{\ell,n}$  are the tunneling amplitudes of particles of type **n** at the left and right quantum point contacts,  $\ell = L$ , R. These amplitudes include the Aharonov-Bohm phase shift:

$$\arg \frac{t_{R,\mathbf{n}}}{t_{L,\mathbf{n}}} = 2\pi i \, Q_{\text{em}}(\mathbf{n}) \frac{\Phi}{\Phi_0},\tag{7.16}$$

where  $\Phi$  is the flux through the interferometer and  $\Phi_0 = hc/e$  is the flux quantum. The current through the interferometer is defined as a rate of change of the elec-

tromagnetic charge  $Q_{\rm em} = \sum_i (Q_i/2\pi) \int dx \, \partial_x \phi_i$  in one of the arms of the interferometer (see Fig. 7.4 for notations):

$$\hat{I} = i[\mathcal{H}, Q_{\text{em}}] = i[\mathcal{H}_T, Q_{\text{em}}]. \tag{7.17}$$

Calculating the commutator in Eq. (7.17) with  $\mathcal{H}_T$  as in Eq. (7.15), we arrive at the following expression for the current operator:

$$\hat{I} = \sum_{\ell, \mathbf{n}} i \, Q_{\text{em}}(\mathbf{n}) (A_{\ell, \mathbf{n}} - A_{\ell, \mathbf{n}}^{\dagger}). \tag{7.18}$$

We evaluate the average current,  $I = Tr(\hat{\rho}\hat{I})$ , to leading order in the tunneling amplitudes  $t_{\ell}$ 

$$I = \sum_{\ell,\ell',\mathbf{n}} Q_{\mathrm{em}}(\mathbf{n}) \int_{-\infty}^{+\infty} dt \langle [A_{\ell,\mathbf{n}}^{\dagger}(t), A_{\ell',\mathbf{n}}(0)] \rangle, \tag{7.19}$$

where the operators  $A_{\ell,n}^{\dagger}$ ,  $A_{\ell,n}$  are taken in the interaction representation, and averaging is defined as  $\langle ... \rangle := Tr \hat{\rho}_0(...)$ , where  $\hat{\rho}_0$  is the density operator of disconnected arms. In Eq. (7.19) we have taken into account that  $\langle \psi_{\bf n}^{\dagger} \psi_{\bf m} \rangle \propto \delta_{{\bf n},{\bf m}}$ , which is a consequence of zero-modes.

It is easy to see that Eq. (7.19) for the current is a sum of four terms:  $I = \sum_{\ell \ell'} I_{\ell \ell'}$ , where  $\ell, \ell' = L, R$ . The first two terms,

$$I_{\ell\ell} = \sum_{\mathbf{n}} Q_{\text{em}}(\mathbf{n}) \int_{-\infty}^{+\infty} dt \langle [A_{\ell,\mathbf{n}}^{\dagger}(t), A_{\ell,\mathbf{n}}(0)] \rangle, \tag{7.20}$$

correspond to incoherent tunneling at either one of the two quantum point contacts. The other two terms depend on the magnetic flux  $\Phi$  and lead to interference:

$$I_{\Phi} \equiv I_{LR} + I_{RL} = 2 \sum_{\mathbf{n}} Q_{\text{em}}(\mathbf{n}) \operatorname{Re} \int_{-\infty}^{+\infty} dt \langle [A_{R,n}^{\dagger}(t), A_{L,n}(0)] \rangle.$$
 (7.21)

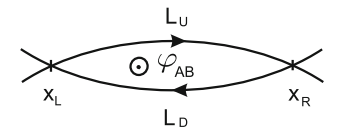


Fig. 7.4 Schematic representation of the Fabry-Perot interferometer. Quasi-particles of electric charge  $Q_{\rm em}(\mathbf{n})$  tunnel at points  $x_L$  and  $x_R$ , with tunneling amplitudes  $t_{L,\mathbf{n}}$  and  $t_{R,\mathbf{n}}$ , respectively. They propagate along paths of length  $L_U$  and  $L_D$  and acquire an Aharonov-Bohm phase  $\varphi_{AB} = 2\pi Q_{\rm em}(\mathbf{n})\Phi/\Phi_0$ . The upper arm is biased with  $\Delta\mu$ 

We focus our attention on the interference term, because it allows us to discriminate between contributions from different excitations. Using Eq. (7.15), we write:

$$I_{\Phi} = 2 \sum_{\mathbf{n}} Q_{\text{em}}(\mathbf{n}) \operatorname{Re} t_{L,\mathbf{n}} t_{R,\mathbf{n}}^{*} \int_{-\infty}^{+\infty} dt$$

$$\times \left\{ \langle \psi_{D,\mathbf{n}}(x_{R},t) \psi_{D,\mathbf{n}}^{\dagger}(x_{L},0) \rangle \langle \psi_{U,\mathbf{n}}^{\dagger}(x_{R},t) \psi_{U,\mathbf{n}}(x_{L},0) \rangle - \langle \psi_{D,\mathbf{n}}^{\dagger}(x_{L},0) \psi_{D,\mathbf{n}}(x_{R},t) \rangle \langle \psi_{U,\mathbf{n}}(x_{L},0) \psi_{U,\mathbf{n}}^{\dagger}(x_{R},t) \rangle \right\}. \tag{7.22}$$

The correlation functions are evaluated in Sect. 2.2. The result is:

$$i\langle \psi_{\mathbf{n}}^{\dagger}(x,t)\psi_{\mathbf{n}}(0,0)\rangle \propto \exp[i\varphi_{0}(\mathbf{n})]\prod_{i}\left\{\frac{v_{i}}{\pi T}\sinh[\pi T(t+\sigma_{i}\frac{x}{v_{i}})]\right\}^{-\delta_{i}(\mathbf{n})}.$$
 (7.23)

The phase  $\varphi_0(\mathbf{n})$  in this equation is determined by the structure of zero-modes and requires a separate consideration. Introducing zero-modes  $\varphi_i$  and  $\pi_i$  via  $\phi_i(x) = \varphi_i + 2\pi x\pi_i + osc.$ , we write the corresponding term in Eq. (7.13) as  $\mathcal{H}_0 = \pi W \sum_i v_i \pi_i^2$ , where W is the total size of the system. The total charge at an edge is given by  $Q_{\rm em} = W \langle \pi_1 \rangle$ . The expectation values of the zero-modes can be related to the applied voltage bias  $\Delta \mu$  by appealing to the well known electrostatic formula  $\Delta \mu = \delta \langle \mathcal{H}_0 \rangle / \delta Q_{\rm em}$ . From this equation it follows that  $\langle \pi_1 \rangle = \Delta \mu / v_1$ , while for the dipole mode  $\langle \pi_2 \rangle = 0$ , because it is not biased. We assume that charge fluctuations are negligible due to the large capacitances of edge channels connected to Ohmic contacts. Thus, the contribution of zero-modes is given by  $\langle e^{2\pi i p_j \pi_j (x + \sigma_j v_j t)} \rangle = e^{2\pi i p_j \langle \pi_j \rangle (x + \sigma_j v_j t)}$ . Substituting the expectation values of zero modes, we find the phase of correlation function (7.23):

<sup>&</sup>lt;sup>2</sup> We assume that both quantum point contacts are either in a weak tunneling regime or in a weak backscattering regime. Moreover, we further assume that two channels at each quantum Hall edge originate from the same Ohmic contact, and therefore, they are equally biased.

$$\varphi_0(\mathbf{n}) \equiv \sum_i p_i \langle \pi_i \rangle (x + \sigma_i v_i t) = \Delta \mu Q_{\text{em}}(t + \frac{x}{v_1}). \tag{7.24}$$

Apparently, this phase is *linear* in the bias  $\Delta \mu$ .

# 7.3.2 Low-Temperature and High-Temperature Behavior of Current

In the zero-temperature limit, T=0, the correlation functions are given by formula (6.41). The time integral in Eq. (7.22), at small biases  $\Delta\mu\ll v_i/L_\alpha$ ,  $\alpha=U$ , D, then yields

$$I_{\Phi} = \sum_{\mathbf{n}} C_{\mathbf{n}} (\Delta \mu)^{2\Delta(\mathbf{n}) - 1} \cos \left[ 2\pi Q_{\text{em}}(\mathbf{n}) \frac{\Phi}{\Phi_0} \right], \tag{7.25}$$

where the  $C_n$  are some (unimportant) constants. In the high-temperature limit, correlation function (7.23) scales as

$$i\langle \psi_{\mathbf{n}}^{\dagger}(x,t)\psi_{\mathbf{n}}(0,0)\rangle \propto \exp\left[-\sum_{i}\pi T\delta_{i}(\mathbf{n})|t+\sigma_{i}\frac{x}{v_{i}}|\right].$$
 (7.26)

With help of this expression, we can calculate the high-temperature asymptotics of the tunneling current. Substituting the correlation function (7.26) into Eq. (7.22), we obtain the following integral:

$$I_{\Phi} \propto \mathbf{Re} \int_{-\infty}^{+\infty} dt \, e^{i\Delta\mu t} T^{2\Delta(\mathbf{n})} e^{-\pi T \sum_{i,\alpha} |t + \sigma_i L_{\alpha}/v_i| \delta_i(\mathbf{n})}. \tag{7.27}$$

In the limit  $T \gg \Delta \mu$ , we approximate  $e^{i\Delta\mu t} \simeq 1 + i\Delta\mu t$ , where only the second term makes a non-zero contribution:

$$I_{\Phi} \propto \Delta \mu T^{2\Delta(\mathbf{n})} \int_{-\infty}^{+\infty} dt \, t \cdot e^{-\pi T \sum_{i,\alpha} |t + \sigma_i L_{\alpha}/v_i| \delta_i(\mathbf{n})}. \tag{7.28}$$

In the high-temperature limit, the largest contribution to this integral comes from a small region around one of the points  $t = -\sigma_i L_\alpha/v_i$ , where the argument of the exponential function acquires the smallest absolute value. Then the time integral can be estimated as

$$\int_{-\infty}^{+\infty} dt \, t \cdot e^{-\pi T \sum_{i,\alpha} |t + \sigma_i L_{\alpha}/v_i|\delta_i(\mathbf{n})} \propto T^{-1} e^{-\pi T/T_0(\mathbf{n})}, \tag{7.29}$$

where the energy scale  $T_0(\mathbf{n})$  is given by

$$\frac{1}{T_0(\mathbf{n})} = \min_{\alpha',i'} \sum_{\alpha,i} \delta_i(\mathbf{n}) \left| \frac{\sigma_i L_{\alpha}}{v_i} - \frac{\sigma_{i'} L_{\alpha'}}{v_{i'}} \right|. \tag{7.30}$$

Using this result, we finally arrive at the asymptotics of the oscillating part of the current of the following form:

$$\frac{I_{\Phi}}{\Delta \mu} = \sum_{\mathbf{n}} C_{\mathbf{n}}' T^{2\Delta(\mathbf{n}) - 1} e^{-\pi T / T_0(\mathbf{n})} \cos \left[ 2\pi Q_{\text{em}}(\mathbf{n}) \frac{\Phi}{\Phi_0} \right], \tag{7.31}$$

where the  $C'_{\mathbf{n}}$  are some constants. For a symmetric interferometer, in the limit  $v_1 \gg v_2$ , Eq. (7.30) for characteristic energy simplifies to

$$T_0^{-1}(\mathbf{n}) = \min(\delta_1(\mathbf{n}), \delta_2(\mathbf{n})) \frac{L}{v_2}.$$
 (7.32)

The range of applicability of our result (7.25) is limited by the conditions  $\Delta\mu \ll v_i/L_\alpha$ ,  $\alpha=U$ , D. Outside of this range, the dependence of the visibility on the bias is non-monotonic, because of charging effects, as has been observed in the experiments [27–30]. Moreover, the behavior (7.25) is valid only if  $\Delta\mu > T$ . For typical experiments [51–57] this implies that  $1\mu V < \Delta\mu < 10\mu V$ . We conclude that it would not be easy, but possible in principle, to extract the exponents of the power-law behavior in Eq. (7.25).

To summarize, the large periods of oscillations can be used to discriminate between different effective models. Namely, they can be fitted by measuring the current through the interferometer as a function of the magnetic flux  $\Phi$  and of the bias  $\Delta\mu$ . Evaluating the Fourier transform with respect to  $\Phi$ , one can investigate the scaling in  $\Delta\mu$  of different harmonics corresponding to contributions of the most relevant excitations for any charge  $Q_{\rm em}$ . To identify the correct model, one must compare the experimentally measured scaling dimensions  $\Delta$  with those in the table of Sect. 7.1. Once the correct model (i.e., its K-matrix) is identified, one may use the temperature dependence (7.31) as an independent check of the theory.

#### 7.4 Conclusion

In the last decade, several proposals for experimental tests of the physics at a quantum Hall edge have been made. They are based on measurements of the electric charge,

7.4 Conclusion 139

the statistical phases and the scaling dimensions of quasi-particles. Some of them have been realized and have shed light on the properties of fractional quantum Hall edges. However, some experiments have brought up open questions. For instance, in the experiment [13], the I-V curve has shown a perfect power-law behavior. However, the measured exponents, which are thought to be proportional to the scaling dimensions of the quasi-particle operators, have turned out to be different from those predicted by theory. Thus, electronic interferometers, which have already shown several interesting features, may be considered to be promising tools for probing the properties of the quantum Hall edge.

These interferometers might be especially useful in the problem of determination of effective model for complex filling fractions. We have applied the classification of effective models to the example of fluids with filling fraction  $\nu=2/m$ , and, in particular, with  $\nu=2/3$ . We have shown that for  $\nu=2/3$  there are at least four inequivalent models satisfying all physical conditions and having the smallest possible number of fields. It is important to note that, in every effective model, the minimal fractional charge is 1/3.

For models with two fields, we have shown that Coulomb interactions lead to universal values of electromagnetic couplings. This universality allowed us to evaluate the scaling dimensions of quasi-particles, see (6.44), with the result given in Eq. (7.5). We have calculated the Aharonov-Bohm-oscillating contribution to the current through a Fabry-Perot interferometer at low and high temperatures, Eqs. (7.25) and (7.31), and shown that the Fourier spectrum of the current as a function of the flux can be used to extract the scaling dimensions of quasi-particle operators. This, in turn, leads to the opportunity to discriminate between different effective models.

Our method of identifying the correct model can be applied to fluids with arbitrary filling fractions and can be summarized as follows:

- First, for a given filling fraction  $\nu$ , one should find solutions of Eq. (6.34) for K-matrices, up to equivalence, as described in Eq. (6.40). In other words, one must identify the effective models satisfying the physical requirements formulated in Sect. 6.1. The most interesting solutions are those with the smallest possible number of fields and minimal statistical phases of electron field operators.
- Second, using Eqs. (6.39) and (6.44), one should calculate the spectra of charges and scaling dimensions for every model.
- Finally, one should attempt to measure the  $\Delta\mu$ -scaling of the Fourier components of the current trough a Fabry-Perot interferometer and compare it with theoretical predictions, in order to identify a correct model.

It is interesting to generalize our approach, which takes into account the strong Coulomb interaction, to fractions such as v = 5/2, which are possibly described by non-Abelian quantum Hall states. The first works which investigate the role of the Coulomb interaction in the bulk of quantum Hall interferometers [58, 59] have shown a great success. Thus, taking into account the Coulomb interaction at the edge of v = 5/2 states might be a reasonable *next step*.

#### References

- 1. G. 't Hooft, Proceedings of the Salamfest, 0284–0296 (1993)
- 2. L. Susskind, J. Math. Phys. 36, 6377 (1995)
- 3. E. Witten, Adv. Theor. Math. Phys. 2, 253 (1998)
- 4. O. Aharony, S.S. Gubser, J.M. Maldacena, H. Ooguri, Y. Oz, Phys. Rep. 323, 183 (2000)
- 5. R.E. Prange, S.M. Girvin (eds.) *The Quantum Hall Effect* (Springer, New York, 1987)
- 6. X.-G. Wen, Phys. Rev. B 41, 12838 (1990)
- 7. J. Fröhlich, A. Zee, Nucl. Phys. B **364**, 517 (1991)
- 8. J. Fröhlich, T. Kerler, Nucl. Phys. B **354**, 369 (1991)
- 9. J. Fröhlich, B. Pedrini, C. Schweigert, J. Walcher, J. Stat. Phys. 103, 527 (2001)
- 10. J. Fröhlich, U.M. Studer, E. Thiran, J. Stat. Phys. **86**, 821 (1997)
- 11. X.-G. Wen, Phys. Rev. B 44, 5708 (1991)
- 12. A.M. Chang, L.N. Pfeiffer, K.W. West, Phys. Rev. Lett. 77, 2538 (1996)
- 13. M. Crayson, D.C. Tsui, L.N. Pfeiffer, K.W. West, A.M. Chang, Phys. Rev. Lett. 80, 1062 (1998)
- 14. For a review, see A.M. Chang, Rev. Mod. Phys. **75**, 1449 (2003)
- 15. D.B. Chklovskii, B.I. Shklovskii, L.I. Glazman, Phys. Rev. B 46, 4026 (1992)
- 16. C.L. Kane, M.P. Fisher, J. Polchinski, Phys. Rev. Lett. 72, 4129 (1994)
- 17. C.L. Kane, M.P.A. Fisher, Phys. Rev. B **51**, 13449 (1995)
- 18. S. Khlebnikov, Phys. Rev. B 73, 045331 (2006)
- 19. C.L. Kane, M.P.A. Fisher, Phys. Rev. Lett. 72, 724 (1994)
- 20. L. Saminadayar, D.C. Glattli, Y. Jin, B. Etienne, Phys. Rev. Lett. 79, 2526 (1997)
- R. de-Picciotto, M. Reznikov, M. Heiblum, V. Umansky, G. Bunin, D. Mahalu, Nature 389, 162 (1997)
- 22. M. Dolev, M. Heiblum, V. Umansky, A. Stern, D. Mahalu, Nature 452, 829 (2008)
- 23. F.E. Camino, W. Zhou, V.J. Goldman, Phys. Rev. Lett. 95, 246802 (2005)
- 24. Y. Ji et al., Nature (London) 422, 415 (2003)
- 25. V.V. Ponomarenko, D.V. Averin, Phys. Rev. Lett. 99, 066803 (2007)
- 26. R. Guyon, P. Devillard, T. Martin, I. Safi, Phys. Rev. B 65, 153304 (2002)
- 27. I. Neder, M. Heiblum, Y. Levinson, D. Mahalu, V. Umansky, Phys. Rev. Lett. 96, 016804 (2006)
- 28. L.V. Litvin, H.-P. Tranitz, W. Wegscheider, C. Strunk, Phys. Rev. B 75, 033315 (2007)
- L.V. Litvin, A. Helzel, H.-P. Tranitz, W. Wegscheider, C. Strunk, Phys. Rev. B 78, 075303 (2008)
- 30. I. Neder, F. Marquardt, M. Heiblum, D. Mahalu, V. Umansky, Nat. Phys. 3, 534 (2007)
- 31. E.V. Sukhorukov, V.V. Cheianov, Phys. Rev. Lett. 99, 156801 (2007)
- 32. I.P. Levkivskyi, E.V. Sukhorukov, Phys. Rev. B 78, 045322 (2008)
- 33. J.T. Chalker, Y. Gefen, M.Y. Veillette, Phys. Rev. B **76**, 085320 (2007)
- 34. I. Neder, E. Ginossar, Phys. Rev. Lett. 100, 196806 (2008)
- 35. S.-C. Youn, H.-W. Lee, H.-S. Sim, Phys. Rev. Lett. 100, 196807 (2008)
- 36. I.P. Levkivskyi, E.V. Sukhorukov, Phys. Rev. Lett. **103**, 036801 (2009)
- 37. X. Zhu, S.G. Louie, Phys. Rev. B **52**, 5863 (1995)
- 38. I.P. Levkivskyi, A. Boyarsky, J. Fröhlich, E.V. Sukhorukov, Phys. Rev. B 80, 045319 (2009)
- 39. X.G. Wen, Phys. Rev. Lett. 64, 2206 (1990)
- 40. A.H. MacDonald, Phys. Rev. Lett. 64, 220 (1990)
- 41. M.D. Johnson, A.H. MacDonald, Phys. Rev. Lett. 67, 2060 (1991)
- 42. J.K. Jain, Phys. Rev. Lett. 63, 199 (1989)
- 43. Z.-X. Hu, H. Chen, K. Yang, E.H. Rezayi, X. Wan, Phys. Rev. B 78, 235315 (2008)
- R.G. Clark, S.R. Haynes, J.V. Branch, A.M. Suckling, P.A. Wright, P.M.W. Oswald, J.J. Harris, C.T. Foxon, Surf. Sci. 229, 25 (1990)
- 45. J.P. Eisenstein, H.L. Stormer, L.N. Pfeiffer, K.W. West, Phys. Rev. B 41, 7910 (1990)
- 46. L.W. Engel, S.W. Hwang, T. Sajoto, D.C. Tsui, M. Shayegan, Phys. Rev. B 45, 3418 (1992)
- 47. P. Roulleau, F. Portier, D.C. Glattli, P. Roche, A. Cavanna, G. Faini, U. Gennser, D. Mailly, Phys. Rev. B 76, 161309 (2007)

References 141

48. P. Roulleau, F. Portier, D.C. Glattli, P. Roche, A. Cavanna, G. Faini, U. Gennser, D. Mailly, Phys. Rev. Lett. 100, 126802 (2008)

- E. Bieri, Correlation and interference experiments with edge states, Ph.D. Thesis, University of Basel, 2007
- E. Bieri, M. Weiss, O. Goktas, M. Hauser, C. Schonenberger, S. Oberholzer, Phys. Rev. B 79, 245324 (2009)
- 51. F.E. Camino, W. Zhou, V.J. Goldman, Phys. Rev. B 72, 075342 (2005)
- 52. F.E. Camino, W. Zhou, V.J. Goldman, Phys. Rev. Lett. 98, 076805 (2007)
- 53. F.E. Camino, W. Zhou, V.J. Goldman, Phys. Rev. B 74, 115301 (2006)
- 54. R.L. Willett, L.N. Pfeiffer, K.W. West, PNAS **106**, 8853 (2009)
- 55. R.L. Willett, L.N. Pfeiffer, K.W. West, arXiv:0911.0345
- 56. J.A. Simmons, H.P. Wei, L.W. Engel, D.C. Tsui, M. Shayegan, Phys. Rev. Lett. 63, 1731 (1989)
- J.A. Simmons, S.W. Hwang, D.C. Tsui, H.P. Wei, L.W. Engel, M. Shayegan, Phys. Rev. B 44, 12933 (1991)
- 58. B. Rosenow, B.I. Halperin, Phys. Rev. Lett. 98, 106801 (2007)
- 59. B.I. Halperin, A. Stern, I. Neder, B. Rosenow, Phys. Rev B 83, 155440 (2011)

# Chapter 8 Microscopic Theory of Fractional Quantum Hall Interferometers

Since its discovery, in 1980, the quantum Hall effect [1] has been a very rich source of interesting problems related to topological and correlation effects in condensed matter systems. As we have mentioned in the introduction, it has been predicted [2–4] that, at fractional fillings of the Landau levels, besides the collective modes the quantum Hall edge states of the two-dimensional electron gas also describe quasi-particles with *fractional charges* and fractional statistics [5]. For instance, in quantum Hall liquids with filling factor  $\nu = 1/m$ , where m is an odd integer, Laughlin quasi-particle excitations have an electric charge  $e^* = e/m$ , where e is the elementary electric charge, and anyonic statistics. Such excitations can be scattered between opposite edges at narrow constrictions forming quantum point contacts, thus contributing to a backscattering current.

The fractional charge of Laughlin quasi-particles has been confirmed experimentally in measurements of the shot noise of weak backscattering currents [6, 7]. The quasi-particle charge in these experiments is inferred from the Fano factor of noise, which is the ratio of the noise power to the average backscattering current. Although, at present, there is a consensus on the interpretation of the experimental results, this type of measurement does not, in general, represent a direct test of the fractional charge of quasi-particles. Indeed, the Fano factor of noise is not universal and may be reduced or enhanced for various reasons [9]. For instance, the so called "charge fractionalization" in nonchiral one-dimensional systems [10, 11] is a property of collective modes that has nothing to do with the existence of fractionally charged quasi-particles. Nevertheless, this phenomenon reduces the Fano factor of noise at relatively high frequencies.<sup>2</sup>

<sup>&</sup>lt;sup>1</sup> Very recently, unexpected values of quasi-particle charges, determined via shot noise measurements, have been reported in [8]. These results may indicate that the Fano factor of a weak backscattering current is not determined solely by the quasi-particle charge.

<sup>&</sup>lt;sup>2</sup> The use of the term "charge fractionalization" in this context is somewhat unfortunate, because, in contrast to the quasi-particle fractionalization, the corresponding process is completely classical in nature. In fact, it is very similar to the displacement current in electrical circuits.

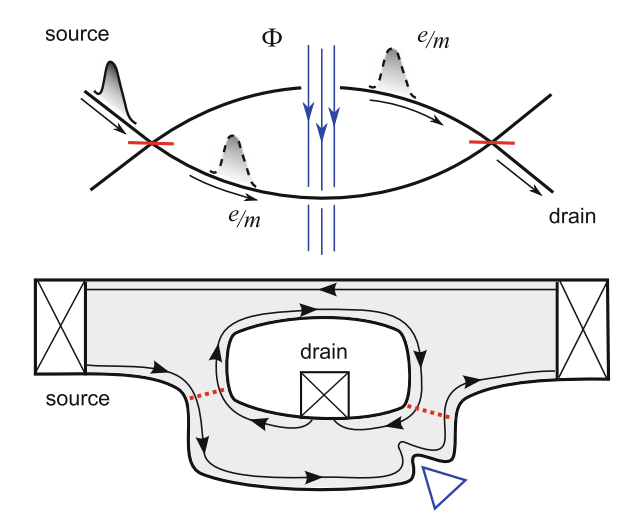


Fig. 8.1 An electronic analogue of an optical Mach–Zehnder interferometer is shown schematically. Upper panel shows a gedanken formulation of the Aharonov–Bohm effect: Quasi-particles with fractional charge e/m propagate from a source to a drain via two beam splitters, and enclose a singular magnetic flux  $\Phi$ . Lower panel shows a schematic sketch of a typical experimental realization of the Mach–Zehnder interferometer in a quantum Hall system [14–22]. Chiral edge states, shown by arrows, play the role of optical beams. They are split at two quantum point contacts indicated by dashed lines. The source and drain are Ohmic contacts. The quantum Hall liquid is confined to a region with the topology of a Corbino disk (indicated by gray shading). The magnetic flux through the interferometer is typically changed by a modulation gate, shown as a blue triangle. However, it is possible, at least in principle, to insert a singular magnetic flux through the hole in the Corbino disk

A direct measurement of the quasi-particle charge should rely on its definition as a coupling constant in the interaction Hamiltonian which couples matter to the electromagnetic field and on the quantum nature of quasi-particles. The most appealing approach is to make use of the Aharonov–Bohm effect [12, 13], which relies on the fact that the interference of quasi-particles is affected by a magnetic flux. Following a commonly used formulation of this effect, we consider a gedanken interference experiment shown in the upper panel of Fig. 8.1. Quasi-particles of charge e/mtraverse two beam splitters and follow paths that enclose a singular magnetic flux Φ. The relative phase between the two amplitudes, for the upper and lower path, is shifted by an amount of  $2\pi\Phi/m\Phi_0$ , which leads to Aharonov–Bohm oscillations in the current from the source to the drain as a function of the flux  $\Phi$  with quasiparticle period  $m\Phi_0$ . Then the quasi-particles can be detected by differentiating their contribution to the Aharonov-Bohm effect from electron oscillations with period  $\Phi_0$ . Such gedanken experiment can be realized in electronic quantum Hall interferometers, studied extensively in recent experimental [14–32] and theoretical [33–40] works, in particular, in a Mach-Zehnder interferometer shown schematically in the lower panel of Fig. 8.1.

## 8.1 Byers-Yang Paradox

The gedanken formulation of the Aharonov–Bohm effect however leads to a paradox: in any electronic system, including fractional quantum Hall systems, Aharonov–Bohm oscillations should have an electronic period  $\Phi_0$ , according to the Byers–Yang theorem [41]. This is so, because, after adiabatic insertion of a flux quantum through a hole in the sample, an electronic system relaxes to its initial state, since the flux quantum can be removed by a single-valued gauge transformation.

Indeed, let us consider the gedanken experiment, illustrated in upper panel of Fig. 8.1. In this formulation, the interferometer consists of two quantum Hall edges of infinite length coupled at two quantum point contacts located at the points  $\xi_L$  and  $\xi_R$ . We denote the boson field describing the upper and lower arms of the interferometer as  $\phi_U(x)$  and  $\phi_D(x)$  correspondingly. The system shown in Fig. 8.1 is open, therefore one can neglect zero modes in the expansion (1.62) for these fields. Next, we describe quasi-particle tunneling with tunneling operators

$$\mathcal{A}_{qp}(\xi_{\ell}) = e^{i\phi_D(x_{\ell})} e^{-i\phi_U(x_{\ell}')}, \tag{8.1}$$

where  $\ell=L$ , R. To leading order in tunneling operators (8.1), the oscillating contribution to the current through the interferometer is given by  $I=2{\rm Re}\int dt \langle [{\cal A}_{\rm qp}^\dagger(\xi_L,t),{\cal A}_{\rm qp}(\xi_R,0)]\rangle$ . Using Eq. (1.58) and integrating out the field  $B_\mu$ , we find that the phase of the oscillating term is given by  $(1/m)\int_\gamma A_\mu dx^\mu$ , where  $\gamma$  is the contour around the interferometer. In the situation, where the singular flux  $\Phi$  threads the interferometer we find that

$$\mathcal{A}_{\mathrm{qp}}(\xi_L)^{\dagger} \mathcal{A}_{\mathrm{qp}}(\xi_R) \propto \exp\left(\frac{2\pi i \Phi}{m\Phi_0}\right),$$
 (8.2)

i.e., the period of Aharonov–Bohm oscillation is  $m\Phi_0$ , contrary to the Byers–Yang theorem. Apparently, the problem with the naive approach arises because it considers a Mach–Zehnder interferometer as an infinite system. In order to resolve the paradox, we need to consider a realistic, finite quantum Hall systems, even if it is strongly coupled to Ohmic reservoirs, as shown in the lower panel of Fig. 8.1. In what follows, we address the problem on the microscopic level, and then compare the results to the effective theory predictions.

There have been several theoretical attempts to resolve this paradox [42–48]. In early work [45, 46], Thouless and Gefen have considered the energy spectrum of a quantum Hall liquid confined to a Corbino disk and weakly coupled to Ohmic contacts, see Fig. 8.2. They have found that as a result of weak quasi-particle tunneling between the inner and the outer edge of the Corbino disk, the energy spectrum, and consequently, "any truly thermodynamic quantity" is a periodic function of the magnetic flux with the electronic period  $\Phi_0$ . Although Thouless and Gefen have made an important first step towards understanding the Aharonov–Bohm effect in quantum Hall interferometers, their analysis is rather qualitative, and some of their

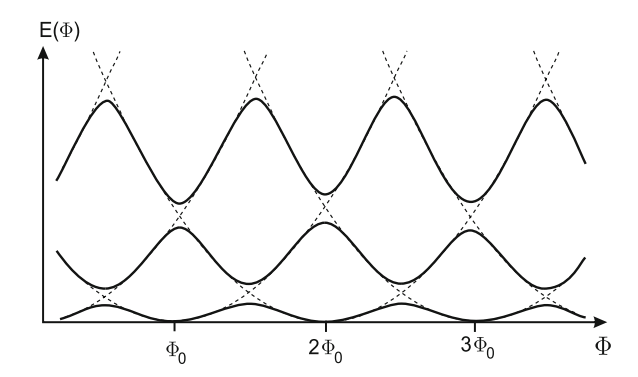


Fig. 8.2 The energy spectrum of a quantum Hall fluid at  $\nu=1/3$  in a Corbino disk is schematically shown. The *dashed lines* show the Coulomb charging energy of an isolated quantum Hall fluid, as a function of the magnetic flux  $\Phi$  threading the Corbino disk. Different branches correspond to different numbers of quasi-particles at the edges. It is suggested in Refs. [45, 46] that in the presence of inter-edge quasi-particle tunneling, and for weak coupling to metallic reservoirs, an energy gap opens at the degeneracy points, where different branches intersect. The authors then argue that if the flux varies adiabatically, the quantum Hall fluid follows the ground state, so that the energy is a periodic function of the flux with the electronic period  $\Phi_0$ 

statements concerning the tunneling rates and currents are not firmly justified.<sup>3</sup> The results of their work are difficult to interpret at the level of effective theories. But, more importantly, they cannot easily be generalized to the situation where the magnetic flux is varied with the help of a gate voltage. This situation has stimulated further interest in the fractional Aharonov–Bohm effect.

More recently, a number of authors (see Refs. [42, 43, 47, 48]) have proposed that the correct description of the Mach–Zehnder interferometers should take into account the presence of additional quantum numbers in a quantum Hall state. In the thermodynamic limit, averaging the quasi-particle current over these quantum numbers is claimed to restore the electronic Aharonov–Bohm periodicity. These quantum numbers are usually introduced ad hoc, with minimal justification. Depending on the particular theoretical discussion, they are represented either in terms of so called Klein factors in the tunneling operators [49], or as additional phase shifts induced by quasi-particles localized at the inner edge of the Corbino disk [43]. We are aware of only one attempt to justify theoretically the introduction of Klein factors in Mach–Zehnder interferometers: in their recent work [44], Ponomarenko and Averin implement a resummation of electron tunneling processes between the inner and outer edge and claim that there is a duality to weak quasi-particle tunneling, where the Klein factors arise naturally. However, their analysis is done entirely at the level of an effective theory, where weak quasi-particle and weak electron tunneling

<sup>&</sup>lt;sup>3</sup> Note, in particular, that the average values of physical observables are not determined solely by the energy spectrum of a system, but also by the matrix elements of the observables. Thus, one is not able to make a definitive conclusion on the periodicity of observables based on the consideration of the spectrum alone.

are the two fixed points of a renormalization group flow. There is no guarantee that microscopic considerations will yield the same result.

## 8.2 Outline of Microscopic Theory

In view of shortcomings of previous theoretical arguments, we reconsider the physics of quantum Hall interferometers on the microscopic level. Namely, we propose a microscopic model of a quantum Hall interferometer with the Corbino disk topology, schematically shown in Fig. 8.3. A quantum Hall liquid at filling factor  $\nu = 1/m$ , confined to a region between two circles of radii  $r_U$  and  $r_D$ , is described by Laughlintype wave functions (8.3) and (8.4). The inner and outer edges of the quantum Hall liquid are connected to Ohmic contacts at points  $\xi_U$  and  $\xi_D$  via strong electronic tunneling. Weak quasi-particle backscattering at two quantum point contacts is indicated in Fig. 8.3 by dashed lines. It is described by the overlap of Laughlin states with an additional quasi-hole located at points  $\xi_L$  and  $\xi_L'$  for the left quantum point contact, and at  $\xi_R$  and  $\xi_R'$  for the right one. The position of Ohmic contacts with respect to quantum point contacts determines whether the interferometer is of the Mach–Zehnder or Fabry–Perot type, as illustrated in Fig. 8.6 below. We generalize the Laughlin wave function (8.3) and (8.4) in order to take into account the deformation of quantum Hall edges caused by the modulation gate and Ohmic contacts. Exactly same procedure may be applied in order to describe more realistic quantum point contacts, for which  $\xi_L \simeq \xi_L'$  and  $\xi_R \simeq \xi_R'$ .

We then use weakly deformed Lauglin states to construct the subspace of lowenergy excitations of a quantum Hall system. The microscopic wave function (8.5) and (8.6), resulting from weak incompressible deformations, is parameterized by an infinite set of variables  $t_k$ . We invoke the classical plasma analogy [5] and follow the steps of Ref. [50] in order to project the microscopic Hamiltonian onto the subspace of these deformations. After the projection, the variables  $t_k$  turn into oscillator operators  $a_k$  with canonical commutation relations (8.32). These operators describe *gapless* plasmon excitations at the edge of the quantum Hall liquid. The projected Hamiltonian (8.41) contains the oscillator part with a linear spectrum and the Coulomb charging energy, which depends on the number of quasi-particles, M, and the number of electrons, N, in the quantum Hall system. The projected tunneling operators take the form of vertex operators (8.49). They are well defined single-valued operators, in contrast to quasi-particle operators taken alone. Interestingly, we do not find any trace of additional Klein factors [49] in the tunneling amplitudes.

So derived low-energy theory agrees well with the effective theory of quantum Hall edge states [2–4], generalized to take into account the finite size of a quantum Hall system, the non-trivial topology of a Corbino disk, and the effects of a modulation gate and of a singular magnetic flux. The effective theory arises as a boundary contribution to the topological Chern–Simons field theory [51] of a quantum Hall state in the bulk of two-dimensional electron gas in the presence of external electromagnetic field. In the context of this theory, our microscopic results for the relative phase of the

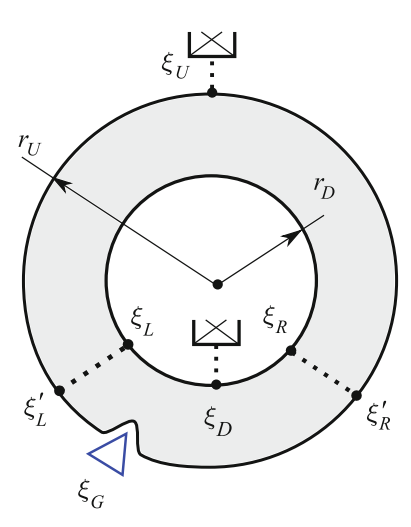


Fig. 8.3 Illustration of our model of a quantum Hall interferometer. The two-dimensional electron gas in the quantum Hall effect regime is confined to a Corbino disk region, shown by grey shadow. The inner and outer edge of the two-dimensional electron gas are circles of radii  $r_D$  and  $r_U$ , respectively. At the points  $\xi_U$  and  $\xi_D$  the Corbino disk is connected to Ohmic reservoirs. The location of the inner Ohmic contact is such that the particular interferometer shown here is of the Mach–Zehnder type. If, in contrast, the inner Ohmic contact is attached to the upper part of the Corbino disk, then such an interferometer belongs to a Fabry–Perot type. The quasi-particle tunneling between the inner and the outer edge takes place at two quantum point contacts, shown by dashed lines, that connect the points  $\xi_\ell$  and  $\xi_\ell'$ , with  $\ell=L$ , R

tunneling amplitudes taken at different spatial points acquire a simple meaning: it can be viewed as a phase picked up by a Wilson loop along the interferometer contour (8.67). There are two contributions to this phase: one is the contour integral of the gauge fields, the other one comes from the charge accumulated at the edges.

Having constructed the low-energy theory of an isolated quantum Hall system, we proceed with the analysis of the quasi-particle transport through the interferometer in response to the voltage bias applied to Ohmic contacts. In our model, Ohmic reservoirs have large capacitances, therefore they perfectly screen edge charges. In other words, any variations of zero modes, gate voltages, or a magnetic flux lead to the charge accumulation at Ohmic contacts, which is described by a local deformation of the edge. This property of Ohmic contacts agrees with the observation [52] that on the effective theory level strong coupling to Ohmic contacts leads to a strong local elongation of edge states near Ohmic contacts. We treat electron and quasi-particle tunneling perturbatively to describe rare transitions that change the numbers  $N_D$  and  $N_U$  of electrons at the inner and outer edge of the Corbino disk, respectively, and the number,  $l=0,\ldots,m-1$ , of quasi-particles at the inner edge. The dynamics of the interferometer on a long time scale is described by a master equation for the probability of finding the system in a state with certain values of the numbers  $N_D$ ,  $N_U$ , and l. Strong coupling to Ohmic contacts, as compared to quasi-particle

tunneling, leads to the equilibration of inner and outer edge states with corresponding electro-chemical potentials.

Solving the master equation in the quasiparticle sector, we finally find the stationary current through the interferometer as a function of the singular magnetic flux  $\Phi$  and the flux  $\Phi_G$  induced by the modulation gate voltage, thereby establishing the main result of this chapter. Namely, we find that quasi-particle tunneling rates in the case of a quantum Hall interferometer with the Mach–Zehnder topology (see Fig. 8.6) depend on the magnetic flux via the combination  $(\Phi + \Phi_G)/\Phi_0 + l$ . Therefore, after the summation over the number l, the Aharonov–Bohm oscillations in the stationary current acquire the electronic periodicity simply because the shift of the flux by the quantum  $\Phi_0$  is compensated by the shift of l by 1. And conversely, for a quantum Hall interferometer with the Fabry–Perot topology, tunneling rates are independent of the singular flux  $\Phi$  and the number l, therefore the stationary current oscillates as a function of  $\Phi_G$  with the quasi-particle period  $m\Phi_0$ . In both cases the Byers–Yang argument is satisfied, and the paradox is resolved.

The rest of this chapter is organized as follows. In Sect. 8.3 we construct the ground state wave function of an electronic interferometer in the fractional quantum Hall effect regime. In Sect. 8.4 we derive the low-energy theory of the interferometer by projecting the microscopic Hamiltonian and quasi-hole wave function overlaps onto the subspace of states corresponding to small incompressible deformations of a quantum Hall liquid. In Sect. 8.5, we propose a model of Ohmic contacts, consider the effects of a singular magnetic flux and of a modulation gate, and develop the kinetic theory of an open quantum Hall interferometer away from equilibrium.

# 8.3 Microscopic Description of a Quantum Hall Interferometer

In this section we construct the many-particle wave functions of the ground state and of gapless excited states of an *isolated* quantum Hall interferometer with the Corbino disk topology, and extend our results to the case of an *open*, connected to Ohmic reservoirs, interferometer in Sect. 8.5. We do this step by step, starting from the Laughlin wave function and manipulating it, in order to arrive at a realistic model of the interferometer. We first present the most important steps before we prove them in Sect. 8.3.1, using the classical plasma analogy [5]. The variational wave function, proposed by Laughlin in Ref. [5] and later justified by Haldane and Rezayi in Refs. [53, 54], describes an approximate ground state,  $|N\rangle$ , of a quantum Hall system with N electrons at filling factor  $\nu = 1/m$ :

$$\langle \underline{z} | N \rangle = \prod_{i < j}^{N} (z_i - z_j)^m \exp\left(-\sum_{i=1}^{N} \frac{|z_i|^2}{4l_B^2}\right).$$
 (8.3)

Here  $\underline{z}$  denotes a set of complex coordinates  $z_i = x_i + iy_i$  describing the position of the *i*th electron,  $i = 1 \dots N$ , and  $l_B = \sqrt{\hbar c/eB}$  is the magnetic length. It is known

[55] that the wave function (8.3) describes a circular droplet of a quantum Hall liquid of constant density  $\rho_{\rm bg} = 1/(2\pi m l_R^2)$  and of radius  $r = l_B \sqrt{2mN}$ .

In the next step, we add to the state (8.3) a macroscopic number, M, of Laughlin quasi-particles [5] at the origin:

$$\langle \underline{\mathbf{z}} | N, M \rangle = \prod_{i}^{N} z_{i}^{M} \langle \underline{\mathbf{z}} | N \rangle. \tag{8.4}$$

In Sect. 8.3.1 we explicitly show that the wave function (8.4) describes a quantum Hall state of constant electron density  $\rho_{\rm bg}$  inside a Corbino disk, as shown in Fig. 8.3. The inner hole of the disk has a radius  $r_D = l_B \sqrt{2M}$ , while the outer radius of the disk is given by  $r_U = l_B \sqrt{2(M+mN)}$ .

Additional small incompressible deformations of the quantum Hall liquid disk may be described as follows. We note that all states of the lowest Landau level can be described by holomorphic functions of electron coordinates. We therefore look for a wave function of the form [50, 56]

$$\langle \underline{\mathbf{z}} | N, M, \underline{\mathbf{t}} \rangle = \exp \left[ m \sum_{i}^{N} \omega(z_{i}) \right] \langle \underline{\mathbf{z}} | N, M \rangle,$$
 (8.5)

where the function

$$\omega(z) = \sum_{k} t_k z^k \tag{8.6}$$

is analytic inside the Corbino disk (shown in Fig. 8.3), and  $\underline{t}$  denotes a set of parameters  $t_k$ ,  $k \in \mathbb{Z}$ . In Sect. 8.3.1 we show that the shape of the deformed disk is given by the solution of a two-dimensional electrostatic problem, with  $\omega(z)$  playing role of an external potential.

We utilize the wave function (8.5) in two ways. First of all, small incompressible deformations are known to be the gapless excitations of the quantum Hall state [55]. Therefore, in order to describe the low-energy physics, we will use the wave functions (8.5) to project the microscopic Hamiltonian of the interferometer onto the subspace corresponding to incompressible deformations. Second, we investigate the effects of a modulation gate located near one of the arms of the interferometer, and of two Ohmic contacts. Both effects may be described by local edge deformations: the charge expelled by the modulation gate or added to the interferometer, is eventually localized at Ohmic contacts. Thanks to the linearity of resulting equations in the case of weak deformations, the spectrum of excitations and properties of the ground state of a realistic model of a quantum Hall interferometer may be first studied separately. We use so derived results in Sect. 8.5, where we investigate the Aharonov–Bohm effect in the current through a quantum Hall interferometer connected to Ohmic reservoirs.

## 8.3.1 Plasma Analogy and Incompressible States

The classical plasma analogy [5] has proven to be an efficient method in the analysis of quantum Hall states [57–61]. It relies on the important observation that the norm of the Laughlin wave function may be written as the partition function of an ensemble of N classical particles interacting via the two-dimensional (logarithmic) Coulomb potential. In the large-N limit the evaluation of the partition function reduces to solving a two-dimensional electrostatic problem. Here we apply this method directly to the wave function (8.5). We write

$$Z = \int d^2 z_1 \dots d^2 z_N |\langle \underline{z} | N, M, \underline{t} \rangle|^2 = \int d^2 z_1 \dots d^2 z_N e^{-mE_{\text{pl}}}, \tag{8.7}$$

where the inverse temperature of the plasma is m and the energy is given by the expression:

$$E_{\rm pl} = -\sum_{i < j} \ln|z_i - z_j|^2 + \sum_i \left[ \frac{|z_i|^2}{2ml_B^2} - \sum_i \frac{M}{m} \ln|z_i|^2 - 2\text{Re}\,\omega(z_i) \right]. \tag{8.8}$$

Introducing the microscopic density operator  $\rho(z) = \sum_i \delta^2(z - z_i)$ , we can formally write

$$E_{\rm pl} = -\frac{1}{2} \iint d^2z d^2w \, \rho(z) \rho(w) \ln|z - w|^2 - \int d^2z \rho(z) \varphi_{\rm ext}(z), \tag{8.9}$$

where

$$\varphi_{\text{ext}}(z) = -\frac{|z|^2}{2ml_B^2} + \frac{M}{m} \ln|z|^2 + 2\text{Re}\,\omega(z), \tag{8.10}$$

and normal ordering is assumed in the first term on the right hand side of Eq. (8.9) in order to remove the self-interaction contribution. This representation makes it obvious, that the partition function (8.7) describes a gas of charged particles interacting via the two-dimensional Coulomb potential that are confined by the external potential  $\varphi_{\rm ext}(z)$ . The first term in Eq. (8.10) describes the interaction with a neutralizing homogeneous background charge of density  $\rho_{\rm bg} = (1/4\pi)\Delta(|z|^2/2ml_B^2) = 1/2\pi ml_B^2$ . The second term can be viewed as describing repulsion from a macroscopic charge M/m at the origin. Finally, the last term describes the effect of an external (chargeless, since  $\Delta {\rm Re}\,\omega(z)=0$ ) potential on the particles in the gas.

The next step is to approximate the integral over coordinates in Eq. (8.7) by a functional integral<sup>4</sup> over the density  $\rho(z)$ :

$$Z = \int \mathcal{D}\rho(z)e^{-mE_{\text{pl}}[\rho]}.$$
 (8.11)

<sup>&</sup>lt;sup>4</sup> Note that the functional integration in Eq. (8.11) over  $\rho(z)$  is constrained to the domain  $\rho(z) \ge 0$ .

By doing so, we neglect the Jacobian of the transformation from variables  $\underline{z}$  to  $\rho(z)$  [62]. Taking the Jacobian into account is crucial for the correct description of the physics at the microscopic length scale  $l_B$ , which however is not a subject of our considerations. After this approximation, the evaluation becomes straightforward. We note that the energy of plasma is a quadratic function of the density. Hence the average density  $\langle \rho(z) \rangle = Z^{-1} \langle N, M, \underline{t} | \rho(z) | N, M, \underline{t} \rangle$  is given by the solution of the saddle-point equation  $\delta E_{\rm pl}/\delta \rho(z) = 0$ , which reads

$$\int d^2w \langle \rho(w) \rangle \ln|z - w|^2 + \varphi_{\text{ext}}(z) = 0$$
 (8.12)

for the domain where  $\langle \rho(z) \rangle \neq 0$ . Thus, an ideal quantum Hall liquid may be described by solving two-dimensional electrostatics problem.<sup>5</sup>

Important consequences of this simple equation are the following ones. First, it implies that the total potential vanishes in the region where  $\langle \rho(z) \rangle \neq 0$ , i.e. where the two-dimensional electron gas is not fully depleted. In other words, the Coulomb plasma is a "perfect metal" that completely screens the external potential  $\varphi_{\rm ext}$ . Applying the Laplacian to (8.12), we find that  $\langle \rho(z) \rangle = \rho_{\rm bg}$ , i.e., the Coulomb plasma is distributed homogeneously to screen the background charge. This confirms that the wave function (8.5) describes an incompressible deformation of the quantum Hall droplet. In particular, the wave function (8.4) describes the approximate ground state of a quantum Hall interferometer with the shape of a Corbino disk. Indeed, the plasma analogy suggests that the hole in the Corbino disk is formed symmetrically around the origin, where the macroscopic charge M/m is located. It serves to screen this charge, so that the total potential vanishes in the region occupied by the twodimensional electron gas. Because of perfect screening, the shape of the outer edge is, however, independent of the shape and position of the hole and displays the symmetry of boundary conditions in the background charge distribution, see first term in Eq. (8.10).

We now investigate the effect of the potential  $\omega(z)$  perturbatively. Let us denote by D the region to which the quantum Hall system is confined. We search for the solution of Eq. (8.12) in the form  $\langle \rho(z) \rangle = \rho_{\rm bg}$ , for  $z \in D$ , and  $\langle \rho(z) \rangle = 0$  otherwise. Thus we can rewrite Eq. (8.12) as

$$\rho_{\text{bg}} \int_{D} d^2 w \ln|z - w|^2 + \varphi_{\text{ext}}(z) = 0.$$

Introducing a small deformation,  $D = D_0 + \delta D$ , and taking into account that the integral over the undeformed Corbino disk,  $D_0$ , cancels the first two terms in Eq. (8.10), we arrive at the following result

<sup>&</sup>lt;sup>5</sup> It is expected that two-dimensional electrostatics for an ideal Coulomb plasma holds for  $1/\nu = m < 7$ , while for larger "inverse temperature" m there is a tendency to Wigner crystallization [55].

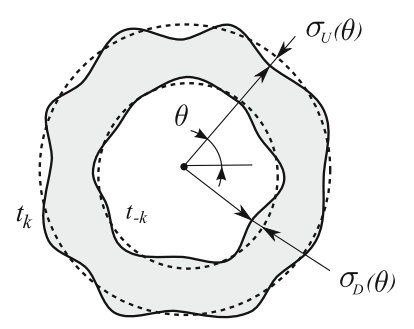


Fig. 8.4 A quantum Hall liquid, whose ground state is given by Eq. (8.5), is shown schematically. The *dashed lines* show the edges of the unperturbed Corbino disk, while an incompressible deformation is shown by the *full lines*. The region of constant electron density  $\langle \rho(z) \rangle = \rho_{\text{bg}}$  is shown by the *grey shadow*. The shape of this region is determined by the complex function  $\omega(z)$  defined in Eq. (8.6). The Fourier components of charge density  $\sigma_U$  accumulated at the *outer* edge are given by the coefficients  $t_k$  of the regular part of the Laurent series for  $\omega(z)$ , while the Fourier components of charge density  $\sigma_D$  accumulated at the *inner* edge are given by the coefficients  $t_{-k}$  with k > 0 of the singular part of  $\omega(z)$  [see Eq. (8.15)]

$$\rho_{\text{bg}} \int_{\delta D} d^2 w \ln|z - w| + \text{Re}\,\omega(z) = 0. \tag{8.13}$$

In polar coordinates (see Fig. 8.4), the boundaries of the deformed disk can be parameterized as  $r(\theta) = r_s \pm \sigma_s(\theta)/\rho_{bg}$ , where s = U, D, and  $\sigma_s(\theta)$  are the one-dimensional charge densities accumulated at the inner and outer edge due to the deformation.

Because of perfect screening in the two-dimensional Coulomb plasma, one can solve Eq. (8.13) independently for each edge. Using the series expansion

$$\ln(z - w) = \ln(w) - \sum_{k>0} (z/w)^k / k, \quad |z| \le |w|, \tag{8.14}$$

and the explicit expression (8.6) for the potential  $\omega(z)$ , we solve Eq. (8.13) by power series. The result can be presented in the form of Fourier series:

$$2\pi r_U \sigma_U(\theta) = 2\text{Re} \sum_{k>0} k t_k r_U^k e^{ik\theta}, \qquad (8.15a)$$

$$2\pi r_D \sigma_D(\theta) = 2\text{Re} \sum_{k>0} k t_{-k} r_D^{-k} e^{-ik\theta}.$$
 (8.15b)

These series show how the microscopic wave function (8.5) determines the shape of the deformed Corbino disk.

Finally, we analyze the effects of a modulation gate and of a singular magnetic flux on an *isolated* quantum Hall droplet, as illustrated in Fig. 8.5. According to the

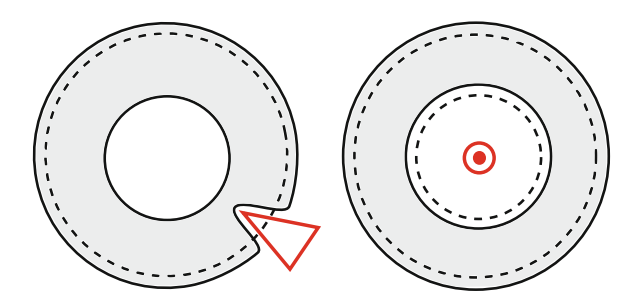


**Fig. 8.5** The effects of a modulation gate and of a singular flux are illustrated. *Left panel* The modulation gate locally depletes the quantum Hall liquid. Due to the incompressibility of the quantum Hall liquid, the repelled charge is accumulated homogeneously along the edge. *Right panel* In the language of the Coulomb plasma, the multiplier in the wave function (8.19) depending on the singular flux can be viewed as a point-like charge placed in the center of the *inner hole*. It homogeneously shifts both edges to preserve the electro-neutrality

result (8.15), the deformation caused by the modulation gate can be described by the wave function

$$\langle \underline{z} | N, M, \Phi_G \rangle = \exp \left[ -\sum_{i}^{N} \frac{\Phi_G}{\Phi_0} f\left(\frac{z_i}{\xi_G}\right) \right] \langle \underline{z} | N, M \rangle,$$
 (8.16)

where we have introduced the function

$$f(x) = \sum_{k>0} x^k / k = -\ln(1-x). \tag{8.17}$$

Indeed, the one-dimensional charge accumulated as a result of the deformation has the following form:

$$r_U \sigma_U(\theta) = -\frac{\Phi_G}{m\Phi_0} \Big( \delta(\theta - \theta_0) - \frac{1}{2\pi} \Big), \tag{8.18}$$

where  $\theta_0$  is the argument of the position,  $\xi_G$ , of the modulation gate. This function correctly captures the effects of a modulation gate on an isolated interferometer: the local depletion of the two-dimensional electron gas at the point  $\xi_G = r_U e^{i\theta_0}$  and the homogeneous expansion of the quantum Hall liquid due to its incompressibility. This observation agrees also with the fact, that the function (8.17) of a complex variable x is electro-neutral from the two-dimensional electrostatics point of view, because it has two branch points, at x=1 and  $x=\infty$ . Finally, it is easy to check that the flux through the depleted area under the modulation gate,  $-B\int (\sigma_U/\rho_{\rm bg})r_Ud\theta$ , is indeed equal to  $\Phi_G$ .

After the adiabatic insertion of a singular magnetic flux  $\Phi$  through the hole in the Corbino disk at the origin, the wave function is multiplied by the phase factor

 $\prod_i \exp[-i\Phi/\Phi_0 \arg z_i]$ . At the same time, the wave function is deformed by the spectral flow preserving its single-valuedness. This effect is described by the additional multiplier  $\prod_i z_i^{\Phi/\Phi_0}$ . The overall effect of a singular flux on the wave function (8.4) can thus be represented by replacing the original wave function with

$$\langle \underline{z} | N, M, \Phi \rangle = \prod_{i}^{N} |z_{i}|^{\Phi/\Phi_{0}} \langle \underline{z} | N, M \rangle.$$
 (8.19)

Thus, in the presence of a singular magnetic flux, the plasma energy contains an additional term

$$\delta E_{\rm pl} = -\frac{\Phi}{m\Phi_0} \sum_{i} \ln|z_i|^2. \tag{8.20}$$

In the language of the Coulomb plasma it describes the addition of a charge  $\Phi/m\Phi_0$  in the hole of the interferometer at the origin. This homogeneously shifts the edges of the Corbino disk by an amount

$$\delta r_s = \frac{\Phi}{m\Phi_0} \frac{1}{2\pi r_s \rho_{\text{bg}}}, \quad s = U, D, \tag{8.21}$$

as illustrated in Fig. 8.5.

## 8.3.2 Low-Energy Subspace

Having found the set of states (8.5) describing incompressible deformations of a quantum Hall liquid, we proceed to construct operators generating the subspace of such low-energy states when applied to the undeformed ground-state and finding their commutation relations. First of all, let us introduce zero-mode operators changing the number of electrons N and quasi-particles M in the system

$$e^{i\phi_M}|N,M,\underline{t}\rangle = |N,M+1,\underline{t}\rangle,$$
 (8.22a)

$$e^{i\phi_N}|N,M,\underline{\mathbf{t}}\rangle = |N+1,M,\underline{\mathbf{t}}\rangle.$$
 (8.22b)

States with different numbers of electrons N are obviously orthogonal. The orthogonality of states with different numbers of quasi-particles M follows from the fact that in a symmetric Corbino disk such states have different angular momenta. Taking this observation into account, one derives from the definitions (8.22) the following commutation relations for the operators of zero modes<sup>6</sup>

<sup>&</sup>lt;sup>6</sup> To be precise, the operators (8.22) are not unitary if N and M are finite. However, in the thermodynamic limit  $(N, M \to \infty)$  these operators become unitary and satisfy the commutation relations (8.23).

$$[M, e^{i\phi_M}] = e^{i\phi_M}, \quad [N, e^{i\phi_N}] = e^{i\phi_N}.$$
 (8.23)

Next, we introduce deformation operators  $a_{ks}$ , s = U, D, for any k > 0, acting on the right as

$$a_{kU}|N, M, \underline{\mathbf{t}}\rangle = -i\sqrt{k}r_U^k t_k |N, M, \underline{\mathbf{t}}\rangle,$$
 (8.24a)

$$a_{kD}|N, M, \underline{\mathbf{t}}\rangle = -i\sqrt{k}r_D^{-k}t_{-k}|N, M, \underline{\mathbf{t}}\rangle.$$
 (8.24b)

The states (8.5) are coherent states under the action of these operators. In order to find commutation relations for these operators, we need to evaluate scalar products of the states (8.5).

We start with the norm of a wave function, which is given by the square root of the partition function of the Coulomb plasma, (8.7) and (8.11), and evaluate the "free energy"

$$F_{\rm pl} = -(1/m)\log(Z).$$
 (8.25)

Considering the potential  $\omega(z)$  as a perturbation, we obtain

$$F_{\rm pl} = F_0 + \frac{\rho_{\rm bg}^2}{2} \iint_{\delta D} d^2 z d^2 w \ln|z - w|^2,$$

where the constant  $F_0$  is the contribution from the unperturbed state and from the determinant of the Gaussian integral. We evaluate this integral with the help of the solution (8.15) and present the result as a bilinear form in the coefficients  $t_k$ ,

$$F_{\text{pl}}(\underline{t}^*,\underline{t}) = F_0 - \sum_{k>0} k[r_U^{2k} t_k^* t_k + r_D^{-2k} t_{-k}^* t_{-k} + t_k t_{-k} + t_k^* t_{-k}^*].$$
 (8.26)

The holomorphic structure of this bilinear form allows us to extend the result for the norm  $Z = \exp\{-mF_{\rm pl}(\underline{\bf t}^*,\underline{\bf t})\}$  to the scalar products

$$\langle N, M, \underline{\mathbf{t}} | N, M, \underline{\mathbf{t}}' \rangle = \exp\{-mF_{\mathrm{pl}}(\underline{\mathbf{t}}^*, \underline{\mathbf{t}}')\}. \tag{8.27}$$

Next, we define differential operators, via their matrix elements, as follows:

$$\langle \Psi | \frac{\partial}{\partial t_k} | N, M, \underline{\mathbf{t}}' \rangle = \frac{\partial}{\partial t_k'} \langle \Psi | N, M, \underline{\mathbf{t}}' \rangle. \tag{8.28}$$

A straightforward calculation then yields:

$$\langle N, M, \underline{\mathbf{t}} | \frac{\partial}{\partial t_k} | N, M, \underline{\mathbf{t}}' \rangle = mk [r_U^{2k} t_k^* + t'_{-k}] \langle N, M, \underline{\mathbf{t}} | N, M, \underline{\mathbf{t}}' \rangle. \tag{8.29}$$

Using definition (8.24), we may write  $\langle N, M, \underline{t} | a_{kU}^{\dagger} | N, M, \underline{t}' \rangle \equiv \langle N, M, \underline{t}' | a_{kU} | N, M, \underline{t} \rangle^* = i \sqrt{k} r_U^k t_k^* \langle N, M, \underline{t} | N, M, \underline{t}' \rangle$ . Substituting this equation in Eq. (8.29) we finally express the adjoint operators acting on the states  $|N, M, \underline{t} \rangle$ , via the parameters  $t_k$ , as

$$a_{kU}^{\dagger} = \frac{ir_U^{-k}}{m\sqrt{k}} \left(\frac{\partial}{\partial t_k} - mkt_{-k}\right). \tag{8.30}$$

Repeating exactly the same calculations for the operators  $\partial/\partial t_{-k}$ , we obtain:

$$a_{kD}^{\dagger} = \frac{ir_D^k}{m\sqrt{k}} \left( \frac{\partial}{\partial t_{-k}} - mkt_k \right). \tag{8.31}$$

Using Eqs. (8.24), (8.30) and (8.31) for the operators  $a_{ks}$  and their adjoints and the relation  $[\partial/\partial t_k, t_{k'}] = -\delta_{kk'}$ , we obtain the commutation relations:

$$[a_{ks}, a_{k's'}^{\dagger}] = \frac{1}{m} \delta_{kk'} \delta_{ss'}.$$
 (8.32)

Similarly, one finds that  $[a_{ks}^{\dagger}, a_{k's'}^{\dagger}] = [a_{ks}, a_{k's'}] = 0$ . Thus the deformation operators,  $a_{ks}$  and  $a_{ks}^{\dagger}$ , introduced in (8.24) satisfy canonical commutation relations, and the subspace of incompressible deformations has a natural Fock space structure with respect to these operators.

# 8.4 Projection onto the Low-Energy Subspace

Starting from the microscopic model, we now explicitly derive the low-energy effective theory of an interferometer. For this purpose, we project the microscopic Hamiltonian and overlaps of wave functions of quasi-particles at the two edges onto the low-energy subspace constructed above. The projection of these operators is defined by  $O \rightarrow POP$ , where the orthogonal projection P is written as:

$$P = \sum_{N,M} \int \prod_{k} d^2 t_k \prod_{k} d^2 t_k' |N, M, \underline{\mathbf{t}}\rangle \langle N, M, \underline{\mathbf{t}}|N, M, \underline{\mathbf{t}}'\rangle^{-1} \langle N, M, \underline{\mathbf{t}}'|, \quad (8.33)$$

where the inverse is defined in the sense of the inverse kernel. We first implement the projection procedure for a symmetric Corbino disk. Then, in Sect. 8.5 we take advantage of the fact that incompressible deformations are weak and lead to linear relations (8.13) and (8.15), and simply shift oscillator operators in order to take into

<sup>&</sup>lt;sup>7</sup> This commutation relation follows form the definition of the derivative operator (8.28), which differs from the standard one.

account additional deformations caused by Ohmic contact, modulation gate, and singular magnetic flux.

## 8.4.1 Edge Hamiltonian

The microscopic Hamiltonian for N electrons, restricted to the lowest Landau level, is given by the expression

$$H = \sum_{i}^{N} U(z_i) + \sum_{i < j}^{N} V(|z_i - z_j|), \tag{8.34}$$

where V(|z|) is the potential of the screened three-dimensional Coulomb interaction and U(z) is the confining potential, which forces electrons to form the interferometer. Note that we have omitted the kinetic energy operator, since, acting on the lowest Landau level, it gives a constant contribution,  $N\hbar\omega_c/2$ , where  $\omega_c=eB/m_ec$  is the cyclotron frequency.

To find the projection of the microscopic Hamiltonian onto the subspace of incompressible deformations  $\mathcal{H} = PHP$  one needs to evaluate the matrix elements

$$E(\underline{\mathbf{t}}^*, \underline{\mathbf{t}}') = \frac{\langle N, M, \underline{\mathbf{t}} | H | N, M, \underline{\mathbf{t}}' \rangle}{\langle N, M, \underline{\mathbf{t}} | N, M, \underline{\mathbf{t}}' \rangle}.$$
(8.35)

We first consider diagonal matrix elements  $E(\underline{t}^*, \underline{t})$  in (8.35). They can be rewritten in terms of the electronic density in the deformed state as follows:

$$E(\underline{\mathbf{t}}^*,\underline{\mathbf{t}}) \simeq \int d^2z U(z) \langle \rho(z) \rangle + \frac{1}{2} \iint d^2z d^2w V(|z-w|) \langle \rho(z) \rangle \langle \rho(w) \rangle, \quad (8.36)$$

where we have applied the approximation  $\langle \rho(z)\rho(w)\rangle \simeq \langle \rho(z)\rangle \langle \rho(w)\rangle$ , neglecting the "exchange" contribution, which is justified in the large-N limit.

Next, we express the projected Hamiltonian in terms of the deformation operators (8.24). To this end, we consider small deformations of the state (8.4) and take into account the fact that the density is constant,  $\langle \rho(z) \rangle = \rho_{\rm bg}$ , for  $z \in D$ . Writing the deformed region as  $D = D_0 + \delta D$ , one can expand the integral (8.36) in the small deformation  $\delta D$  and evaluate the correction term with the help of the result (8.15):

$$E(\underline{t}^*, \underline{t}) = E_0 + m \sum_{k>0} [\varepsilon_U(k)(r_U)^{2k} k t_k^* t_k + \varepsilon_D(k)(r_D)^{-2k} k t_{-k}^* t_{-k}].$$
 (8.37)

where  $E_0$  is the energy of a quantum Hall system confined to an undeformed Corbino disk, and the last two terms originate from the deformation  $\delta D$ . The excitation spectra,  $\varepsilon_s(k)$ , s = U, D, are determined by the three-dimensional Coulomb interaction and

by the confining potential:

$$\varepsilon_s(k) = \frac{kU'(r_s)}{2\pi m \rho_{\text{bg}} r_s} + \frac{k}{m} \int_0^{2\pi} d\varphi V \left( 2r_s |\sin\frac{\varphi}{2}| \right) [e^{ik\varphi} - e^{i\varphi}]. \tag{8.38}$$

Using again the holomorphic structure of the bilinear form (8.37) to extend this result to off-diagonal matrix elements, we arrive at the projected Hamiltonian in the following form:

$$\mathcal{H} = E_0 + m \sum_{s=U} \sum_{k>0} \varepsilon_s(k) a_{ks}^{\dagger} a_{ks} . \tag{8.39}$$

We further assume that the potential V describes Coulomb interactions screened at a distance d. In the low-energy limit, i.e., for  $kd/r_s \ll 1$ , the deformation energy in (8.38) is then linear as a function of the mode number:  $\varepsilon_s(k) \simeq v_s k/r_s$ , where the constants  $v_s$  are the group velocities of edge excitations. The energy of the undeformed state takes the following form as a function of the number of electrons N and the number of quasi-particles M:

$$E_0(N, M) = \frac{v_D}{2mr_D}M^2 + \frac{v_U}{2mr_U}(M + mN)^2.$$
 (8.40)

Replacing the mode number with the wave vector  $k \to kr_s$ , we arrive at the final expression for the edge Hamiltonian

$$\mathcal{H} = E_0(N, M) + m \sum_{s=U,D} \sum_{k>0} v_s k a_{ks}^{\dagger} a_{ks} . \tag{8.41}$$

We conclude this section with the following important remark. The right hand side of Eq. (8.38) contains two terms: the first one originates from the confining potential and the second one comes from Coulomb interaction. Consequently, the velocities of edge excitations contain two contributions:

$$v_s = cE(r_s)/B + (e^2/m\hbar)\ln(d/l_B).$$
 (8.42)

The first term is the drift velocity, proportional to the boundary electric field,  $E(r_s)$ , while the second one is proportional to the "Coulomb logarithm". The ultraviolet cutoff in (8.42) is determined by correction terms in a 1/N-expansion of the two-point density correlation function. In fact, result (8.42) coincides with an expression proposed earlier in Ref. [38] in the framework of the effective theory on the basis of the classical electrostatic picture.

## 8.4.2 Tunneling Hamiltonian

The tunneling Hamiltonian of an interferometer may be written as a sum of tunneling operators at the left and right quantum point contacts:

$$\mathcal{H}_T = \sum_{\ell=L,R} [\mathcal{A}_{\mathrm{qp}}(\xi_\ell) + \mathcal{A}_{\mathrm{qp}}^{\dagger}(\xi_\ell)].$$

The tunneling operator  $\mathcal{A}_{qp}(\xi)$  is an operator annihilating a quasi-particle at a point  $\xi'$  on one edge and recreating it at a point  $\xi$  on the other edge. At low energies, the tunneling operator can be defined as an operator whose matrix elements in deformed states are equal to the overlaps of two states with quasi-particle located at the opposite edges:

$$\langle N, M, \underline{\mathbf{t}} | \mathcal{A}_{qp}(\xi) | N, M', \underline{\mathbf{t}}' \rangle \equiv \int \prod_{i} d^{2} z_{i} \langle N, M, \underline{\mathbf{t}} | \psi_{qp}^{\dagger}(\xi) | \underline{\mathbf{z}} \rangle$$

$$\times \langle \underline{\mathbf{z}} | \psi_{qp}(\xi') | N, M', \underline{\mathbf{t}}' \rangle. \tag{8.43}$$

However, here we face the problem that a wave function of a quantum Hall system with one quasi-particle,  $\langle \underline{z} | \psi_{qp}(\xi) | N, M, \underline{t} \rangle$ , is not well defined. This is because one is not able to remove a charge 1/m form a system consisting of electrons. Therefore, we first construct the electron tunneling operator  $\mathcal{A}_{el}$  and then derive the quasi-particle tunneling operator from the observation that tunneling of m quasi-particles at the same point is equivalent to tunneling of an electron.

The electron operator is formally defined by  $\langle z_1, \ldots, z_N | \psi_{el}(\xi) | \Psi \rangle = \sqrt{N+1} \langle z_1, \ldots, z_N, \xi | \Psi \rangle$ , which leads to the result:

$$\langle \underline{z} | \psi_{\text{el}}(\xi) | N+1, M, \underline{t} \rangle = \xi^M e^{-|\xi|^2/4l_B^2 + m\omega(\xi)} \prod_i (\xi - z_i)^m \langle \underline{z} | N, M, \underline{t} \rangle, \quad (8.44)$$

where we omitted a combinatorial factor, because it can be absorbed into the tunneling amplitudes. Then, using the expression (8.43) with operators  $\psi_{qp}$  replaced by  $\psi_{el}$  from Eq. (8.44), we obtain

$$\langle N, M, \underline{\mathbf{t}} | \mathcal{A}_{el}(\xi) | N, M', \underline{\mathbf{t}}' \rangle = e^{m\omega(\xi') + m\omega^*(\xi^*)} \int \prod_{i} d^2 z_i (\xi' - z_i)^m \times (\xi^* - z_i^*)^m \langle N, M, \underline{\mathbf{t}} | \underline{\mathbf{z}} \rangle \langle \underline{\mathbf{z}} | N, M', \underline{\mathbf{t}}' \rangle.$$
(8.45)

where we have dropped the prefactor  $(\xi'\xi^*)^M \exp[-(|\xi|^2 + |\xi'|^2)/4l_B^2)$ , because for a short tunneling path,  $\xi' \to \xi$ , which is typically the case, it has no essential physical meaning and may be absorbed into the tunneling amplitude. Now, it becomes obvious that the matrix element of the quasi-particle tunneling operator may be written as

$$\langle N, M, \underline{\mathbf{t}} | \mathcal{A}_{qp}(\xi) | N, M', \underline{\mathbf{t}}' \rangle = e^{\omega(\xi') + \omega^*(\xi^*)} \int \prod_i d^2 z_i (\xi' - z_i) \times (\xi^* - z_i^*) \langle N, M, \underline{\mathbf{t}} | \underline{\mathbf{z}} \rangle \langle \underline{\mathbf{z}} | N, M', \underline{\mathbf{t}}' \rangle, \quad (8.46)$$

i.e., roughly speaking, we set  $\mathcal{A}_{qp} = \mathcal{A}_{el}^{1/m}$ . We would like to stress, that this quasiparticle tunneling operator is unique and well defined. First of all, in term of the electron coordinates  $z_i$ , the matrix element (8.46) is a single-valued function, i.e., the criterion (iii) formulated in the beginning of the Sect. 6.1 is satisfied. Second, this matrix element is also a single-valued function of the coordinates of the tunneling points  $\xi$  and  $\xi'$ . Thus, on the microscopic level no ambiguity of the definition of a tunneling operator arises.

In order to evaluate the matrix elements (8.46), we first assume that  $\underline{t}' = \underline{t}$ , as in the previous section, and then generalize our findings. The product  $\prod_i (\xi' - z_i)$  in Eq. (8.46) can be rewritten as  $\exp\left[\sum_i \ln(\xi' - z_i)\right]$ , and one obtains similar expression for  $\prod_i (\xi^* - z_i^*)$ . Expanding the logarithms in power series (8.14) on the inner,  $|\xi| < |z_i|$ , and outer,  $|\xi'| > |z_i|$  edges, we arrive at the following expression for the matrix elements (8.46):

$$\langle N, M, \underline{t} | \mathcal{A}_{qp}(\xi) | N, M', \underline{t} \rangle = \exp[\omega(\xi') + \omega^*(\xi^*) + N \ln \xi']$$

$$\times \int \prod_{i} d^2 z_i z_i^* \exp\left\{ -\sum_{k>0} \left[ \frac{z_i^k}{k \xi'^k} + \frac{(\xi^*)^k}{k (z_i^*)^k} \right] \right\}$$

$$\times \langle N, M, \underline{t} | \underline{z} \rangle \langle \underline{z} | N, M', \underline{t} \rangle. \tag{8.47}$$

Taking into account that  $m \sum_i z_i^k \langle \underline{z} | N, M', \underline{t} \rangle = \partial/\partial t_k \langle \underline{z} | N, M', \underline{t} \rangle$ , and  $m \sum_i (z_i^*)^{-k} \langle N, M, \underline{t} | \underline{z} \rangle = \partial/\partial t_{-k}^* \langle N, M, \underline{t} | \underline{z} \rangle$ , we pull out of the integral the power series in  $z_i$ . Then we use the fact that  $\langle N, M, \underline{t} | \underline{z} \rangle \prod_i z_i^* = \langle N, M+1, \underline{t} | \underline{z} \rangle$  to rewrite Eq. (8.47) in the following form:

$$\langle N, M, \underline{\mathbf{t}} | \mathcal{A}_{qp}(\xi) | N, M', \underline{\mathbf{t}} \rangle = \exp[\omega(\xi') + \omega^*(\xi^*) + N \ln \xi']$$

$$\times \exp\left\{ -\frac{1}{m} \sum_{k>0} \left[ \frac{1}{k\xi'^k} \frac{\partial}{\partial t_k} + \frac{(\xi^*)^k}{k} \frac{\partial}{\partial t_{-k}^*} \right] \right\}$$

$$\times \langle N, M+1, \underline{\mathbf{t}} | N, M', \underline{\mathbf{t}} \rangle.$$
(8.48)

One can immediately see that the matrix element (8.48) vanishes unless M' = M + 1. Finally, using Eq. (8.26) for the logarithm of the norm  $Z = \langle M, N, \underline{t} | N, M, \underline{t} \rangle$  and definition (8.24), we can write the projection of the tunneling operator (8.43) in terms of the deformation operators as follows:

$$\mathcal{A}_0(\xi) = \exp\left[-i\phi_M + N\ln\xi' + i\varphi_U(\xi') - i\varphi_D^{\dagger}(\xi)\right],\tag{8.49}$$

where we have introduced the subindex 0 to denote the quasi-particle tunneling operator for a symmetric Corbino disk, i.e., before deformations that are considered in Sect. 8.4.3. We have also introduced the following fields:

$$\varphi_U(\xi') = \sum_{k>0} \frac{1}{\sqrt{k}} \left[ (r_U/\xi')^k a_{kU}^{\dagger} + (\xi'/r_U)^k a_{kU} \right], \tag{8.50a}$$

$$\varphi_D(\xi) = \sum_{k>0} \frac{1}{\sqrt{k}} \left[ (\xi/r_D)^k a_{kD}^{\dagger} + (r_D/\xi)^k a_{kD} \right]. \tag{8.50b}$$

Here several remarks are in order. One can easily see that the quasi-particle tunneling operator (8.49), together with definitions (8.50), almost coincide with the tunneling operator found within the effective theory, given by Eqs. (1.60) and (1.62). These operators differ only by the parametrization of the boundary  $\partial D$  of a quantum Hall system [two-dimensional coordinates  $\xi = re^{i\theta}$  in (8.49) versus one-dimensional coordinates  $x = r\theta$  in (1.60)], and by zero modes, which are different in the case of single edge considered in introduction. Note, also, that the wave number k in Eqs. (8.50) has to be replaced with the wave vector:  $k \to kr_s$ . We would also like to mention that two tunneling operators (8.49) taken at to different points commute:

$$[A_0(\xi_L), A_0(\xi_R)] = 0.$$
 (8.51)

This is because two fields  $\phi_s$  in (8.49) have opposite chiralities, and in the case of symmetric Corbino disk considered so far their contributions to the exponent of the commutator cancel exactly. Is this property a consequence of the symmetry of the Corbino disk, or it can be extended to an arbitrary geometry? We propose the following argument, which suggests the universality of the relation (8.51). Note, that in order to arrive at the expression (8.49) for the quasi-particle tunneling operator, we have dropped the prefactor  $(\xi'\xi^*)^M$  in the electron tunneling operator (8.45), and consequently, the prefactor  $(\xi'\xi^*)^{M/m}$ , motivating this by the proximity of tunneling points in a real experimental situation. If we relax this requirement and assume an arbitrary location of tunneling points at the boundaries of the Corbino disk, then the commutator  $[\mathcal{A}_0(\xi_L), \mathcal{A}_0(\xi_R)]$  acquires additional contributions from zero modes and from the oscillators. It turns out, that these contributions cancel exactly, suggesting the universality of the commutation relation (8.51).

Next, we find the projected charge density operators at the edges of a quantum Hall system,  $\rho_D(\theta) = P\sigma_D(\theta)P - M/2\pi mr_D$  and  $\rho_U(\theta) = P\sigma_U(\theta)P + (M+mN)/2\pi mr_U$ , by rewriting the result (8.15) directly in terms of the operators (8.24):

$$\rho_D(\theta) = -\frac{1}{2\pi r_D} \partial_{\theta} \varphi_D(\xi) - \frac{M}{2\pi m r_D}, \tag{8.52a}$$

$$\rho_U(\theta) = \frac{1}{2\pi r_U} \partial_\theta \varphi_U(\xi) + \frac{M + mN}{2\pi m r_U}.$$
 (8.52b)

here the homogeneous contributions describe the charge accumulation caused by the variation of quantum numbers M and N. We note that again these results agree with the effective theory presented in Sect. 6.1. In particular, setting M=0 in Eq. (8.52b) and changing the parametrization of the boundary, we arrive at the expression (1.58), complemented by (1.62). Note also that Eqs. (8.52) lead to the following commutation relations

$$[\mathcal{A}_0(\xi), \rho_s(\theta)] = \pm \frac{1}{mr_s} \delta(\theta - \theta_s) \mathcal{A}_0(\xi), \tag{8.53}$$

where the angles  $\theta_D$  and  $\theta_U$  parameterize the position of the tunneling point in coordinates of the inner and outer edge. These commutation relations show that the tunneling operator (8.49) creates a pair of point-like charges of magnitude  $\pm 1/m$ .

Finally, we must find the projection of the operators of electron tunneling from the quantum Hall edges to the Ohmic contacts. This can be done by applying the technique used above to the electron annihilation operator (8.44). The result of the projection is given by

$$A_{U} = c_{U}^{\dagger} \exp\left[im\varphi_{U}(\xi_{U})\right] \exp\left[-i\phi_{N} + (mN + M)\ln\xi_{U}\right]$$
(8.54)

for tunneling from the outer edge to the upper Ohmic contact (see Fig. 8.3 for notations), while the tunneling operator on the inner edge is given by

$$A_D = c_D^{\dagger} \exp\left[im\varphi_D(\xi_D)\right] \exp\left[-i\phi_N + im\phi + M\ln\xi_D\right], \tag{8.55}$$

where  $c_U$  and  $c_D$  are the electron operators in Ohmic reservoirs.

# 8.4.3 Deformations of the Ground State

We are now in the position to investigate the effects of the deformation of the symmetric Corbino disk on the collective and local excitations. Let us consider for this purpose the combined effect of the ground state deformation, described by some function  $\omega_d(z) = \sum_k t_{dk} z^k$ , and of the deformations caused by excitations,  $\omega(z) = \sum_k t_k z^k$ . The total deformation function then reads

$$\omega_{\text{tot}}(z) = \omega(z) + \omega_d(z) = \sum_k (t_k + t_{dk}) z^k.$$
 (8.56)

This function has to be substituted to the wave function (8.5). According to the classical plasma analogy, the deformation  $\omega_d$  adds to the charge density at the edge, given by Eqs. (8.15). However, since we consider the deformation of a ground state, e.g., by a modulation gate, the Coulomb energy (8.37) of the overall deformation does

not change. We therefore choose to keep the definition (8.24), so that the Hamiltonian (8.41) of the collective modes remains unchanged.

At the same time, the ground state deformation effects the adjoint operators of the collective modes. This simply follows from the scalar products of deformed wave functions:

$$\langle N, M, \underline{\mathbf{t}} | N, M, \underline{\mathbf{t}}' \rangle = \exp \left[ -m F_{\text{pl}}(t_k^* + t_{dk}^*, t_k' + t_{dk}) \right], \tag{8.57}$$

where  $F_{\rm pl}$  is given by Eq. (8.27). Repeating steps that lead to Eqs. (8.30) and (8.31), we find the adjoint operators acquire a simple shift:

$$a_{kU}^{\dagger} \to a_{kU}^{\dagger} + i\sqrt{k}(r_{U}^{k}t_{dk}^{*} + r_{U}^{-k}t_{d,-k}),$$
 (8.58a)

$$a_{kD}^{\dagger} \rightarrow a_{kD}^{\dagger} + i\sqrt{k}(r_{D}^{k}t_{dk} + r_{D}^{-k}t_{d,-k}^{*}).$$
 (8.58b)

Obviously, this shift does not change canonical commutation relations (8.32).

Next, we evaluate the modified quasi-particle tunneling operator  $\mathcal{A}_{qp}(\xi)$ . For doing so, we repeat steps starting from Eq. (8.46) and leading to the result (8.49), but now using new collective mode operators (8.58) and the deformation function (8.56). The result of the calculations reads

$$A_{qp}(\xi) = A_0(\xi) \exp\left\{2i \operatorname{Im}[\omega_d^+(\xi') - \omega_d^-(\xi)]\right\},$$
 (8.59)

where we have introduced the functions

$$\omega_d^+(z) = \sum_{k>0} t_{dk} z^k, \quad \omega_d^-(z) = \sum_{k>0} t_{d,-k} z^{-k},$$
 (8.60)

which are the parts of  $\omega_d = \omega_d^+ + \omega_d^-$ , analytical respectively inside the inner edge and outside of the outer edge of the Corbino disk. Thus the sole effect of the deformations of the ground state of the symmetric Corbino disk is the appearance of the phase shift in the quasi-particle tunneling operator. The structure of the term is also quite natural: deformations of the outer edge lead to the phase shift in the mode  $\varphi_U$  via the function  $\omega_d^+$ , while the deformations of the inner edge, controlled by the function  $\omega_d^-$ , shift the mode  $\varphi_D$ .

Next, we note that using Eqs. (8.15) one may express the phase shifts in (8.59) in terms of the one-dimensional charge densities accumulated at the edges as a result of the deformations:  $2\partial_{\theta} \text{Im} \omega_d^+(\xi') = r_U \sigma_U(\theta)$  and  $2\partial_{\theta} \text{Im} \omega_d^-(\xi) = -r_D \sigma_U(\theta)$ . Thus, we may conclude that neutral deformations caused, e.g., by a modulation gate, lead to the phase shifts in the tunneling operator, which may be evaluated as simple contour integrals of the charge densities accumulated at the edges. In the next section, on the other hand, we would like to consider variations of zero modes,  $\delta N$  and  $\delta M$ , which lead to specific variations of the charge densities at the edge. These effects may be described by the phase shifts already accounted for in the bare tunneling operator (8.49), accompanied by the phase shifts due to neutral deformations considered so

far. Taking into account the Eqs. (8.52) we finally arrive at the following simple and general result:

$$\mathcal{A}_{\rm qp}(\xi) = \mathcal{A}_0(\xi) \exp\left\{i\delta\varphi_U(x') - i\delta\varphi_D(x)\right\},\tag{8.61a}$$

$$\delta\varphi_U = 2\pi \int dx' \delta\rho_U(x'), \quad \delta\varphi_D = 2\pi \int dx \delta\rho_D(x),$$
 (8.61b)

where for the convenience we choose the one-dimensional parametrization,  $x' = r_U \theta$  and  $x = -r_D \theta$ , which accounts for the opposite chiralities of the edge states, and we recall that  $A_0$  is the bare quasi-particle tunneling operator for a symmetric Corbino disk, given by Eq. (8.49). The operators  $\delta \varphi_s$  in this expression account for the specific phase shifts, which are the subject of the next section, while the operator  $A_0$  determines the scaling behavior of tunneling rates.

To summarize this section, Eqs. (8.49-8.55) complete the projection procedure, and the resulting low-energy theory of a quantum Hall system isolated in a Corbino disk agrees well with the effective theory of Refs. [2] and [3, 4]. However, in addition to this important conclusion, we obtain an information which cannot be extracted from the effective theory alone. Namely, the effective theory does not specify precisely how zero modes enter the tunneling operators. For example, our direct microscopic calculations suggest that the quasi-particle tunneling operators (8.49) do not contain the zero mode M that counts the number of quasi-particles localized in the central hole of the Corbino disk. Moreover, we do not find traces of additional Klein factors [49] in the tunneling operators.

# 8.5 Quantum Hall Interferometer Away From Equilibrium

In this section we return to the model of a quantum Hall interferometer, shown in Fig. 8.3, and investigate various effects of inserting a singular magnetic flux, applying a modulation gate voltage, and of attaching Ohmic contacts. The most important effect is the accumulation of the charge density at the edges,  $\delta \rho_s$ . It leads to the phase sift in quasi-particle tunneling operators, which may be easily evaluated using Eq. (8.61b). Electron tunneling operators (8.54) and (8.55) also acquire the phase shifts, but they cancel in tunneling rates. In contrast, the phase shifts of quasiparticle tunneling operators add to the Aharonov-Bohm phase in the oscillating part of the quasi-particle tunneling rates. The consequence of this is twofold. First, the Aharonov-Bohm effect may be observed by simply applying a modulation gate voltage or a singular magnetic flux. We, then, find the corresponding periods of Aharonov–Bohm oscillations. Second, the phase shifts  $\delta \varphi_s$ , and consequently the quasi-particle tunneling rates, depend on the variations of zero modes,  $\delta N$  and  $\delta M$ . Therefore, we describe tunneling processes, and eventually a stationary quasi-particle current on a long time scale, by solving the master equation for the probability distributions in the space of zero modes.

#### 8.5.1 Ohmic Contacts

So far, we have considered a quantum Hall system to be confined inside a Corbino disk and electrically isolated from the measurement circuit. In fact, such a system, complemented by two quantum point contacts connecting inner and outer edges of the Corbino disk, may nevertheless be considered a quantum Hall interferometer. The time-dependent quasi-particle current in such a system may be investigated by using, e.g., the time domain capacitance spectroscopy method [63, 64]. As we will see, there is no reason for the quasi-particle Aharonov–Bohm effect not to be observed in such measurements with the Mach–Zehnder interferometer. However, the Byers–Yang theorem is formulated for a stationary current, and our original naive argument presented at beginning of this chapter considers a Mach–Zehnder interferometer as an opens system. Experimentally [16], such a situation is achieved by attaching a quantum Hall system to Ohmic contacts.

A correct physical description of Ohmic contacts to quantum Hall edge states is a complex theoretical problem. We think that despite several attempts [52, 65, 66], this problem has not been fully solved. In particular, we are not aware of a discussion in the literature about how different models of Ohmic contacts can be discriminated (or verified) experimentally. The difficulty of modeling Ohmic contacts is related to the fact, that Ohmic reservoirs, typically being realized by heavily doping a part of the semiconductor substrate, represent entirely different physical system than a two-dimensional electron gas in a quantum Hall state. In this situation it is best to rely on minimal obvious requirements for a model to correctly describe an Ohmic contact: (i) An Ohmic contact is a metallic reservoir, which has a large capacitance, and as a result, suppresses fluctuations of the total charge localized at quantum Hall edges; (ii) it has a resistance much smaller than that of the system, and creates negligible noise; (iii) Ohmic contact efficiently equilibrates edge states. If such requirements are satisfies, it becomes experimentally difficult to distinguish a model Ohmic contact from an ideal one.

Here we focus on the first requirement and address other two in Sect. 8.5.2. An ideal Ohmic contact suppresses charge fluctuations at the edges by accommodating all the excess charges arising from variations of zero modes, and of the magnetic field flux. Thus, no variations of the charge densities  $\delta \rho_s$  arise except at the points  $\xi_U = r_U e^{i x_U'/r_U}$  and  $\xi_D = r_D e^{-i x_D/r_U}$ , where Ohmic contacts are located, and at the position  $\xi_G = r_U e^{i x_G'/r_U}$  of the modulation gate, see Fig. 8.3. Denoting these charges with  $Q_U$ ,  $Q_D$ , and  $Q_G$ , respectively, we may write:

$$\delta \rho_U(x') = Q_U \delta(x' - x'_U) + Q_G \delta(x' - x'_G),$$
 (8.62a)

$$\delta \rho_D(x) = Q_D \delta(x - x_D). \tag{8.62b}$$

These equations have to be substituted to Eq. (8.61), giving phase shifts to quasi-particle tunneling operators.

Next, we evaluate the excess charges in different situations. When the zero mode N changes by  $\delta N$  due to the electron tunneling at Ohmic contacts, this leads to the

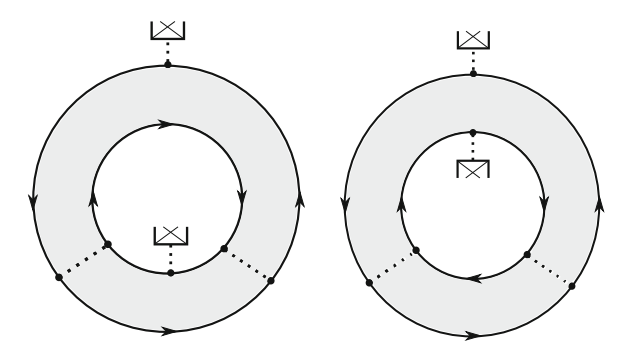


Fig. 8.6 Schematic illustration of the interferometers of the Mach–Zehnder type (left panel) and of the Fabry–Perot type (right panel)

accumulation of the charge at the outer edge of the Corbino disk at the upper Ohmic contact, therefore  $Q_U = \delta N$ . When the zero mode M changes by  $\delta M$  as a result of quasi-particle tunneling at quantum point contacts, this leads to the accumulation of the charge at the upper Ohmic contact,  $Q_U = \delta M/m$ , and depletes the charge at the inner Ohmic contact,  $Q_D = -\delta M/m$ . If one applies the modulation gate voltage in order to deform the (outer) path of the interferometer, and thus changes the total magnetic flux through it by  $\Phi_G$ , according to Eq. (8.18) this leads to a neutral deformation and removes the charge  $\Phi_G/m\Phi_0$  at the point  $\xi_G$ . Therefore, in this case  $Q_G = -\Phi_G/m\Phi_0$ . However, since the homogeneous part of the edge density is screened by Ohmic contacts, the excess charge is accumulated at the upper Ohmic contact, and thus  $Q_U = \Phi_G/m\Phi_0$ . Finally, adiabatically threading a singular magnetic flux Φ through the hole in the Corbino disk leads to the homogeneous shift of the edges, given by Eq. (8.21). And again,  $Q_U = \Phi/m\Phi_0$  and  $Q_D = -\Phi/m\Phi_0$ , as a result of perfect screening by Ohmic contacts. Adding all the effects considered here, we obtain

$$Q_U = \delta N + \frac{\delta M}{m} + \frac{\Phi + \Phi_G}{m\Phi_0},$$
 (8.63a)  
 $Q_D = -\frac{\delta M}{m} - \frac{\Phi}{m\Phi_0}, \quad Q_G = -\frac{\Phi_G}{m\Phi_0}.$  (8.63b)

$$Q_D = -\frac{\delta M}{m} - \frac{\Phi}{m\Phi_0}, \quad Q_G = -\frac{\Phi_G}{m\Phi_0}.$$
 (8.63b)

Already at this level we can trace the Byers–Yang argument: changing the magnetic flux  $\Phi$  by the flux quantum may be compensated if one reduces the number of quasi-particles  $\delta M$  by 1.

The result of the variations of the excess charges is twofold. First of all, the charges  $Q_U$  and  $Q_D$  are screened by Ohmic reservoirs with their own charge capacitances  $C_U$ and  $C_D$ , which are much larger than the capacitances of the Corbino disk. Therefore, the equation (8.40) for the ground state energy has to be replaced with the following expression

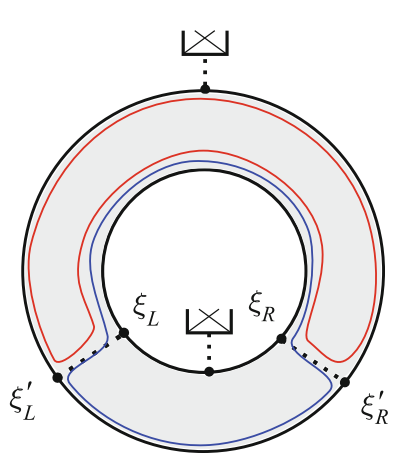


Fig. 8.7 Two possible choices of the integration path in Eqs. (8.65), (8.66), and (8.67) are shown. In both cases the result is the same: if one chooses the *lower* (*blue*) contour, then the contributions of the edge densities are zero, while the bulk fields give the phase  $2\pi(\delta M + \Phi/\Phi_0)$ . If one chooses the *upper* (*red*) contour, then the contribution of the bulk fields is zero, since the contour does not enclose the hole. However, the contribution of the charge density, accumulated at the edge near the Ohmic contact, gives the contribution exactly equal to the calculated above

$$E_0 = \sum_{s=U,D} \frac{Q_s^2}{2C_s}, \qquad \frac{C_s v_s}{r_s} \gg 1, \tag{8.64}$$

i.e., the states with different values of zero modes are almost degenerate, which leads to their strong fluctuations in equilibrium. We will see, however, that these fluctuations do not suppress the Aharonov–Bohm oscillations. Second, as demonstrate below, to leading order in tunneling the Aharonov–Bohm oscillation in tunneling rates originate from the term  $\mathcal{A}_{qp}^{\dagger}(\xi_L)\mathcal{A}_{qp}(\xi_R)$ , which contains a closed path integral over the densities (8.62) and thus depends on excess charges. However, before evaluating this term, we would like to make an important remark.

We stress, that by choosing the positions of Ohmic contacts with respect to the positions of the quantum point contacts as shown in Fig. 8.6, one can model both Fabry–Perot and Mach–Zehnder type interferometers based on the Corbino disk topology. If the Ohmic contacts are located at the opposite sides of the Corbino disk, as illustrated in the left panel, there are only two coherent paths connecting them, which is the case for a Mach–Zehnder interferometer. In contrast, if the Ohmic contacts are located on the same side of the Corbino disk (see the right panel), then there are several coherent paths connecting them, which differ by the number of reflections between the quantum point contacts, as in the case of a Fabry–Perot type interferometer.

We expect, that the singular magnetic flux  $\Phi$  threading the hole of the Corbino disk enters differently the quasi-particle tunneling operators in the cases of Mach–Zehnder and Fabry–Perot type interferometers. And indeed, when evaluating the term  $\mathcal{A}_{qp}^{\dagger}(\xi_L)$ 

 $\mathcal{A}_{qp}(\xi_R)$  with the help of expressions (8.61), (8.62) and (8.63), one should also take into account the position of the inner Ohmic contact, which leads to

$$\mathcal{A}_{qp}^{\dagger}(\xi_L)\mathcal{A}_{qp}(\xi_R) = \mathcal{A}_0^{\dagger}(\xi_L)\mathcal{A}_0(\xi_R) \exp\left\{-2\pi i \left(\frac{\delta M}{m} + \frac{\Phi + \Phi_G}{m\Phi_0}\right)\right\}$$
(8.65)

for a Mach-Zehnder type interferometer, and

$$\mathcal{A}_{qp}^{\dagger}(\xi_L)\mathcal{A}_{qp}(\xi_R) = \mathcal{A}_0^{\dagger}(\xi_L)\mathcal{A}_0(\xi_R) \exp\left\{-\frac{2\pi i \Phi_G}{m\Phi_0}\right\}$$
(8.66)

for a Fabry–Perot type interferometer. The difference in these results agrees with the observation that the Fabry–Perot interferometer does not enclose a singular magnetic flux. Note, also, that when evaluating the phase shifts in (8.65) and (8.66) as integrals of the densities  $\delta \rho_s$  over closed paths, there are four possibilities to choose these paths. Two of them are shown in Fig. (8.7): one is connecting the tunneling points in the lower part of the Corbino disk, and the other encloses the upper part of it. As one can see from Eqs. (8.63), the difference is equal to  $2\pi\delta N$ , i.e., two paths are equivalent.

Finally, we note that all the results obtained here may be formulated on the level of the effective theory. On can use Eqs. (1.58) and (1.59) in order to find the phase factor in the product of the two tunneling operators:

$$\mathcal{A}_{qp}^{\dagger}(\xi_L)\mathcal{A}_{qp}(\xi_R) \propto \exp\Big\{2\pi i \int dx [\delta\rho_U(x) - \delta\rho_D(x)] + i \int_{\gamma} B_{\mu} dr^{\mu} + (2i/m) \int_{\gamma} A_{\mu} dr^{\mu}\Big\}, \tag{8.67}$$

where the contour  $\gamma$  connects tunneling points  $\xi_L, \xi_L', \xi_R'$  and  $\xi_R$ , and the accumulated edge densities  $\delta \rho_s$  are integrated along the corresponding parts of the edges. It follows from the action (1.50) that  $\langle B_\mu \rangle = -A_\mu/m + \mathcal{B}_\mu$ , where the second term is the topological contribution of the charge localized at the inner edge, i.e.,  $\int_{\gamma} \mathcal{B}_\mu dx^\mu = 2\pi M/m$ , for an arbitrary contour  $\gamma$  enclosing the hole in the interferometer. In other words, the bulk and edge degrees of freedom are not completely decoupled in the case of a non-trivial topology. It is also important to mention, that the total phase (8.67) is independent of the choice of the contour  $\gamma$  (see Fig. 8.7). This is because the tunneling operators in our approach are single valued and bring this property over to the level of the effective theory.

# 8.5.2 Current Through the Interferometer

To satisfy the second and third criteria of an ideal Ohmic contact (see Sect. 8.5.1), we consider a quantum Hall interferometer with strong electron tunneling to Ohmic

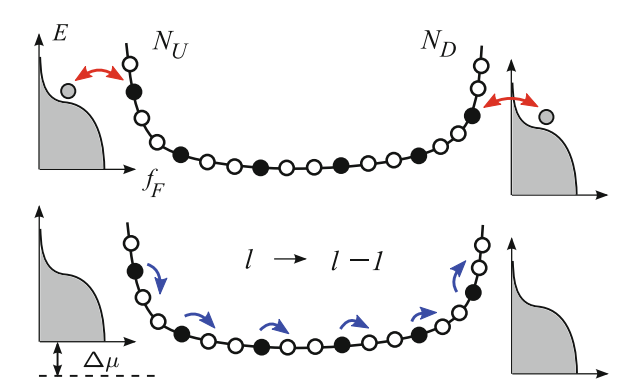


Fig. 8.8 Schematic illustration of the processes at Ohmic contacts and quantum point contacts. *Upper panel*: Electrons tunnel between Ohmic contacts and quantum Hall edges, preserving the incompressibility of the quantum Hall liquid. These processes change the numbers  $N_U$  and  $N_D$ . *Lower panel*: Tunneling of a quasi-particle from one edge of the Corbino disk to another leads to the reconstruction of the wave function and changes the number l by 1. It is accompanied by a change of the electric charge at the inner edge by the value 1/m

reservoirs and weak quasi-particle tunneling between inner and outer edge (see Fig. 8.8). The strong electron coupling to Ohmic contacts guarantees that the inner and outer edge states are in equilibrium with the metallic reservoirs with corresponding electro-chemical potentials  $\mu_U$  and  $\mu_D$ . The charge current between Ohmic contacts, arising as a response to the potential difference  $\Delta\mu = \mu_U - \mu_D$ , is due to weak quasi-particle tunneling at the quantum point contacts. It is then convenient to introduce a new notation for zero modes. We denote by  $N_U$  and  $N_D$  the numbers of electrons at the outer and inner edge of the interferometer, respectively. The number of quasi-particles localized on the inner edge is denoted by  $l=0,\ldots,m-1$ :

$$\delta M = -mN_D - l, \tag{8.68a}$$

$$\delta N = N_U + N_D. \tag{8.68b}$$

The electron quantum numbers,  $N_U$  and  $N_D$ , change due to tunneling at the Ohmic contacts while the quantum number l changes by 1 when a quasi-particle tunnels from one edge to the other, as illustrated in Fig. 8.8.

We consider the zero modes to be classical variables and derive a master equation for the probability distribution functions. Quantum coherence manifests itself in oscillations of the quasi-particle tunneling rates as functions of the magnetic fluxes  $\Phi$  and  $\Phi_G$ . These oscillations originate from the interference of the two quasi-particle tunneling amplitudes at the left and right quantum point contact. Formally, these oscillations stem from the  $\Phi$ -dependent phase factor in the tunneling operators. The strong coupling to Ohmic contacts implies that, after every event of quasi-particle tunneling, the edge states relax to the equilibrium state described by the probability distribution function

$$P_l(N_U, N_D) = \frac{1}{Z_l} e^{-\beta(E_0 - \sum_s \mu_s N_s)}, \tag{8.69}$$

where  $\beta$  is the inverse temperature, and  $Z_l$  is the partition function. The probability  $P_l(N_U, N_D)$  depends on the number l of quasi-particles via the ground-state energy  $E_0(N_U, N_D, l)$ , given by Eqs. (8.63) and (8.64). Importantly, one does not need to specify the precise form of coupling to the Ohmic contacts, because the only role of this coupling is to equilibrate the edge states.<sup>8</sup>

To lowest order in quasi-particle tunneling, the full distribution function of zero modes may be written as

$$P(N_U, N_D, l) = \mathcal{P}_l P_l(N_U, N_D),$$
 (8.70)

where  $\mathcal{P}_l$  is the probability of finding the system in a state with l quasi-particles, and  $P_l(N_U, N_D)$  plays the role of a conditional probability of finding the interferometer in a state with  $N_U$  and  $N_D$  electrons at the edges, for a given number l of quasi-particles. Then, considering quasi-particle tunneling as a weak process that changes the number l, we may describe it with the master equation

$$\dot{\mathcal{P}}_{l} = \Omega_{l-1}^{+} \mathcal{P}_{l-1} + \Omega_{l+1}^{-} \mathcal{P}_{l+1} - (\Omega_{l}^{+} + \Omega_{l}^{-}) \mathcal{P}_{l}, \tag{8.71}$$

where  $\Omega_l^+$  and  $\Omega_l^-$  are the rates of transition from the state with l quasi-particles to the state with l+1 and l-1 quasi-particles, respectively. These rates are given by the expression:

$$\Omega_l^{\pm} = \sum_{N_U, N_D} W_l^{\pm}(N_U, N_D) P_l(N_U, N_D), \tag{8.72}$$

where  $W_l^{\pm}(N_U, N_D)$  are the rates of quasi-particle tunneling between two states with fixed numbers of electrons,  $N_U$  and  $N_D$ .

At time scales much larger than the characteristic times of tunneling, the interferometer reaches a steady state regime with  $\dot{P}_l = 0$ . It is easy to see that in this regime the following quantity is independent of l

$$I = \Omega_l^+ \mathcal{P}_l - \Omega_{l+1}^- \mathcal{P}_{l+1}. \tag{8.73}$$

This quantity is in fact the charge current that we are looking for. This follows from the expression for the current

$$I = (1/m) \sum_{l} (\Omega_{l}^{+} - \Omega_{l}^{-}) \mathcal{P}_{l}, \tag{8.74}$$

<sup>&</sup>lt;sup>8</sup> On may check that solving the detailed balance equation with tunneling rates calculated with the amplitudes (8.54) and (8.55) leads to the distribution (8.69).

and from the periodic boundary condition,  $\mathcal{P}_0 = \mathcal{P}_m$ , which can be verified directly using Eqs. (8.69) and (8.70). Note that the detailed balance equation  $\Omega_l^+ \mathcal{P}_l = \Omega_{l+1}^- \mathcal{P}_{l+1}$  is satisfied only if I = 0. Thus, the quantum Hall interferometer in a non-equilibrium steady-state regime represents an interesting example of a system with broken detailed balance.

We evaluate the tunneling rates  $W_l^{\pm}(N_U, N_D)$  to leading order in the tunneling Hamiltonian  $\mathcal{H}_T = \mathcal{A} + \mathcal{A}^{\dagger}$ , where  $\mathcal{A} \equiv \mathcal{A}_{qp}(\xi_L) + \mathcal{A}_{qp}(\xi_R)$ . A straightforward calculation, based on the Fermi Golden Rule, gives the following expression:

$$W_l^+(N_U, N_D) = \int dt \operatorname{Tr} \{ \rho_{\text{eq}} \mathbb{P}(N_U, N_D, l) \mathcal{A}^{\dagger}(t) \mathcal{A}(0) \}, \tag{8.75}$$

and a similar expression for  $W_l^-(N_U, N_D)$ . Here the operator  $\mathbb{P}(N_U, N_D, l)$  projects onto states with given numbers  $N_s$  and l, and the operator  $\rho_{eq}$  is the equilibrium density matrix for the oscillators. Now we consider the solution of the master equation (8.71) with tunneling rates given by (8.75) for two possible types of the quantum Hall interferometer (see Fig. 8.6).

In fact, one can find the periodicity of current without an explicit evaluation of the integral in (8.75). Indeed, in the case of the Mach–Zehnder interferometer the product of two tunneling operators which gives the coherent contribution to (8.75) has the following dependence on the zero mode l and the fluxes [see Eq. (8.65)]:

$$\mathcal{A}_{\mathrm{qp}}^{\dagger}(\xi_L)\mathcal{A}_{\mathrm{qp}}(\xi_R) \propto \exp\left\{2\pi i \left(\frac{l}{m} - \frac{\Phi + \Phi_G}{m\Phi_0}\right)\right\}.$$
 (8.76)

Importantly, the flux enters these products and, thus, the transition rates (8.72) solely in the combination  $l-(\Phi+\Phi_G)/\Phi_0$ . A shift of the flux  $\Phi$  by one flux quantum  $\Phi_0$  may be then compensated by the shift  $l\to l+1$ . The quasi-particle current is given by Eq. (8.74), where the probabilities satisfy Eqs. (8.73) with the constraint  $\sum_l \mathcal{P}_l = 1$ . All these equations are periodic in l with period equal to m and invariant under the replacement  $\Omega_l^{\pm} \to \Omega_{l+1}^{\pm}$ . This implies that the average current has the electronic periodicity,  $I(\Delta\mu,\Phi) = I(\Delta\mu,\Phi+\Phi_0)$ , in agreement with the Byers–Yang theorem.

For example, the solution of Eqs. (8.73) and (8.74) for  $\nu=1/3$  gives the average current

$$I = \frac{\Omega_2^+ \Omega_1^+ \Omega_0^+ - \Omega_2^- \Omega_1^- \Omega_0^-}{\sum_l (\Omega_{l+1}^+ \Omega_l^+ + \Omega_{l+1}^+ \Omega_l^- + \Omega_{l+1}^- \Omega_l^-)},$$
(8.77)

which is explicitly periodic function of  $\Phi$  with the electronic period  $\Phi_0$ . At the same time, each tunneling rate  $\Omega_l^{\pm}$  has a quasi-particle periodicity. Therefore, the quasi-particle periodicity with respect to a singular flux may in principle be observed via, e.g., the current noise measurements at finite frequencies. The last fact does not violate the Byers–Yang theorem, because this theorem applies only to a stationary state and to long-time measurements.

In contrast to the above, it follows from Eq. (8.65) that the coherent combination of the tunneling amplitudes does not depend on l in the case of the Fabry–Perot interferometer. Therefore, the current has a quasi-particle periodicity  $m\Phi_0$  with respect to the modulation gate. Note however, that this does not violate the Byers–Yang theorem. The quasi-particle periodicities with respect to the modulation gate allow one to perform the edge spectroscopy proposed in Ref. [38]. The product (8.66) does not depend on the singular flux, however, which is natural, since the interference contour does not go around the flux tube. The periodicity of the current with respect to the singular flux is thus determined only by the Coulomb blockade effect, if present in case of weak coupling to Ohmic contacts, and it is equal to  $\Phi_0$ .

#### 8.6 Conclusion

Recently, the physics of Aharonov–Bohm oscillations in electronic interferometers has become a subject of a debate. A number of works have claimed that only the electronic periodicity may be observed in Mach–Zehnder interferometers based on quantum Hall states at fractional filling factors  $\nu=1/m$ . We have briefly reviewed those papers at beginning of this chapter. Here we recall that the main argument against the observability of Aharonov–Bohm oscillations with a longer, quasi-particle periods is based on the Byers–Yang theorem, which states that the steady-state current through the interferometer oscillates with the electronic period  $\Phi_0$  as a function of the singular magnetic flux  $\Phi$  threading the interferometer's loop.

We construct the microscopic model of a quantum Hall interferometer to find how and in which cases the electron periodicity can be restored. Our starting point is the Laughlin wave-function which is a good approximation for the true ground state of quantum Hall liquid. We consider small incompressible deformations of the ground state of an electronic interferometer and project the microscopic Hamiltonian onto the subspace of states which describe these deformations. The projected Hamiltonian (8.41) and projected tunneling operators (8.49) are consistent with chiral conformal effective theory [2–4] modified in order to take into account the non-trivial topology of the system. Interestingly, we do not find any trace of additional Klein factors [49] in the quasi-particle tunneling operators, which are not excluded by the effective theory. Moreover, these operators are the single-valued functions of the coordinate of the tunneling point.

The crucial ingredients of our model are Ohmic contacts. We describe them as regions of the edges, which accommodate any excess charge, thus perfectly screening slow charge fluctuations at the edges. Ohmic contacts have large capacitance and lead to the equilibration and dephasing of edge states. The current through the interferometer caused by a bias voltage applied to the Ohmic contacts is found with the help of the master equation describing tunneling at quantum point contacts. We find that the tunneling rates in a Mach–Zehnder interferometer oscillate with the number of quasi-particles *l*. Therefore, after the resummation over *l*, the current through the interferometer oscillates as a function of the magnetic flux with the electronic period

 $\Phi_0$ . Meanwhile, in the Fabry–Perot interferometer case, the tunneling rates are independent of l, and the current oscillates with the period  $m\Phi_0$  as a function of the flux induced by a modulation gate. Thereby, the Byers–Yang paradox is resolved.

In conclusion, we note that the proposed microscopic construction of the effective theory of an electronic interferometer can be generalized to states with other filling factors, in particular, to the states with non-Abelian statistics of excitations. Moreover, our results can be easily generalized to systems with a different geometry. Although, the physics in general will remain the same, detailed considerations may bring new interesting results. In view of our new findings concerning the nature of the quasiparticle interference, it is very interesting to reconsider the effects of quasi-particle exchange and statistics.

#### References

- 1. K.v. Klitzing, G. Dorda, M. Pepper, Phys. Rev. Lett. 45, 494 (1980)
- 2. X.-G. Wen, Phys. Rev. B 41, 12838 (1990)
- 3. J. Fröhlich, A. Zee, Nucl. Phys. B 364, 517 (1991)
- 4. J. Fröhlich, T. Kerler, Nucl. Phys. B 354, 369 (1991)
- 5. R.B. Laughlin, Phys. Rev. Lett. **50**, 1395 (1983)
- 6. L. Saminadayar, D.C. Glattli, Y. Jin, B. Etienne, Phys. Rev. Lett. 79, 2526 (1997)
- R. de-Picciotto, M. Reznikov, M. Heiblum, V. Umansky, G. Bunin, D. Mahalu, Nature, 389, 162 (1997)
- M. Dolev, Y. Gross, Y.C. Chung, M. Heiblum, V. Umansky, D. Mahalu, Phys. Rev. B 81, 161303(R) (2010)
- 9. Y.M. Blanter, M. Büttiker, Phys. Rep. **336**, 1 (2000)
- 10. I. Safi, H.J. Schulz, Phys. Rev. B **52**, 17040 (1995)
- 11. H. Steinberg, G. Barak, A. Yacoby, L.N. Pfeiffer, K.W. West, B.I. Halperin, K. Le Hur, Nat. Phys. 4, 116 (2008)
- 12. W. Ehrenberg, R.E. Siday, Proc. Phys. Soc. B 62, 8 (1949)
- 13. Y. Aharonov, D. Bohm, Phys. Rev. **115**, 485 (1959)
- 14. I. Neder, M. Heiblum, Y. Levinson, D. Mahalu, V. Umansky, Phys. Rev. Lett. 96, 016804 (2006)
- 15. I. Neder, F. Marquardt, M. Heiblum, D. Mahalu, V. Umansky, Nat. Phys. 3, 534 (2007)
- 16. Y. Ji et al., Nat. (Lond.) 422, 415 (2003)
- P. Roulleau, F. Portier, D.C. Glattli, P. Roche, A. Cavanna, G. Faini, U. Gennser, D. Mailly, Phys. Rev. B 76, 161309 (2007)
- P. Roulleau, F. Portier, D.C. Glattli, P. Roche, A. Cavanna, G. Faini, U. Gennser, D. Mailly, Phys. Rev. Lett. 100, 126802 (2008)
- 19. L.V. Litvin, H.-P. Tranitz, W. Wegscheider, C. Strunk, Phys. Rev. B 75, 033315 (2007)
- L.V. Litvin, A. Helzel, H.-P. Tranitz, W. Wegscheider, C. Strunk, Phys. Rev. B 78, 075303 (2008)
- E. Bieri, Correlation and Interference Experiments with Edge States, Ph.D. thesis, University of Basel (2007).
- E. Bieri, M. Weiss, O. Goktas, M. Hauser, C. Schonenberger, S. Oberholzer, Phys. Rev. B 79, 245324 (2009)
- 23. J.A. Simmons, H.P. Wei, L.W. Engel, D.C. Tsui, M. Shayegan, Phys. Rev. Lett. 63, 1731 (1989)
- J.A. Simmons, S.W. Hwang, D.C. Tsui, H.P. Wei, L.W. Engel, M. Shayegan, Phys. Rev. B 44, 12933 (1991)
- 25. F.E. Camino, W. Zhou, V.J. Goldman, Phys. Rev. Lett. 95, 246802 (2005)
- 26. F.E. Camino, W. Zhou, V.J. Goldman, Phys. Rev. B 72, 075342 (2005)

References 175

- 27. F.E. Camino, W. Zhou, V.J. Goldman, Phys. Rev. Lett. 98, 076805 (2007)
- 28. F.E. Camino, W. Zhou, V.J. Goldman, Phys. Rev. B 74, 115301 (2006)
- 29. R.L. Willett, L.N. Pfeiffer, K.W. West, PNAS 106, 8853 (2009)
- 30. R.L. Willett, L.N. Pfeiffer, K.W. West, arXiv:0911.0345
- 31. F.E. Camino, W. Zhou, V.J. Goldman, Phys. Rev. B 76, 155305 (2007)
- 32. W. Zhou, F.E. Camino, V.J. Goldman, Phys. Rev. B 73, 245322 (2006)
- 33. E.V. Sukhorukov, V.V. Cheianov, Phys. Rev. Lett. 99, 156801 (2007)
- 34. J.T. Chalker, Y. Gefen, M.Y. Veillette, Phys. Rev. B 76, 085320 (2007)
- 35. I. Neder, E. Ginossar, Phys. Rev. Lett. 100, 196806 (2008)
- 36. S.-C. Youn, H.-W. Lee, H.-S. Sim, Phys. Rev. Lett. 100, 196807 (2008)
- 37. I.P. Levkivskyi, E.V. Sukhorukov, Phys. Rev. B **78**, 045322 (2008)
- 38. I.P. Levkivskyi, A. Boyarsky, J. Fröhlich, E.V. Sukhorukov, Phys. Rev. B 80, 045319 (2009)
- 39. D.L. Kovrizhin, J.T. Chalker, Phys. Rev. B 81, 155318 (2010)
- 40. B. Rosenow, B.I. Halperin, Phys. Rev. Lett. 98, 106801 (2007)
- 41. N. Byers, C.N. Yang, Phys. Rev. Lett. 7, 46 (1961)
- 42. C.L. Kane, M.P. Fisher, J. Polchinski, Phys. Rev. Lett. 72, 4129 (1994)
- 43. K.T. Law, D.E. Feldman, Y. Gefen, Phys. Rev. B 74, 045319 (2006)
- 44. V.V. Ponomarenko, D.V. Averin, Phys. Rev. Lett. 99, 066803 (2007)
- 45. D.J. Thouless, Y. Gefen, Phys. Rev. Lett. 66, 806 (1991)
- 46. Y. Gefen, D.J. Thouless, Phys. Rev. B 47, 10423 (1993)
- 47. D.E. Feldman, A. Kitaev, Phys. Rev. Lett. 97, 186803 (2006)
- 48. D.E. Feldman, Y. Gefen, A. Kitaev, K.T. Law, A. Stern, Phys. Rev. B 76, 085333 (2007)
- 49. R. Guyon, P. Devillard, T. Martin, I. Safi, Phys. Rev. B 65, 153304 (2002)
- 50. A. Boyarsky, V.V. Cheianov, O. Ruchayskiy, Phys. Rev. B 70, 235309 (2004)
- M. Marino, Chern-Simons Theory, Matrix Models, and Topological Strings (Oxford University Press, Oxford, 2005)
- 52. V.V. Ponomarenko, D.V. Averin, Europhys. Lett. **61**, 102 (2003)
- 53. F.D.M. Haldane, E.H. Rezayi, Phys. Rev. Lett. **54**, 237 (1985)
- 54. F.D.M. Haldane, in Ref. [55], Chap. 8
- 55. R.E. Prange, S.M. Girvin (eds.) The Quantum Hall Effect, (Springer, New York, 1987)
- J. Fröhlich, The Fractional QHE, CS Theory, and Integral Lattices, in *Proceedings of ICM'94*,
   Basel, Boston, 1995, ed. by S.D. Chatteji. (Birkhäuser Verlag, Berlin, 1995)
- 57. A. Cappelli, C.A. Trugenberger, G.R. Zemba, Phys. Lett. B 306, 100 (1993)
- 58. B. Blok, X.G. Wen, Phys. Rev. B 43, 8337 (1991)
- 59. I. Kogan, A.M. Perelomov, G.W. Semenoff, Phys. Rev. B 45, 12084 (1992)
- 60. V. Gurarie, C. Nayak, Nucl. Phys. B 506, 685 (1997)
- 61. R. de Gail, N. Regnault, M.O. Goerbig, Phys. Rev. B 77, 165310 (2008)
- 62. F.J. Dyson, J. Math. Phys. 3, 140, 157, 166 (1962)
- 63. O.E. Dial, R.C. Ashoori, L.N. Pfeiffer, K.W. West, Nature 464, 566 (2010)
- 64. H.B. Chan, P.I. Glicofridis, R.C. Ashoori, M.R. Melloch, Phys. Rev. Lett. 79, 2867 (1997)
- 65. C.L. Kane, M.P.A. Fisher, Phys. Rev. B **52**, 17393 (1995)
- 66. C. de C. Chamon, E. Fradkin, Phys. Rev. B 56, 2012 (1997)

# **Chapter 9 Summary of Results**

In this thesis, we have considered the physics of the quantum Hall effect at mesoscopic length scales. This physics is mainly determined by the edge states, which are the only gapless excitations. We have investigated such mesoscopic effects as interaction induced dephasing of edge states, noise induced dephasing, and equilibration along the quantum Hall edge channels. This investigation allowed us to explain several experiments, to make some experimental proposals and to resolve certain theoretical problems as summarized below.

#### 9.1 Integer Quantum Hall Effect

We developed a new theoretical technique which allows one to extend the bosonization approach to the non-equilibrium situations. The main idea of this technique is to include the non-equilibrium effects via the corresponding boundary conditions in the equations of motion for the boson field operators. Thus, all the information about the interaction is encoded in the Green function of these equations, while the non-equilibrium state is encoded in the boundary conditions. The calculation of electron correlation functions for an interacting system can be therefore reduced to finding of averages over the free electrons. In certain cases, this approach allows one to express the correlator in terms of the full counting statistics of the boundary charges.

We have proposed a simple physical model which describes dephasing in the electronic Mach-Zehnder interferometer at integer filling factors. This model explains very recent experimental results at filling factor  $\nu=2$ , such as the unusual lobetype structure in the visibility of Aharonov-Bohm oscillations, phase rigidity, and the asymmetry of the visibility as a function of transparencies of quantum point contacts. According to our model, dephasing in the interferometer originates from strong Coulomb interaction at the edge of two-dimensional electron gas. The long-range character of the interaction leads to a separation of the spectrum of edge excitations on slow and fast mode. These modes are excited by electron tunneling and carry

away the phase information. The new energy scale associated with the slow mode determines the temperature dependence of the visibility and the period of its oscillations as a function of voltage bias. Moreover, the variation of the lobe structure from one experiment to another is explained by specific charging effects, which are different in all experiments. We propose to use a strongly asymmetric Mach-Zehnder interferometer with one arm being much shorter than the other for the spectroscopy of quantum Hall edge states.

We have considered dephasing in the electronic Mach-Zehnder interferometer strongly coupled to current noise created by a voltage biased quantum point contact. We find the visibility of Aharonov-Bohm oscillations as a function of voltage bias and express it via the cumulant generating function of noise. In the large-bias regime, high-order cumulants of current add up to cancel the dilution effect of a quantum point contact. This leads to an abrupt change in the dependence of the visibility on voltage bias which occurs at the quantum point contact's transparency T=1/2. Quantum fluctuations in the vicinity of this point smear out the sharp transition.

We have used the proposed non-equilibrium bosonization technique in order to construct the theory of the energy relaxation process at the quantum Hall edge. We find that the relaxation of the energy distribution function goes through several intermediate asymptotics. Namely, the distribution function at short distances is found to be strongly asymmetric due to the non-Gaussian noise effects. At larger distances, the higher order cumulants become suppressed and the distribution function becomes a symmetric Lorentzian. Importantly, the width of this Lorentzian scales linearly with transparency T of quantum point contact, in striking contrast with the Fermi distribution function, whose width scales as  $\sqrt{T}$  at low transparencies. Thus, we propose to make measurements at low transparencies in order to discover all the intermediate regimes of relaxation. We also have found that the missing energy flux in recent experiments can be explained by the non-linear dispersion of edge plasmons.

## 9.2 Fractional Quantum Hall Effect

We considered the classification of the edge effective models in fractional quantum Hall regime. This classification is based on the idea that the fundamental edge degrees of freedom are gapless chiral bosons. The main requirements to the effective model such as gauge invariance and existence of the electron excitation in the spectrum significantly reduces the number of allowed models. These edge models are then classified by the integer valued matrix of the relative statistical phases of electron excitations, velocities of edge modes, and mixing matrix between the electrons and boson eigenmodes. The last two objects have shown to be important in the description of the mesoscopic experiments in integer case. Strong Coulomb interaction at the edge leads to a number of universalities, similar to integer case, and allowed us to reduce further the number of edge models with two edge states.

We also propose direct experimental tests of the effective models of fractional quantum Hall edge states. We illustrate the general classification of edge models with the example of a quantum Hall fluid at filling factor  $\nu=2/3$  and show that, in this example, it is impossible to describe the edge states with only one chiral channel and that there are several inequivalent models of the edge states with two fields. We focus our attention on the four simplest models of the edge states of a fluid with  $\nu=2/3$  and evaluate charges and scaling dimensions of quasi-particles. We study transport through an electronic Fabry-Perot interferometer and show that scaling properties of the Fourier components of Aharonov-Bohm oscillations in the current provide information about the electric charges and scaling dimensions of quasi-particles. Thus Fabry-Perot interferometers can be used to discriminate between different effective models of fluids corresponding to the same filling factor. They therefore can be used to test fundamental postulates underlying the low-energy effective theory of edge states.

We propose a resolution of the Byers-Yang paradox by considering a microscopic model of an electronic interferometer made from a quantum Hall liquid at filling factor v = 1/m in the shape of a Corbino disk. Depending on the position of Ohmic contacts attached to the disk one distinguishes interferometers of Fabry-Perot and Mach-Zehnder type. An approximate ground state of such interferometers is described by a Laughlin type wave function, and low-energy excitations are incompressible deformations of this state. We construct a low-energy effective theory by projecting the state space of the liquid onto the space of incompressible deformations and show that the theory of the quantum Hall edge so obtained is a generalization of a chiral conformal field theory. A quasi-particle tunneling operator in our theory is found to be a single-valued function of tunneling point coordinates, and its phase depends on the topology, determined by the positions of Ohmic contacts. We describe strong coupling of the edge states to Ohmic contacts and the resulting quasi-particle current through the interferometer with the help of master equation. We find that the coherent contribution to the average quasi-particle current through Mach-Zehnder interferometers vanishes after the summation over quasi-particle degrees of freedom. Remaining contribution originates from electron tunneling and oscillates with the electronic period, in agreement with the Byers-Yang theorem. Importantly, in contrast to previous models our theory does not rely on any ad-hoc constructions, such as Klein factors, etc. When a magnetic flux through Fabry-Perot interferometers is varied with a modulation gate, current oscillations have the quasi-particle periodicity, thus allowing for the spectroscopy of quantum Hall edge states.

To conclude, we have applied several approaches to the quantum Hall effect at the mesoscopic length scales, such as single-particle, effective, and microscopic approach. We have found that all these approaches suggest a common picture of edge states based on boson modes. Within this single simple picture, we have explained several experimental results and made some predictions, part of which has been already confirmed. Finally, we have shown that the physics at the intersection of two areas research such as the quantum Hall effect and the mesocopics is very reach and interesting and certainly deserves further intensive theoretical and experimental investigation.

#### **A Solution of Equations of Motion**

In this appendix we solve the equations of motion (2.39a) with the boundary conditions (2.39b) in the case of the potential  $U_{\alpha\beta}(x-y)$  of a finite range, where the plasmon spectrum is non-linear. For doing this, we first write down the normal mode expansion for the edge boson fields:

$$\phi_{\alpha}(x) = \varphi_{\alpha} + 2\pi \cdot \pi_{\alpha}x + \sum_{k} \sqrt{\frac{2\pi}{kW}} [a_{\alpha k}e^{ikx} + a_{\alpha k}^{\dagger}e^{-ikx}]. \tag{A.1}$$

We consider zero modes to be classical variable, because the commutator  $[\pi_{\alpha}, \varphi_{\alpha}] = i/W$  vanishes in the thermodynamic limit  $W \to 0$ . Then, we rewrite the operators  $a_{\alpha k}$  in the new basis  $\tilde{a}_{jk}$ , which diagonalizes the edge Hamiltonian (4.1):

$$\tilde{a}_{ik}(t) = \tilde{a}_{ik}e^{-i\omega_j(k)t},\tag{A.2}$$

where j=1,2, and  $\omega_j(k)$  is the dispersion of the *j*th mode. In the case, where the in-channel interaction strength is approximately equal to the intra-channel one,  $U_{\alpha\beta}(x-y)\approx U(x-y)$ , and the interaction is strong,  $U(k)=\int dx e^{ikx}U(x)\gg 2\pi v_F$ , the transformation to the new basis is simple and universal:

$$a_{1k}(t) = \frac{1}{\sqrt{2}} \left( \tilde{a}_{1k} e^{-i\omega_1(k)t} + \tilde{a}_{2k} e^{-i\omega_2(k)t} \right),$$
 (A.3a)

$$a_{2k}(t) = \frac{1}{\sqrt{2}} \left( \tilde{a}_{1k} e^{-i\omega_1(k)t} - \tilde{a}_{2k} e^{-i\omega_2(k)t} \right).$$
 (A.3b)

Some text sections in this chapter are reproduced from Phys. Rev. B 78, 045322 (2008), Phys. Rev. B 80, 045319 (2009), Phys. Rev. Lett. 103, 036801 (2009), Phys. Rev. B 85, 075309 (2012), © American Physical Society.

Then,  $\omega_1(k) = k[v_F + U(k)/\pi]$  for the charged plasmon, and  $\omega_2(k) = vk$  for the dipole mode, where  $v \approx v_F$ .

In the next step, we use the boundary conditions (2.39b) to connect the current operators to the operators (A.2):

$$\tilde{a}_{1k} = \frac{i}{\omega_1} \frac{\partial \omega_1}{\partial k} \sqrt{\frac{\pi k}{W}} [j_1(\omega_1) + j_2(\omega_1)], \tag{A.4a}$$

$$\tilde{a}_{2k} = \frac{i}{\omega_2} \frac{\partial \omega_2}{\partial k} \sqrt{\frac{\pi k}{W}} [j_1(\omega_2) - j_2(\omega_2)], \tag{A.4b}$$

where  $j_{\alpha}(\omega) = \int dt e^{i\omega t} j_{\alpha}(t)$ , and we have used the obvious relation  $j_{\alpha}(-\omega) = j_{\alpha}^{\dagger}(\omega)$ . Finally, substituting relations (A.4a, A.4b) into Eq. (A.3a) and then to the expansion (A.1), we find the solution of the equations of motion for the boson fields. In particular,

$$\phi_{1}(x,t) = -2\pi \langle j_{1} \rangle t + \frac{i}{2} \int_{-\infty}^{\infty} \frac{d\omega}{\omega} \left\{ j_{1}(\omega) \left( e^{ik_{1}x} + e^{ik_{2}x} \right) + j_{2}(\omega) \left( e^{ik_{1}x} - e^{ik_{2}x} \right) \right\} e^{-i\omega t},$$
(A.5)

where we set  $k_j(-\omega) = -k_j(\omega)$ . In addition, we have omitted the contribution of the zero mode  $\pi_1$ , because we need local correlators, and replaced the zero mode  $\varphi_1(t)$  by its expectation value.

#### **B** Evaluation of the Measured Heat Flux

The experimentally found heat flux defined in Eq. (5.19) may be written in time representation as

$$I_{\rm m} = -i\hat{o}_t \left[ K(t) - \frac{e^{i\langle \Delta \mu \rangle t}}{2\pi i t} \right]_{t=0}. \tag{B.1}$$

Then, we may use Eq. (5.8) and results of the Appendix A in order to evaluate the correlation function K(t). The difficulty of finding this function is related to the fact that according to Eq. (A.5) the correlators of the operator  $\phi_1(t)$  are determined by the currents  $j_{\alpha}(t)$ , which are in general non-Gaussian. However, in the present case we need to take the limit  $t \to 0$  in Eq. (B.1). The high-order cumulants of currents originate from a non-equilibrium process and are suppressed at short times  $t\Delta\mu\ll 1$ . Therefore, we are allowed to evaluate K(t) in Gaussian approximation.

This may be done by expanding the right hand side of the Eq. (5.8) to second order in  $\phi_1$ :

$$\ln K(t) = \langle [\phi_1(t) - \phi_1(0)]\phi_1(0)\rangle + 2\pi i \langle j_1 \rangle t, \tag{B.2}$$

where the averaging is over the fluctuations of the currents  $j_{\alpha}$ . We then use the Eq. (A.5) and the stationary correlators of the currents

$$\langle j_{\alpha}(\omega_1)j_{\beta}(\omega_2)\rangle = 2\pi S_{\alpha}(\omega_1)\delta_{\alpha\beta}\delta(\omega_1 + \omega_2) \tag{B.3}$$

to present the electron correlation function in the following form

$$\ln K = \ln K_{\rm n} + 2\pi i \langle j_1 \rangle t - \ln t. \tag{B.4}$$

Here the fluctuation contribution reads

$$\ln K_{n} = \pi \int_{-\infty}^{\infty} \frac{d\omega}{\omega^{2}} (e^{-i\omega t} - 1) 
\times \{\mathbb{S}_{1}(\omega)[1 + \cos(\Delta kL)] + \mathbb{S}_{2}(\omega)[1 - \cos(\Delta kL)]\},$$
(B.5)

where we have introduced the excess noise spectral densities  $\mathbb{S}_{\alpha}(\omega) = S_{\alpha}(\omega) - \omega\theta(\omega)/2\pi$  and  $\Delta k = k_1(\omega) - k_2(\omega)$ .

It is easy to see that for a non-vanishing contribution to  $I_{\rm m}$ , given by the expression (B.1), we need to expand  $\ln K_{\rm n}$  to second order in t. Note, however, that linear in t term in this expansion adds to the corresponding term in Eq. (B.4) to give  $2\pi i \langle \Delta \mu \rangle t$ . This follows directly from the definition (5.18) of the "average" bias, which in time representation may be written as  $\langle \Delta \mu \rangle = 2\pi \partial_t [tK(t)]_{t=0}$ . Therefore, only  $t^2$  term in  $\ln K_{\rm n}$  contributes to  $I_{\rm m}$ , and we obtain

$$I_{\rm m} = -\frac{1}{4\pi} \hat{\sigma}_t^2 \ln K_{\rm n}(t)|_{t=0}.$$
 (B.6)

Finally, we use Eq. (B.5) and obtain the result (5.27).

Next, we want to rewrite the measured flux  $I_{\rm m}$  in terms of the plasmon distributions  $n_j(k) = \langle \tilde{a}_j^{\dagger}(k)\tilde{a}_j(k)\rangle, j=1,2$ . For doing so, we now use Eqs. (A.1) and (A.3a, A.3b), repeat the steps that lead to (B.5), and take the limit of  $L\gg L_{\rm ex}$ . The result may be presented in following form:

$$\ln K_{\rm n} = -\sum_{j} \int_{0}^{\infty} \frac{dk}{k} \, n_{j}(k) [1 - \cos(\omega_{j}t)] + \frac{1}{2} \sum_{j} \int_{0}^{\infty} \frac{dk}{k} \, \left( e^{-i\omega_{j}t} - e^{-iv_{j}kt} \right), \quad (B.7)$$

where the last term is the quantum contribution due to the non-linear plasmon dispersion, and  $v_j = \partial \omega_j / \partial k$  are the plasmon speeds at k = 0. Substituting expressions (B.7) into Eq. (B.6), we obtain the final result (5.30) and (5.31) for the measured heat flux.

#### C Suppression of Higher Order Cumulants

Here we show that a weak dispersion of plasmon modes leads to the suppression of the contribution of higher order cumulants of current  $j_{\alpha}$  to the electron correlation function at long distances L from the source of currents. We demonstrate this using an example of the weakly dispersive spectrum of plasmons in the form  $k_j = \omega/v_j + \gamma_j \omega^2 \mathrm{sign}(\omega), j = 1, 2$ . Since we are interested in the behavior of the electron distribution function close to the Fermi level, we need the long-time asymptotics of the electron correlation function K(t). Therefore, the contributing currents  $j_{\alpha}$  can be considered Markovian processes and fields  $\phi_{\alpha}$  can be treated as classical variables.

Let us consider the *n*th cumulant:

$$M^{(n)}(L,t) \equiv \langle \langle [\phi_1(L,t) - \phi_1(L,0)]^n \rangle \rangle. \tag{C.1}$$

According to Eq. (A.5), at large distances  $L \gg L_{\rm ex} = v_j/\Delta\mu$  and long times  $t\Delta\mu \gg 1$  it may be written as

$$M^{(n)}(L,t) = \sum_{\alpha} M_{\alpha}^{(n)}(L,t),$$
 (C.2)

where:

$$M_{\alpha}^{(n)}(L,t) = 2\pi S_{\alpha}^{(n)} \int \prod_{l=1}^{n} \frac{d\omega_{l}}{\omega_{l}} (i/2) (e^{-i\omega_{l}t} - 1)$$

$$\times \delta(\omega_{1} + \dots + \omega_{n}) \left[ e^{i\sum_{l} k_{1}(\omega_{l})L} + e^{i\sum_{l} k_{2}(\omega_{l})L} \right]$$
(C.3)

and  $S_{\alpha}^{(n)} \equiv \langle \langle j_{\alpha}^{n} \rangle \rangle$ . Here we have neglected the cross terms containing fast oscillating functions. These terms have the same origin as fast oscillating terms in (5.27) and vanish at distances  $L \gg L_{\rm ex}$ . Dropping those terms is also equivalent to neglecting in (5.9) correlations of charges taken at different times  $t_u$  and  $t_v$ . Finally, we note that in our particular case, where the quantum point contact is connected to the outmost edge channel only,  $S_2^{(n)} = 0$  for n > 2.

One can easily see that  $\sum_l k_j(\omega_l) = \sum_l \gamma_j \omega_l^2 \mathrm{sign}(\omega_l)$ , because the integrals in (C.3) are limited to  $\sum_l \omega_l = 0$ . For the second cumulant this implies that  $k_j(\omega_1) + k_j(\omega_2) = 0$ , i.e., the dispersion correction cancels too. Therefore the second cumulant is not suppressed at long distances. Below we consider high-order cumulants. Using the identity  $2\pi\delta(\omega_1+\ldots+\omega_n) = \int d\tau \exp[i(\omega_1+\ldots+\omega_n)\tau]$  we can write

$$M_{\alpha}^{(n)}(L,t) = S_{\alpha}^{(n)} \sum_{j} \int_{-\infty}^{\infty} d\tau [F_{j}(\tau,t,L)]^{n}, \qquad (C.4)$$

where we have introduced the integrals

$$F_{j} = \frac{i}{2} \int \frac{d\omega}{\omega} (e^{-i\omega t} - 1) e^{i\omega \tau + i\gamma_{j} L\omega^{2} \operatorname{sign}(\omega)}.$$
 (C.5)

At large distances  $L\gamma_j\gg t^2$  the contribution to the integrals  $F_j$  comes from small  $\omega$ , where one can approximate  $e^{-i\omega t}-1\approx -i\omega t$ . Therefore, Eq. (C.5) can be further simplified:

$$F_j = (t/2) \int d\omega e^{i\omega\tau + i\gamma_j L\omega^2 \mathrm{sign}(\omega)} \propto \frac{t}{\sqrt{\gamma_j L}} e^{\pm i\tau^2/4\gamma_j L}.$$
 (C.6)

Substituting this result into Eq. (C.4) and then to (C.2), we find that

$$M^{(n)}(L,t) \propto t \sum_{\alpha} S_{\alpha}^{(n)} \sum_{i=1,2} \left(\frac{t^2}{\gamma_i L}\right)^{\frac{n-1}{2}}, \ n > 2,$$
 (C.7)

where, we recall, the sum is over the plasmon eigenmode number j and over the channel number  $\alpha$ .

We note, that at large distances L the cumulants  $M^{(n)}(L,t)$  are suppressed by the small dimensionless parameter  $t^2/\gamma_j L \ll 1$ . In our case  $S_1^{(n)} \sim T\Delta\mu$  and  $S_2^{(n)} = 0$ , therefore high-order cumulants may be neglected at distances larger than  $L_{\rm g} = 1/\gamma_j (T\Delta\mu)^2$ , and noise may be considered Gaussian. Obviously, if only one plasmon mode of two is dispersive, e.g.,  $\gamma_2 = 0$ , then at distances  $L \gg L_{\rm g}$  the cumulant (C.2) is suppressed by the factor of 2. One can interpret the result (C.7) as the renormalization of the effective coupling constant  $\lambda$  in (5.11), which is caused by spreading of a plasmon wave packets due to the dispersion.

#### **D** Calculation of Scaling Dimensions

Using Eq. (6.42) for  $\delta_i$ , we calculate the total scaling dimension  $\Delta$ . As it has already been mentioned, in the general (non-chiral) case, the scaling dimension is a function of the full matrix q. Therefore, apart from the matrix K, it depends only on one additional variable, which can be fixed by choosing the Hamiltonian. We are interested in a matrix K of the following form:

$$K = \begin{pmatrix} a & b \\ b & a \end{pmatrix}. \tag{D.1}$$

The connection between matrices K and q in the non-chiral case is  $K = q\sigma q^T$ . Therefore we can introduce the following parametrization of the matrix q,

$$q/\sqrt{a} = \begin{pmatrix} \cosh \vartheta_1 & \sinh \vartheta_1 \\ \cosh \vartheta_2 & \sinh \vartheta_2 \end{pmatrix}, \tag{D.2}$$

where  $\cosh(\vartheta_2 - \vartheta_1) = b/a$ . Although the case a < 0 requires a different parametrization, it leads to the same result.

The evaluation of the scaling dimension  $\Delta(\mathbf{n}) = \mathbf{n}(qq^T)^{-1}\mathbf{n}$  requires to invert the matrix:

$$qq^{T} = a \begin{pmatrix} \cosh 2\theta_{1} & \cosh(\theta_{1} + \theta_{2}) \\ \cosh(\theta_{1} + \theta_{2}) & \cosh 2\theta_{2} \end{pmatrix}.$$
 (D.3)

For convenience, we introduce the angle  $\vartheta_+ = \vartheta_1 + \vartheta_2$  which takes arbitrary values, and the angle  $\vartheta_- = \vartheta_1 - \vartheta_2$  which is fixed by the condition

$$\cosh \vartheta_{-} = b/a. \tag{D.4}$$

Inverting the matrix  $qq^T$  (see Eq. D.3), we find the following expression for the scaling dimensions:

$$\Delta(\mathbf{n}) = \frac{1}{b^2 - a^2} \begin{pmatrix} n_1 \\ n_2 \end{pmatrix}^T \begin{pmatrix} A_- & B \\ B & A_+ \end{pmatrix} \begin{pmatrix} n_1 \\ n_2 \end{pmatrix}, \tag{D.5}$$

where

$$\begin{split} A_{\pm} &= b \cosh \vartheta_+ \pm \sqrt{b^2 - a^2} \sinh \vartheta_+, \\ B &= -a \cosh \vartheta_+. \end{split}$$

We see that  $\Delta$  indeed depends on the additional free parameter, the angle  $\vartheta_{+}$ .

If we assume that the strong long-range Coulomb interaction is a dominant contribution to the Hamiltonian, then we may approximate  $q_{11}=q_{12}$ , or equivalently,  $\vartheta_2=-\vartheta_1$ . This condition leads to  $\cosh\vartheta_+=1$  and  $\sinh\vartheta_+=0$ , so that the expression for the scaling dimension simplifies:

$$\Delta(\mathbf{n}) = \frac{1}{b^2 - a^2} \begin{pmatrix} n_1 \\ n_2 \end{pmatrix}^T \begin{pmatrix} b & -a \\ -a & b \end{pmatrix} \begin{pmatrix} n_1 \\ n_2 \end{pmatrix}. \tag{D.6}$$

Calculating the product, we arrive at the final result (7.5).

Next, we evaluate the exponents  $\delta_1$  and  $\delta_2$ . In the chiral case, which we consider as an example,  $K = qq^T$ , and the following parametrization is required

$$q/\sqrt{a} = \begin{pmatrix} \cos \theta_1 & \sin \theta_1 \\ \cos \theta_2 & \sin \theta_2 \end{pmatrix} \tag{D.7}$$

with the condition that  $\cos(\theta_2 - \theta_1) = b/a$ . Then, using definition (6.42), we find

$$\delta_1(\mathbf{n}) = \frac{a}{a^2 - h^2} (n_1 \cos \vartheta_1 - n_2 \cos \vartheta_2)^2, \tag{D.8}$$

$$\delta_2(\mathbf{n}) = \frac{a}{a^2 - b^2} (n_1 \sin \vartheta_1 - n_2 \sin \vartheta_2)^2. \tag{D.9}$$

Thus, we see that by measuring the exponents  $\delta_1$  and  $\delta_2$  one can in principle extract the parameter  $\vartheta_+$ . However, we stress again that, for strong Coulomb interaction,  $\vartheta_+=0$ . In this case, expressions for exponents simplify. Namely, taking into account that  $a+b=2/\nu$ , we find that

$$\delta_1(\mathbf{n}) = \frac{(n_1 - n_2)^2}{2(a - b)}, \quad \delta_2(\mathbf{n}) = \frac{\nu}{4}(n_1 + n_2)^2.$$
 (D.10)

In the non-chiral case, analogous calculations lead to similar expressions:

$$\delta_1(\mathbf{n}) = \frac{(n_1 - n_2)^2}{2(b - a)}, \quad \delta_2(\mathbf{n}) = \frac{\nu}{4}(n_1 + n_2)^2.$$
 (D.11)

#### E Mathematical Aspects of the Theory of Quantum Hall Lattices

In this section we wish to describe briefly the quantum Hall lattice construction proposed in Refs. [1, 2]. This construction is a mathematical reformulation of physical requirements for the effective theory of a quantum Hall system discussed in Sects. 6.1 and 6.2. It provides a method, based on using invariants of lattices, to classify physically allowed low-energy effective models of quantum Hall edge states. The main physical consequences of the lattice construction include a determination of the minimal charge of quasi-particle, of the minimal number of edge channels, for given filling factor, etc. Here we summarize the lattice construction and present the results without proof.

First, we recall that action (6.24) of the effective theory is parameterized by the vector of coupling constants,  $\mathbf{Q} = \{Q_i\}$ , introduced in Sect. 6.2. Local excitations are represented by vertex operators,  $\exp\left(i\sum_j q_j\phi_j\right)$ , and labeled by vectors  $\mathbf{q} = \{q_i\}$ ; so the sum of two such vectors corresponds to the product of operators. Defining the scalar product:

$$\langle \mathbf{a}, \mathbf{b} \rangle = \sum_{i} a_i b_i \sigma_i,$$
 (E.1)

where  $\sigma_i$  is the chirality of  $i^{th}$  channel, we represent the electric charge (6.29) of an excitation corresponding to the vector  $\mathbf{q}$  and the statistical phase (6.28) of two excitations corresponding to  $\mathbf{q}_1$  and  $\mathbf{q}_2$  as

$$Q_{\text{em}} = \langle \mathbf{Q}, \mathbf{q} \rangle, \quad \theta_{12} = \pi \langle \mathbf{q}_1, \mathbf{q}_2 \rangle,$$
 (E.2)

respectively.

As discussed in Sect. 6.2, after fixing the coupling constants  $Q_i$  (i.e. fixing the action), we have to choose electronic excitations. We denote them with  $\mathbf{q}_{\alpha}$ . Multielectron excitations form an integral lattice  $\Gamma$ :  $\Gamma = \{k_{\alpha}\mathbf{q}_{\alpha}|k_{\alpha} \in \mathbb{Z}\}.$  (E.3)

It has been mentioned in Sect. 6.2.2 that choosing some different sets of elementary electronic excitations is equivalent to choosing different bases in the same lattice  $\Gamma$ . Thus, the lattice  $\Gamma$  describes an effective theory in a basis-independent way. The condition that the electric charge  $\langle \mathbf{Q}, \mathbf{q} \rangle$  of any combination of electrons  $\mathbf{q} \in \Gamma$  is integer implies that the vector of couplings  $\mathbf{Q}$  belongs to the dual lattice  $\Gamma^*$ . Thus, by choosing the lattice  $\Gamma$  and a vector  $\mathbf{Q}$  of its dual, one selects a particular effective model.

Next, important physical constraints on the effective models discussed in Sect. 6.1 can be formulated as following:

- The condition of anomaly cancellation, for a given filling fraction  $\nu$ , implies that  $\langle \mathbf{Q}, \mathbf{Q} \rangle = \nu$ .
- The correct charge of electronic operators is guaranteed if the greatest common divisor of the coordinates of  $\mathbf{Q}$  in  $\Gamma^*$  is equal to 1, because this divisor is equal to the minimal value of  $\langle \mathbf{Q}, \mathbf{q} \rangle$  for  $\mathbf{q} \in \Gamma$ .
- The correct statistical phase of electronic excitations is a consequence of the condition  $\langle \mathbf{Q}, \mathbf{q} \rangle \equiv \langle \mathbf{q}, \mathbf{q} \rangle (\text{mod } 2), \ \forall \mathbf{q} \in \Gamma.$

The spectrum of allowed local excitations follows from the requirement that the wave function of the quantum Hall state is single-valued in the presence of an excitation  $\exp\left(i\sum_{j}p_{j}\phi_{j}\right)$ . We mentioned in Sect. 6.1 that this condition is equivalent to having integer relative statistical phases between electrons and quasiparticles:

$$\langle \mathbf{p}, \mathbf{q}_{\alpha} \rangle \in \mathbb{Z}.$$
 (E.4)

Thus, the lattice of allowed excitations is  $\Gamma^* \supseteq \Gamma$ . As we have shown in Sect. 6.2, the scaling dimension,  $\Delta$ , of the correlation function of the excitation  $\mathbf{p}$  does not depend on the Hamiltonian in a purely chiral theory. It is equal to the statistical phase  $\Delta = \langle \mathbf{p}, \mathbf{p} \rangle$ . So, for purely chiral models, the pair  $(\Gamma, \mathbf{Q})$  provides complete information about the effective theory. In order to do explicit calculations, one needs to introduce a particular basis for  $\Gamma$ . It is, however, not trivial to verify whether two different bases generate the same lattice. To distinguish effective models and, therefore, classify them, one needs basis-independent information about lattices. Such information is provided by *lattice invariants*.

To classify the pairs  $(\Gamma, \mathbf{Q})$  satisfying the conditions discussed above, we introduce most important lattice invariants. Obvious invariants are the filling factor  $\nu = n_H/d_H$ , with  $n_H$  and  $d_H$  as coprime integers, and the dimension (or rank) of the lattice  $N = \dim \Gamma$ . One may show that, for any basis,  $\{\mathbf{e}_{\alpha}\}$ , of  $\Gamma$ , the determinant of the Gram matrix  $\Delta_{\Gamma} = \det \langle \mathbf{e}_{\alpha}, \mathbf{e}_{\beta} \rangle$  is also an invariant [3]. An interesting property of this determinant is the factorization  $\Delta_{\Gamma} = ld_H$ , where l is an integer number called *level*. Moreover, one may show that, for any basis  $\{\mathbf{e}^{\alpha}\}$  of  $\Gamma^*$ , the greatest common divisor  $g = \gcd(Q^1, \ldots, Q^N)$  of the numbers  $Q^{\alpha} = \Delta_{\Gamma} \langle \mathbf{Q}, \mathbf{e}^{\alpha} \rangle$  is an invariant, and that  $l = \lambda g$ , where  $\lambda$  is an integer. This number  $\lambda$  is an important parameter often called the *charge parameter*. It determines the minimal possible electric charge of a quasi-particle:

$$e^* = \min_{\mathbf{p} \in \Gamma^*, \langle \mathbf{Q}, \mathbf{p} \rangle \neq 0} |\langle \mathbf{Q}, \mathbf{p} \rangle| = \frac{1}{\lambda d_H}.$$
 (E.5)

Finally, one introduces two further invariants, called minimal and maximal relative angular momenta. The minimal relative angular momentum is defined as

$$\ell_{\min} = \min_{\mathbf{q} \in \Gamma, \langle \mathbf{O}, \mathbf{q} \rangle = 1} \langle \mathbf{q}, \mathbf{q} \rangle. \tag{E.6}$$

Introducing the set,  $B_{\mathbf{Q}}$ , of all possible electronic bases,  $\{\mathbf{q}_{\alpha}\}$ , of  $\Gamma$ , for a given  $\mathbf{Q}$  (i.e., such that  $\forall \alpha : \langle \mathbf{Q}, \mathbf{q}_{\alpha} \rangle = 1$ ), one defines the maximal relative angular momentum as

$$\ell_{\max} = \min_{\{\mathbf{q}_{\alpha}\} \in \mathcal{B}_{\mathbf{Q}}} \left( \max_{\alpha} \langle \mathbf{q}_{\alpha}, \mathbf{q}_{\alpha} \rangle \right). \tag{E.7}$$

The invariants  $\ell_{\text{min}}$  and  $\ell_{\text{max}}$  cannot take arbitrary values. For instance, in purely chiral models, they are constrained by the inequality  $1/\nu \le \ell_{\text{min}} \le \ell_{\text{max}}$ .

The simplest examples of such lattice construction appear in the case of dimension N=1. For one-dimensional lattices, there is only one independent invariant  $\ell_{\max}=\ell_{\min}=\Delta_{\Gamma}=m$ , where m is an odd integer. This number is nothing but the statistical phase of an electron, therefore  $Q=1/\sqrt{m}$  and the filling factor  $\nu=1/m$ . Moreover, it is easy to see that the level  $l=\Delta_{\Gamma}/d_H=1$ , hence the charge parameter  $\lambda=1$ , and we find that the minimal electric charge is  $e^*=1/m$ . We conclude that the quantum Hall lattices

$$\Gamma_m = \{ n\sqrt{m}\mathbf{e} | n \in \mathbb{Z} \} \tag{E.8}$$

with coupling  $\mathbf{Q}_m = \mathbf{e}/\sqrt{m}$  and  $\nu = 1/m$  are the only ones allowed for N = 1.

For the two-field case, N=2, the construction of allowed lattices is more complex. From the definition of relative angular momenta it follows that we may choose electronic bases with a Gram matrix of the following form:

$$K = \begin{pmatrix} \ell_{\min} & b \\ b & \ell_{\max} \end{pmatrix}. \tag{E.9}$$

We consider lattices with  $\ell_{\text{max}} < 7$ , which are physically most relevant. Then one may simply list all models by going through all possible values of  $\ell_{\text{max}}$ ,  $\ell_{\text{min}}$  and b [1]. Furthermore, we limit our attention to the case  $\ell_{\text{min}} = \ell_{\text{max}}$ , which is most important in the context of Chap. 7.

For convenience, we choose coordinates such that  $\mathbf{Q}=(\sqrt{\nu},0)$ . The condition of unit charge,  $\langle \mathbf{Q}, \mathbf{q}_{\alpha} \rangle = 1$ , for  $\alpha=1,2$ , partially fixes the form of electron vectors,  $\mathbf{q}_{\alpha}$ , in these coordinates. Namely,  $\mathbf{q}_{1}=(1/\sqrt{\nu},s)$  and  $\mathbf{q}_{2}=(1/\sqrt{\nu},-s)$ , where the number s is yet to be determined. It follows from the requirement

<sup>&</sup>lt;sup>1</sup> Numerical simulations [4] show that for larger values of statistical phases the quantum Hall state is not stable, and electrons form a Wigner crystal [5].

 $|\mathbf{q}_1|^2 = |\mathbf{q}_2|^2 = \ell_{\max}$  that  $s^2 = \ell_{\max} - 1/\nu$ . The mutual statistical phase of two electrons,  $\theta_{12} = \pi(1/\nu - s^2)$ , should be an integer. This implies that  $\ell_{\max} + \theta_{12}/\pi = 2/\nu$  is an integer number. Thus we see that the special case  $\ell_{\min} = \ell_{\max}$  corresponds to  $\nu = 2/m$  where m is an integer. Note that, for  $\ell_{\max} < 7$ , the converse statement is also true, i.e., for  $\nu = 2/m$ , all the two-dimensional lattices have  $\ell_{\min} = \ell_{\max}$ .

After some elementary calculations, we find that for  $\nu=2/m$  Gram matrix (E.9) may be expressed as:

$$K = \begin{pmatrix} \ell_{\text{max}} & \ell_{\text{max}} - l \\ \ell_{\text{max}} - l & \ell_{\text{max}} \end{pmatrix}. \tag{E.10}$$

From condition (6.34), applied to Eq. (E.10), we find that the level  $l=2\ell_{\rm max}-m=2s^2$ . Therefore, all the lattices in the case  $\nu=2/m$  can be parameterized by *only two* numbers, m and l. It is important to observe that, for all these lattices,  $\lambda=1$ . Hence, for two-field models with  $\nu=2/m$ , the minimal charge is always  $e^*=1/m$ . Introducing a pair of orthogonal vectors,  $\mathbf{e}_{1,2}$ , so that  $\mathbf{q}_{1,2}=\sqrt{m/2}\mathbf{e}_1\pm\sqrt{l/2}\mathbf{e}_2$ , the lattices may be written explicitly as

$$\Gamma_{ml} = \{ \sqrt{m/2} (n_1 + n_2) \mathbf{e}_1 + \sqrt{l/2} (n_1 - n_2) \mathbf{e}_2 | n_{1,2} \in \mathbb{Z} \},$$
 (E.11)

and the couplings  $\mathbf{Q}_{ml} = \sqrt{2/m} \, \mathbf{e}_1$ . Finally, we stress that *K*-matrices (7.8) and (7.9) proposed in Sect. 7.1 are exactly the Gram matrices (E.10) for the particular case  $\nu = 2/3$ .

## F Quantization of Chern-Simons Theory

The purpose of this appendix is to recall basic aspects of the quantization of the topological Chern–Simons theory, described by the action (1.42), which is invariant under the gauge transformations (1.40). The most important property of the action (1.42) is that it is topologically invariant. This action is generally covariant, i.e., it does not depend on the metric tensor  $g_{\mu\nu}$ , and it is invariant under arbitrary smooth transformation of coordinates. Indeed, under the change of coordinates  $x^{\mu} \to y^{\mu'}(x^{\mu})$ , the  $B_{\mu}$  field transforms as  $B_{\mu'} \partial y^{\mu'} / \partial x^{\mu}$ , so that the action takes the following form in the new coordinates:

$$S_0[B] = \alpha_0 \int d^3x \epsilon^{\mu\nu\lambda} B_\mu \hat{\partial}_\nu B_\lambda = \alpha_0 \int \frac{d^3y}{|\det J|} \epsilon^{\mu\nu\lambda} J_\mu^{\mu'} J_\nu^{\nu'} J_\lambda^{\lambda'} B_{\mu'} \hat{\partial}_{\nu'} B_{\lambda'}, \qquad (F.1)$$

<sup>&</sup>lt;sup>2</sup> In our presentation, we choose readability over mathematical rigor. A more detailed and rigorous discussion can be found in, e.g., Ref. [6].

$$\langle \bigcirc \rangle = \langle \bigcirc \rangle \neq \langle \bigcirc \rangle$$

**Fig. F.1** Schematic illustration of the topological invariance of the Chern–Simons theory. The vacuum average (F.4) for the contours  $C_1$  and  $C_2$  (shown by *red lines*) on the *left* is equal to the average for the contours shown in the *center*. At the same time, the averages for the contours shown in the *middle* and on the *right* may be different, because the corresponding contours are topologically inequivalent, i.e., they can not be transformed to each other by smooth deformations

where  $J_{\mu}^{\mu'}=\partial y^{\mu'}/\partial x^{\mu}$  is the Jacobian of the transformation. Next, by using the property of the antisymmetric tensor  $\epsilon^{\mu\nu\lambda}$ 

$$\epsilon^{\mu\nu\lambda}J^{\mu'}_{\mu}J^{\nu'}_{\nu}J^{\lambda'}_{\lambda}=\epsilon^{\mu'\nu'\lambda'}\det J, \tag{F.2}$$

we find that the action remains unchanged in new coordinates. Note, that the situation is different with the Maxwell-type contribution to the action (1.41), which has been neglected in the low-energy limit. This contribution must explicitly depend on the metric  $g_{\mu\nu}$  in order to be generally covariant:

$$S_1[B] = \alpha_1 \int d^3r \sqrt{\det g} F_{\mu\nu} F_{\lambda\rho} g^{\mu\lambda} g^{\nu\rho}, \tag{F.3}$$

where  $F_{\mu\nu} = \partial_{\mu}B_{\nu} - \partial_{\nu}B_{\mu}$ .

The topological invariance of the action (1.42) implies that the expectation value of an arbitrary observable depends only on the topological properties of this observable. For example, the vacuum average of the "fluxes" through the contours  $C_1$  and  $C_2$ 

$$\mathcal{L}(C_1, C_2) = 2i\alpha_0 \langle \oint_{C_1} B_\mu dx^\mu \oint_{C_2} B_\nu dx^\nu \rangle \tag{F.4}$$

does not depend on the shapes of the contours, as illustrated in Fig. F.1. This is because the shape of the contours can be changed with the help of the coordinate transformations, while the action is invariant under such transformations.

In the next step, we analyze the equations of motion for the fields  $B_{\mu}$  in order to identify physical states in the Chern–Simons theory. Variation of the action (1.42) with respect to  $B_{\mu}$  yields:

$$\epsilon^{\mu\nu\lambda} \partial_{\mu} B_{\lambda} = 0.$$
 (F.5)

Introducing time and spacial components,  $B_{\mu} = (B_t, \vec{B})$ , as well as the "electric"  $\vec{E} = \vec{\nabla} B_t - \partial_t \vec{B}$  and "magnetic"  $B = \partial_x B_y - \partial_y B_x$  fields, we rewrite Eq. (1.40) as follows:

$$E_{\rm r} = E_{\rm v} = B = 0.$$
 (F.6)

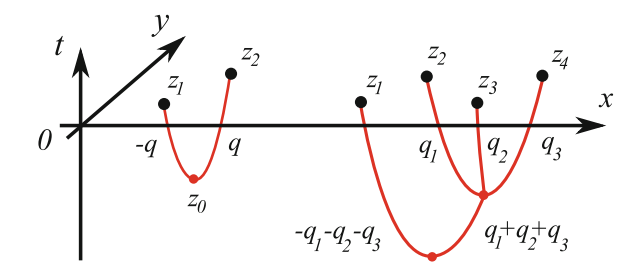


**Fig. F.2** Simple examples of states in the Chern–Simons field theory, created by Wilson lines (shown in *red color*). The state shown on the *left* is created by the operator  $\exp[iq\int_{z_0}^{z_1}B_\mu dx^\mu-iq\int_{z_0}^{z_2}B_\mu dx^\mu]$ . All the endpoints (shown by *black dots*) lie on the plane t=0. The state shown on the *right* is a more complex example of allowed states. Note the "charge conservation" condition (F.10) at all vertexes (shown by *red dots*)

Thus, the dynamics of a quantum Hall liquid is similar to the dynamics of a condensate in a superconducting metal. Moreover, in a topologically trivial region, the only solution of the equations of motion (F.5) up to the gauge transformations (1.40) is

$$B_{\mu} = 0. \tag{F.7}$$

Physically, this behavior reflects the presence of a gap for charge density excitations in bulk, which are, therefore, not present in the effective theory. We conclude, that the dynamics of a quantum Hall liquid is trivial, unless some topological defects are present.

The topological defects, which bear some similarities with Abrikosov vortexes in superconductors, may be described by the so called Wilson line operators:

$$W[\underline{C}] = \exp\left\{i\sum_{i} q_{i} \int_{C_{i}} B_{\mu} dx^{\mu}\right\}.$$
 (F.8)

They are generally parameterized by the set  $\underline{C} = \{C_i, q_i\}$  of contours  $C_i$  with numbers  $q_i$ . The operator (F.8) creates the vortexes along contours  $C_i$  with "vorticities"  $q_i$ . It turns out that, as we show in the following, these vortexes are local quasi-particle excitations with charges proportional to  $q_i$ . The space of states of the quantum Hall liquid described by the action (1.42) is then defined as a linear span of all vectors

$$|\underline{C}\rangle = \mathcal{W}[\underline{C}]|0\rangle,\tag{F.9}$$

created by Wilson lines which end on the surface t = 0, and satisfy the condition

$$\sum_{i} q_i = 0 \tag{F.10}$$

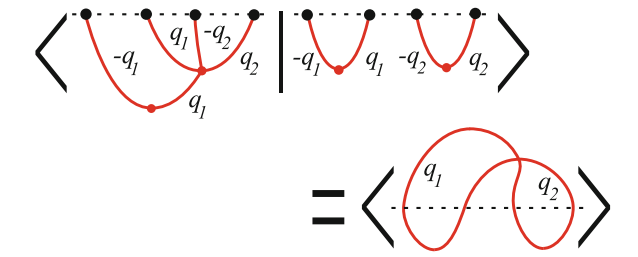


Fig. F.3 An example of the scalar product (F.11) in the Chern–Simons theory. Left and right states are described by corresponding Wilson lines. The dashed line shows the position of the plane t = 0. The Wilson line creating the left state should be inverted in time and combined with the Wilson line which creates the right state. The scalar product is then given by the average of the resulting closed Wilson line, which can be evaluated with the help of Eq. (F.12)

at all vertexes. In the following we show, that this condition guarantees the gauge-invariance of the theory. Two examples of such lines are presented in Fig. F.2. Obviously, the lines with the same endpoints  $z_i$  and vorticity  $q_i$ , which are topologically equivalent, create the same state.

The scalar product of two arbitrary states (F.9) is given by the expression

$$\langle \underline{C}_1 | \underline{C}_2 \rangle = \langle \mathcal{W}[\underline{C}_1^* + \underline{C}_2] \rangle, \tag{F.11}$$

where  $\underline{C}_1^*$  denotes the set of contours, which are time reversed with respect to the contours of the set  $\underline{C}_1$ . This procedure is illustrated in Fig. F.3. We show below, that the scalar products of vectors created by Wilson lines with different endpoints or with non-matching  $q_i$  are zero, i.e. the corresponding states are orthogonal. For non-vanishing products, the average on the right hand side of Eq. (F.11) can be found as a Gaussian path integral:

$$\langle \mathcal{W}_{\underline{C}} \rangle = \int \mathcal{D}B_{\mu} \exp \left\{ iS_0[B] + i \sum_i q_i \oint_{C_i} B_{\mu} dx^{\mu} \right\}.$$
 (F.12)

The set  $\underline{C} = \underline{C}_1^* + \underline{C}_2$  contains only closed contours. Therefore, taking into account the condition (F.10), we conclude that all the scalar products in the theory are gauge invariant. The definition (F.11) of the scalar product completes the construction of the *quantum* Chern–Simons theory. In what follows, we use this definition in order to find properties of the excitations created by Wilson lines.

One of the most important properties of local excitations is their statistical phase. In the Chern–Simons theory, the statistical phase  $\theta_{12}$  of two excitations, labeled by  $q_1$  and  $q_2$ , is defined as the relative phase of the wave functions, which differ by braiding of corresponding Wilson lines. In the example shown in Fig. F.4, the overlap of the wave functions is equal to  $\exp(2i\theta_{12})$ . In order to find this phase, one needs to evaluate the corresponding vacuum average. Using the Gaussian character of the theory, we write

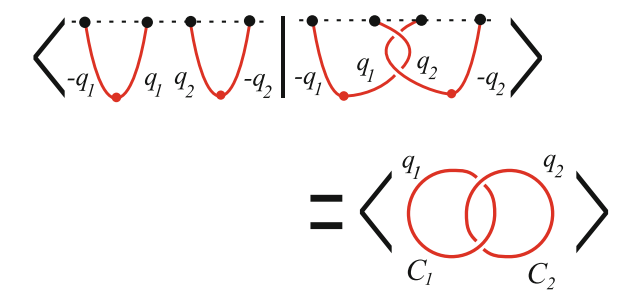


**Fig. F.4** The calculation of the statistical phase  $\theta_{12}$  of two excitations labeled by  $q_1$  and  $q_2$  is illustrated. The scalar product of the two states shown on the *left hand side* is equal to  $\exp(2i\theta_{12})$ . According to Eqs. (F.11) and (F.16), the resulting *Wilson line* on the *right hand side* is proportional to the linking number of the two loops  $C_1$  and  $C_2$ 

$$\theta_{12} = \frac{iq_1q_2}{2} \left\langle \oint_{C_1} B_{\mu} dx^{\mu} \oint_{C_2} B_{\mu} dx^{\mu} \right\rangle = \frac{iq_1q_2}{2} \oint_{C_1} dx^{\mu} \oint_{C_2} dy^{\mu} G_{\mu\nu}(x - y), \quad (F.13)$$

where the correlation function is defined as

$$G_{\mu\nu}(x-y) = \langle B_{\mu}(x)B_{\nu}(y)\rangle. \tag{F.14}$$

And again, because the action (1.42) is quadratic, the correlation function is the Green function of the corresponding equations of motion (F.5):

$$\epsilon^{\mu\rho\lambda} \partial_{\lambda} G_{\rho\nu}(x-y) = (i/2\alpha_0) \delta^{\mu}_{\nu} \delta(x-y).$$
 (F.15)

Applying the Stokes' theorem in Eq. (F.15) to the integral over the contour  $C_1$ , we find that

$$\theta_{12} = \frac{q_1 q_2}{4\alpha_0} \int_{D_1} n_{\mu} d^2 x \oint_{C_2} dy^{\mu} \delta(x - y), \tag{F.16}$$

where  $n_{\mu}$  is the unit vector, orthogonal to the surface  $D_1$  bounded by  $C_1$ . The integral on the right hand side of Eq. (F.16) is known as the linking number  $\mathcal{L}(C_1,C_2)$  of the contours  $C_1$  and  $C_2$ . It counts how many times one of the contours pinches through a surface bounded by another. This number is obviously independent on the choice of the surface, and is topologically invariant. In the case we consider, illustrated on right hand side of the Fig. F.4, this number equals to one, and thus the statistical phase is

$$\theta_{12} = \frac{q_1 q_2}{4\alpha_0}. (F.17)$$

Another important property of local excitations is their charge. First, we note that the Wilson lines (F.8) contain open contours and therefore are not gauge-

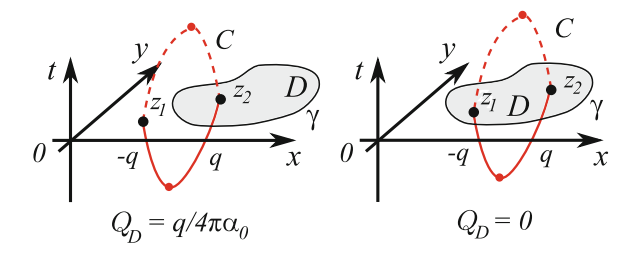


Fig. F.5 The evaluation of the value of charge operator  $Q_D$ , defined in Eq. (F.19), is illustrated. Left panel Only one endpoint  $z_2$  is inside the region D. Therefore, Eq. (F.21) gives  $Q_D = q/4\pi\alpha_0$ . Right panel Both endpoints  $z_1$  and  $z_2$  belong to the region D, therefore the charge is zero. These results are easily understood in terms of the linking number of the boundary  $\gamma$  enclosing the charge, and of the Wilson line C, obtained as a combination of the initial (solid) Wilson line and of the corresponding time-reversed (dashed) line (see Eq. F.20)

invariant. The states (F.9) transform under the gauge transformations (1.40) as following:

$$|\underline{C}\rangle \to \exp\left\{i\sum_{i}q_{i}\beta(z_{i})\right\}|\underline{C}\rangle.$$
 (F.18)

In other words, the states (F.9) behave as wave functions of charged particles localized at points  $z_i$ . From this it follows that any two states  $|\underline{C}\rangle$  and  $|\underline{C}'\rangle$  with different end points of Wilson lines, or with non-matching  $q_i$ , are orthogonal. This is because the overlap of those states vanishes upon the integration over the gauge  $\beta$ .

In order to find the values of charges of the quasi-particles, we recall that the connection between the bulk current density of the quantum Hall liquid and the Chern–Simons field is given by Eq. (1.39). Therefore, the operator of the charge confined in a region D, namely,  $Q_D \equiv \int_D d^2z J^0$ , can be written as

$$Q_D = \frac{1}{2\pi} \int_D d^2 z \epsilon^{0\mu\nu} \partial_\mu B_\nu = \frac{1}{2\pi} \oint_{\gamma} B_\mu dx^\mu, \tag{F.19}$$

where we have applied the Stokes' theorem, and the contour  $\gamma = \partial D$  is the boundary of the region D (see Fig. F.5).

Next, we can formally evaluate the following average using the result (F.17) for braiding:

$$\langle \underline{C} | \exp(i\lambda Q_D) | \underline{C} \rangle = \exp\left\{ -\frac{i\lambda}{4\pi\alpha_0} \sum_i q_i \mathcal{L}(\gamma, C_i) \right\} \langle \underline{C} | \underline{C} \rangle. \tag{F.20}$$

It follows from Eq. (F.20), as well as from the orthogonality of the states with different end points of Wilson lines, that all the sates (F.9) are the eigenstates of the charge operator (F.19), so that one can write

$$[Q_D, \mathcal{W}[\underline{C}]] = \frac{1}{4\pi\alpha_0} \sum_i q_i \theta(z_i \in D) \mathcal{W}[\underline{C}], \qquad (F.21)$$

where the step function  $\theta$  is equal to one if the endpoint  $z_i$  lies inside the region D, as illustrated in Fig. F.5. In other words, each Wilson line indeed annihilates a local excitation with the charge  $q_i/4\pi\alpha_0$  at endpoint  $z_i$ . In Sect. 6.1 we show that the charge of the quasi-particles is quantized. This effect resembles the quantization of the magnetic flux in superconductors.

#### References

- 1. J. Fröhlich, U.M. Studer, E. Thiran, J. Stat. Phys. 86, 821 (1997)
- J. Fröhlich, B. Pedrini, in Statistical Field Theories (Kluwer Academic Publishers, Dordrecht, 2002)
- 3. J. Fröhlich, E. Thiran, J. Stat. Phys. **76**, 209 (1994)
- 4. X. Zhu, S.G. Louie, Phys. Rev. B 52, 5863 (1995)
- 5. R.E. Prange, S.M. Girvin (eds.) The Quantum Hall Effect (Springer, New York, 1987)
- M. Marino, Chern–Simons Theory Matrix Models and Topological Strings (Oxford University Press, Oxford, 2005)